

**Advanced Analysis of Well Treatment and Microseismic Events for Two Parallel
Horizontal Wells in The Utica Shale**

by

Yaareb Al Taweel

Bachelor of Science – Geology, University of Baghdad, 2003

Submitted to the Graduate Faculty of the
Dietrich School of Arts and Sciences in partial fulfillment
of the requirements for the degree of
Master of Science

University of Pittsburgh

2020

UNIVERSITY OF PITTSBURGH

DIETRICH SCHOOL OF ARTS AND SCIENCES

This thesis was presented

by

Yaareb Al Taweel

It was defended on

July 13, 2020

and approved by

Michael Ramsey, PhD, Professor of Volcanology & Planetary Science

Charles E. Jones, PhD, Senior Lecturer & Geology Advisor

Thesis Advisor: William Harbert, PhD, Professor of Geophysics

Copyright © by Yaareb Al Taweel

2020

Advanced Analysis of Well Treatment and Microseismic Events for Two Parallel Horizontal Wells in The Utica Shale

Yaareb Al Taweel, MS

University of Pittsburgh, 2020

Because unconventional reservoirs have become a major oil and gas resource there have been hundreds of studies and methods targeting every aspect of hydraulic fracturing, all attempting to optimize the treatment process and maximize well production of hydrocarbons. This is uniquely important in tight formations such as shales due to their low permeability and large spatial distribution. Hydraulic fracturing stimulation creates additional permeability and increase pore pressure within the formation by injecting fluids directly into the target formation. Microseismic data provide an insight into the effectiveness and efficiency of the hydraulic fracturing operation and show how fractures are progressing during treatment. Collections of injection specific microseismic emissions, or microseismic clouds show the stimulated volume and any possible communication with preexisting fracture systems. However, cloud volume whether it is a stage or the entire well could be exaggerated and misleading if irrelevant events are not excluded from the analyzes, such as dry events and/ or low frequent events, which are distinguished by the Gutenberg–Richter relation. In order to identify and separate those irrelevant events, this study utilizes multiple microseismic analytical techniques: triggering fronts and RT plots (Shapiro 2015), seismogenic index (Shapiro, et al. 2010) and the variation of b-value/ D-value for each stage. The triggering front method provides an approximate outermost envelope of the distances between event locations and the injection point as function of the time (Hummel and Shapiro 2012). Where it serves as quality control measure to separate between relevant microseismic

events or wet events and dry events that occurred on preexisting fractures. This becomes important where there is pattern, which can be recognized through multiple stages as this study shows.

My study showed that distinguishing between dry and wet events plays an important role in the interpretation of communication between wells. It also reveals preexisting fractures and their pattern. The collective analysis of formation properties and stimulation data has revealed that under similar circumstances the formation returns similar results.

Table of Contents

Acknowledgments	xxiv
1.0 Introduction.....	1
1.1 Hydraulic Fracturing	2
1.1.1 Utica Study.....	4
1.1.2 Marcellus Study.....	4
1.2 Data & Samples	5
1.2.1 Hydraulic Stimulations.....	7
1.2.2 Microseismic Data.....	7
1.2.3 Well Logs	10
1.3 Ground Operation	10
1.3.1 Equipment.....	10
1.3.1.1 Hydration Unit (Hydro).....	10
1.3.1.2 Hydraulic Pumps.....	11
1.3.1.3 Blender	12
1.3.1.4 Manifold Trailer.....	13
1.3.1.5 Densitometer	14
1.3.1.6 Acid Tube.....	14
1.3.2 Material.....	15
1.3.2.1 Fresh Water	15
1.3.2.2 Sand	15
1.3.2.3 Chemical Additives	15

1.3.3 Data Van	16
1.3.4 Execution of Treatment	17
1.4 Geology Overview.....	18
1.4.1 Depositional History.....	19
2.0 Theoretical Background.....	23
2.1 The b-value.....	23
2.2 The D-value	25
2.3 The Triggering Fronts and The R-T Plots	27
2.4 The Seismogenic Index (Σ)	29
2.5 The Well Logs	30
2.6 The Parent Child Relationship Quantification	33
2.7 The Integration of Microseismic Data with The Injection Process	35
3.0 Methods.....	38
3.1 The b-value.....	38
3.2 The D-value	39
3.3 The R-T Plot.....	40
3.4 The Seismogenic Index Σ	40
3.5 The Cumulative Moment Plot	41
3.6 The Elastic Properties and Lithology	41
3.7 Frac Hit.....	42
3.8 The Energy Budget.....	43
4.0 Results and Analysis	48
4.1 The Microseismic Catalog	48

4.2 The R-T Plots	53
4.3 The Mechanical Properties and Lithology	60
4.4 The Energy Budget and The Stimulated Volume.....	65
4.5 Individual Stage Analysis.....	67
5.0 Discussion.....	79
6.0 Conclusions.....	81
Appendix A Data Tables	83
Appendix B Complete Set of Stage Analyses.....	88
Bibliography	147

List of Tables

Table 1 Microseismic data statistics.	8
Table 2 A08 b-value and manitude of completeness calculation from three different methods .	83
Table 3 B11 b-value and manitude of completeness calculation from three different methods..	84
Table 4 Volume and energy calculation for each stage in A08 well, plus overlap volume and its energy.....	85
Table 5 Volume and energy calculation for each stage in B11 well, plus overlap volume and its energy.....	86

List of Figures

Figure 1 Schematic diagram showing the general features of a fracking operation. Source: ProPublica web site http://www.propublica.org/series/fracking	3
Figure 2 3D illustration of A08, O08, B11 and O11 wells with respect to the formations. The formations from top to bottom are Queenston (green), Utica (red), Point Pleasant (blue) and Trenton (yellow).	6
Figure 3 Map view illustration of A08 (red), O08 (blue), B11 (purple) and O11 (yellow) wells and microseismic events for both.	6
Figure 4 3D illustration of A08 and O08 showing locations of perforation and tool array configuration.	9
Figure 5 3D illustration of B11 and O11 showing locations of perforation and tool array configuration.	9
Figure 6 A trailer, engine, hydraulic system, open top hydration tank, image by: http://indpress.com	11
Figure 7 Hydraulic pump, image by: (Malone, et al. 2007).	12
Figure 8 Blender, image by: https://www.goes-well.com/frac-equipment/	13
Figure 9 Manifold trailer, image by: https://www.goes-well.com/frac-equipment/#Anker_Iron_Handling_Equipment	14
Figure 10 (left) The cross section above shows the subsurface position of the Marcellus Shale, Utica Shale and the continental basement rock. The line of cross section is shown as line A-B on the inset map (King 2016). (right) The green area on this map marks the geographic extent of the Utica Shale. Included in this extent are two laterally equivalent rock units: the Antes Shale of	

central Pennsylvania and Point Pleasant Formation of Ohio and western Pennsylvania. These rocks extend beneath several U.S. states, part of Lake Erie, part of Lake Ontario and part of Ontario, Canada. If developed throughout this extent, the Utica Shale gas play will be larger than any natural gas field known today (King 2016)..... 19

Figure 11 Late Ordovician paleogeographic reconstruction (445 Ma) exhibiting North America. Modified after Blakey (2011) (Popova 2017)..... 20

Figure 12 Geological cross-section through the Appalachian basin with the regional stratigraphic schema of the Ordovician interval (Popova 2017). 22

Figure 13 Example of frequency-magnitude plot showing cumulative curve versus magnitude and a b-value of 1.05 (Boroumand 2014). 24

Figure 14 The different stress regimes (top), the associated rock deformation (center), and resulting microseismicity (bottom). The little balls under the diagrams at the top represent the focal mechanisms for each stress regime. P and T denote the pressure axis (maximum compressive stress direction) and the tension axis (minimum compressive stress direction), respectively. The left column depicts the extensional regime with the associated normal faulting, opening of fractures, and large amount of small-magnitude events that are evenly distributed spatially. The strike-slip regime (center column) creates planar fractures which produce an even proportion of small-to-large events during slipping oriented along a plane. The right column shows the compressive stress regime which implies reverse faulting and closing of fractures with many large-magnitude events evenly distributed in space. In the center row, S_h and S_H represent, respectively, minimum and maximum horizontal stress, and S_v indicates vertical stress. Arrow thickness is proportional to stress magnitude. On the bottom row, event circle size is proportional to magnitude (Grob and Baan 2011). 26

Figure 15 R-t plots created for two case studies on water injection experiments in the framework of two different enhanced geothermic system projects - one at Fenton Hill, USA and the other at Soultz, France (Shapiro 2015). 28

Figure 16 Average seismogenic index computed for different hydraulic fracturing locations in hydrocarbon reservoirs (bottom) and in geothermal systems and other brine injections (top) (Shapiro, et al. 2010)..... 29

Figure 17 Cross plot of $\lambda\rho$ versus $\mu\rho$ depicting the orthogonal separation of lithologies. Terms listed above are defined as: SH – Shale, SS – Sandstone, SSG – Gas saturated Sandstone, SST – Cemented Sandstones, *CO3 – Carbonates (Anderson et al. 2001)..... 32

Figure 18 Plot of Mu-rho ($\mu\rho$) and Lambda-rho ($\lambda\rho$) logs showing sand and shale lithologies and the variation in the sandstone reservoirs based on dissimilar fluid content (Shadlow 2014). 33

Figure 19 These modeling illustrations show how 600-ft well spacing after 1 year of depletion can affect the pressure (left) and fracture geometry of the child well, which leads to negative impacts from fracture hits (black circles). The white circles show how longitude fractures may also form as a result, which are unlikely to be significant contributors to production. Source: Schlumberger (Jacobs 2017)..... 34

Figure 20 The top figure illustrates that if frac hits are not observed it may mean that an operator is leaving a portion of the reservoir untapped. A happy medium is shown in the bottom, in which a frac hit might take place but because it mainly involved fluids and not proppant, negative communication will be short-lived as any unproped fractures close. Source: Shell (Jacobs 2017). 35

Figure 21 Various scenarios based on pressure microseismic activity rates. (a) Uniform fractured growth in homogeneous reservoir with effective proppant placement. (b)Formation hardening

with increased stress and proppant screen out. (c) Formation weakening with decreased stress and effective proppant placement. (d) Fracture resistance with few pre-existing fractures and effective proppant placement. (e) Fracture compliance with fault activation and effective proppant placement (Maxwell 2014). 36

Figure 22 Schematic of various microseismic histograms (dark gray), relative to stimulation parameters and corresponding potential interpretation (Maxwell 2014). 37

Figure 23 Plot of magnitude with time, for a fault-activation example. Hatched area on left is the time period of active injection. Post-injection microseismicity rates and magnitude begin to subside, but, after 20 minutes, an increase in microseismicity and magnitude was recorded as a known fault was activated (Maxwell 2014). 37

Figure 24 Map view illustration of A08 (east well, red symbols) and B11 (west well, yellow symbols) and microseismic events for both. Symbol size is proportion to moment magnitude. The heel of each stimulation is positioned closest to the surface location of the well, the toe of each stimulation is farthest away from this surface location. 45

Figure 25 Map view illustrates well A08, stage 2 (yellow) and stage 4 (green). Well B11, stage 18 (purple) and stage 23 (blue). Symbol size is proportion to moment magnitude. The heel of each stimulation is positioned closest to the surface location of the well, the toe of each stimulation is farthest away from this surface location. 47

Figure 26 A08: D-value =1.79, b-value 1.16 and $M_c = -2.2$ 48

Figure 27 B11: D-value =2.01, b-value 1.13 and $M_c = -2.5$ 48

Figure 28 A08 and B11 magnitude vs. depth plots scaled by surface pressure (left) and GR log (right). 49

Figure 29 A08 (left) and B11 (right), Distance/ magnitude plots scaled by surface pressure, it illustrates the distance of events from the geophones array. 50

Figure 30 The results of b-value (sold lines) and M_c (dash lines) calculation on a stage level from three different methods analysing the microseismic catalog of well A08 and well B11.... 51

Figure 31 The linear regression models between the b-value the seismogenic index for A08 (top) and B11 (bottom). where R^2 are 0.8 and 0.6 respectively. The models illustrate the negative correlation between the b-value the seismogenic index. 52

Figure 32 A08 (top) and B11 (bottom) r-t plots illustrate the distance of microseismic events from the injection point vs. time, where black curve is the triggering front..... 53

Figure 33 Multiple views of the microseismic clouds showing dry and wet events for both wells. Where blue dots represent A08 wet events, red dots represent A08 dry events, green dots represent B11 wet events, and black dots represent B11 dry events. 55

Figure 34 A08 map view of dry events (red points) and wet events (black points) superimposed over the map of b-value distribution. 56

Figure 35 B11 map view of dry events (red points) and wet events (black points) superimposed over the map of b-value distribution. 57

Figure 36 B11 stage 1 rose diagram (left), best fitting plane (right). 58

Figure 37 B11 stage 1 map view plot, r-t plot, magnitude plot and cumulative moment plot. 59

Figure 38 A possible strik-slip fault events and the fault plane..... 59

Figure 39 B11 vertical logs: GR, density, shear modulus, bulk modulus, Young’s modulus, brittleness, lambda, and Poisson’s ratio. 60

Figure 40 The LMR cross plots for the vertical portion (right) and the lateral (right) scaled by depth..... 61

Figure 41 B11 horizontal logs: GR, density, shear modulus, bulk modulus, Young's modulus, brittleness, lambda, and Poisson's ratio.	62
Figure 42 B11 horizontal logs superimposed along the lateral. From top to bottom (GR log, brittleness index, and the microseismic catalog).	63
Figure 43 B11 stage 18 rose diagram (left), best fitting plane (right).	63
Figure 44 A08 stage 4 rose diagram (left), best fitting plane (right).	64
Figure 45 3D view illustrate the stimulated volume of each stage on both wells based on the triggering front	65
Figure 46 Bar plots for stimulated volume and overlap volume for both wells (blue & red). Bar plots for radiated energy and overlap energy (yellow & blue).	66
Figure 47 A08 stage 1 rose diagram (left), best fitting plane (right).	67
Figure 48 A08 stage 1 map view plot, r-t plot, magnitude plot and cumulative moment plot.	68
Figure 49 A08, stage 1 D-value =1.27, b-value ~1 and $M_c = -2.3$	69
Figure 50 A08 stage 2 rose diagram (left), best fitting plane (right).	70
Figure 51 A08 stage 2A map view plot, r-t plot, magnitude plot and cumulative moment plot. .	71
Figure 52 A08, stage2A D-value =1.24, b-value =1.46 and $M_c = -2.3$	72
Figure 53 A08 stage 4A rose diagram (left), best fitting plane (right).	73
Figure 54 A08 stage 4A map view plot, r-t plot, magnitude plot and cumulative moment plot. .	73
Figure 55 A08, stage 4A D-value =0.66, b-value =1.22 and $M_c = -2.4$	74
Figure 56 B11, stage 18 D-value =1.31, b-value =1.19 and $M_c = -2.5$	76
Figure 57 B11 stage 38 rose diagram (left), best fitting plane (right).	77
Figure 58 B11 stage 38 map view plot, r-t plot, magnitude plot and cumulative moment plot. ..	77
Figure 59 B11, stage 38 D-value =1.06, b-value =0.86 and $M_c = -3$	78

Figure 60 A08 stage 3 map view plot, r-t plot, magnitude plot and cumulative moment plot.	88
Figure 61 A08 Stage 3 best fitting plane.	88
Figure 62 A08 stage 5 map view plot, r-t plot, magnitude plot and cumulative moment plot.	89
Figure 63 A08 stage 5 best fitting plane.	89
Figure 64 A08 stage 6 map view plot, r-t plot, magnitude plot and cumulative moment plot.	90
Figure 65 A08 stage 6 best fitting plane.	90
Figure 66 A08 stage 7 map view plot, r-t plot, magnitude plot and cumulative moment plot.	91
Figure 67 A08 stage 7 best fitting plane.	91
Figure 68 A08 stage 8 map view plot, r-t plot, magnitude plot and cumulative moment plot.	92
Figure 69 A08 stage 8 best fitting plane.	92
Figure 70 A08 stage 9 map view plot, r-t plot, magnitude plot and cumulative moment plot.	93
Figure 71 A08 stage 9 best fitting plane.	93
Figure 72 A08 stage 10 map view plot, r-t plot, magnitude plot and cumulative moment plot. ..	94
Figure 73 A08 stage 10 best fitting plane.	94
Figure 74 A08 stage 11 map view plot, r-t plot, magnitude plot and cumulative moment plot. ..	95
Figure 75 A08 stage 11 best fitting plane.	95
Figure 76 A08 stage 12 map view plot, r-t plot, magnitude plot and cumulative moment plot. ..	96
Figure 77 A08 stage 12 best fitting plane.	96
Figure 78 A08 stage 13 map view plot, r-t plot, magnitude plot and cumulative moment plot. ..	97
Figure 79 A08 stage 13 best fitting plane.	97
Figure 80 A08 stage 14 map view plot, r-t plot, magnitude plot and cumulative moment plot. ..	98
Figure 81 A08 stage 14 best fitting plane.	98
Figure 82 A08 stage 15 map view plot, r-t plot, magnitude plot and cumulative moment plot. ..	99

Figure 83 A08 stage 15 best fitting plane.	99
Figure 84 A08 stage 16 map view plot, r-t plot, magnitude plot and cumulative moment plot.	100
Figure 85 A08 stage 16 best fitting plane.	100
Figure 86 A08 stage 17 map view plot, r-t plot, magnitude plot and cumulative moment plot.	101
Figure 87 A08 stage 17 best fitting plane.	101
Figure 88 A08 stage 18 map view plot, r-t plot, magnitude plot and cumulative moment plot.	102
Figure 89 A08 stage 18 best fitting plane.	102
Figure 90 A08 stage 19 map view plot, r-t plot, magnitude plot and cumulative moment plot.	103
Figure 91 A08 stage 19 best fitting plane.	103
Figure 92 A08 stage 20 map view plot, r-t plot, magnitude plot and cumulative moment plot.	104
Figure 93 A08 stage 20 best fitting plane.	104
Figure 94 A08 stage 21 map view plot, r-t plot, magnitude plot and cumulative moment plot.	105
Figure 95 A08 stage 21 best fitting plane.	105
Figure 96 A08 stage 22 map view plot, r-t plot, magnitude plot and cumulative moment plot.	106
Figure 97 A08 stage 22 best fitting plane.	106
Figure 98 A08 stage 23 map view plot, r-t plot, magnitude plot and cumulative moment plot.	107
Figure 99 A08 stage 23 best fitting plane.	107
Figure 100 A08 stage 24 map view plot, r-t plot, magnitude plot and cumulative moment plot.	108
Figure 101 A08 stage 24 best fitting plane.	108
Figure 102 A08 stage 25 map view plot, r-t plot, magnitude plot and cumulative moment plot.	109
Figure 103 A08 stage 25 best fitting plane.	109

Figure 104 B11 stage 2 map view plot, r-t plot, magnitude plot and cumulative moment plot.	110
Figure 105 B11 stage 2 best fitting plane.	110
Figure 106 B11 stage 3 map view plot, r-t plot, magnitude plot and cumulative moment plot.	111
Figure 107 B11 stage 3 best fitting plane.	111
Figure 108 B11 stage 4 map view plot, r-t plot, magnitude plot and cumulative moment plot.	112
Figure 109 B11 stage 4 best fitting plane.	112
Figure 110 B11 stage 5 map view plot, r-t plot, magnitude plot and cumulative moment plot.	113
Figure 111 B11 stage 5 best fitting plane.	113
Figure 112 B11 stage 6 map view plot, r-t plot, magnitude plot and cumulative moment plot.	114
Figure 113 B11 stage 6 best fitting plane.	114
Figure 114 B11 stage 7 map view plot, r-t plot, magnitude plot and cumulative moment plot.	115
Figure 115 B11 stage 7 best fitting plane.	115
Figure 116 B11 stage 8 map view plot, r-t plot, magnitude plot and cumulative moment plot.	116
Figure 117 B11 stage 8 best fitting plane.	116
Figure 118 B11 stage 9 map view plot, r-t plot, magnitude plot and cumulative moment plot.	117
Figure 119 B11 stage 9 best fitting plane.	117
Figure 120 B11 stage 10 map view plot, r-t plot, magnitude plot and cumulative moment plot.	118
Figure 121 B11 stage 10 best fitting plane.	118
Figure 122 B11 stage 11 map view plot, r-t plot, magnitude plot and cumulative moment plot.	119
Figure 123 B11 stage 11 best fitting plane.	119

Figure 124 B11 stage 12 map view plot, r-t plot, magnitude plot and cumulative moment plot.	120
Figure 125 B11 stage 12 best fitting plane.	120
Figure 126 B11 stage 13 map view plot, r-t plot, magnitude plot and cumulative moment plot.	121
Figure 127 B11 stage 13 best fitting plane.	121
Figure 128 B11 stage 14 map view plot, r-t plot, magnitude plot and cumulative moment plot.	122
Figure 129 B11 stage 14 best fitting plane.	122
Figure 130 B11 stage 15 map view plot, r-t plot, magnitude plot and cumulative moment plot.	123
Figure 131 B11 stage 15 best fitting plane.	123
Figure 132 B11 stage 16 map view plot, r-t plot, magnitude plot and cumulative moment plot.	124
Figure 133 B11 stage 16 best fitting plane.	124
Figure 134 B11 stage 17 map view plot, r-t plot, magnitude plot and cumulative moment plot.	125
Figure 135 B11 stage 17 best fitting plane.	125
Figure 136 B11 stage 19 map view plot, r-t plot, magnitude plot and cumulative moment plot.	126
Figure 137 B11 stage 19 best fitting plane.	126
Figure 138 B11 stage 20 map view plot, r-t plot, magnitude plot and cumulative moment plot.	127

Figure 139 B11 stage 20 best fitting plane.	127
Figure 140 B11 stage 21 map view plot, r-t plot, magnitude plot and cumulative moment plot.	128
Figure 141 B11 stage 21 best fitting plane.	128
Figure 142 B11 stage 22 map view plot, r-t plot, magnitude plot and cumulative moment plot.	129
Figure 143 B11 stage 22 best fitting plane.	129
Figure 144 B11 stage 23 map view plot, r-t plot, magnitude plot and cumulative moment plot.	130
Figure 145 B11 stage 23 best fitting plane.	130
Figure 146 B11 stage 24 map view plot, r-t plot, magnitude plot and cumulative moment plot.	131
Figure 147 B11 stage 24 best fitting plane.	131
Figure 148 B11 stage 25 map view plot, r-t plot, magnitude plot and cumulative moment plot.	132
Figure 149 B11 stage 25 best fitting plane.	132
Figure 150 B11 stage 26 map view plot, r-t plot, magnitude plot and cumulative moment plot.	133
Figure 151 B11 stage 26 best fitting plane.	133
Figure 152 B11 stage 27 map view plot, r-t plot, magnitude plot and cumulative moment plot.	134
Figure 153 B11 stage 27 best fitting plane.	134

Figure 154 B11 stage 28 map view plot, r-t plot, magnitude plot and cumulative moment plot.	135
Figure 155 B11 stage 28 best fitting plane.	135
Figure 156 B11 stage 29 map view plot, r-t plot, magnitude plot and cumulative moment plot.	136
Figure 157 B11 stage 29 best fitting plane.	136
Figure 158 B11 stage 30 map view plot, r-t plot, magnitude plot and cumulative moment plot.	137
Figure 159 B11 stage 30 best fitting plane.	137
Figure 160 B11 stage 31 map view plot, r-t plot, magnitude plot and cumulative moment plot.	138
Figure 161 B11 stage 31 best fitting plane.	138
Figure 162 B11 stage 32 map view plot, r-t plot, magnitude plot and cumulative moment plot.	139
Figure 163 B11 stage 32 best fitting plane.	139
Figure 164 B11 stage 33 map view plot, r-t plot, magnitude plot and cumulative moment plot.	140
Figure 165 B11 stage 33 best fitting plane.	140
Figure 166 B11 stage 34 map view plot, r-t plot, magnitude plot and cumulative moment plot.	141
Figure 167 B11 stage 34 best fitting plane.	141
Figure 168 B11 stage 35 map view plot, r-t plot, magnitude plot and cumulative moment plot.	142

Figure 169 B11 stage 35 best fitting plane.	142
Figure 170 B11 stage 36 map view plot, r-t plot, magnitude plot and cumulative moment plot.	143
Figure 171 B11 stage 36 best fitting plane.	143
Figure 172 B11 stage 37 map view plot, r-t plot, magnitude plot and cumulative moment plot.	144
Figure 173 B11 stage 37 best fitting plane.	144
Figure 174 B11 stage 39 map view plot, r-t plot, magnitude plot and cumulative moment plot.	145
Figure 175 B11 stage 39 best fitting plane.	145
Figure 176 B11 stage 40 map view plot, r-t plot, magnitude plot and cumulative moment plot.	146
Figure 177 B11 stage 40 best fitting plane.	146

List of Equations

Equation 1 (Gutenberg and Richter Formula) $\log_{10} N = a - b * M$	24
Equation 2 (Fractal Dimension) $\log_{10} N (R < r) = a - D * \log_{10} R$	25
Equation 3 (Euclidian Distance) $r (a \rightarrow b) = \sqrt{[(x_a - x_b)^2 + (y_a - y_b)^2 + (z_a - z_b)^2]}$	25
Equation 4 (Unique Pairs) $P = (x^2 - x) / 2$	26
Equation 5 (Triggering Front) $r_t = \sqrt{4\pi D t}$	27
Equation 6 (Shear Modulus) $\mu = \rho * V_s^2$	30
Equation 7 (Bulk Modulus) $K = (\rho * V_p^2) - (4/3 * V_s^2)$	31
Equation 8 (Young's Modulus) $E = (9 K \mu) / (3 K + \mu)$	31
Equation 9 (Poisson's Ratio) $\nu = (3K - 2 \mu) / (2 (3K + \mu))$	31
Equation 10 (Lame's Constant) $\lambda = E * \nu / ((1 + \nu) * (1 - 2 \nu))$	31
Equation 11 (Brittleness Index) $BR = (((E - 1) / 7) * 100) + (((\nu - 0.4) / -0.25) * 100) / 2$	31
Equation 12 (Order of Detectability) $\gamma = 10^{((1.5 M_w + 16.1) / 2)} / r$	39
Equation 13 (Seismogenic Index) $\Sigma = \log_{10} (N > M_c) - \log_{10} Q_c(t) + (b\text{-value} * M_c)$	40
Equation 14 (Seismic Moment) $Moment = 10^{(3/2 \text{ Magnitude} + 16.1)}$	41
Equation 15 (Injection Energy) $E_{in} = P(t) * Q(t) * t$	43
Equation 16 (Seismic Energy) $\log E = 1.5 M_w + 11.8$	43
Equation 17 (Seismic Energy) $E = 10^{(11.8 + 1.5 * \text{Magnitude})}$	43

Acknowledgments

My thanks go to EQT Corporation. for providing me with the excellent microseismic datasets and supporting data used within this thesis and allowing publication of this work. I want to thank my colleagues at Allegheny Printed Plastics for their support and encouragement.

I would like to express my gratitude to my advisor Dr. William Harbert for his guidance and support for my research. The practical knowledge, patience, and humor he brought to our interactions have helped me tremendously. I could not have picked a better advisor for my master's study. Also, I want to thank the rest of my committee: Dr. Michael Ramsey and Dr. Charles E. Jones. I have profound respect for every one of these individuals, not only as academics and mentors, but also as individuals. Each member possesses professional and personality traits that I strive to emulate, and I am honored to have them on my thesis committee.

I want to thank my family. My departed father Dr. Qahtan Altaweel, my mother and brothers, I could not have come this far without your love and guidance.

Finally, thank you to my children and my lovely wife Mays for always supporting me and pushing me to do my best and standing by my side in my darkest moment. I love you

1.0 Introduction

This thesis is a detailed analysis of hydrofracturing conducted at two wells within the Utica and Queenston formations. For the purpose of confidentiality, these wells will be referred to as A08 well and B11 well. A08 and B11 wells drilling process was completed in 2013. Both wells had been treated through hydraulic-fracturing stimulation using a plug and perf completion style. In a plug-and-perf operation, a plug and perforating guns are pumped to the appropriate depth. The plug is set, the zone perforated, and tools removed from the well. A ball is pumped down to isolate the zones below the plug, and the fracture stimulation treatment is pumped. The ball-activated plug diverts fracture fluids through the perforations into the formation. After the stage is completed, the next plug and set of perforations are delivered, and the process is repeated, moving up the well from the toe to the heel (Schlumberger). A08 was treated in 2013 and B11 was treated a year later.

When the data was presented to the University of Pittsburgh the main questions to be answered were 1) How could hydrofracturing stimulation be improved using insights from this investigation? 2) What relationships between stimulation and seismic expression of stimulation could be determined? 3) What relationships between a parent stimulation along one horizontal well and a microseismic emission from a location associated with the other horizontal well or far distant location (child event) might exist? 4) Why had they behaved differently throughout the process? Previous studies of hydrofracturing have been extensive and will be briefly reviewed along with fundamental physical relationships and observations.

The datasets which we had available for analysis included a detailed microseismic event catalog, well logs and pumping data. These were combined into a single geodatabase, which included all parameters. In addition, we had the topology of wells and some estimates of the

locations of formation tops. We did not have any seismic data available to constrain three-dimensional structure.

1.1 Hydraulic Fracturing

Hydraulic fracturing stimulates wells drilled into these formations, making profitable otherwise prohibitively expensive extraction. Within the past decade, the combination of hydraulic fracturing with horizontal drilling has opened shale deposits across the country and brought large-scale natural gas drilling to new regions. The fracking process occurs after a well has been drilled and steel pipe (casing) has been inserted in the well bore. The casing is perforated within the target zones that contain oil or gas, so that when the fracturing fluid is injected into the well it flows through the perforations into the target zones. Eventually, the target formation will not be able to absorb the fluid as quickly as it is being injected. At this point, the pressure created causes the formation to crack or fracture. Once the fractures have been created, injection ceases and the fracturing fluids begin to flow back to the surface. Materials called proppants (e.g., usually sand, or ceramic beads), which were injected as part of the frac fluid mixture, remain in the target formation to hold open the fractures. Typically, a mixture of water, proppants and chemicals is pumped into the rock or coal formation (Figure 1). There are, however, other ways to fracture wells. Sometimes fractures are created by injecting gases such as propane or nitrogen, and sometimes acidizing occurs simultaneously with fracturing. Acidizing involves pumping acid (usually hydrochloric acid), into the formation to dissolve some of the rock material to clean out pores and enable gas and fluid to flow more readily into the well (Earthworks 2019).

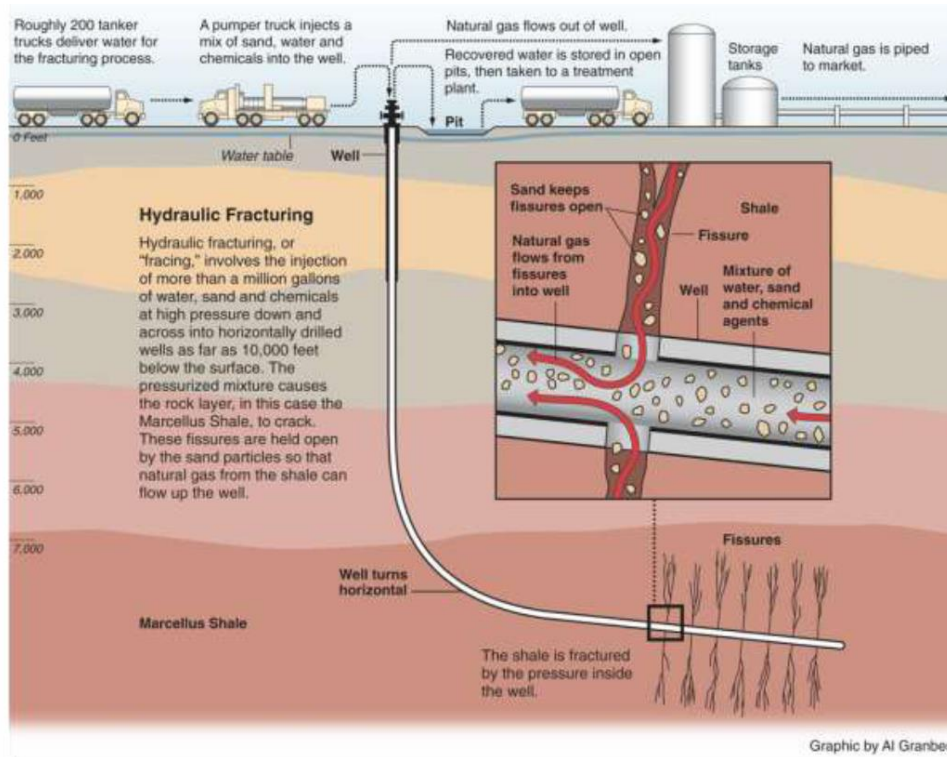


Figure 1 Schematic diagram showing the general features of a fracking operation. Source: ProPublica web site <http://www.propublica.org/series/fracking>.

Hydraulic fracturing has evolved into a technique suitable to stimulate most wells under extremely varying circumstances. Originally suggested for low-permeability gas, it still plays a crucial role in developing low-permeability sandstone formations and is increasingly used to produce from low permeability carbonates, shales, and coal seams. In general, a vertical well drilled and completed in a tight gas reservoir must be successfully stimulated to produce at commercial gas-flow rates and produce commercial gas volumes. Although in some naturally fractured tight gas reservoirs horizontal wells are successful, often they also need fracture stimulation. In this sense hydraulic fracturing is truly a reservoir stimulation technique. However, in higher-permeability soft formations (for instance in the Gulf of Mexico) hydraulic fracturing is primarily a near-wellbore flow enhancement (well stimulation) technique, and often its side effects – such as sanding prevention – might be the primary reason of application. In recent years high-

permeability fracturing has become as significant in the economic sense as low-permeability fracturing (Martin and Valkó 2007).

1.1.1 Utica Study

The example from the Utica Formation in Ohio is particularly interesting. Micro-seismic showed events occurring very early in the stimulation as much as 1220 m away from the injection location. It is difficult to reasonably explain how water could be reaching such a long distance away so quickly (Starr and Dennis 2016). After the calculation of the distance for each microseismic event from the injection point and the triggering front, it was determined that microseismic events above the curve (or dry events) were accruing during the pumping time, whereas events under triggering front (or wet events) were observed after pumping terminates and matched to the diffusivity trend. They concluded that clusters of dry events can indicate water being channeled by faults and fractures in the formation in advance of the main triggering front.

1.1.2 Marcellus Study

In late 2015, two parallel, horizontal wells at the Marcellus Shale Energy and Environmental Laboratory (MSEEL) site in Monongalia County, West Virginia were drilled and hydraulically fractured in the Marcellus Shale over 58 stages. The wells were stimulated separately from each other, with the more northerly well completed first, then the southerly well second, as opposed to a “zipper-frac” or simulfrac. Additionally, standard well logs including p-sonic, s-sonic, bulk density, total porosity, and natural gamma were acquired in the vertical well, and a full suite of geomechanical well logs were acquired along the length of one of the horizontal wells

(Zorn, et al. 2017). One of the main findings of this study was the negative correlation between Young's modulus (E), which is a measure of material stiffness and Poisson's ratio (ν), which is defined as a measure of the material toughness. A material that possesses a high ν will likely have a low E , and vice versa. They determined that the observed relationships between microseismic properties and elastic properties of organic shale rocks are a result of these slight interactions between E and ν along with other factors, such as pore pressure, pore shape, permeability/diffusivity, pumping pressure, rate, volume, and duration. These observations revealed the relationship between b-value (therefore, magnitudes and event count) and the values of E and ν . Where highest b-values correspond to the lowest values of E and ν and vice versa. The authors concluded that ν exerts a strong influence on the average moment magnitude of seismicity. ν and E influence the abundance and frequency magnitude distribution of seismicity. The elasticity of the rock, in the context of toughness and stiffness, directly affects the local in-situ state of stress, which in turn, affects the magnitude and abundance of microseismicity.

1.2 Data & Samples

The data include 2 horizontal wells for which microseismic data has been provided. The two wells have been treated through the hydrofracturing process, which is a necessary step to increase permeability and production in such a low permeability shale.

Well A08 is roughly 2 km lateral, whereas well B11 is 1.5 km lateral. In addition, there are 2 observation wells, which will be referred to as O08 and O11. Both observation wells were used to monitor seismic activity during treatment. These wells can be seen in relation to the microseismic study wells and formations in Figure 2 and Figure 3.

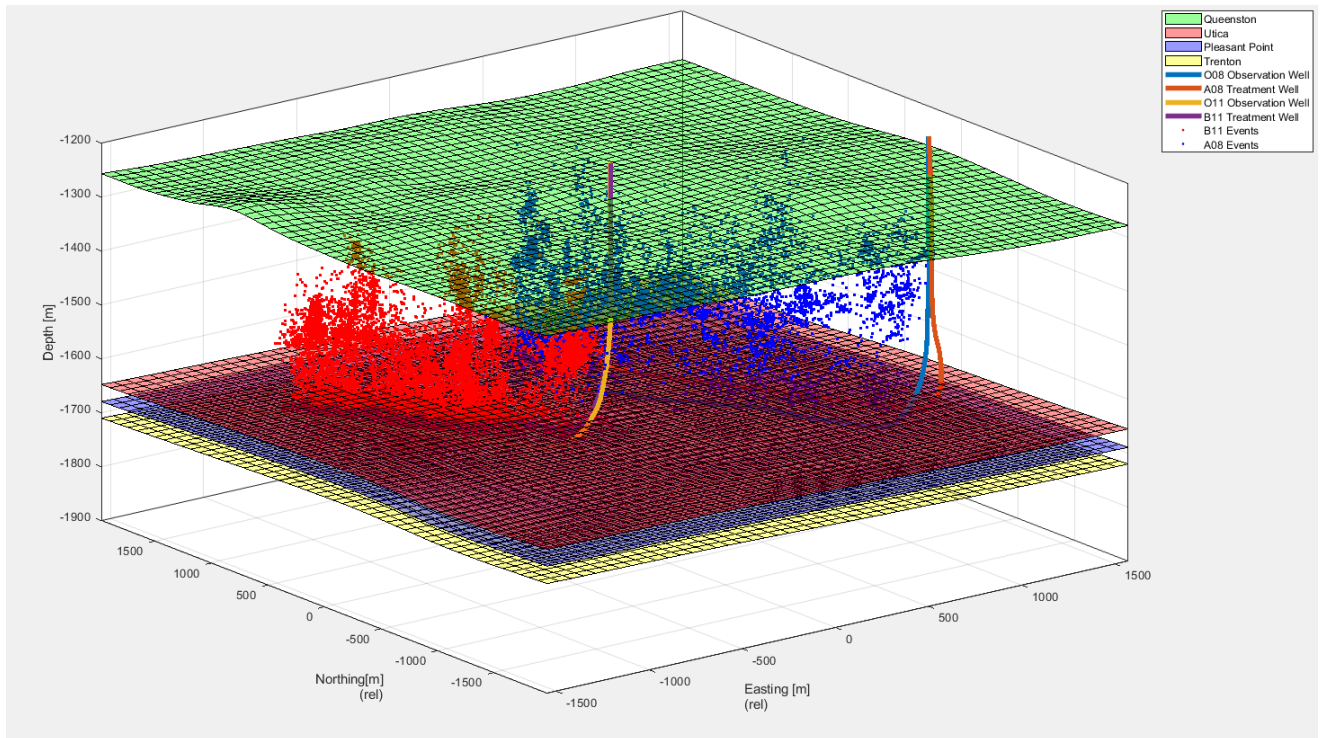


Figure 2 3D illustration of A08, O08, B11 and O11 wells with respect to the formations. The formations from top to bottom are Queenston (green), Utica (red), Point Pleasant (blue) and Trenton (yellow).

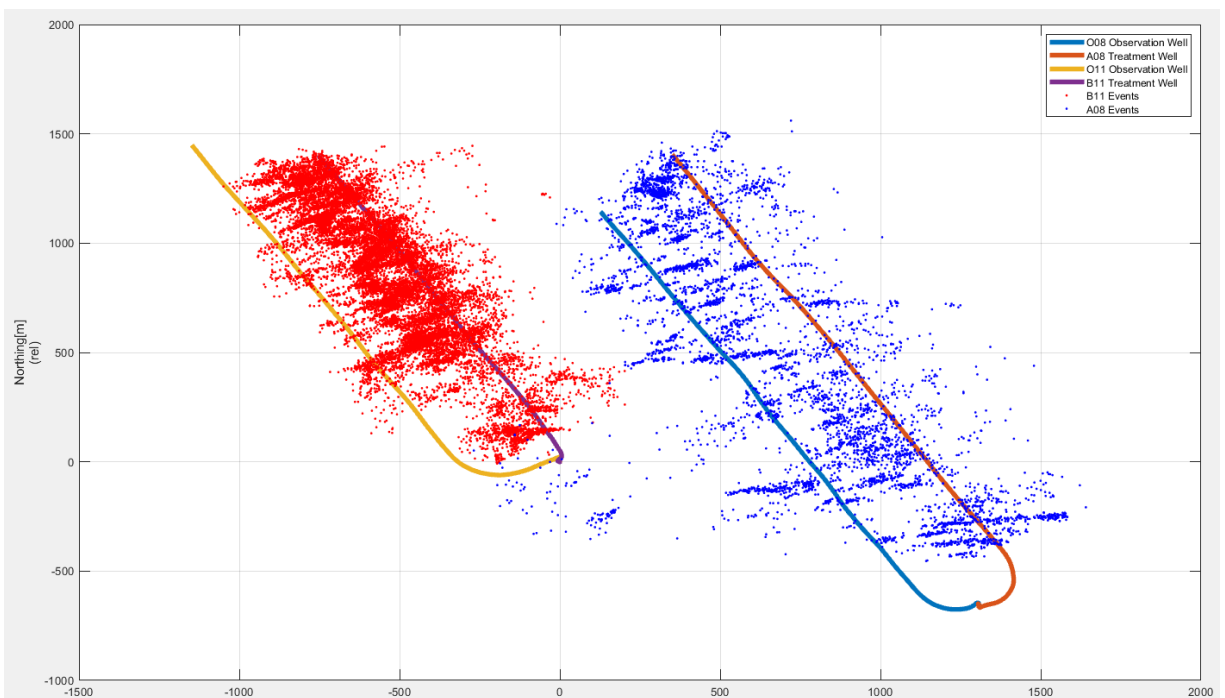


Figure 3 Map view illustration of A08 (red), O08 (blue), B11 (purple) and O11 (yellow) wells and microseismic events for both.

1.2.1 Hydraulic Stimulations

In shale reservoirs such as Utica and Point Pleasant, hydraulic stimulation and treatment programs must be used to improve production and create economically viable wells. In simple terms, this process requires the injection of fluids at high pressures into the reservoir until the formation fails and fractures, connecting permeable pathways to the wellbore. Proppant, usually in the form of sand, is also injected during this process to keep the induced fractures from closing after the stimulation.

The two study wells, Well A08 and B11, were both hydraulically stimulated using a Plug and Perf completion style, but the number of treatment stages as well as the type of fluid and proppant varied between wells. Well A08 contains 25 treatment stages, Well B11 contains 40 treatment stages. Wells were injected with fluid primarily consisting of slickwater, but Well A and B also had a crosslink gel included in its treatment fluid. This allowed for higher proppant concentrations to be injected into the formation. The proppants used were 100 mesh, 30/50 and 20/40 white sand.

1.2.2 Microseismic Data

Microseismic data were recorded from horizontal observation wells O08 and O11. The distance between treatment wells and their observation wells is about 320 m.

For well A08, in 25 stages; 5460 events were recorded that had depths between 1295 m and 1752 m, magnitudes between -0.69 and -3.08 (average -2.07 and std. of 0.3635). Stages 1-21

were registered by horizontal array configuration, whereas stages 22-25 were registered by vertical array (Figure 4).

For well B11, in 40 stages; 17248 events were recorded that had depths between 1313 m and 1820 m, magnitudes between -0.17 and -3.3 (average -2.3 and std. of 0.3648). Stages 1-34 were registered by horizontal array configuration, whereas stages 35-40 were registered by vertical array (Figure 5).

Table 1 Microseismic data statistics.

Well/stages	Min depth	Max depth	Total events	Min moment magnitude	Max moment magnitude	Avg. event moment magnitude	STD. magnitude
A08/25	1295 m	1752 m	5460	-3.08	-0.69	-2.07	0.3635
B11/40	1313 m	1820 m	17248	-3.3	-0.17	-2.3	0.3648

I used Petrel (BGC Mistral Team 2019), and MATLAB (The MathWorks, Inc 2015) to fit best fitting planes to the microseismic events for each well. Using these tools I found that the overall best fitting plane method and rose diagrams from Petrel show that the dominant azimuthal trend of the microseismic data for both wells is 235° and 242° respectively, this is consistent with the global maximum horizontal stress orientation (from the SHINE website), which is 241°. SHINE web-based application calculates the maximum horizontal stress orientation of the present-day stress field for any point on the Earth’s surface. it interpolates data records from regional or global dataset (Carafa and Tarabusi 2015). However, not all stages of each well show this azimuthal trend, but each study well has several stages that do display this characteristic microseismic event propagation direction.

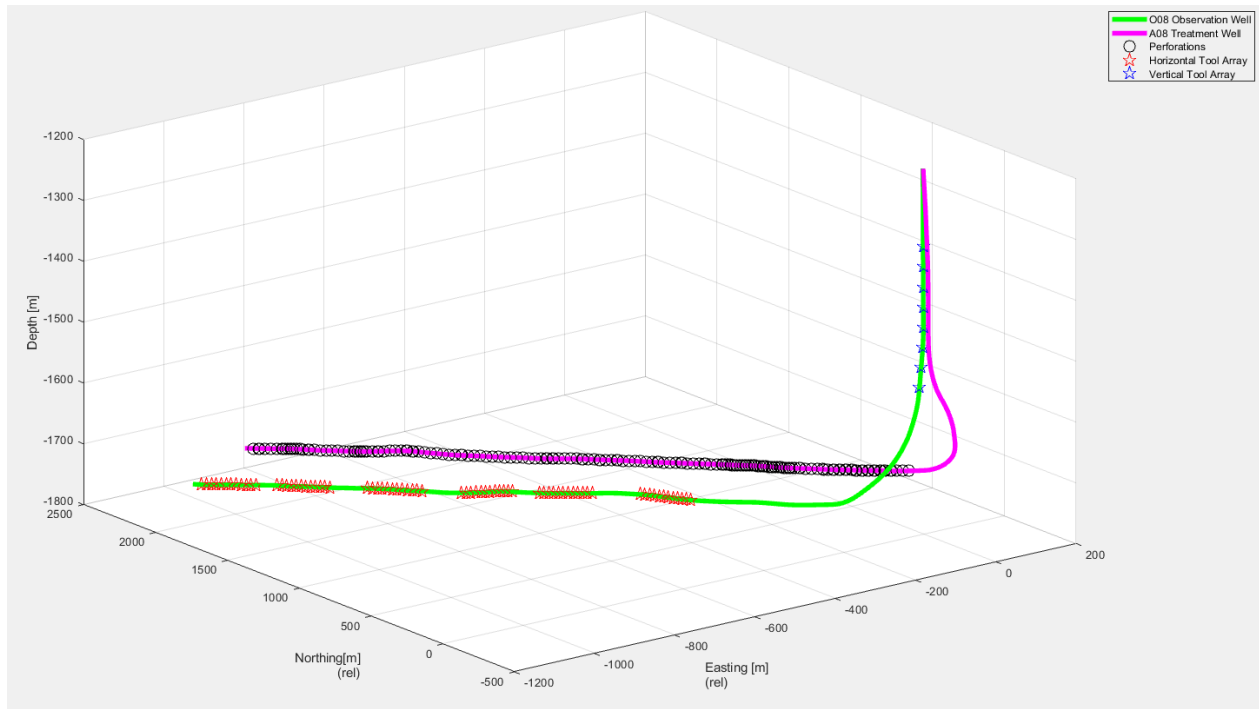


Figure 4 3D illustration of A08 and O08 showing locations of perforation and tool array configuration.

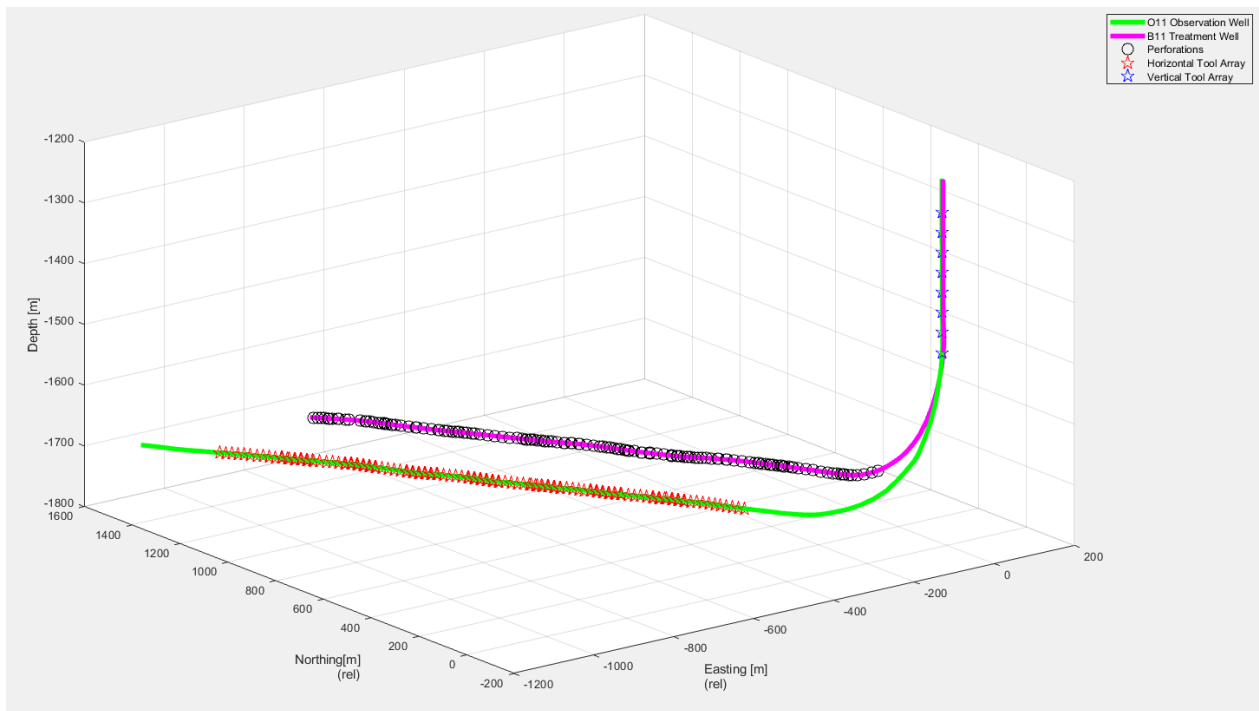


Figure 5 3D illustration of B11 and O11 showing locations of perforation and tool array configuration.

1.2.3 Well Logs

Well logs investigated in our analysis include gamma ray, density, deep resistivity, sonic and shear sonic. For B11, logs were provided for the entire lateral starting from 1768 m to 3477 m measured depth. However, the A08 logs were only present between 1798 m to 2129 m measured depth. Gamma ray logs are a complete set (vertical and horizontal) for both wells. All other logs were calculated based on the provided logs utilizing several equations in section 2.5 to produce moduli, brittleness and acoustic impedance.

1.3 Ground Operation

Hydrofracturing operation involves much specialized equipment, tasks, skills, and experience. Every command must be executed safely and carefully to prevent any possible injuries or fatalities in some cases, to prevent any damage to property equipment or both, which could lead to a disaster when the situation is out of control, and within timely manner. The purpose of this section is to explain how the frac operation is conducted and how the treatment data is acquired. I will briefly explain the frac operation, equipment, material needed, treatment data and plots.

1.3.1 Equipment

1.3.1.1 Hydration Unit (Hydro)

Hydro is a 53 feet trailer consisting of large open tank and manifolds to hold, mix and deliver water to the blender. The Hydro (Figure 6) has one centrifugal suction pump, and no

discharge pumps. The presence of the Hydro on any pad depends on the size of the pad. However, it is important to have it as a buffer between frac tanks and the blender. When a chemical (such as Gel) needs hydration, chem-add hose will be connected to the Hydro. The Hydro holds about 195 barrels (bbl).



Figure 6 A trailer, engine, hydraulic system, open top hydration tank, image by: <http://indpress.com>.

1.3.1.2 Hydraulic Pumps

These pumps provide the horsepower to push fluids and sand down hole (Figure 7). Pumps share the same characteristics. However, valves, seats and packing may vary between different brands. They are classified into two types:

- Tri pump (3 cylinders): Tri-plex plungers are 6” in diameter.
- Quintus Pump (5 cylinders): Quinta-plex plungers are 4.5” in diameter.

Although both pumps serve the same purpose, it is important to mention that tri plex has more discharge horsepower unlike quinta plex, which has smoother and more stable discharge rate.

Boost pressure or suction must be at 80 psi or higher, discharge pressure may reach 10,000 psi or higher depending on the well. Pumps can be centrally operated remotely from the vehicle control facility (datavan) or locally through a control panel on each pump. Before starting a new stage, all high-pressure manifolds and iron must be tested for leaks or issues, which is called pressure test.



Figure 7 Hydraulic pump, image by: (Malone, et al. 2007).

1.3.1.3 Blender

This device comes in different brands and with different controlling software. However, blenders (Figure 8) have the purpose which is mixing sand and chemical-adds with water and pushing the mixture to the hydraulic pumps through the low-pressure manifold of the manifold trailer.



Figure 8 Blender, image by: <https://www.goes-well.com/frac-equipment/>.

1.3.1.4 Manifold Trailer

The manifold trailer is a combination of low-pressure and high-pressure manifolds (Figure 9). It has an engine and a boost pump for the clean water, which is fluid that does not contain proppant. The manifold trailer also has several butterfly valves to direct the flow as required for the job. Where hydraulic pumps push fluid through the high-pressure manifold into the well. Low-pressure manifold is divided into 2 parts; 1. suction manifold for slurry and clean 2. discharge manifold to push fluid to pumps.



Figure 9 Manifold trailer, image by: https://www.goes-well.com/frac-equipment/#Anker_Iron_Handling_Equipment.

1.3.1.5 Densitometer

The densitometer is a radioactive tool installed to measure fluid density and sand concentration in the discharge manifold of the blender. There is another densitometer installed on the high-pressure manifold to read sand concentration going into the well. Both are connected to the data van for monitoring.

1.3.1.6 Acid Tube

The acid tube is a 53-foot long tank trailer designed to hold acid. it typically holds a 5000 gallons maximum capacity. Because hydrochloric acid is heavier than water, this tube can only transport 4300 – 4500 gallons due to regulations of Department of Transportation (DOT) regarding weight limits. The concentration of HCl is 28% from the vender and will be diluted as needed depending on the formation and the type of rocks. Typically, venders fill the acid tube from the

top port, the operator uses the bottom port controlled by a valve for discharge. When swapping to acid, the suction rate cannot be read anymore because the meter is in the blender. One hydraulic pump is designated for the acid whereas another pump pushes water to dilute the acid.

1.3.2 Material

1.3.2.1 Fresh Water

Fresh water is the fluid to be mixed with sand to produce injection slurry. The term fresh water does not necessarily mean potable water, it could be brine or recycled frac water depending on the available nearby water source.

1.3.2.2 Sand

The type of sand (proppant) required for the job is determined by the design. Typical proppant sizes are generally between 8 and 140 mesh (106 μm - 2.36 mm), for example 16-30 mesh (600 μm – 1180 μm), 20-40 mesh (420 μm - 840 μm), 30-50 mesh (300 μm – 600 μm), 40-70 mesh (212 μm - 420 μm) or 70-140 mesh (106 μm - 212 μm). When describing frac sand, the product is frequently referred to as simply the sieve cut, i.e. 20/40 sand (Horiba 2010).

1.3.2.3 Chemical Additives

The main functions of a fracturing fluid are to create and extend the fracture, transport proppant through the mixing and pumping equipment and into the fracture and place the proppant at the desired location in the fracture. Failure to adequately perform any one of these functions may compromise the stimulation benefit of the treatment (Gupta, et al. 2007). To help ensure

success, operators add a variety of chemicals to the fracturing mixture that depend on the formation and local circumstance:

- i. Friction reducer is an additive, generally in slurry or liquid form, used to reduce the friction forces experienced by tools and tubulars in the wellbore.
- ii. NE1 Non-emulsifier is a liquid additive, the main function of a non-emulsification agent is to break such an emulsion in-situ before the stimulated well is put back to production.
- iii. Biocide is an additive that kills bacteria. Bactericides are commonly used in water muds containing natural starches and gums that are especially vulnerable to bacterial attack.
- iv. Scale inhibitor is a liquid additive, it is used to control or prevent scale deposition in the production conduit or completion system.
- v. Buffer is an additive used to adjust and control the pH of stimulation fluids.
- vi. Crosslink is a compound, typically a metallic salt, mixed with a base-gel fluid, such as a guar-gel system, to create a viscous gel used in some stimulation or pipeline cleaning treatments.
- vii. Frac Gel is the primary fluid used in hydraulic fracturing operations. Several chemical additives generally will be added to the frac gel to form a treatment fluid specifically designed for the anticipated wellbore, reservoir, and operating conditions.
- viii. Gel breaker is a chemical used to reduce the viscosity of specialized treatment fluids such as gels and foams (Schlumberger 2020).

1.3.3 Data Van

The Data van is the central unit or operation nerve center where all data from all equipment are collected and recorded such as pumping rate (slurry and clean), sand concentration, chemical

additives, and pressure. Data van personal will monitor, collect, and record all stage data as a function of time such as:

- i. Surface Pressure and calculated bottom hole pressure.
- ii. Clean and slurry rate.
- iii. Proppant rate and type.
- iv. Chemical additives rate.
- v. Fluid density and viscosity.
- vi. Seismic activity (P-wave & S-wave), to be analyzed by geophysicists later.

1.3.4 Execution of Treatment

Well treatment is divided into stages based on treatment design, which include the amount of water, proppant amount and type, chemical additives and expected pressure. Rock type and condition will dictate the horsepower needed for the job.

Every stage starts with pressure test, where all hydraulic pumps, manifold and the well head are tested to specific pressure. The treatment pressure (surface pressure) is defined as the pressure of the treatment fluid measured at the well head. The surface pressure cannot exceed the pressure test under any circumstances, or it will result in a shutdown and replacement of all pressure equipment due to safety and performance issues. After a successful pressure test, the pressure is reduced to the ambient well pressure so the crew can open the well head for treatment.

Then next step is to start pumping fresh water to reach 15 bbl/min for the acid. Surface pressure will rise and then a sudden drop indicates the breakdown where the acid has reached the formation. At this point pump operators will increase the rate according to the design with respect to pressure. Next, the blender operator starts adding proppant into the blender tub measured by

pound/gallon (ppg), at this point the fluid is no longer fresh but slurry. As the stage progresses proppant rate will increase until the designated amount has been delivered into the well. Sufficient water should be on location to pump the designed fracture treatment and provide an adequate volume to flush or displace the final proppant stage to the top perforation in the wellbore (Malone, et al. 2007). The shutdown procedure will be performed by the supervisor, where he directs pump operators to drop the rate in 3 steps by shifting number of hydraulic pumps to neutral at every step until all pumps are in neutral. After the stage is concluded wireline will seal the stage with a rubber ball and perforate the next stage.

The crew might face many problems during the treatment. Some of these issues are complicated and require more specialized equipment, and many others can be solved by pumping more fresh water, acid or perforation depending on the nature of the issue, available data, and crew experience. During this study some of these issues will be discussed.

1.4 Geology Overview

The Point Pleasant and Utica formations are organic-rich units deposited in the Late Ordovician Appalachian Basin. The Point Pleasant Formation consists of interbedded limestone and generally organic-rich shales. The overlying Utica Formation is an organic-rich shale. They extend in the subsurface across the Appalachian basin from New York state in the north to northeastern Kentucky and Tennessee in the south. The play has seen substantial growth in natural gas production in the past four years. Currently, the deeper Point Pleasant formation is more often targeted for drilling because of its higher productivity. The most prolific areas of the Point Pleasant formation are in eastern Ohio and western Pennsylvania (Popova 2017).

The thickness of the Utica Shale ranges in thickness from less than 100 feet to over 500 feet. Thickest areas are on its eastern side of its extent, and it generally thins to the northwest (Figure 10). Although thickness of a rock unit is important in determining its oil and gas potential, the organic content, thermal maturity and other characteristics must all be favorable (King 2016).

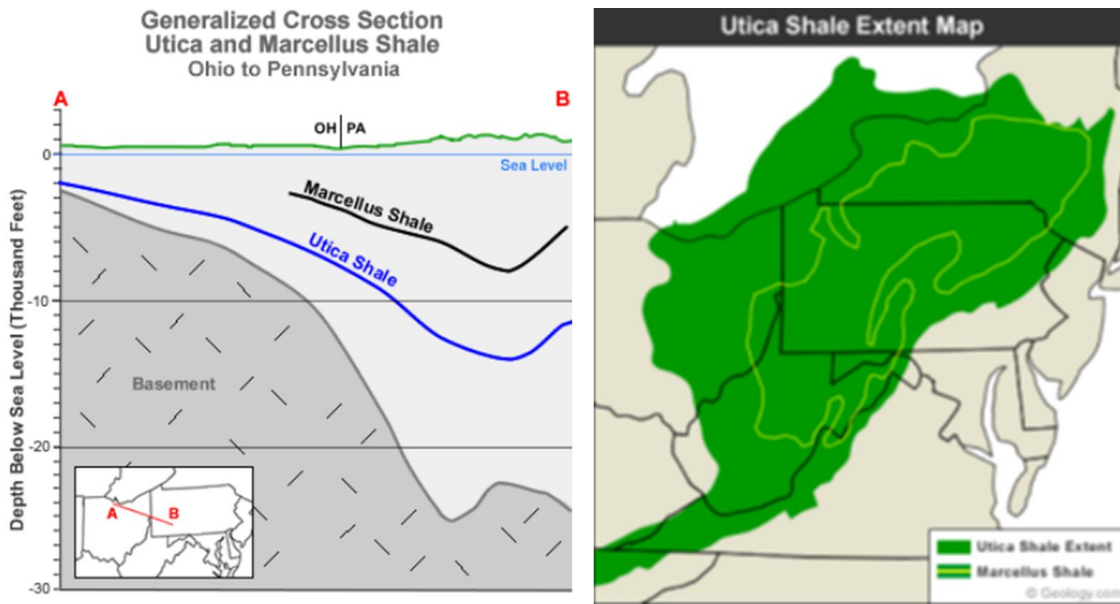


Figure 10 (left) The cross section above shows the subsurface position of the Marcellus Shale, Utica Shale and the continental basement rock. The line of cross section is shown as line A-B on the inset map (King 2016). (right) The green area on this map marks the geographic extent of the Utica Shale. Included in this extent are two laterally equivalent rock units: the Antes Shale of central Pennsylvania and Point Pleasant Formation of Ohio and western Pennsylvania. These rocks extend beneath several U.S. states, part of Lake Erie, part of Lake Ontario and part of Ontario, Canada. If developed throughout this extent, the Utica Shale gas play will be larger than any natural gas field known today (King 2016).

1.4.1 Depositional History

The Point Pleasant and Utica formations were deposited in a foreland basin roughly paralleling the structural front of the present-day Appalachian Mountains during the Late Ordovician time about 445 million years ago (Figure 11) (Popova 2017) cited (Harper, 1999). The Utica Point Pleasant interval is described as carbonaceous grey to black shale that encloses scattered carbonate concretions and locally abundant fossils. The Utica-Point Pleasant lithology

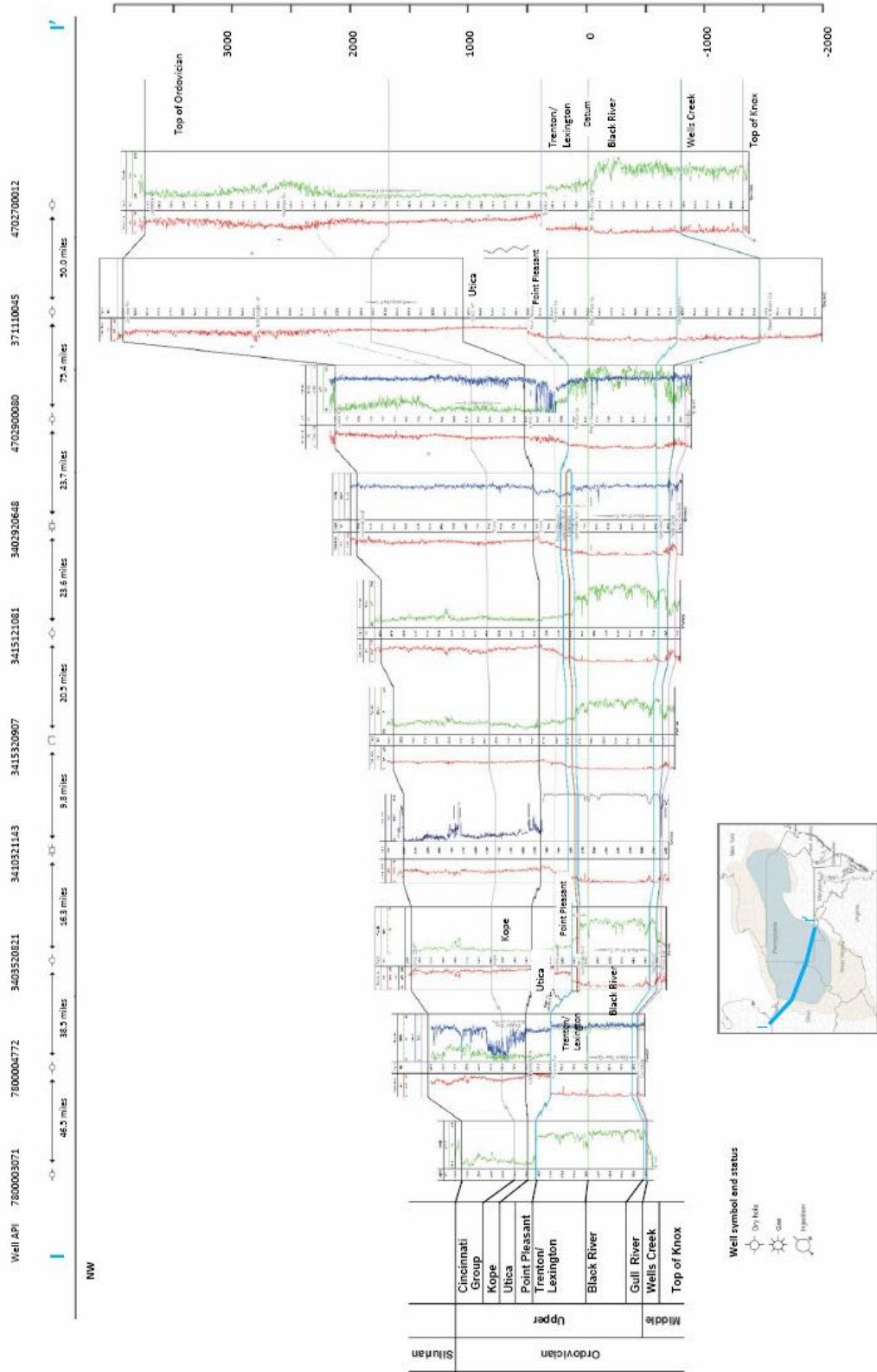
varies significantly across the Appalachian basin. This lithological heterogeneity is controlled by depositional and diagenetic processes (Popova 2017) cited (Roen and Walker, 1996).



Figure 11 Late Ordovician paleogeographic reconstruction (445 Ma) exhibiting North America. Modified after Blakey (2011) (Popova 2017).

The Point Pleasant formation is an organic-rich calcareous shale with some limestone beds. It extends beneath the Utica Shale and is composed of interbedded, fossiliferous limestone, shale, and minor siltstone (Figure 12). The upper interval of the Point Pleasant Formation is an organic-poor gray shale with abundant thin carbonate beds. Total Organic Carbon (TOC) is generally low (in the most samples it is less than 1%). This interval is primarily non-reservoir (Popova 2017). The lower interval of the Point Pleasant Formation is organic-rich calcareous shale (roughly 40%–60% carbonate content) with average TOC content 4%–5%. The Point Pleasant has abundant storm beds, is a clearly storm-influenced formation, and has common burrows, even in the organic-rich

facies. Typically, the Utica formation consists of interbedded gray to black and brown calcareous shale (10% to 60% calcite), locally fossiliferous. This shale is commonly laminated, tends to be bioturbated, and generally has TOC content of approximately 3.5%, which is lower than the underlying organic-rich carbonate facies of the Point Pleasant and Lexington-Trenton (Smith 2015).



Source: U.S. Energy Information Administration based on the Trenton-Black River Appalachian Research Consortium final report, Stratigraphic Cross-section, Line I-I'

Figure 12 Geological cross-section through the Appalachian basin with the regional stratigraphic schema of the Ordovician interval (Popova 2017).

2.0 Theoretical Background

The overall goal of this study is to utilize microseismic data to characterize and understand the differences and similarities in treatment and response between two parallel horizontal wells. To gain these insights, it is necessary to analyze the distribution of b-value over the region and its relationship with D-value; to identify the types of rock failure. Furthermore, the calculation of the hydraulic diffusivity for every treatment stage will identify dry and wet events to determine fluid and stress communication pathways, and the true stimulated volume of every stage. Any communication (parent/ child relationship or frac hit) between the two wells can be identified and quantified by plotting the true stimulated volume for both wells. Additionally, the analyses of well logs and elastic constants and their correlation with the microseismic catalog can explain the density of events and magnitude levels. There is no one plot or one equation that can explain everything. One must look at every aspect available to define and record relationships between all variables.

2.1 The b-value

The b-value (size distribution) is a measure for the relative abundance of the strong to the weak earthquakes and is related to the tectonic regime of the area under consideration. The b-value anomalies may indicate low or high stress levels, anomaly in the thermal gradient or the crustal heterogeneity (Jafari 2008). The b-value is believed to be an indicator of the stress regime as the latter will influence the size of the rupture and as such the magnitude of an event (Grob and Baan

2012). Many studies classify faults and fractures based on b-value, where low b-value ~ 1 is related to natural fault activity, whereas high b-value ~ 2 is related to fracture stimulation. The analysis and discussion of b-value is relevant because it directly relates the magnitude to the abundance of microseismicity, where low b-value is associated with high magnitude and low event count, and high b-value is associated with low magnitude and high event count (Zorn, et al. 2017).

The parameter b is defined according to the frequency–magnitude Gutenberg–Richter relation:

$$\text{Equation 1 (Gutenberg and Richter Formula) } \log_{10} N = a - b \cdot M$$

where N is the number of seismic events with magnitude $M \geq$ Magnitude of completeness (M_c) occurring within a specified period of time, a and b are the constant parameters where the value of a denotes the seismicity level in an area where b is the slope of magnitude frequency curve. In general, the parameters a and b depend on the tectonic features of the area (Kijko and Smit 2017).

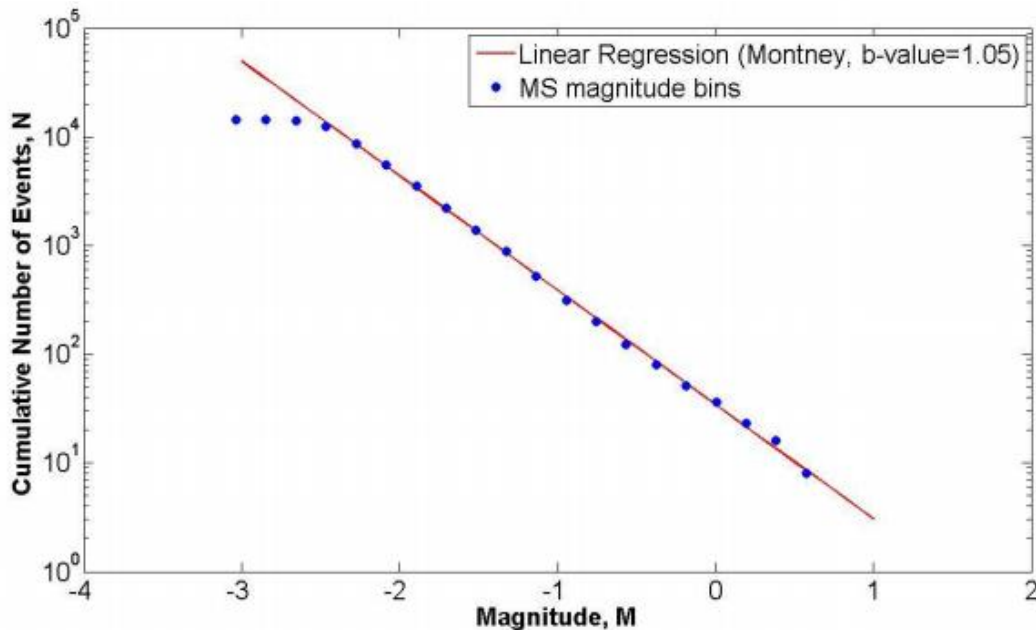


Figure 13 Example of frequency-magnitude plot showing cumulative curve versus magnitude and a b-value of 1.05 (Boroumand 2014).

The magnitude of completeness (M_c) is the minimum magnitude above which all microseismic events within a certain region are reliably recorded. Figure 13 shows the log of cumulative number of events versus magnitude, high number of events with relatively low magnitude can only be recorded near the geophone array and they form a flat line in the plot. These events (magnitudes $< M_c$) are excluded from the calculation of b-value because similar events occurred farther away from the array were not recorded due to of low energy.

2.2 The D-value

Fractal dimension (D-value) is characterizing the spatial distribution of hypocenters. It is likely related to changes in the stress field as well as the spatial distribution of damage and brittle failure, which is the quantification of the shape of clustering of events, which emphasize specific rock weaknesses (Grob and Baan 2011). D-value is defined by the equation:

$$\text{Equation 2 (Fractal Dimension)} \log_{10} N(R < r) = a - D * \log_{10} R$$

where N is the total number of events and $N(R < r)$ is the number of pairs of events separated by a distance r greater than a given distance R in a log-log space. D is the absolute value of the slope of the linear portion of the distribution (Zorn 2016).

The D-value analysis requires calculation of the distance between all possible unique pairs of events in the seismic catalog. Three-dimensional distance, r , between two points, a and b , is calculated using the Euclidian distance equation:

$$\text{Equation 3 (Euclidian Distance)} r(a \rightarrow b) = \sqrt{[(x_a - x_b)^2 + (y_a - y_b)^2 + (z_a - z_b)^2]}$$

where x , y , and z are the coordinates of each point in space. The number of possible unique pairs, P , is given by the following equation:

$$\text{Equation 4 (Unique Pairs)} P = (x^2 - x) / 2$$

where x is the total number of events in the catalog of interest (Zorn, et al.2014).

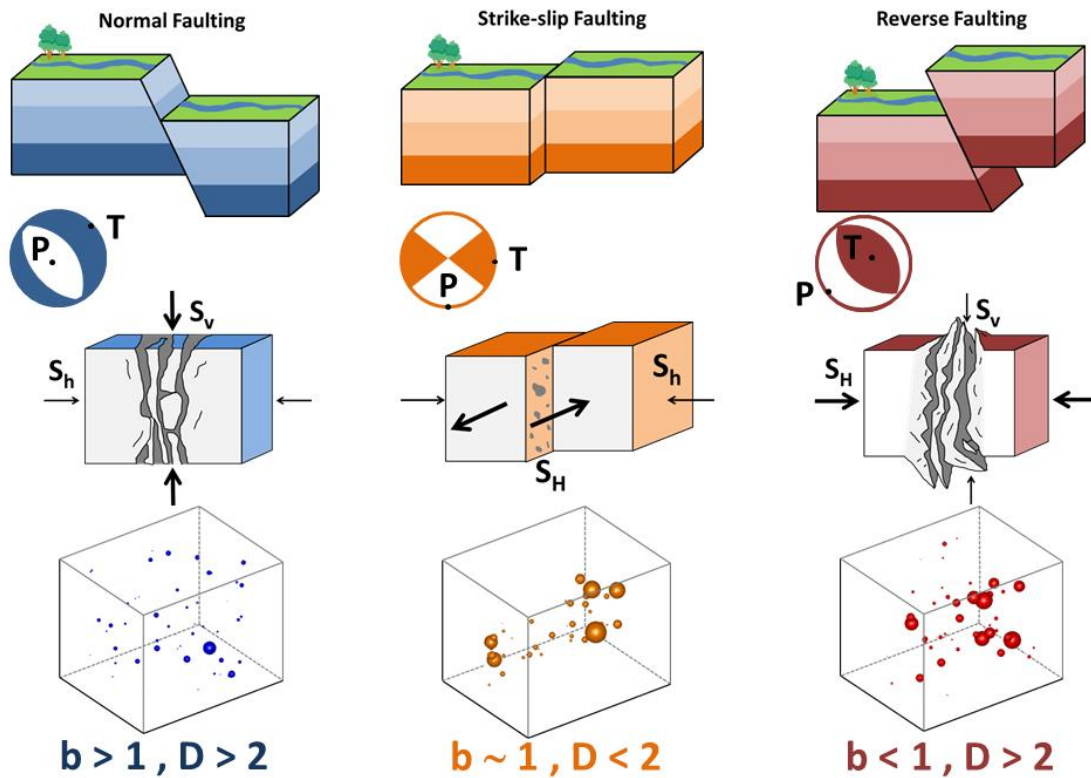


Figure 14 The different stress regimes (top), the associated rock deformation (center), and resulting microseismicity (bottom). The little balls under the diagrams at the top represent the focal mechanisms for each stress regime. P and T denote the pressure axis (maximum compressive stress direction) and the tension axis (minimum compressive stress direction), respectively. The left column depicts the extensional regime with the associated normal faulting, opening of fractures, and large amount of small-magnitude events that are evenly distributed spatially. The strike-slip regime (center column) creates planar fractures which produce an even proportion of small-to-large events during slipping oriented along a plane. The right column shows the compressive stress regime which implies reverse faulting and closing of fractures with many large-magnitude events evenly distributed in space. In the center row, S_h and S_H represent, respectively, minimum and maximum horizontal stress, and S_v indicates vertical stress. Arrow thickness is proportional to stress magnitude. On the bottom row, event circle size is proportional to magnitude (Grob and Baan 2011).

According to the significance of b and D values, these statistical coefficients can be used to infer the local stress regimes into the reservoir at the time when the corresponding microseismic

events are occurring. The D-value varies according to the clustering of the events. If D equals 0, all events occur at the same place (a point); if it's close to 1, events are aligned along a line; if its value is around 2, events are distributed over a plane; and if it equals 3, then events are spatially uniformly distributed. Given the rock deformation happening in extensional and compressive stress regimes, a D-value around 3 is usually observed, whereas D is found to be equal or less than 2 for strike-slip regimes (Figure 14) (Grob and Baan 2011).

2.3 The Triggering Fronts and The R-T Plots

It is natural to assume that the probability of the triggering of microseismic events is an increasing function of the magnitude of the pore pressure perturbation. Thus, at a given time t_0 , it is probable that events will occur at distances, that are smaller or equal to the size of the relaxation zone of the pore pressure. The events are characterized by significantly lower occurrence probability for larger distances. The spatial surface that separates these two spatial domains is called the triggering front (Shapiro 2015). In a homogeneous and isotropic medium the triggering front r_t has the following form:

$$\text{Equation 5 (Triggering Front) } r_t = \sqrt{4\pi Dt}$$

where r is the radius of the triggering front (a sphere in a homogeneous isotropic medium), D is scalar hydraulic diffusivity, and t is the time from the start of fluid injection. Figure 15 shows a plot of the distance of the microseismicity from the injection point versus elapsed time (Shapiro 2015). Such a plot is a common method to distinguish wet and dry events. The wet events are found to form a cloud of activity growing away from the injection point with time, consistent with diffusion type models. In distant regions ahead of the diffusion front, only dry events are observed.

If the pre-existing fractures are permeable, the pressure can be transmitted from these fractures into other connected fractures, possibly triggering microseismic events, those events are defined as a dry disconnected pressure-driven events. R-t plot is effective at eliminating these events, which potentially overestimating the microseismic volume. However, many dry events occur within the triggering front. In several locations, dry events are observed that subsequently take fluid and become wet. This form of dry activity is potentially important in terms of stress preconditioning the reservoir and may be a potential mechanism for fracture growth. However, these dry and then later wet regions do not impact the microseismic interpretation of the fracture network (Maxwell, et al. 2015). The triggering front provides an approximate outermost envelope of the distances between event locations and the injection point r as function of the time t elapsed since beginning of injection (Hummel and Shapiro 2012).

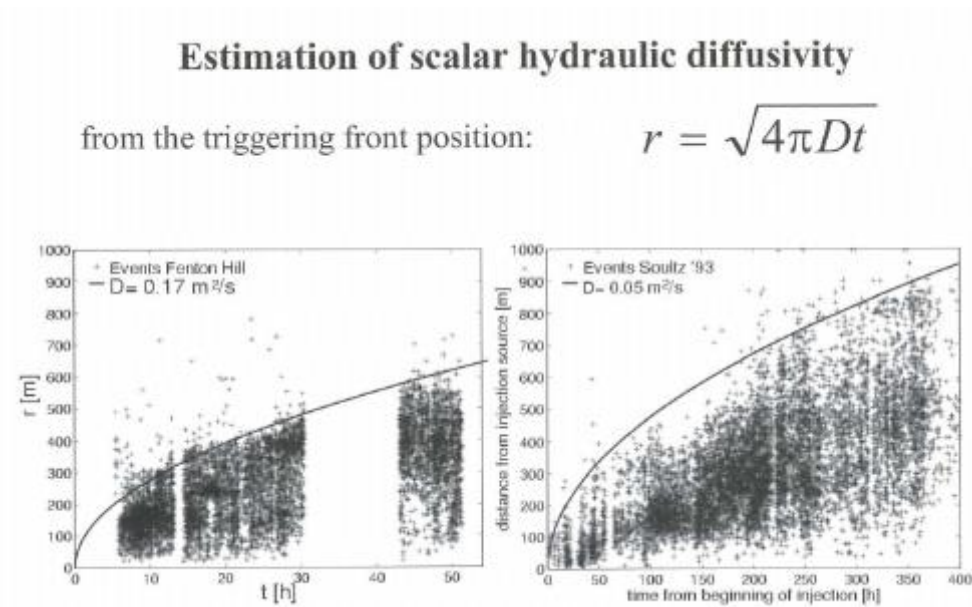


Figure 15 R-t plots created for two case studies on water injection experiments in the framework of two different enhanced geothermic system projects - one at Fenton Hill, USA and the other at Soultz, France (Shapiro 2015).

2.4 The Seismogenic Index (Σ)

The seismogenic index (Σ) indicates the level of seismic activity one should expect from injecting fluid into rocks (Shapiro, et al. 2010). Σ is independent of injection time or any other injection characteristics. The seismogenic index is a convenient quantity for a quantitative comparison of seismotectonic activity at different locations, a higher seismogenic index leads to a higher probability of significant events. (Figure 16) (Shapiro, et al. 2010).

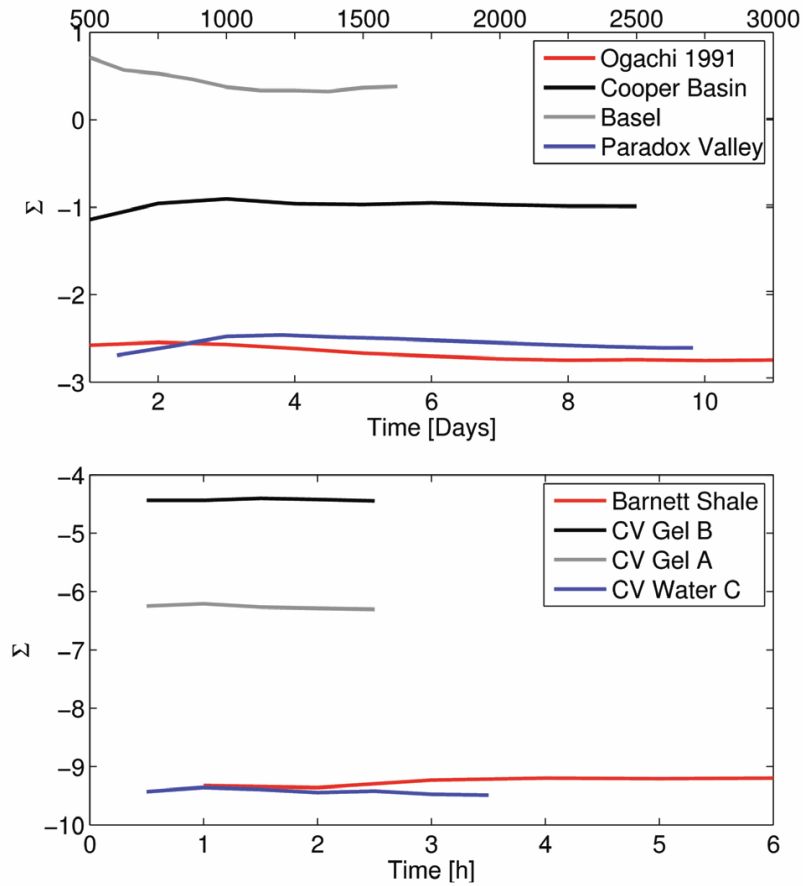


Figure 16 Average seismogenic index computed for different hydraulic fracturing locations in hydrocarbon reservoirs (bottom) and in geothermal systems and other brine injections (top) (Shapiro, et al. 2010).

2.5 The Well Logs

Well logs give an insight into the geomechanical properties of rock formations. There are many logs used for different purposes such as gamma ray logs which measure the number of natural gamma rays emitted by the rocks surrounding the tool. This is commonly proportional to the amount of shale in the rocks (Crain 2017), given the fact that shale contain more radioactive elements than any other sedimentary rocks. Bulk density log (RHOB) provides a continuous record of a formation's bulk density along the length of a borehole. Bulk density is a function of the density of the minerals forming a rock (i.e. matrix) and the fluid enclosed in the pore spaces (Density Logging 2019). Sonic logs measure the travel time of sound through the rock, recorded in microseconds per foot or per meter (abbreviated as usec/ft or usec/m, sometimes us/ft or us/m). The tool emits a sound pulse about once or twice per second from a transmitter. The first arrival of sound is detected at two or more receivers a few feet from each other and from the transmitter. The time elapsed between the arrival of sound at two detectors is the desired travel time (Crain 2017).

Well logs are generally used to determine the mechanical properties of rocks. These properties are commonly called the elastic properties or elastic constants of rocks. The dynamic elastic constants can be derived with appropriate equations, using sonic log compressional and shear travel time along with density log data. Crain (2017) listed and explained all relative moduli as the following:

- The shear modulus (μ) is defined as the applied stress divided by the shear strain.

$$\text{Equation 6 (Shear Modulus)} \mu = \rho * V_s^2$$

where ρ is density (kg/m^3) and V_s is shear velocity (m/sec).

- The bulk modulus (K) is the hydrostatic pressure divided by volumetric strain.

$$\text{Equation 7 (Bulk Modulus)} K = (\rho * Vp^2) - (4/3 * Vs^2)$$

where Vp is P-wave velocity (m/sec).

- The Young's modulus (E) is applied uni-axial stress divided by normal strain.

$$\text{Equation 8 (Young's Modulus)} E = (9 K \mu) / (3 K + \mu)$$

where K is bulk modulus and μ is shear modulus.

- The Poisson's ratio (ν) is the lateral strain divided by longitudinal strain. In other words, how much the material will deform in the lateral direction.

$$\text{Equation 9 (Poisson's Ratio)} \nu = (3K - 2 \mu) / (2 (3K + \mu))$$

- Lamé's constant (λ) is a measure of a rock's brittleness, which is a function of both Young's modulus and Poisson's ratio.

$$\text{Equation 10 (Lamé's Constant)} \lambda = E * \nu / ((1 + \nu) * (1 - 2 \nu))$$

- Brittleness index (BR) was proposed by Mullin as practical model that is widely used as a brittleness indicator. Young's modulus in the Mullin equation is the static value and must be in psi.

$$\text{Equation 11 (Brittleness Index)} BR = (((E-1)/7)*100) + (((\nu - 0.4)/-0.25)*100) / 2$$

In these equations, it is important to note the E and ν threshold values that affect the total brittleness calculation. When E = 8 Mpsi and $\nu = 0.15$, the resulting material will be “100%” brittle. E = 1 Mpsi and $\nu = 0.4$ will produce a “0%” brittle material (Zorn et al. 2017).

The lithology can be determined from the mechanical properties, which can be identified by cross-plots of $\lambda\rho$ versus $\mu\rho$. Each lithology has a different rock properties response subject to fluid content and mineral properties (including grain shape). The combination of the fluid compressibility along with the mineral properties and grain shapes yielding different Lambda-Mu-Rho (LMR) results. For example, in a gas sand, the high compressibility (or low incompressibility)

of gas combined with the high rigidity of the spherical sand grains, result in a low $\lambda\rho$ value ($\sim < 20$ GPa.) and a high $\mu\rho$ response ($\sim > 20$ GPa.). With an understanding of these properties for the lithologies and fluids present, typically from petrophysics, a relatively high degree of precision in lithologies and fluids can be obtained. LMR cross plot analysis can be used for lithology discrimination (Figure 17). Neither $\lambda\rho$ nor $\mu\rho$ are powerful lithologic indicators by themselves but used in combination can reveal a great deal about lithology (Figure 18) (Anderson et al. 2001).

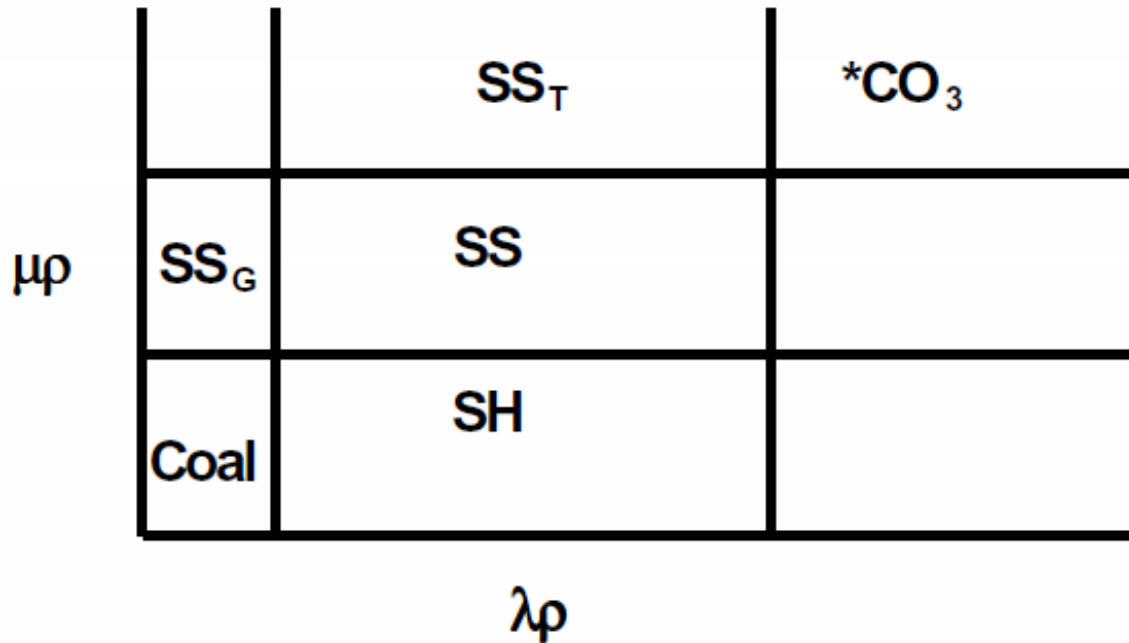


Figure 17 Cross plot of $\lambda\rho$ versus $\mu\rho$ depicting the orthogonal separation of lithologies. Terms listed above are defined as: SH – Shale, SS – Sandstone, SSG – Gas saturated Sandstone, SST – Cemented Sandstones, $*CO_3$ – Carbonates (Anderson et al. 2001).

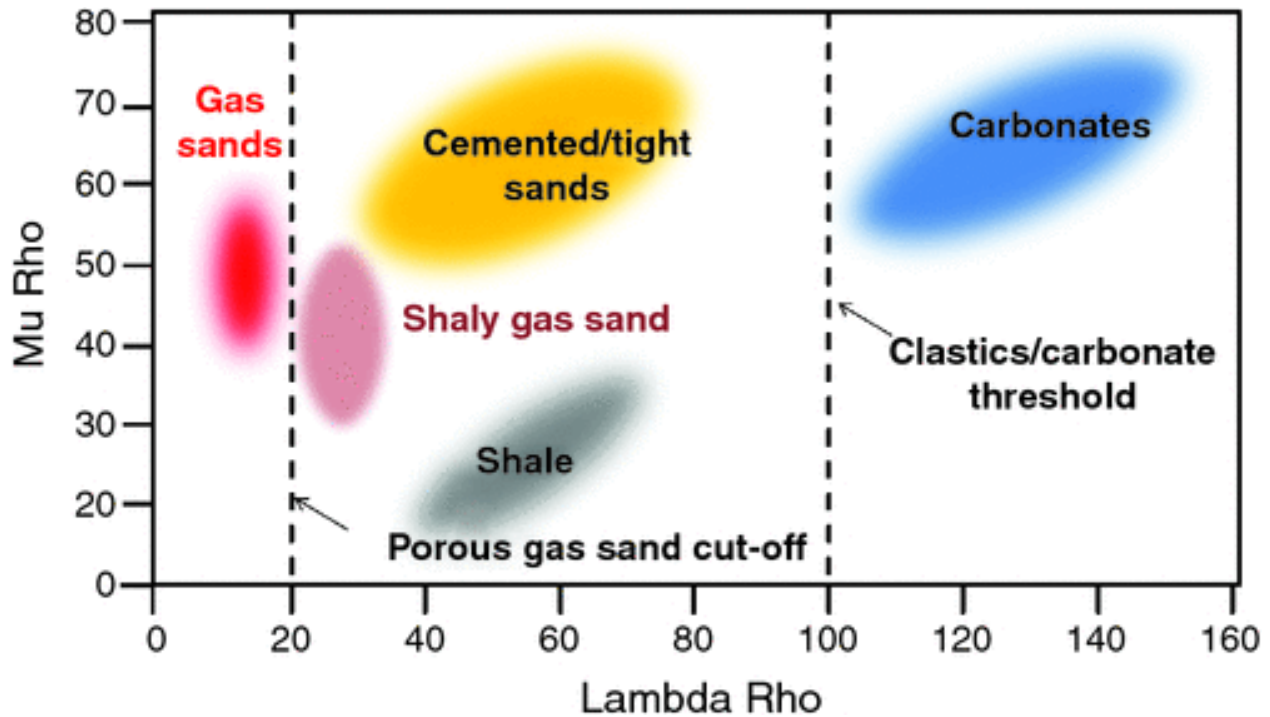


Figure 18 Plot of Mu-rho ($\mu\rho$) and Lambda-rho ($\lambda\rho$) logs showing sand and shale lithologies and the variation in the sandstone reservoirs based on dissimilar fluid content (Shadlow 2014).

2.6 The Parent Child Relationship Quantification

The parent child relationship (also known in the industry as frac hit) is typically described as an interwell communication event in which an offset well, commonly termed a parent well in this setting, is affected by the pumping of a hydraulic fracturing treatment in a new well, called the child well (Figure 19). As the name suggests, frac hits can be a violent affair as they are known to be strong enough to damage production tubing, casing, and even wellheads (Jacobs 2017). Many studies show the impact of such events on production. Parent well production typically benefits from the fracturing of a nearby child well in the Bakken and Haynesville plays, whereas parent well production typically suffers with the fracturing of a nearby child well in the Woodford, Eagle

Ford and Niobrara plays. Interference between parent and child wells is observed in the form of pressure hits and microseismic data (Manchanda, et al. 2018).

The first solution comes to mind is well spacing, which means increasing spacing between wells to reduce or eliminate fracture communication. Cao, et al. (2017) makes the point that if horizontal wells on a pad site show no signs of frac hits, then it is likely they are spaced too far apart, lowering the overall economic recovery of that section. As wells are drilled closer and hydraulically fractured, Cao notes that the odds of frac hits rises, at which point they become a “direct indicator” of just how many wells can economically fit in a drilling section (Figure 20).

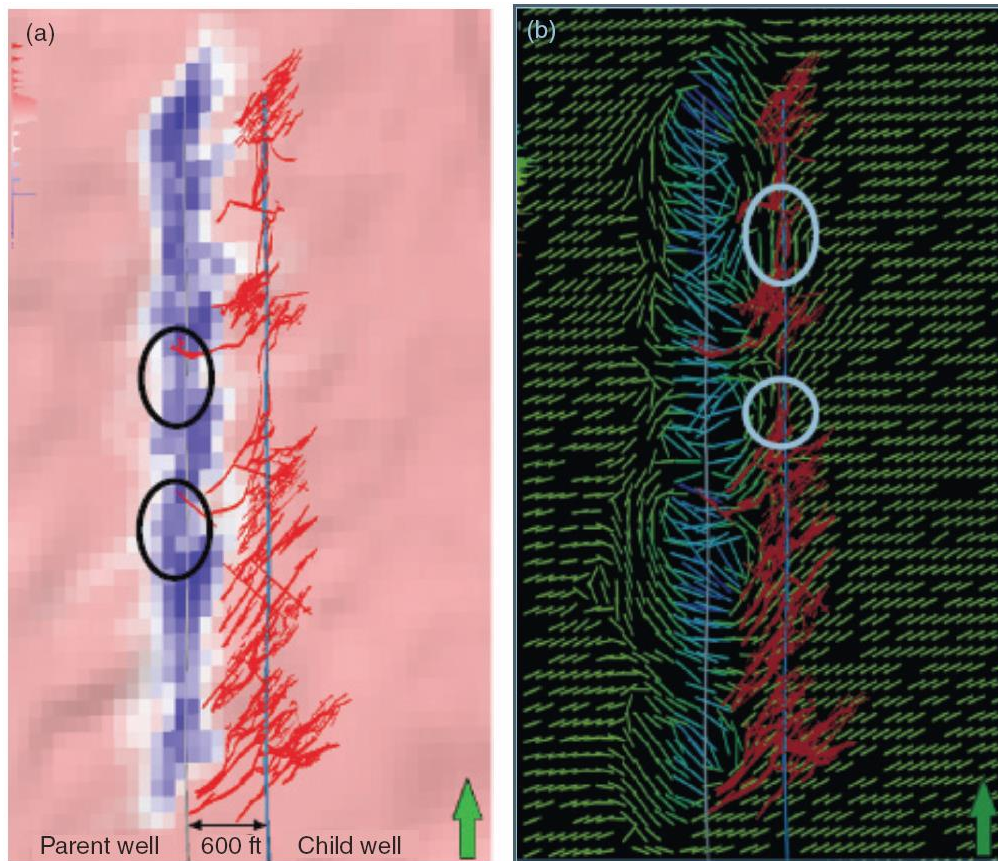


Figure 19 These modeling illustrations show how 600-ft well spacing after 1 year of depletion can affect the pressure (left) and fracture geometry of the child well, which leads to negative impacts from fracture hits (black circles). The white circles show how longitude fractures may also form as a result, which are unlikely to be significant contributors to production. Source: Schlumberger (Jacobs 2017).



Figure 20 The top figure illustrates that if frac hits are not observed it may mean that an operator is leaving a portion of the reservoir untapped. A happy medium is shown in the bottom, in which a frac hit might take place but because it mainly involved fluids and not proppant, negative communication will be short-lived as any unpropped fractures close. Source: Shell (Jacobs 2017).

2.7 The Integration of Microseismic Data with The Injection Process

To properly relate the microseismic events to the injection process, an accurately time-stamp record is needed of injection rate, pressure, and proppant concentration. Then the timeline of the microseismic occurrence can be compared to the injection characteristics, especially paying attention to any anomalous conditions (Maxwell 2014). Figure 21 shows various scenarios which can be used as a guideline to interpret the increase or decrease of surface pressure with respect to microseismicity.

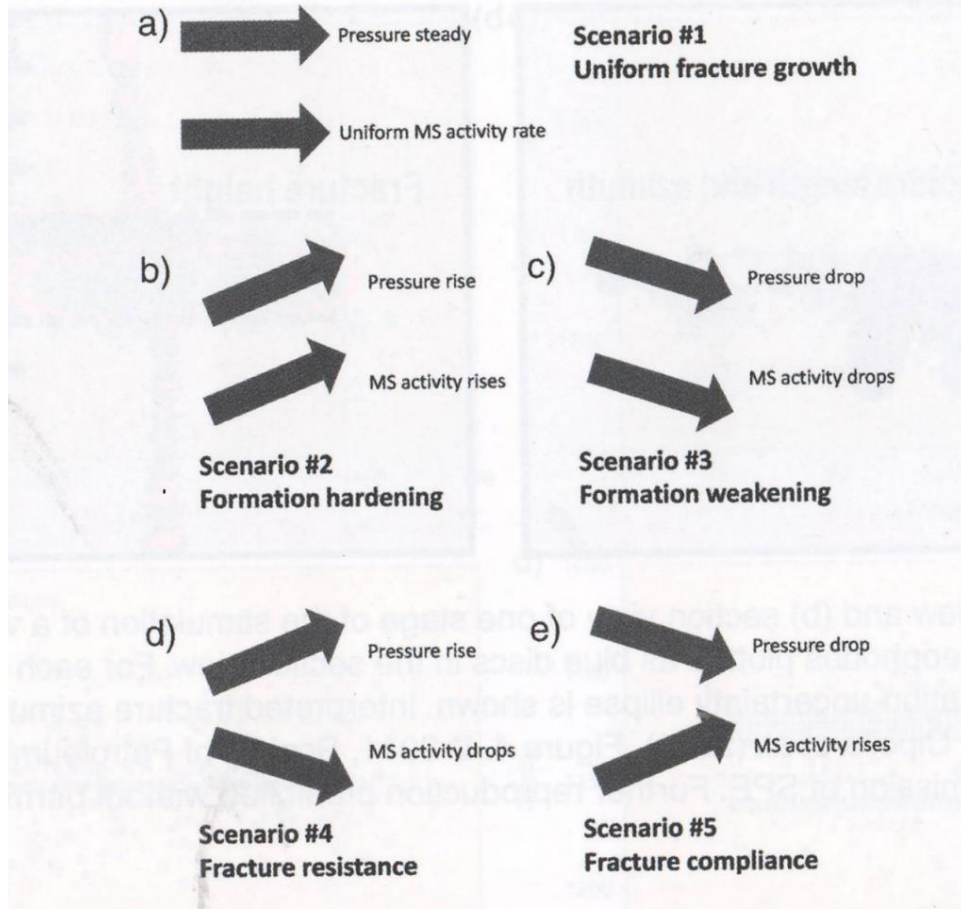


Figure 21 Various scenarios based on pressure microseismic activity rates. (a) Uniform fractured growth in homogeneous reservoir with effective proppant placement. (b) Formation hardening with increased stress and proppant screen out. (c) Formation weakening with decreased stress and effective proppant placement. (d) Fracture resistance with few pre-existing fractures and effective proppant placement. (e) Fracture compliance with fault activation and effective proppant placement (Maxwell 2014).

Considering Figure 22, the distribution of microseismicity can be correlated with stage parameters with the assumption of constant injection rate, characteristics fracture responses can be concluded. Based on the work of Maxwell (2014), the sudden increase in microseismicity rate and magnitude could be an indication of a fault activation. The increase can be detected by plotting magnitude with time as shown in Figure 23.

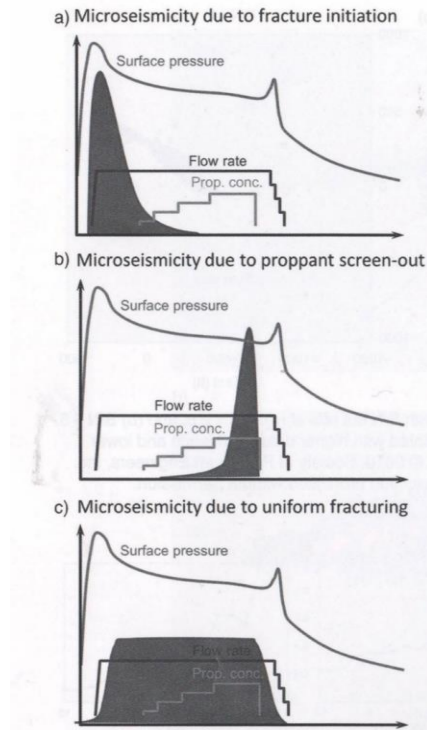


Figure 22 Schematic of various microseismic histograms (dark gray), relative to stimulation parameters and corresponding potential interpretation (Maxwell 2014).

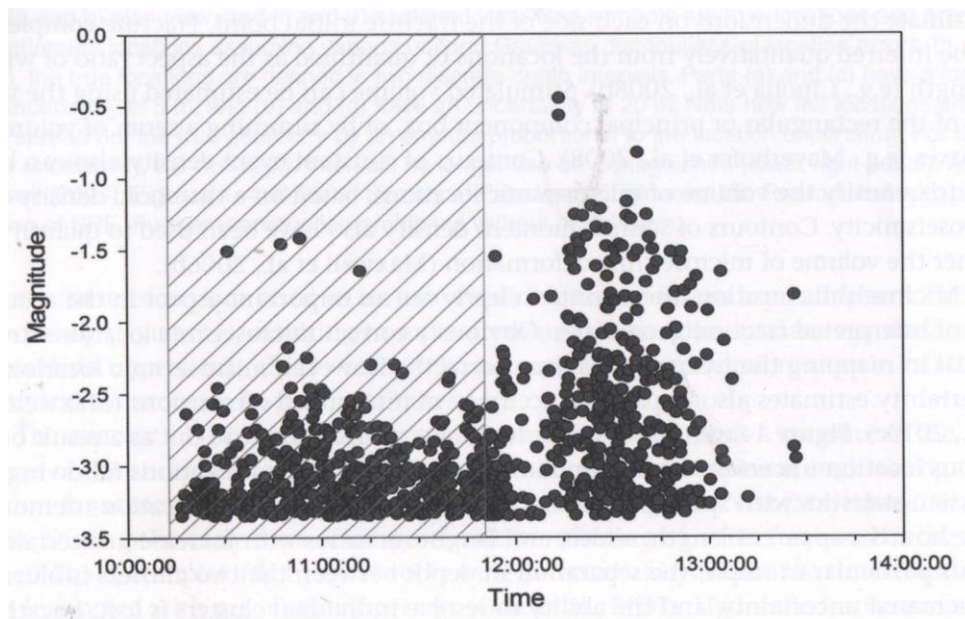


Figure 23 Plot of magnitude with time, for a fault-activation example. Hatched area on left is the time period of active injection. Post-injection microseismicity rates and magnitude begin to subside, but, after 20 minutes, an increase in microseismicity and magnitude was recorded as a known fault was activated (Maxwell 2014).

3.0 Methods

There are many software packages that can analyze the special relationship of microseismic events and the interaction of microseismic clouds, such as MATLAB, Petrel, SMT Kingdom and more. It is significant to note that a MATLAB workflow was used to generate most figures in this section, because this process is easily reproducible for any given set of microseismic data, making future applications of these workflows computationally inexpensive with a short turnaround time.

By plotting relative easting, northing and depth for the microseismic cloud for each well and separately stage by stage, a 3d image can be used to visualize the lateral part of the well and formations. A map view also is generated by plotting relative easting and northing and colored based on magnitude, confidence, time of the stage or depth. Formations can be plotted by taking the relative easting, northing and depth of each formation top and create a surface using the interpolant function (The MathWorks, Inc 2015), which shows the topography of the formation top and the dip. To plot wells, perforation, and array tools, the plot3 function is used. In addition to the microseismic data, treatment data such as slurry rate, proppant concentration and surface pressure must be plotted as a function of time.

3.1 The b-value

There are many approaches to calculate b-values, Petrel provide us with two methods for microseismic b-value analysis: Spatially Varying Magnitude of Completeness (SVMC) and

Magnitude of Completeness (MC). In the SVMC and MC methods, event magnitude and distance from the array are combined to calculate b-values based on the order of detectability

$$\text{Equation 12 (Order of Detectability)} \quad \gamma = 10^{((1.5M_w+16.1)/2)} / r$$

where M_w is magnitude, r is the distance between event and the array. Then we take the least value of γ to be γ_0 , which is used to reconstruct the frequency-magnitude distribution with the Lynden–Bell algorithm. I calculate the Gutenberg-Richter b-value from the reconstructed profile and calculate the difference between the reconstructed profile and the theoretical Gutenberg-Richter distribution of estimated b-value (BGC Mistral Team 2019). Whereas the SVMC uses the Lynden–Bell algorithm, which is a maximum likelihood estimator for recovering frequency-magnitude profile, the MC runs without it, and that is the main difference between the two methods. Zmap (Wiemer 2001) is an application in MATLAB that calculates b-value, and it follows the same method as SVMC. Zmap catalog needs to have latitude, longitude year, month day, magnitude, depth, hour, minutes and seconds (in this order) for every microseismic event in the catalog to be accepted in order to calculate other variables, and to create a map of distribution of them such as b-value, fractal dimension, M_c and others .

3.2 The D-value

To produce the D-value plot, microseismic catalog must be uploaded to zmap. Then the fractal dimension must be calculated from time series analysis, where the D-value is the absolute value of the slope of the linear portion of the distribution (Zorn 2016).

3.3 The R-T Plot

To generate the triggering front in the plot, I must calculate the distance of each event within the microseismic cloud to the treatment well and the array. This can be achieved by using the `point_to_line_distance` MATLAB function (Wisselink 2019), which calculates the distance of every microseismic event to the perforated section of the well and array for the relevant stage. This method creates a matrix of the distance between microseismic events and the lateral. Then I create plot where the time of the stage is plotted along the X axis and distance is plotted along the Y axis. The calculated triggering front is plotted for every stage, where t_0 is the beginning of the injection and the scalar hydraulic diffusivity value (D) is displayed on the top right corner. All events outside the triggering front are considered as outliers and for some analyses they are filtered and removed. But these events can identify potentially dry microseismic events that result from stress and pore-pressure migration that likely occur prior to the movements of fluid through the formation (Maxwell 2014). Dry events can be distinguished by isolating all events outside the triggering front curve, then identifying these points in the main microseismic events file, where magnitude and spatial location can be plotted with respect to wet events.

3.4 The Seismogenic Index Σ

Σ is defined by the following equation:

$$\text{Equation 13 (Seismogenic Index)} \quad \Sigma = \log_{10} (N > M_c) - \log_{10} Q_c(t) + (b\text{-value} * M_c)$$

where N are events with magnitude larger than the M_c , and $Q_c(t)$ is a cumulative injected fluid volume (Shapiro, et al. 2010). Any event equal or less than M_c was excluded from this analysis.

The Σ plot is a function of time, where x axis is the time of the stage and y axis is the result of the equation above.

3.5 The Cumulative Moment Plot

The seismic moment is defined by the equation

$$\text{Equation 14 (Seismic Moment) Moment} = 10^{(3/2 \text{ Magnitude} + 16.1)}$$

The moment units are given in newton-meter. After calculating the moment for each event, the results are added to get the cumulative moment. Cumulative moment plot shows the progress of the frac. Any sudden increase in the number and magnitude of the microseismic events in the plot could be an indication of natural fault activation. This can be visualized in the plot of magnitude with time which illustrates the progress of the fracture throughout the stage (Maxwell 2014). We can plot all events within the time of the sudden increase to reveal the plane and the specific location of the fault.

3.6 The Elastic Properties and Lithology

I divided the logs into two sections, vertical and horizontal. I plotted the formations depth on the vertical section to relate the well logs to the formations. Additionally, I superimposed gamma ray log and brittleness index along the lateral to correlate them with the treatment stages, which can explain the size, the density of the microseismic cloud.

The lithology can be identified by the cross-plots of $\lambda\rho$ versus $\mu\rho$ or Lambda-Mu-Rho (LMR). Zorn (2016) explained that scaling the LMR cross-plots by average magnitude from the lateral well indicates that as brittleness increases, the magnitude decreases. In other words, as the rock becomes more brittle, its ability to store potential energy before rupturing diminishes.

3.7 Frac Hit

In order to define frac hits; the stimulated volume for each stage must be determined first, based on its microseismic cloud. The stimulated volume is the size of the treated portion of the formation by a treatment stage. It can be defined by plotting latitude, longitude, and depth of microseismic cloud using the MATLAB command Alphashape. An Alphashape creates a bounding area or volume that envelops a set of 2-D or 3-D points. An Alphashape command can manipulate object to tighten or loosen the fit around the points to create a nonconvex region. It also can add or remove points or suppress holes or regions. Then the command (Volume) returns the volume of the alpha shape (The MathWorks, Inc 2015). Depending on the coordinate system used to plot the microseismic cloud; the volume unit is determined. All Alphashape for all stages can be plotted with respect to the treatment well and observation well in order to visualize the overlap between stages.

The next step is to define the overlap between stages in 3D space and isolate all microseismic events within the overlap volume. To execute this step; the command inShape returns logical 1 (true) values for the 3-D query points (qx,qy,qz) that are within 3-D alpha shape. Otherwise, inShape returns values of logical 0 (false). The qx, qy and qz arguments are numeric arrays whose corresponding elements specify the (x,y,z) query point coordinates (The MathWorks,

Inc 2015). Overlap data can be extracted by applying logical 1 (true) values to the main stage data. Then AlphaShape needs to be plotted in order to get the overlap volume. After recording both volumes, the ratio between overlap and total stage volume must be calculated to reveal the relationship between stages over the course of the treatment.

3.8 The Energy Budget

Based on the work of (Boroumand and Eaton 2012) and (Zorn et al. 2014) injection energy can be defined by the equation:

$$\text{Equation 15 (Injection Energy)} \quad E_{in} = P(t) * Q(t) * t$$

where P(t) is average surface pressure, Q(t) is the injection rate and t is injection duration measured by minutes. Radiated Energy (RE) is the cumulative energy from the microseismic events. According to Gutenberg-Richter relation between Energy and Mw (Hanks and Kanamori 1979)

$$\text{Equation 16 (Seismic Energy)} \quad \log E = 1.5 Mw + 11.8$$

by solving for seismic energy using Richter and Gutenberg method

$$\text{Equation 17 (Seismic Energy)} \quad E = 10^{(11.8 + 1.5 * \text{Magnitude})}$$

Total RE can be calculated for the entire stage, by summing all energy outcome for all events. Then the same method can be applied for the events of the overlap to compare the outcome.

As a first step I reviewed the geometry of geophones recording the microseismic events. In these two hydrofracturing activities there were both a vertical three-component geophone array near the heel of each well and, parallel to each horizontal well, a second horizontal lateral in which a tracted, or mobile, three component array of geophones was positioned. As hydrofracturing progressed, this horizontal mobile array was positioned for best sensitivity of expected

microseismic emissions. As a second step, I investigated the statistics and the overall quality of the microseismic data. These data were provided by a geophysical contractor and were used along with stimulation pumping data for our analysis. The map view of the microseismic data for both wells show multiple gaps between stages on A08, gaps on B11 are more observable towards the heel of the well (Figure 24). These data can be analyzed by their seismic emissions attributes, such as magnitude, their positions, and the time of their occurrence. Statistically speaking, as I analyzed the microseismic cloud for each stage a pattern emerged in which there is a sharp drop in total number of events recorded per stage, starting in stages where the geophone array transitioned from horizontal to vertical setup in the observation well, then the number of events increased as stages got closer to the heel. This pattern was observed on both wells while the treatment did not show any sign of difficulties. This observation has led to the formulation of a hypothesis: The sharp drop in the event count is due to the background noise from the treatment well because the distance between treatment well and observation well is at minimum for the vertical receiving array.

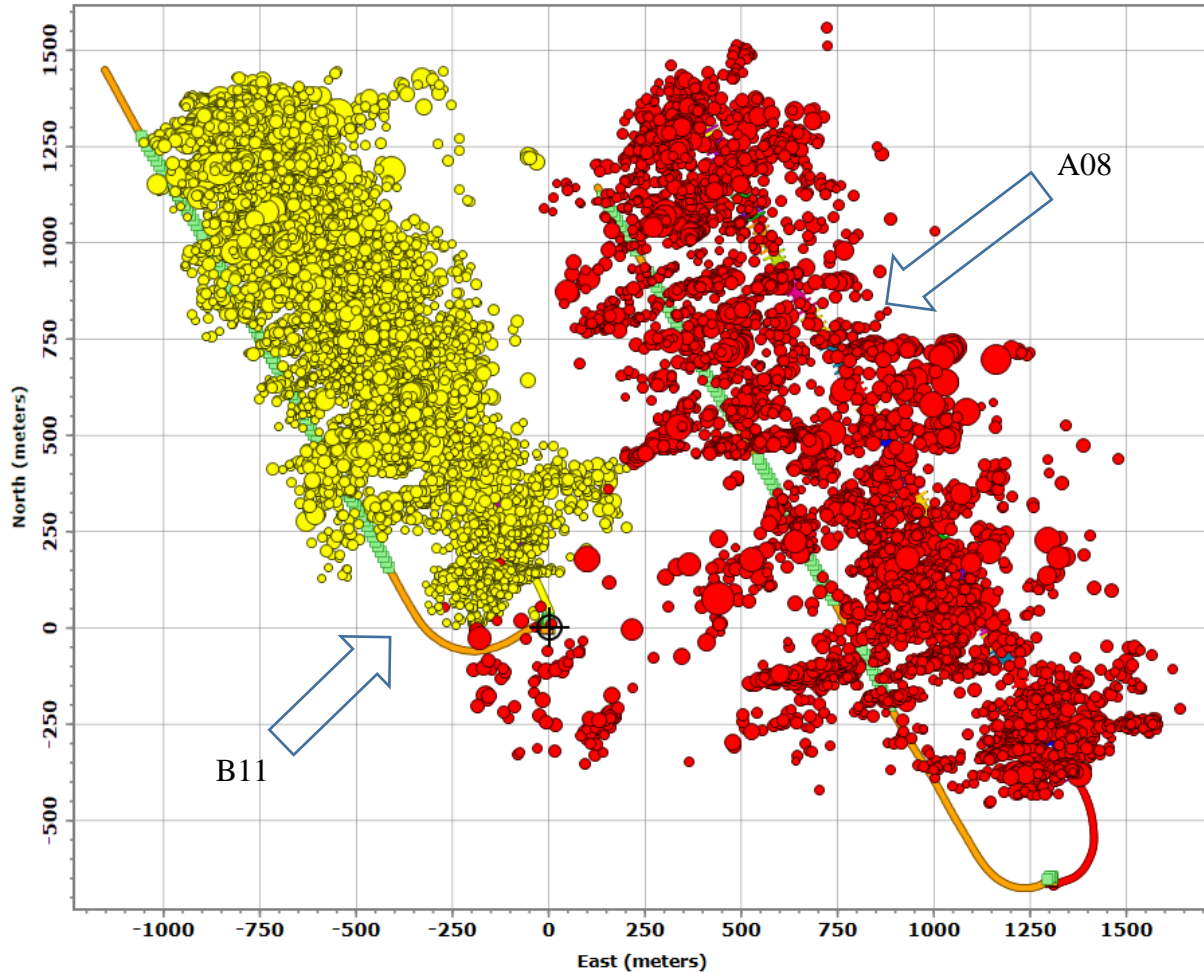


Figure 24 Map view illustration of A08 (east well, red symbols) and B11 (west well, yellow symbols) and microseismic events for both. Symbol size is proportion to moment magnitude. The heel of each stimulation is positioned closest to the surface location of the well, the toe of each stimulation is farthest away from this surface location.

The second hypothesis lies in the center of the map in Figure 24. I observed that during hydrofracturing stimulation, multiple microseismic events from both wells had occurred within the same spatial location. The emission of seismic energy during hydrofracturing is sometimes called a frac hit. This microseismic event is an indication of well communication or frac hit. Because A08 was treated first, it is considered as the parent well and B11 is the child well. Generally, frac hit is a negative impact on both wells in some case because it leads to pressure depletion zones (Jacobs 2017). This observation raises further questions with respect to this study:

how severe was the parent-child relationship between the wells? How can we quantify it? Furthermore, does the quantification method apply to stages within the same well? In other words what would this method show on a stage level? It turns out by illustrating the stage volume I can define the overlap between stages, where no overlap means a gap.

A fault can result in a sudden increase in the number and magnitude of microseismic events (Maxwell 2014). Thus, activation of a fracture or fault can be detected by plotting microseismic moment magnitude versus the time of occurrence. In this cross-plot space, an increase of microseismicity rate could be an indication of a fracture or fault activation. Therefore, by plotting cumulative stage seismic moment and moment magnitude as time functions for each stage, B11-stage1 natural fracture or fault activation can be estimated following this approach.

We had detailed pumping information for each hydrofracturing stage. In reviewing these pumping data for both wells, 4 stages show difficulties where proppant was not delivered to the formation as projected from stages 18 and 23 on B11, or it took second attempt and more time to achieve the goal as seen on stages 2 and 4 on A11 (Figure 25). I found that the microseismic data shows a pattern where the fractures were being activated horizontally. The fourth hypothesis with respect to these stages is that the difficulties with stages 2 & 4 on A08 and 18 & 23 on B11 were because the fractures moved through the formation bedding boundaries where vertical stress is dominant.

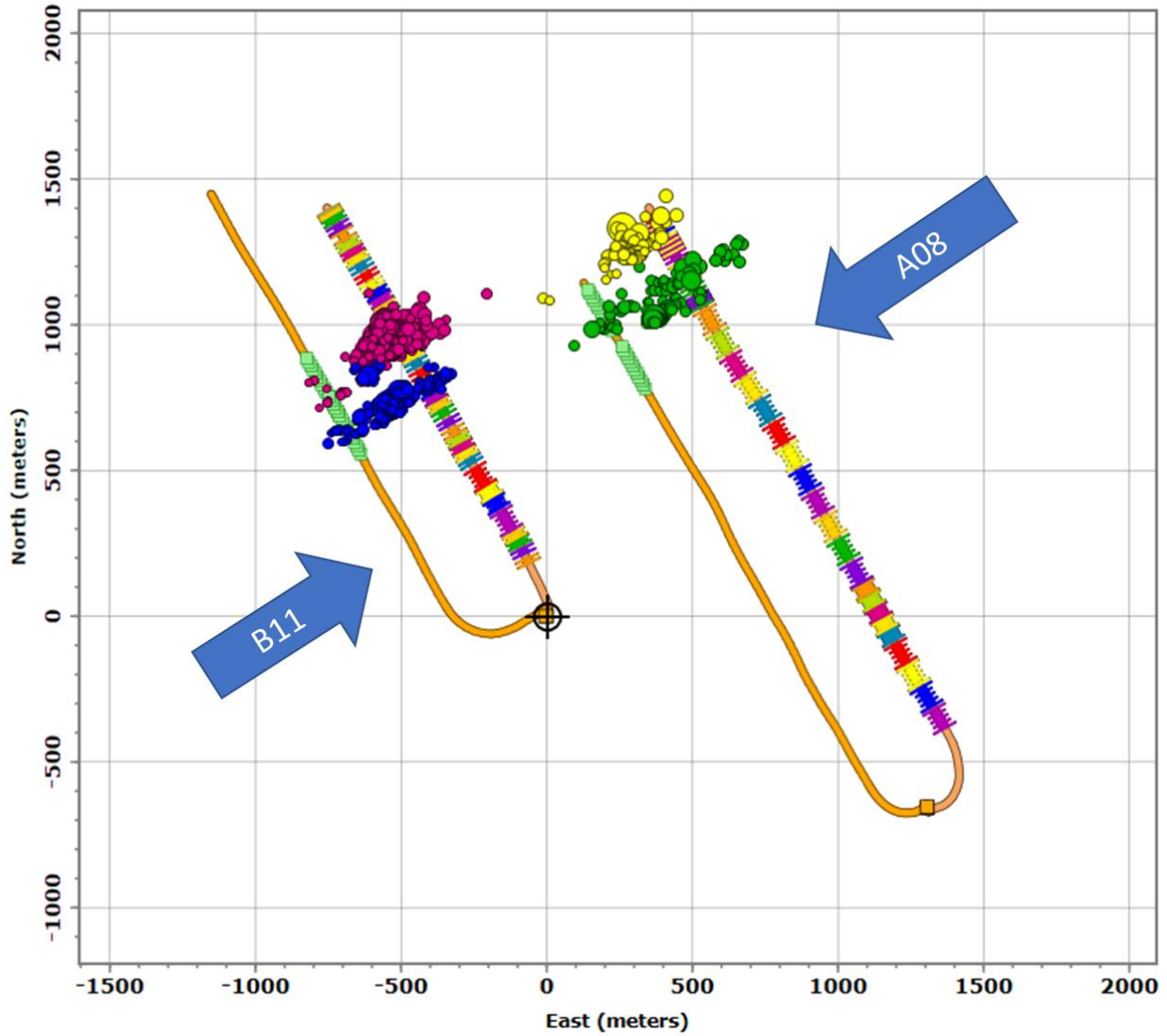


Figure 25 Map view illustrates well A08, stage 2 (yellow) and stage 4 (green). Well B11, stage 18 (purple) and stage 23 (blue). Symbol size is proportion to moment magnitude. The heel of each stimulation is positioned closest to the surface location of the well, the toe of each stimulation is farthest away from this surface location.

4.0 Results and Analysis

4.1 The Microseismic Catalog

A08 treatment consisted of 25 stages, total microseismic events recorded were 5460, the overall D value is 1.79, b-value is 1.16 and M_c -2.2 as seen in Figure 26, whereas B11 treatment consisted of 40 stages, total microseismic events recorded were 17248, overall D value is 2.01, b-value is 1.13 and M_c -2.5 as seen in Figure 27.

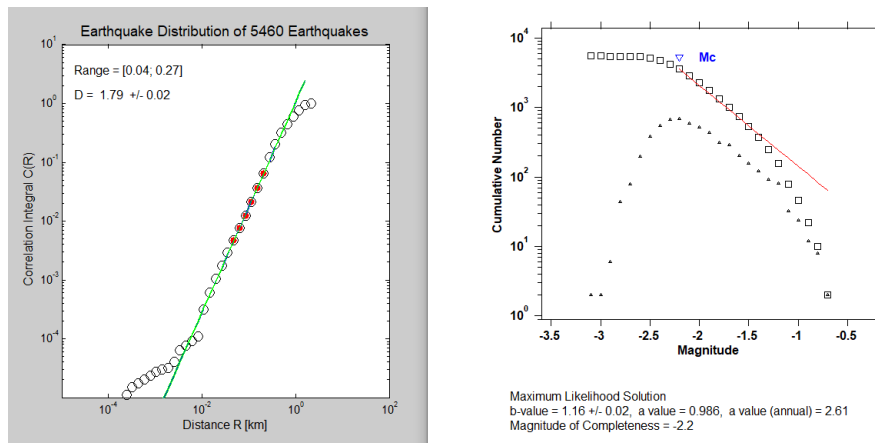


Figure 26 A08: D-value =1.79, b-value 1.16 and M_c =-2.2.

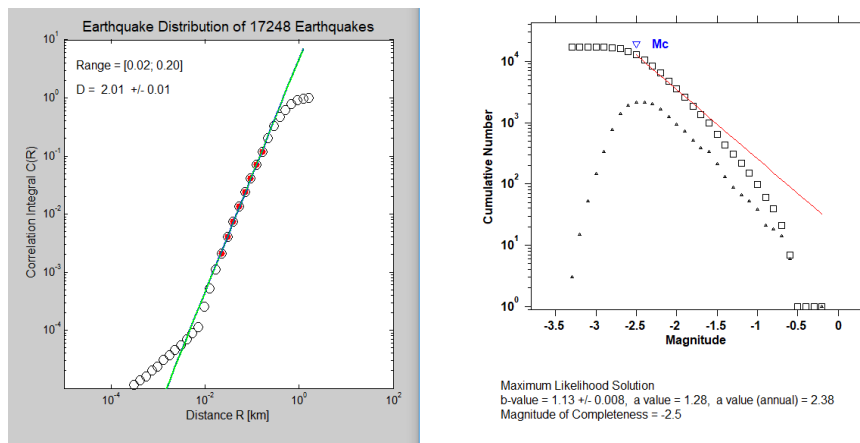


Figure 27 B11: D-value =2.01, b-value 1.13 and M_c =-2.5.

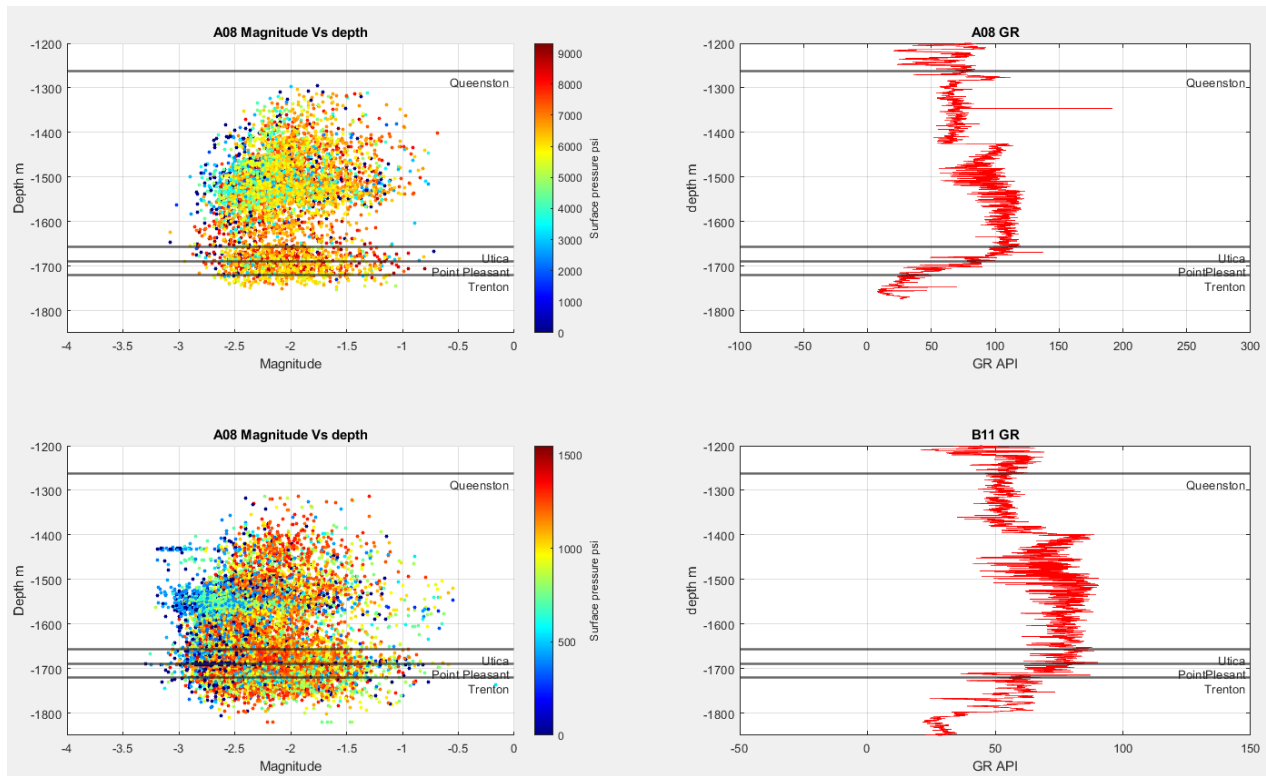


Figure 28 A08 and B11 magnitude vs. depth plots scaled by surface pressure (left) and GR log (right).

Well A08 and B11 magnitude vs. depth plots (Figure 28) illustrate the distribution of microseismic events with respect to the formations scaled by the surface pressure, which indicates that low magnitudes are often associated with low surface pressure. A08 (top plot) shows that the main cluster of events lies within the Queenston Formation with total of 4451 events or 81.5% of the microseismic catalog, 420 events or 7.7% of the catalog were recorded in Utica Formation, 435 events or 8% of the catalog were recorded in Point Pleasant and the rest of the catalog was recorded in Trenton Formation with total of 154 events or 2.8%. In well B11 (bottom plot), the largest cluster of events lies within the Queenston Formation, with total of 6940 events or 40.2% of the microseismic catalog, 3937 events or 22.9% of the catalog were recorded in Utica Formation, 4532 events or 26.3% of the catalog were recorded in Point Pleasant and the rest of the catalog was recorded in Trenton Formation with total of 1839 events or 10.6%. Visually, the lower

density of microseismic events around depth 1550 m can be correlated to the gamma ray vertical logs from both wells, which indicate the increase of shale content at this depth.

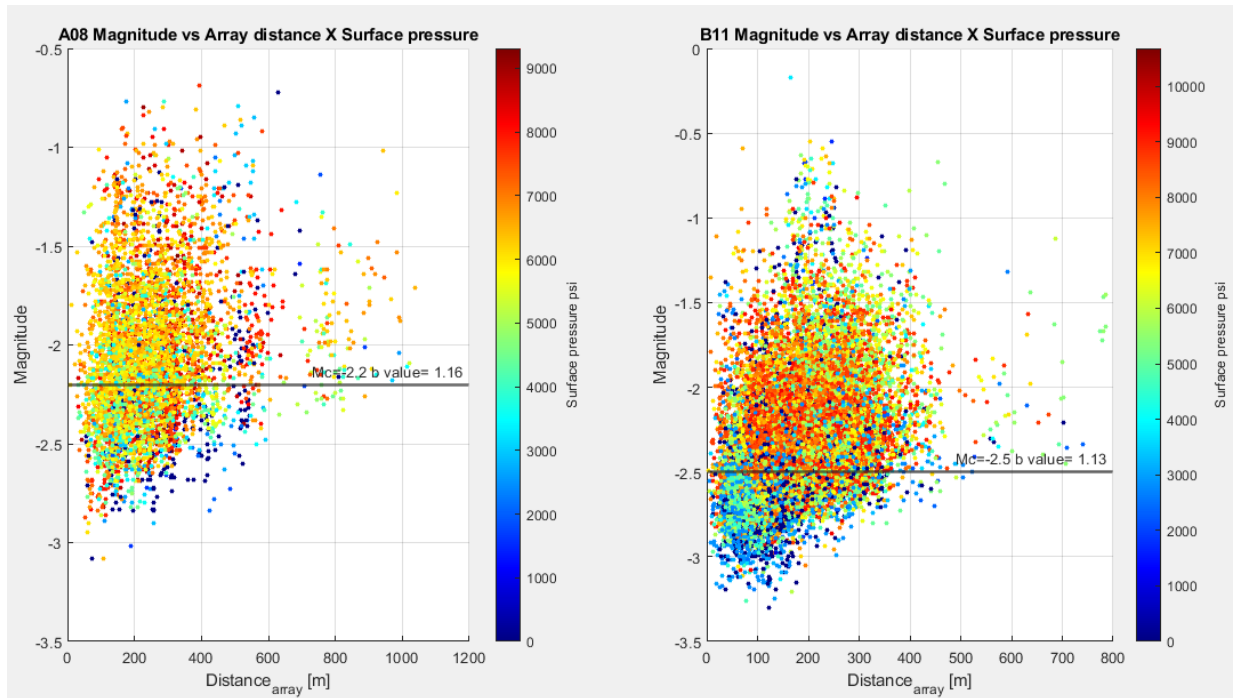


Figure 29 A08 (left) and B11 (right), Distance/ magnitude plots scaled by surface pressure, it illustrates the distance of events from the geophones array.

The distance vs. magnitude plots (Figure 29) illustrate the distance of events from the geophones array where 60.2% of the microseismic catalog of A08 and 67.5% of B11 microseismic catalog meet the criteria of b-value calculation. Any microseismic events below the value of magnitude of completeness are excluded from this analysis for the purpose of b-value calculation because lower magnitude events cannot be detected at a farther distance from the array.

The analysis of the b-value is significant because it reveals the relationship between the magnitude and the event count with respect to local stress regimes. The plot in Figure 30 shows the results of 3 methods to calculate b-value where the red solid and dashed lines are the b-value and M_c calculated by Petrel based on the method of Spatially Varying Magnitude of Completeness, the blue solid and dashed lines are the b-value and M_c calculated by the method of Magnitude of

Completeness, and the black solid and dashed lines are the b-value and Mc calculated by zmap based on the frequency of moment magnitude. The plot reveals that the method of Magnitude of Completeness is less accurate in the calculation of the b-value on a stage level. This is because the calculation in this method assumes higher Mc regardless of event count, which results of outliers on the top plot (A08). The bottom plot (B11) shows less variation utilizing the same method due to higher event count in most of the stages. Therefore, all results from the method of Magnitude of Completeness were ignored due to high level of uncertainty.

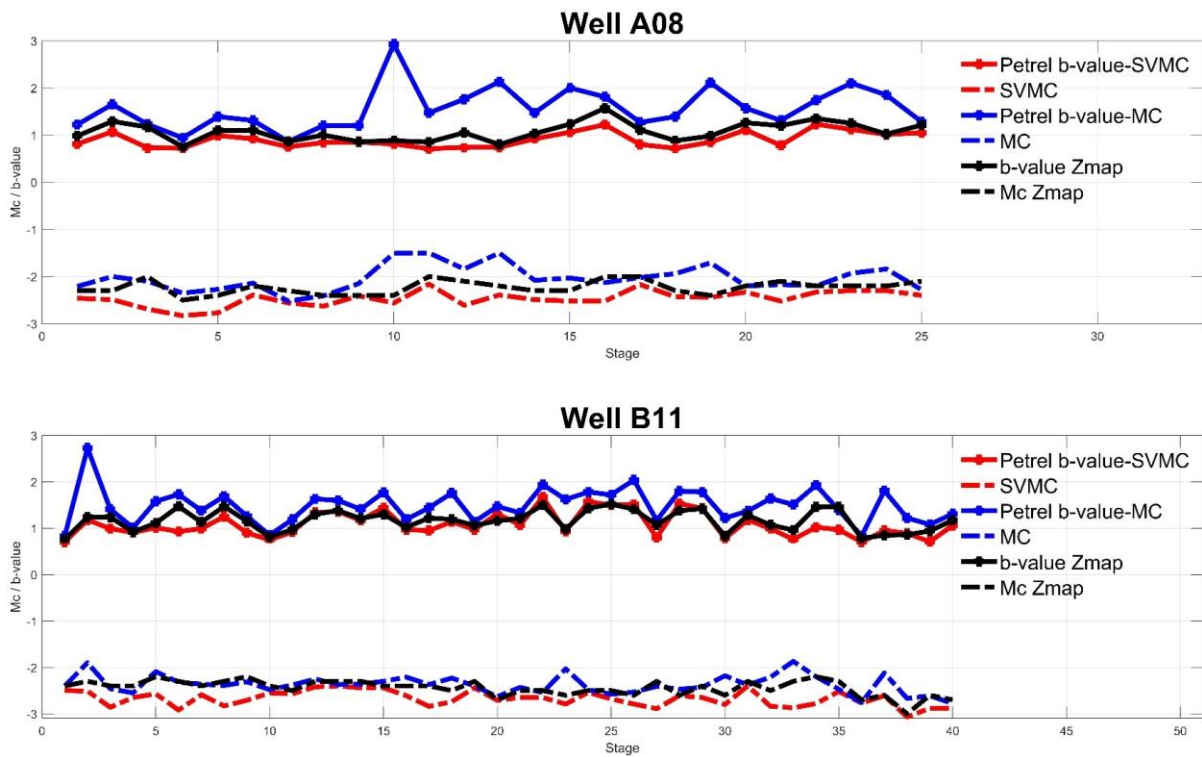


Figure 30 The results of b-value (solid lines) and Mc (dash lines) calculation on a stage level from three different methods analysing the microseismic catalog of well A08 and well B11.

The seismicogenic index average of A08 is -3.37, standard deviation is 0.43, whereas the index average of B11 is 3.4, standard deviation is 0.54. Furthermore, the linear regression model between the b-value and the seismicogenic index revealed a negative correlation, where the

coefficient of determination (R^2) is 0.8 and 0.6 for A08 and B11, respectively (Figure 31). Based on this relationship, the b-value can be used to identify the regions with higher probability of significant events, where it leads to the activation of a natural fracture or a fault. However, this does not mean every case of low b-value (or high seismogenic index) is a confirmation of a natural fault activation. Locally, other factors must be considered before making this determination, such as events distribution, magnitudes, cumulative moment, and time duration.

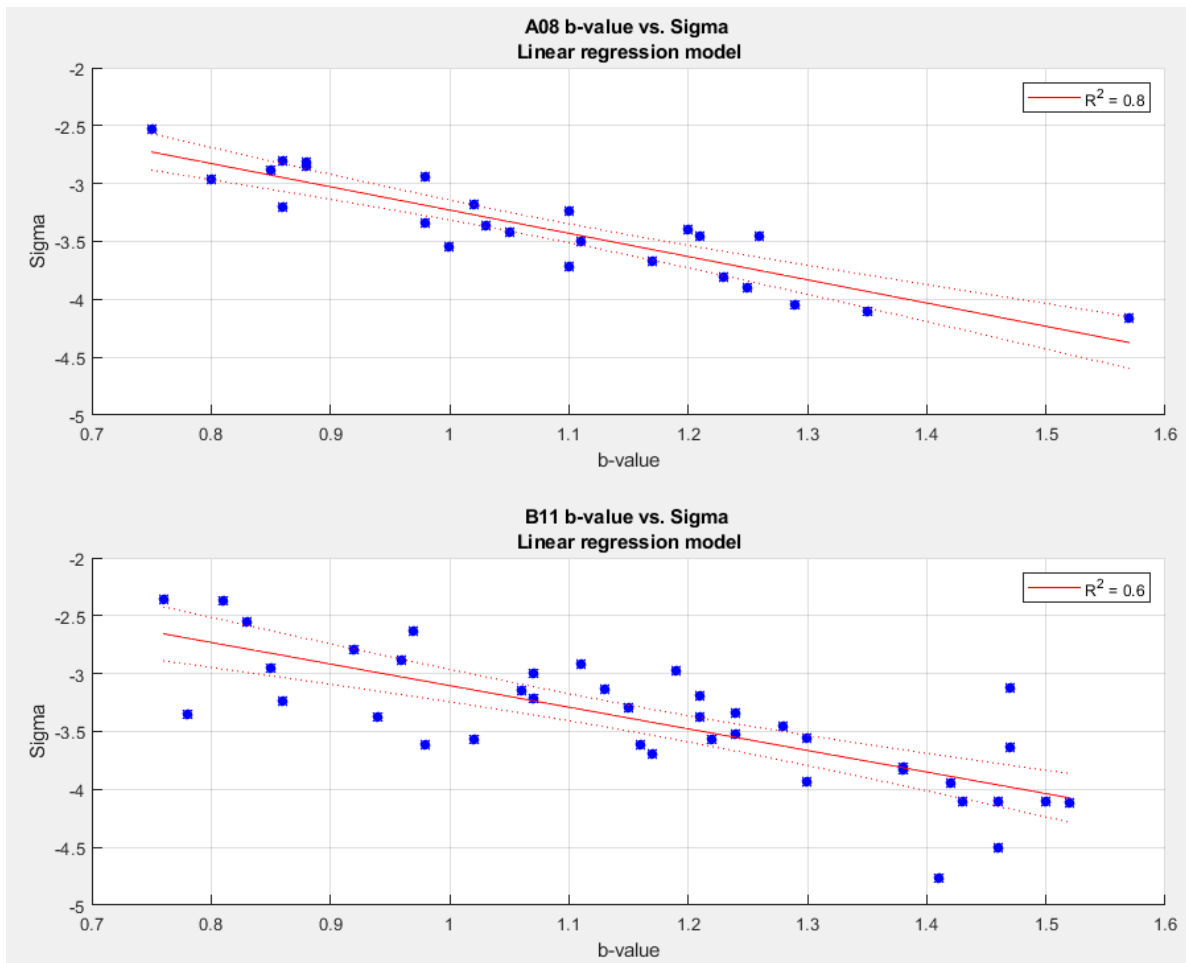


Figure 31 The linear regression models between the b-value the seismogenic index for A08 (top) and B11 (bottom), where R^2 are 0.8 and 0.6 respectively. The models illustrate the negative correlation between the b-value the seismogenic index.

4.2 The R-T Plots

The r-t plots show that events that fall below the triggering front curve (Figure 32) are considered to be wet events, whereas the rest of the microseismic catalog or events that fall above the curve are thought to be mostly dry events not directly related to the fluid-injection. However, as the fractures grow, dry events within the distance of the triggering front were observed to become wet. Which is around 700 m and 500 m for A08 and B11, respectively.

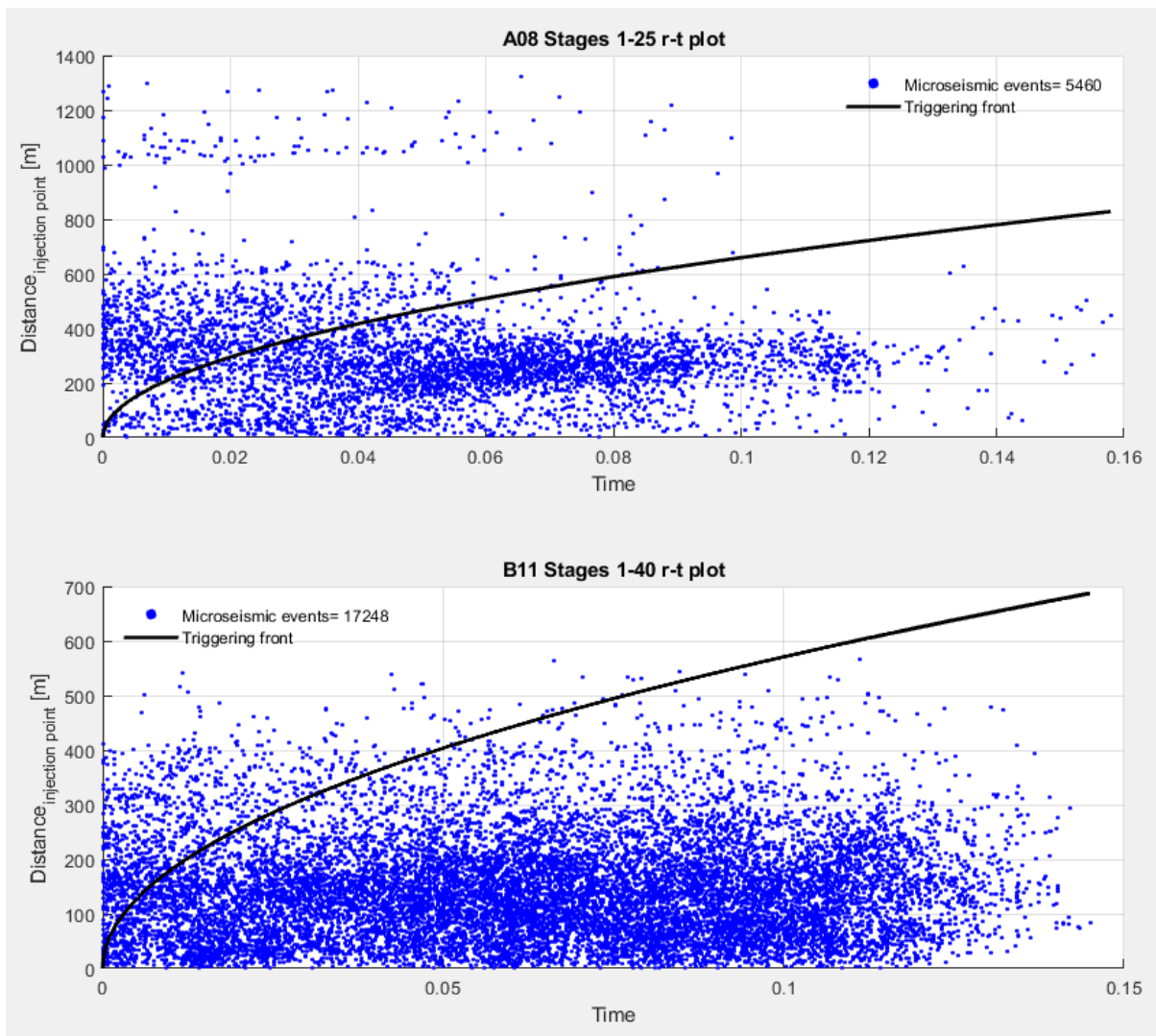


Figure 32 A08 (top) and B11 (bottom) r-t plots illustrate the distance of microseismic events from the injection point vs. time, where black curve is the triggering front.

In many stages on A08 (top plot), microseismic activity was observed very early in the stage, as far as 1300 m from the injection point at an opening pressure about 2500 psi. This occurrence cannot be explained as a fracture created by the injection, because the triggering front did not reach that region. Therefore, it is reasonable to assume that there are permeable pre-existing fractures, where the pressure can be transmitted from these fractures into other connected fractures, triggering microseismic events. These events are defined as dry disconnected pressure-driven events. Eliminating these events indicates that the assumption of frac hit is incorrect and there is no sign of treatment fluid communication between the two wells.

The results of the r-t plots for both wells are shown in Figure 33. A08 total number of wet events is 3257 events with total radiated energy of 5.1553×10^5 joules, whereas dry events are 1811 events with total radiated energy of 1.7807×10^5 joules. The remaining 392 or 7.18% of the catalog which consists of stages 2&4 are not included in this analysis due to many problems during treatment, which make them poor representatives of the microseismic catalog.

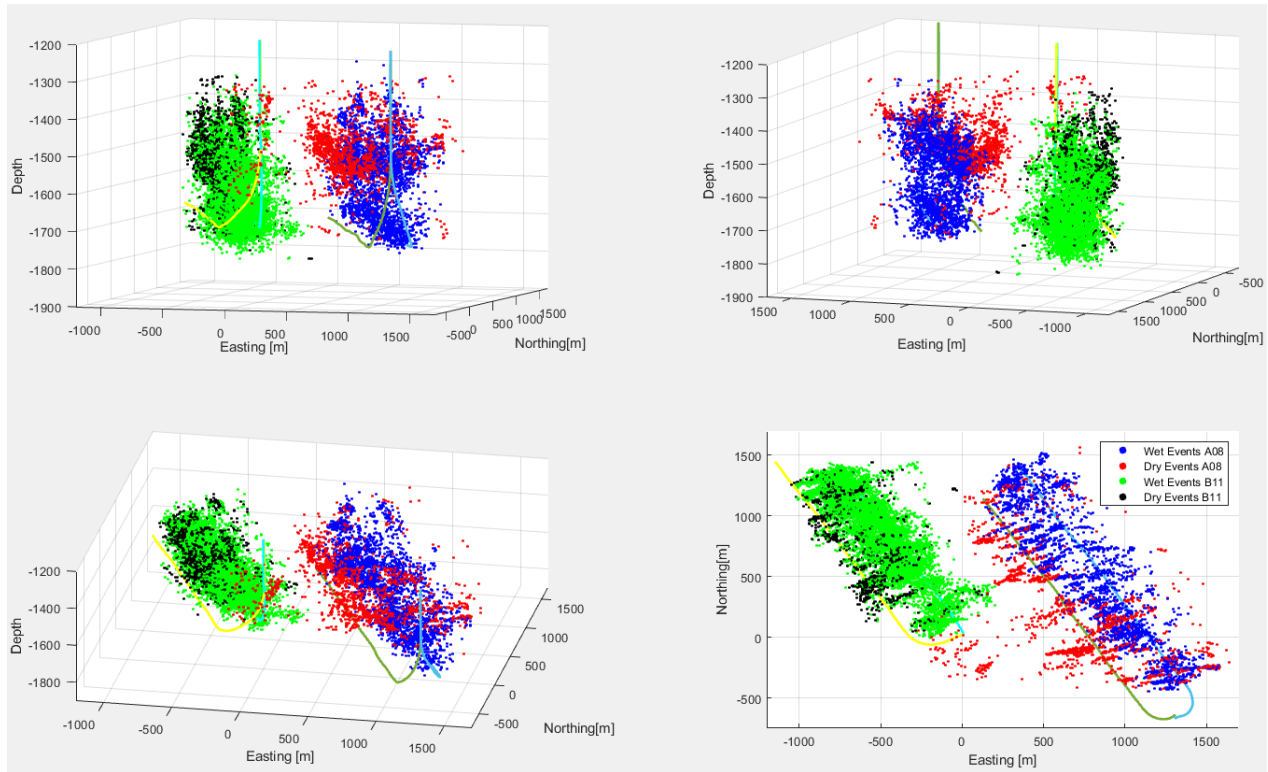


Figure 33 Multiple views of the microseismic clouds showing dry and wet events for both wells. Where blue dots represent A08 wet events, red dots represent A08 dry events, green dots represent B11 wet events, and black dots represent B11 dry events.

A08 wet events account for 64.27% of the catalog and 74.33% of the radiated energy, whereas dry events account for 35.73% of the microseismic catalog and 25.67% of the radiated energy.

B11 total number of wet events is 15614 events with total radiated energy of 1.2293×10^6 joules, whereas dry events are 1636 events with total radiated energy of 7.5266×10^4 joules. Wet events account for 90.5% of the catalog and 94.2% of the radiated energy, whereas dry events account for 9.5% of the microseismic catalog and 5.8% of the radiated energy.

Superimposing the results of the r-t plots on the map of b-value distribution (Figure 34 & Figure 35) reveals that dry event clusters are often associated with higher b-value than the surrounding regions. This is due to the relationship of between the number of events and

magnitudes, where these clusters contained more events with low magnitude than other regions. Additional, B11 map illustrates more visible changes in b-value than A08 map, because B11 treatment produced far more microseismic events and larger distribution than A08, which made the number of events more significant in the calculation of b-values in those regions. However, these observations do not impact the overall calculation of the b-values for both wells.

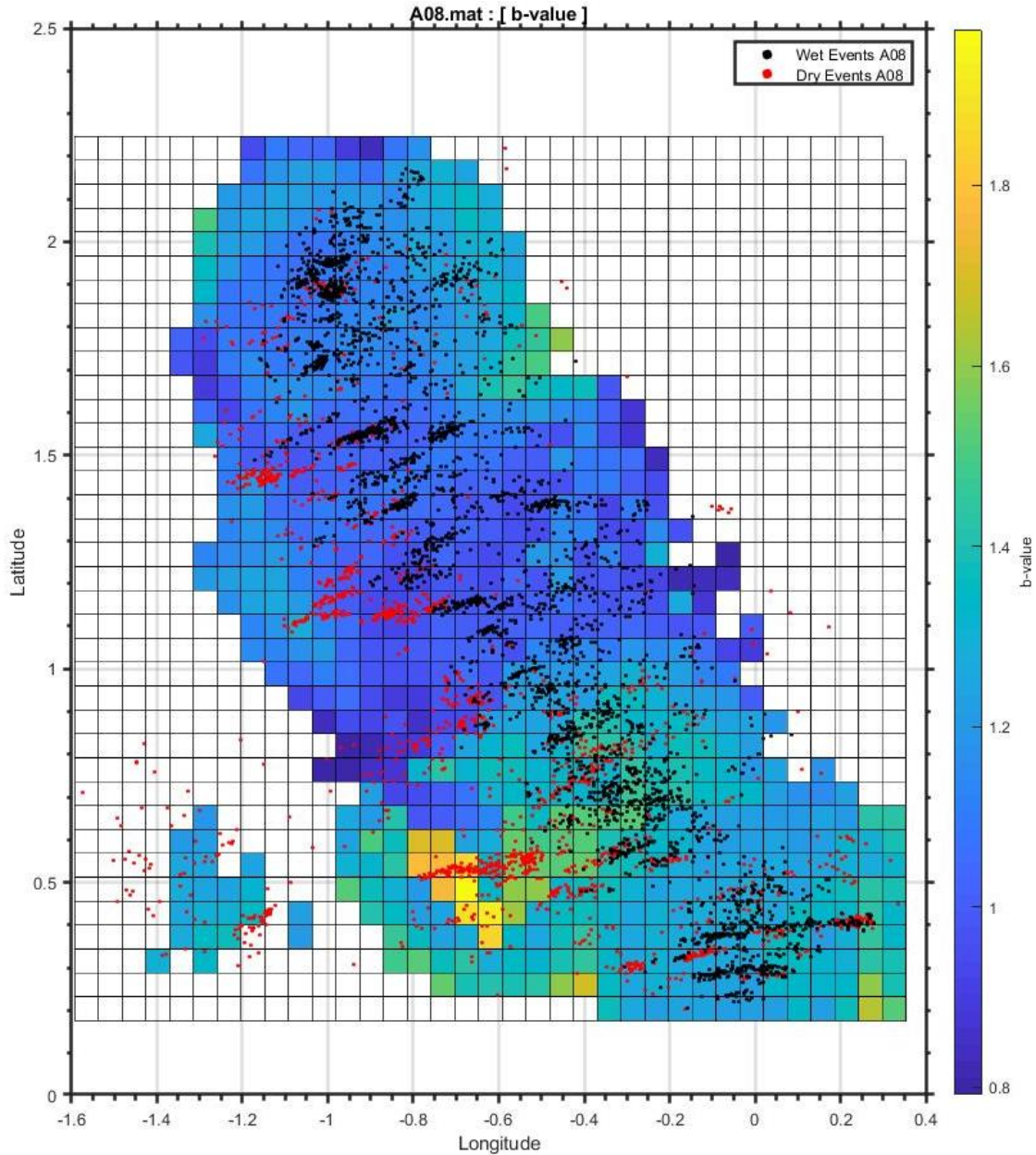


Figure 34 A08 map view of dry events (red points) and wet events (black points) superimposed over the map of b-value distribution.

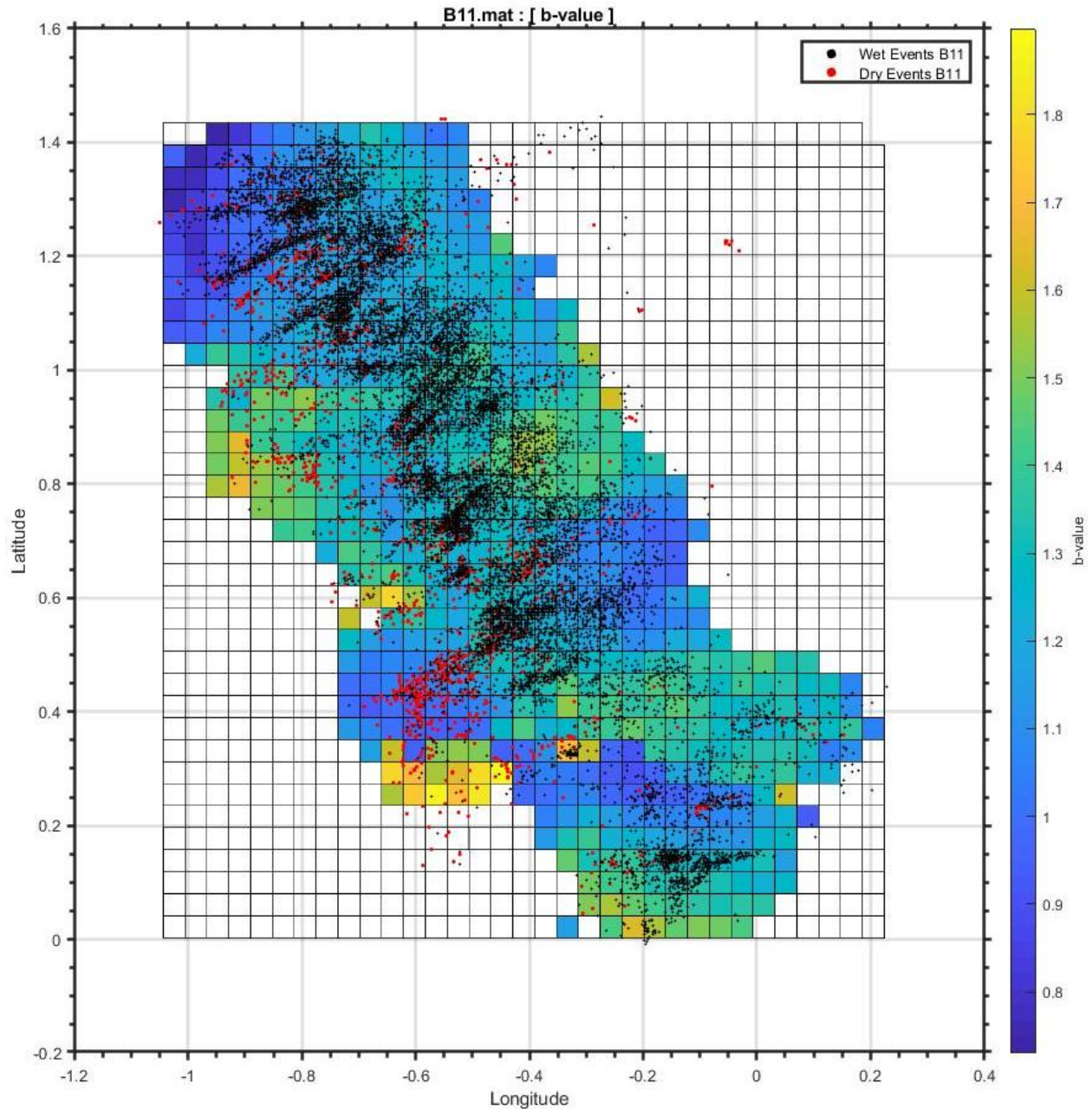


Figure 35 B11 map view of dry events (red points) and wet events (black points) superimposed over the map of b-value distribution.

Visually, the lowest b-value is located at the northwest region on B11 map (Figure 35), which is the location of the stage 1. Further analysis revealed that the overall b-value for the stage is 0.76, D-value is 1.59, M_c is -2.4, and Σ is -2.36. the total injected energy is 2.74×10^{10} joules and radiated energy is 1.52×10^5 joules, whereas the total stimulated volume is 1.44×10^6 m³. The

rose diagram shows dominant azimuth 245° , and best fitting plane shows azimuth 238° and dip 75° (Figure 36).

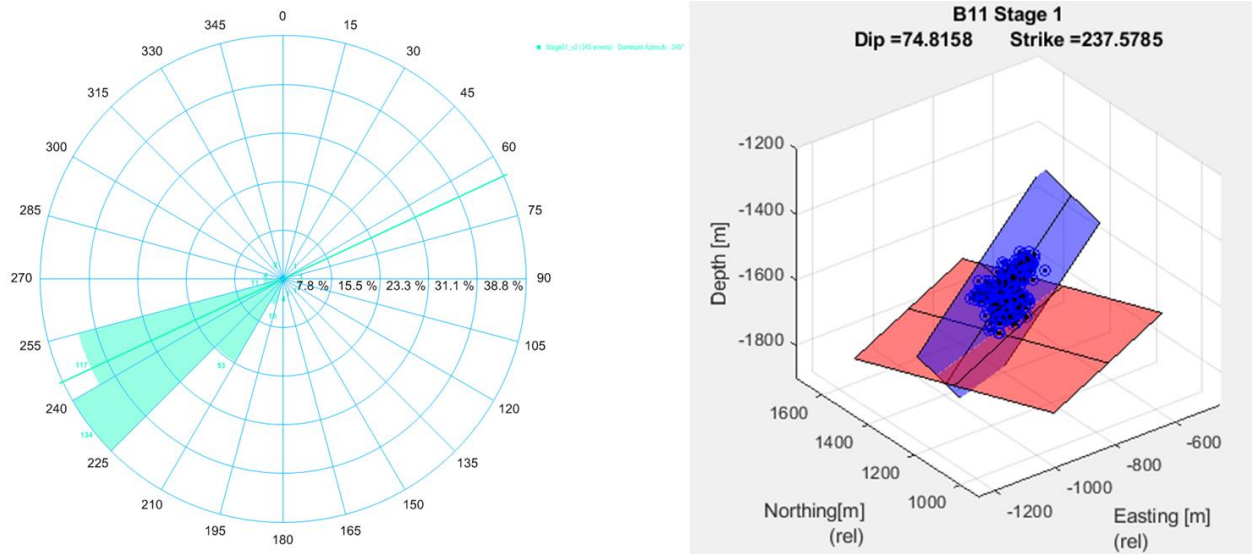


Figure 36 B11 stage 1 rose diagram (left), best fitting plane (right).

The map view of events (Figure 37) shows growth in the direction of $S_{h_{max}}$, and growth is mostly vertical. The total microseismic events recorded is 345 ranged between moment magnitude of -2.76 and -0.55. The total dry events count is 24 and wet events count is 321 illustrated in the r-t plot. The magnitude-time and cumulative moment plots (bottom plots) show the possibility of a fault activation based on the increase of number of events and magnitude at time 0.04 of the stage. The spike of moment magnitude and cumulative moment versus time indicates a possible strike-slip fault was activated, where b value is 0.76 and D value is 1.59. This can be visualized by isolating the relevant events to produce 3D plot with the plane of the possible fault in Figure 38.

B11
Stage 1

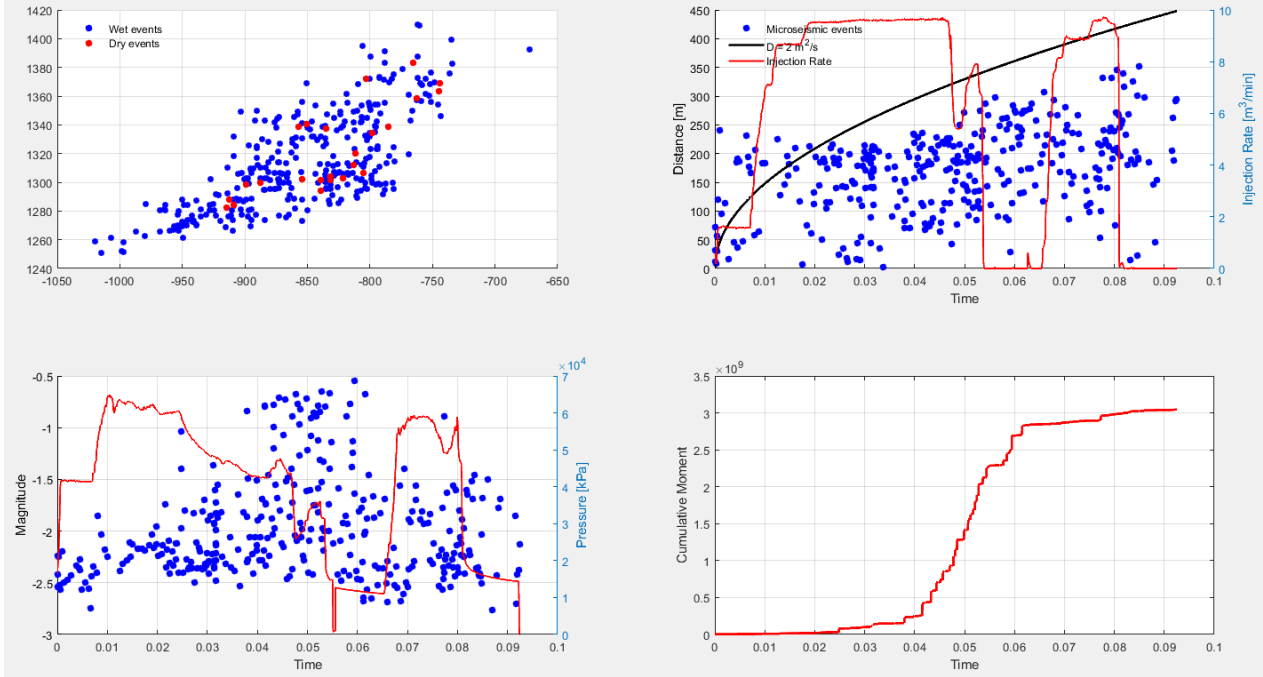


Figure 37 B11 stage 1 map view plot, r-t plot, magnitude plot and cumulative moment plot.

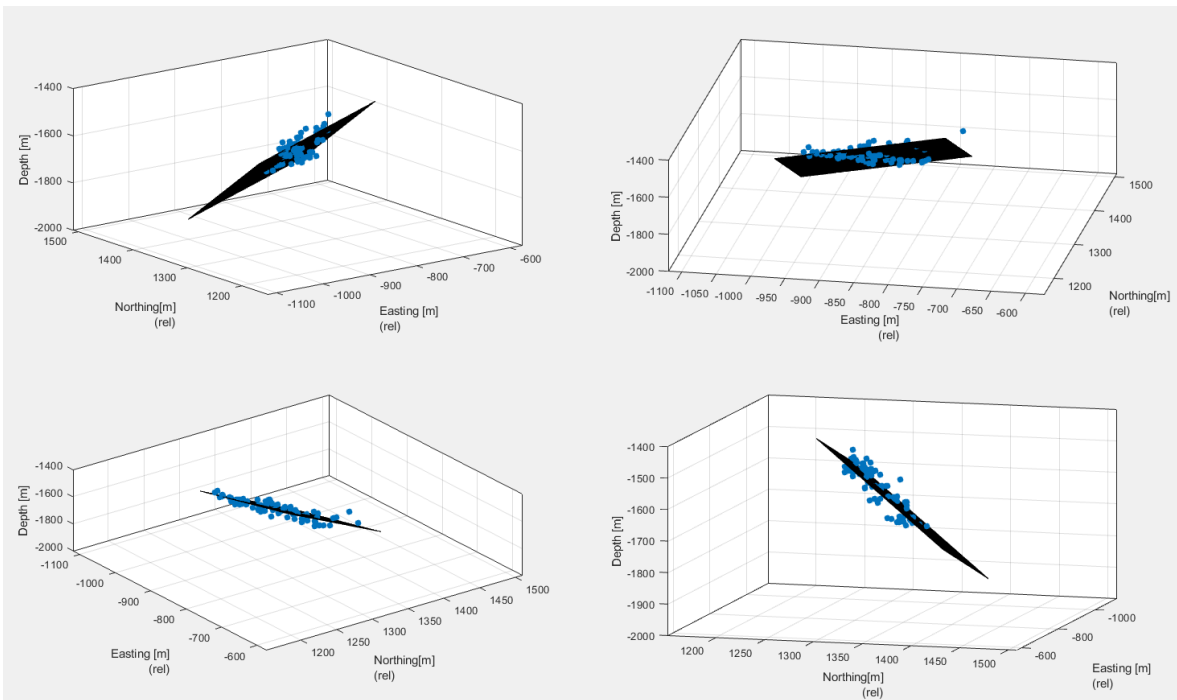


Figure 38 A possible strike-slip fault events and the fault plane.

4.3 The Mechanical Properties and Lithology

Well logs can provide a host of data useful in understanding the lithology and physical properties of the rock units penetrated by the well. Unfortunately, since A08 lacks detailed logs, I will have to focus mainly on B11. Because these logs were recorded using measured depth (MD) as one axis, I will present those logs in two sections, vertical and horizontal.

The gamma ray log of the vertical portion of B11 (Figure 39) shows that shale content is higher in the Queenston Formation than the other formation. As shale content decreases with depth around 1680 m through the Utica and Point Pleasant, the brittleness index increases where it reaches its highest value in Point Pleasant. It is important to note that the Trenton formation is plotted on the vertical logs as a depth reference only, there are no logs provided for it because the lateral was drilled through Point pleasant.

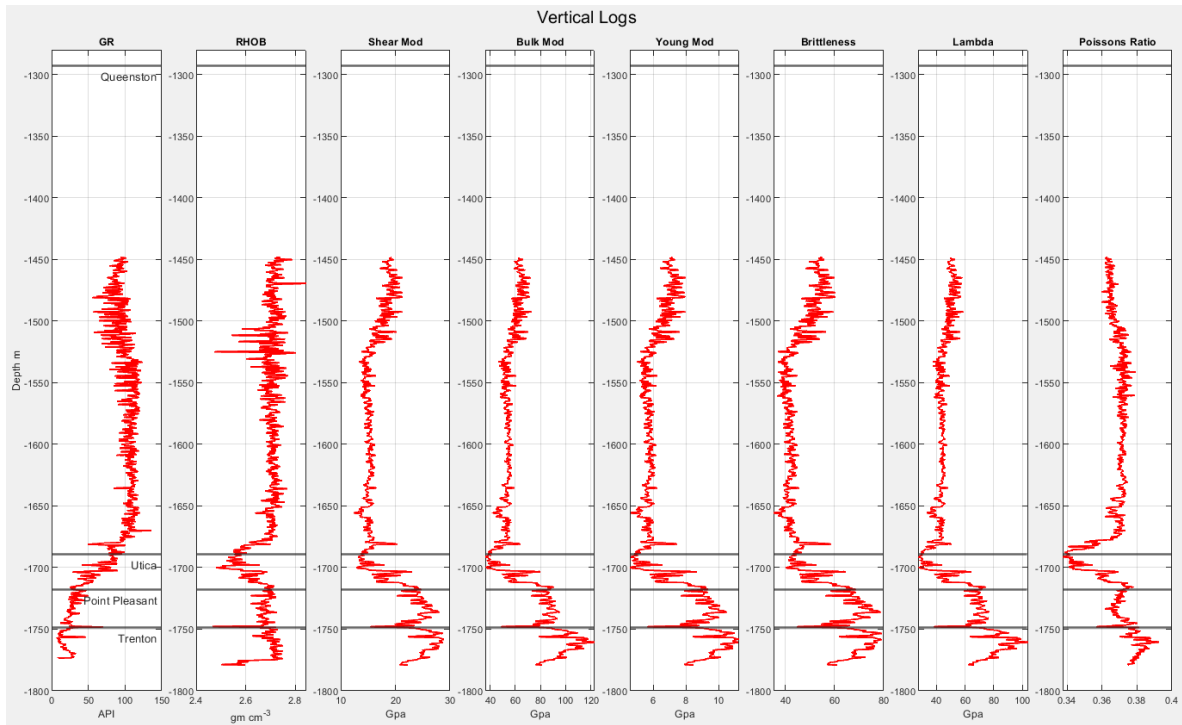


Figure 39 B11 vertical logs: GR, density, shear modulus, bulk modulus, Young's modulus, brittleness, lambda, and Poisson's ratio.

The LMR cross plot for the vertical section of the well in Figure 40 (the left plot) revealed that the lithology of Queenston between 1500 m and 1690 m MD is mostly carbonate. Whereas the interval between 1690 m and 1720 m MD, or the Utica Formation is sandy limestone, sandstone, and shale. The Pleasant Point is mostly carbonate.

The LMR cross plot for the lateral section of the well (the right plot) is solely Point pleasant and it shows variation in lithology, which is due to the topography of the formation and the geometry of the well, where the heel is deeper than the rest of the lateral. Thus, it shows a substantial section of Point Pleasant, where the lower interval of the formation is carbonate-rich based on gamma log.

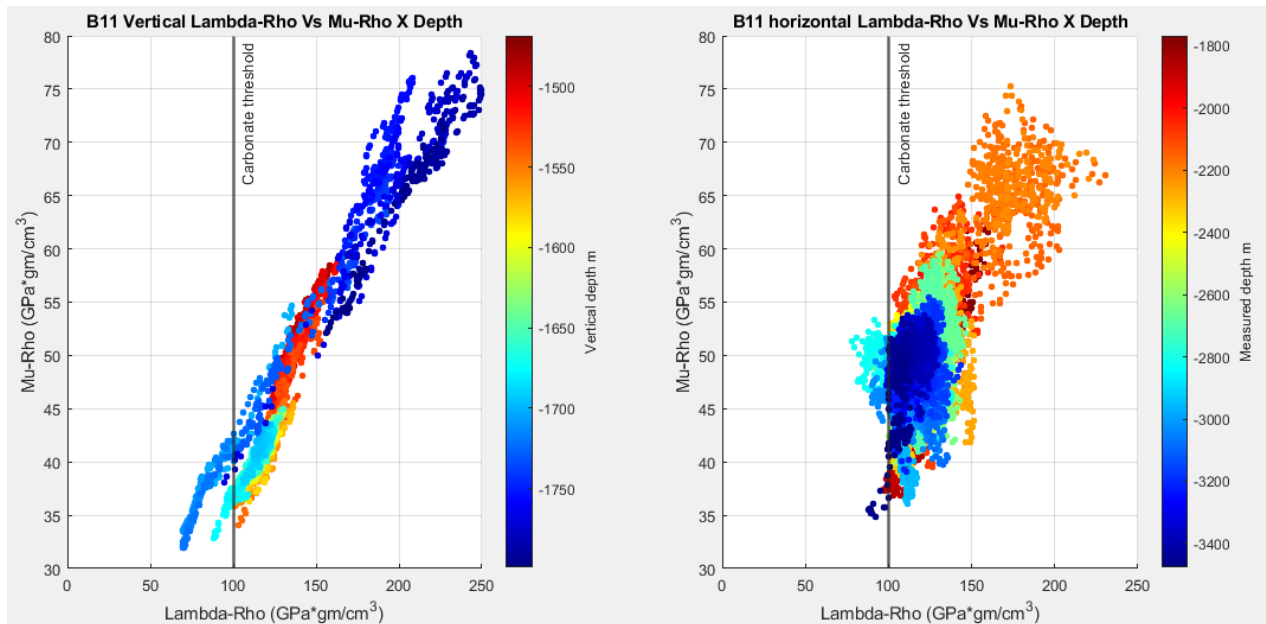


Figure 40 The LMR cross plots for the vertical portion (left) and the lateral (right) scaled by depth.

The gamma ray log of the horizontal portion of B11 (Figure 41) shows a drop in shale content at 2110 m and 2230 m MD, whereas the brittleness increases, which indicates higher concentration of carbonate at the heel. The interval between 2750 m MD and 2821 m MD shows

a drop in shale content followed by an increase at 2900 m MD. Moreover, the same interval shows a sharp drop in the bulk modulus, lambda, and the Poisson's ratio, whereas the brittleness increased.

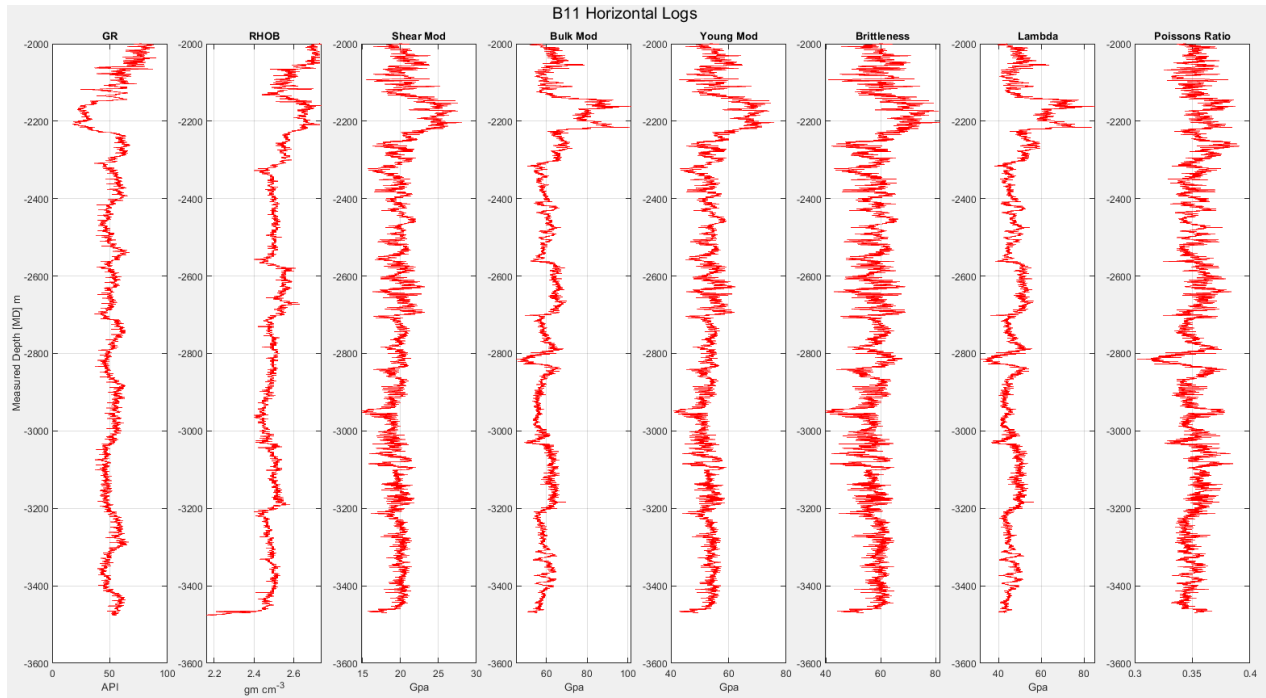


Figure 41 B11 horizontal logs: GR, density, shear modulus, bulk modulus, Young's modulus, brittleness, lambda, and Poisson's ratio.

The impact of these observations is better understood by superimposing the logs along the lateral to correlate them with the treatment stages and their microseismic activity. In fact, the interval between 2110 m and 2230 m MD is related to stages 35 through 40 (Figure 42), where fewer events were recorded per stage. This observation is explained by the increase of the brittleness index, where the microseismic activity decreases as the brittleness increases.

The second observation is related to the interval between 2750 m and 2900 m MD, where it is correlated to stages 18 and 23. These stages were incomplete because no proppant was delivered to the formations. Further analyses of stage 18 show that the overall b-value for the stage is 1.19, D-value is 1.31, Mc is -2.5 and Σ is -2.98. The total microseismic events recorded is 837

ranged between moment magnitude of -3.26 and -1.0. Whereas the total injected energy is 2.50×10^{10} joules and radiated energy is 3.93×10^4 joules. The total stimulated volume is $7.39 \times 10^6 \text{ m}^3$.

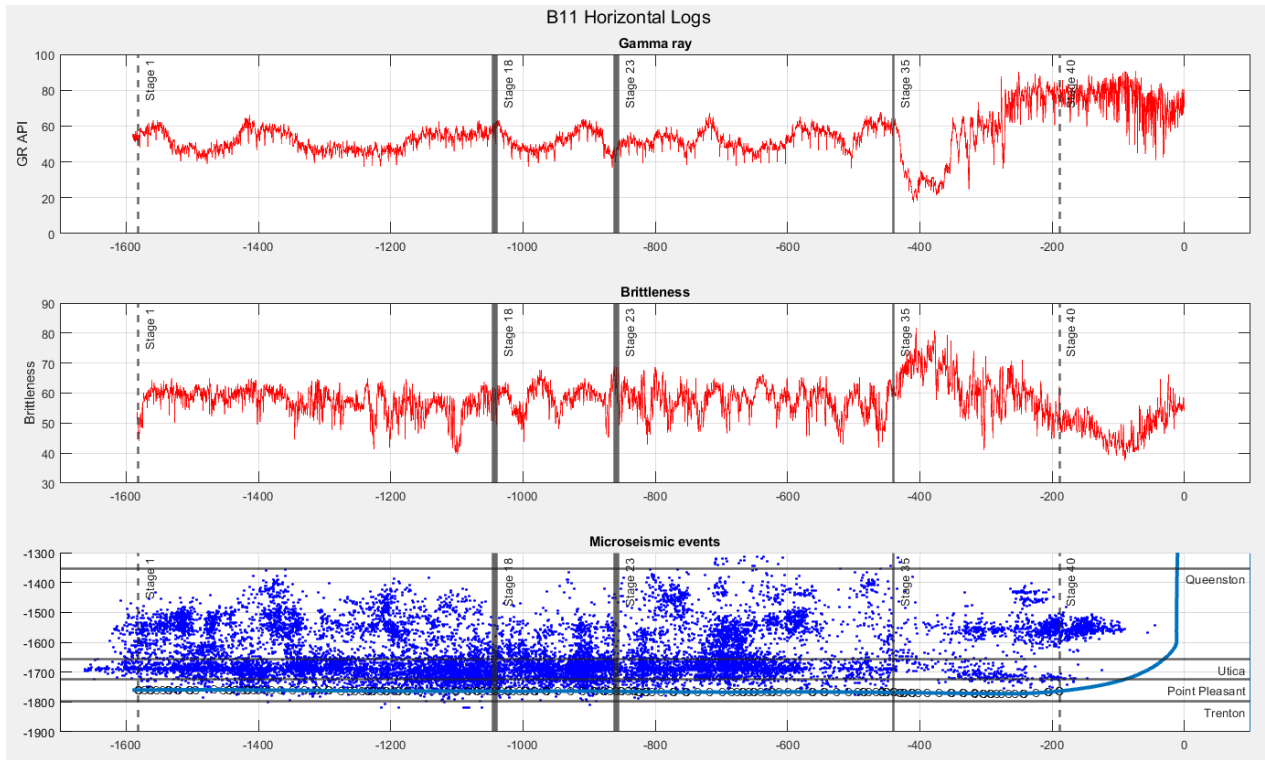


Figure 42 B11 horizontal logs superimposed along the lateral. From top to bottom (GR log, brittleness index, and the microseismic catalog).

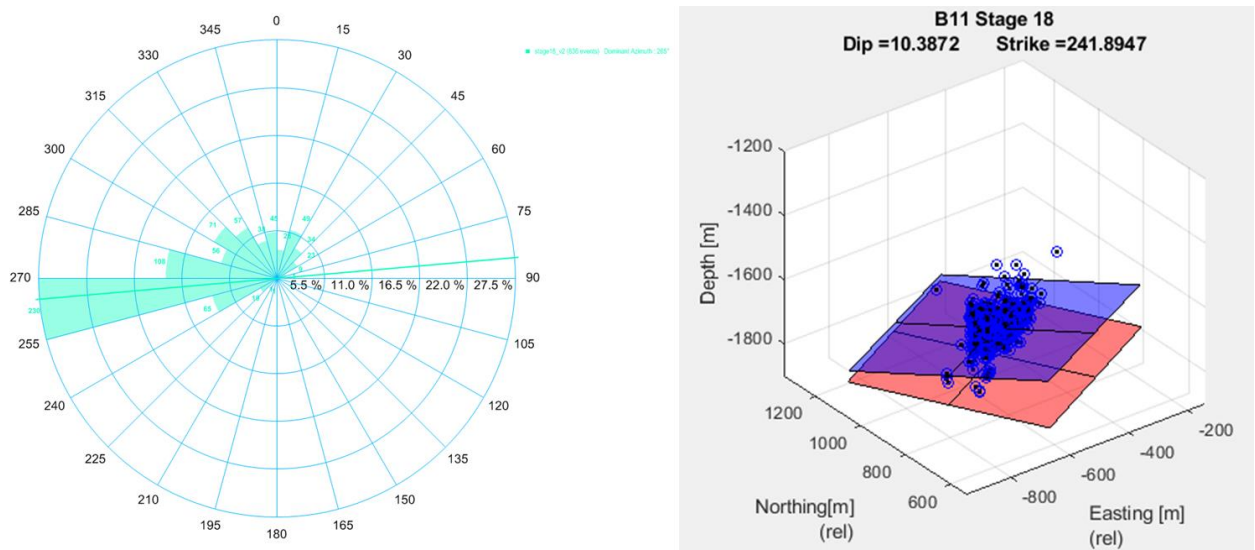


Figure 43 B11 stage 18 rose diagram (left), best fitting plane (right).

The rose diagram (Figure 43) shows the dominant azimuth is 265°, the best fitting plane azimuth is 242°, and the dip is 10°. Similarly, stage 4 on A08 was also problematic due to spikes in the surface pressure. The analyses of stage 4 show that the overall b-value is 1.22, D-value is 0.66, Mc is -2.4 and Σ is -2.53. The rose diagram (Figure 44) shows the dominant azimuth is 245°, the best fitting plane azimuth is 221°, whereas 75% of the catalog forms a cluster, where the dip is 14°.

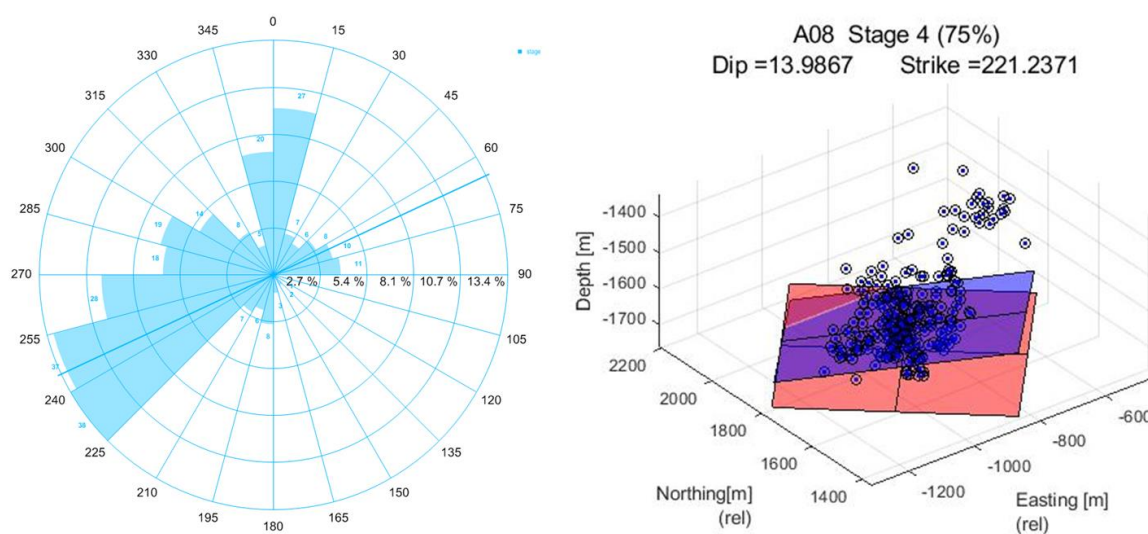


Figure 44 A08 stage 4 rose diagram (left), best fitting plane (right).

The low dip angle along with the depth of the microseismic activity indicate that the fracture moved through the bedding plane of the Point Pleasant Formation. The proximity, spatial alignment, well logs, and the similarities in responses suggest that preexisting fractures or faults filled with cementing minerals. These have different mechanical properties from the overall formation that led to the fracture moving through the bedding plane and leaking to previous stages.

4.4 The Energy Budget and The Stimulated Volume

It is important to distinguish between preexisting fracture system and events occurring on the same fracture system of the previous stage, isolating these events will result of more accurate calculation of the stimulated volume and overlap volume. The stimulated volume of each stage was calculated form the 3D alphashape of the microseismic cloud (Figure 45).

A08 and B11 results of the volume and energy calculation are shown in Table 4 and Table 5, respectively. A08 total stimulated volume for all stages is $1.3 \times 10^8 \text{ m}^3$. Total of 9 stages show no overlap at all, which is an indication of undertreatment for these stages. The overall average stage volume overlap is 2.14%, standard deviation is 4.1. The total injected energy is 1.13×10^{12} joules and radiated energy is 6.99×10^5 joules. The B11 total stimulated volume for all stages is $8.48 \times 10^6 \text{ m}^3$. All stages show an average of 18% overlap volume, standard deviation is 16.93. The total injected energy is 1.23×10^{12} joules and radiated energy is 1.3×10^6 joules.

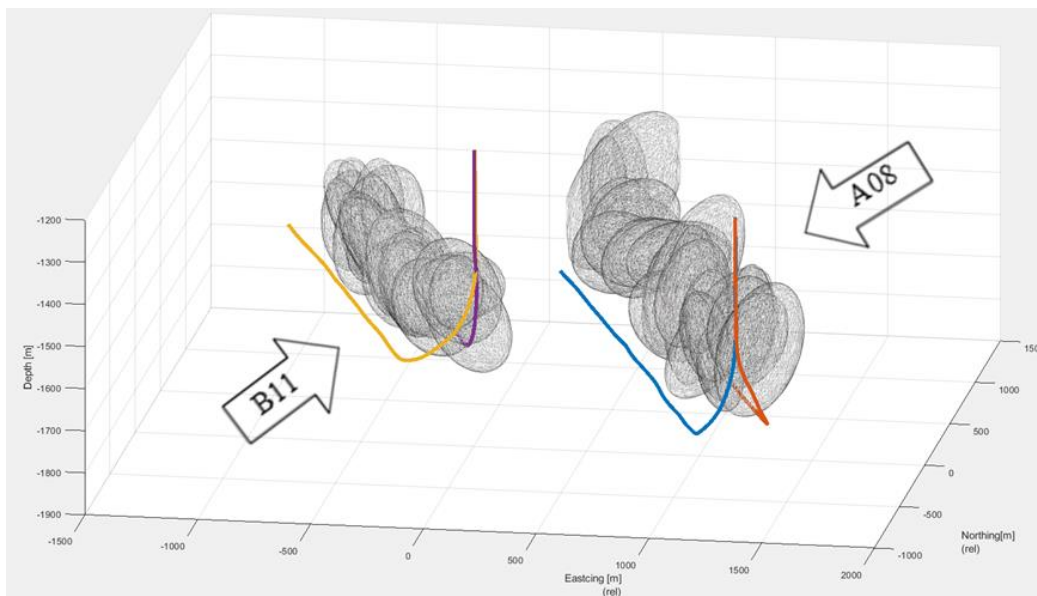


Figure 45 3D view illustrate the stimulated volume of each stage on both wells based on the triggering front .

Figure 46 (top plots) shows the relative sizes of the stimulated and overlap. The highest ratio of overlap on A08 is stage 25 with 16.7%, whereas B11 highest overlap ratio is stage 10 at 44.7%. The radiated energy plots (bottom plots) show a different picture because the microseismic events are neither distributed evenly over the stimulated volume nor are they the same magnitude. The highest ratio of overlap for A08 is also stage 25 with 40.26% and for B11 is stage 23 at 87%. The average energy overlap ratio for A08 is 6.4% with std of 8.88 and B11 is 40.4% std 24.1.

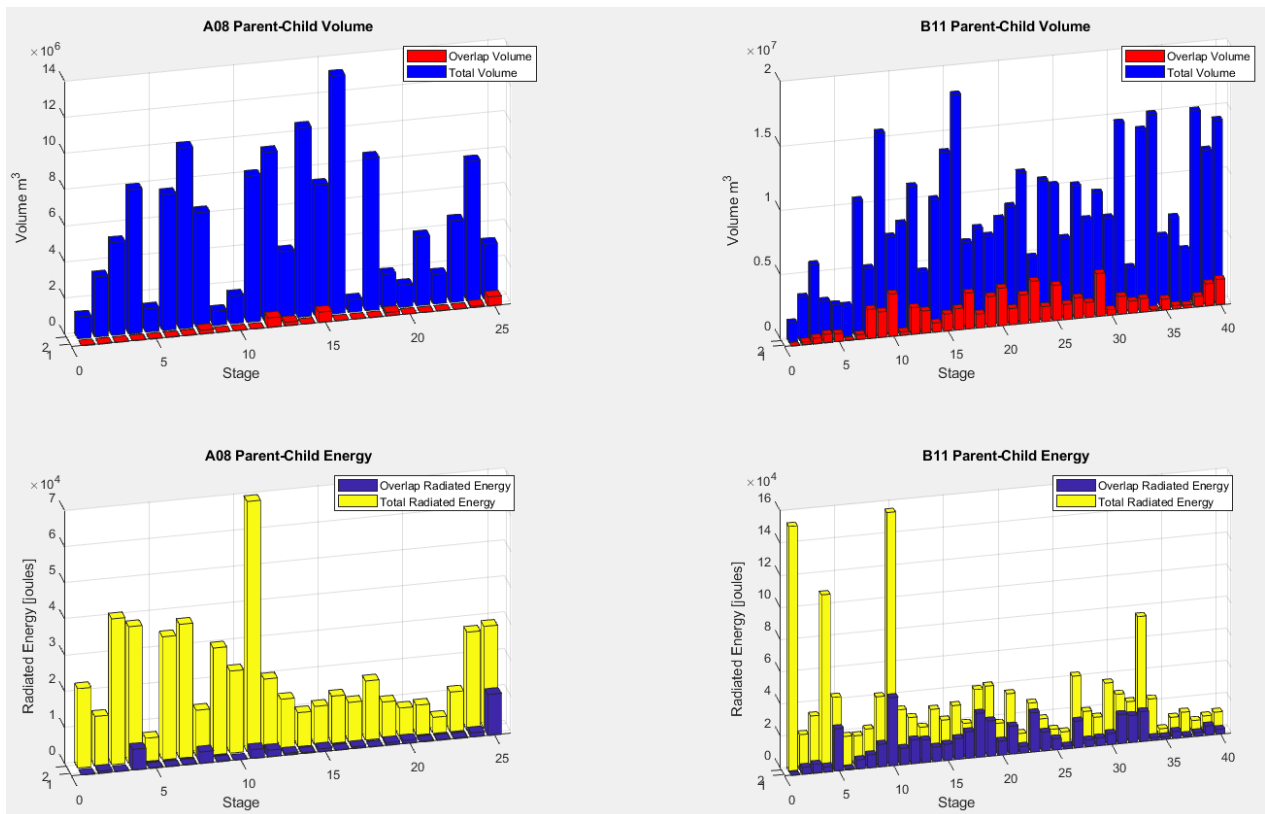


Figure 46 Bar plots for stimulated volume and overlap volume for both wells (blue & red). Bar plots for radiated energy and overlap energy (yellow & blue).

4.5 Individual Stage Analysis

A08 Stage 1: The stage started with injection rate of 10.2 bpm and surface pressure of 6296 psi, microseismic events occurred at the beginning. The rate was elevated to 30 bpm for the acid injection (HCl 15%) at a pressure of 8341 psi. The surface pressure dropped to 6175 psi which indicates the breakdown, when the acid reached the formation. The rate was increased to reach maximum of 100 bpm. The proppant started at an injection rate of 75.5 bpm and pressure 8386 psi, 3 types of sand was delivered into the stage 100 mesh, 30/50 and 20/40 with highest concentration of 5.3 ppg. After about 2 hours the stage ended with closing pressure 2150 psi. The microseismic events occurred throughout the stage and 30 min after the stage, which shows how the formation adjusting to the new stress. Total clean water pumped was 40,491 gal, total 100 mesh 126.3 sacks, total 30/50 194.1 sacks and total 20/40 184.1 sacks.

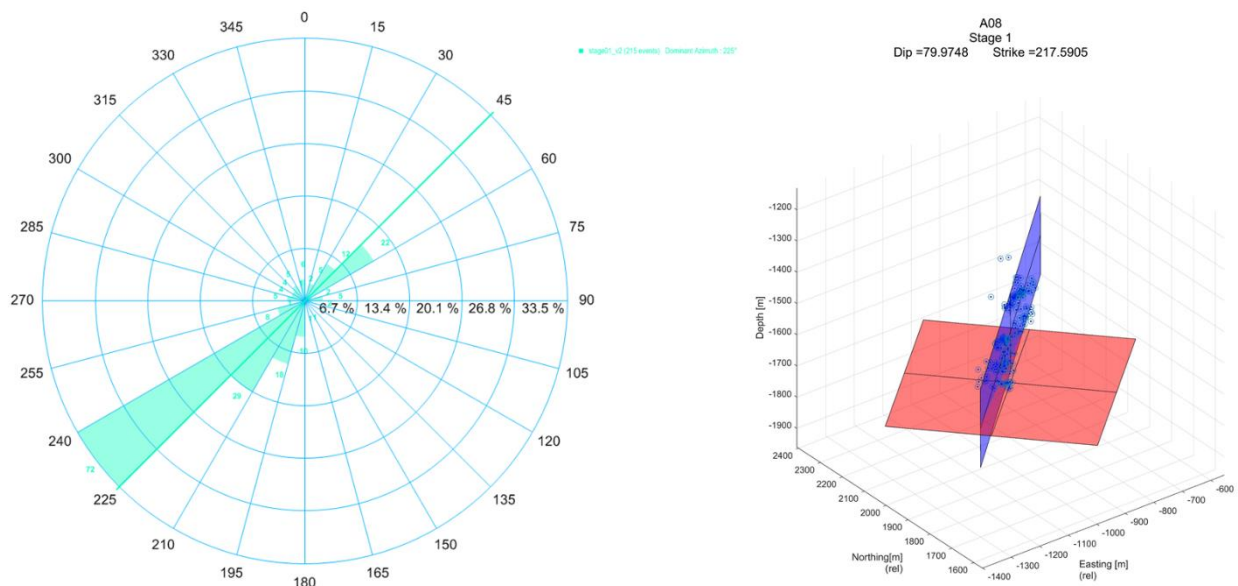


Figure 47 A08 stage 1 rose diagram (left), best fitting plane (right).

Total microseismic events recorded for the stage was 216. The rose diagram (Figure 47) shows dominant azimuth 225°, while best fitting plane shows azimuth 218° and dip 80°. The map view of events (Figure 48) shows growth in the direction of $S_{h_{min}}$, and growth is mostly vertical. The r-t plot shows almost all events are wet events.

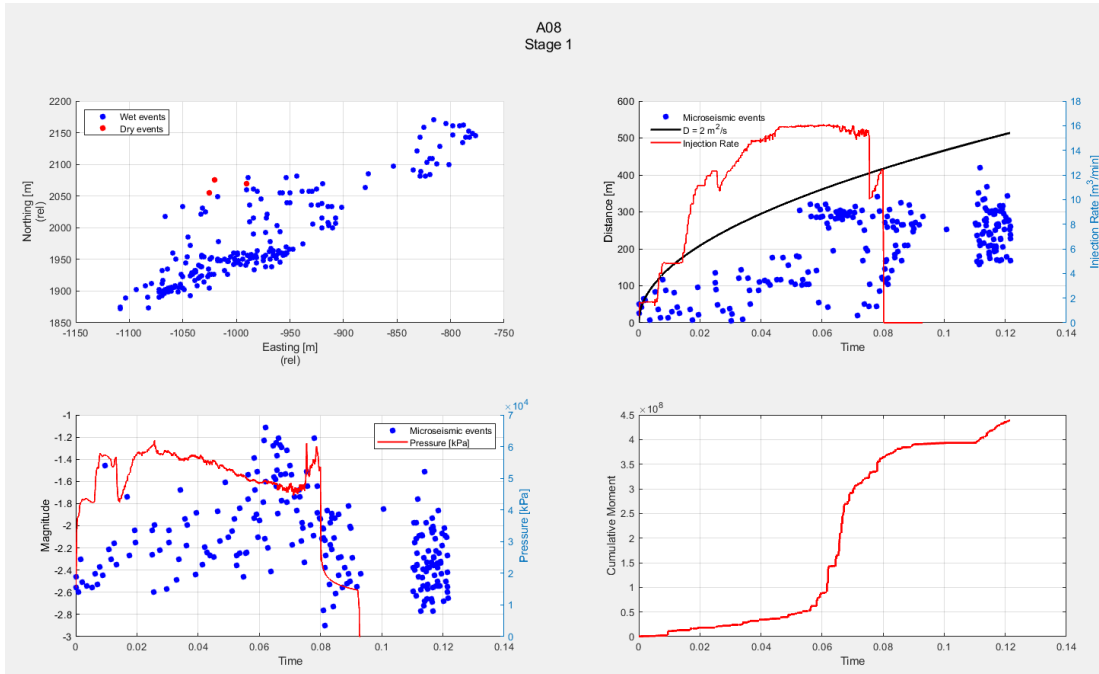


Figure 48 A08 stage 1 map view plot, r-t plot, magnitude plot and cumulative moment plot.

The overall b-value for the stage is 0.97, D-value is 1.27, M_c is -2.3, and Σ is -3.34 (Figure 49). The total injected energy is 5.36×10^{10} joules and radiated energy was 2.19×10^2 joules. The total stimulated volume was 1.20×10^6 m³ with no overlap.

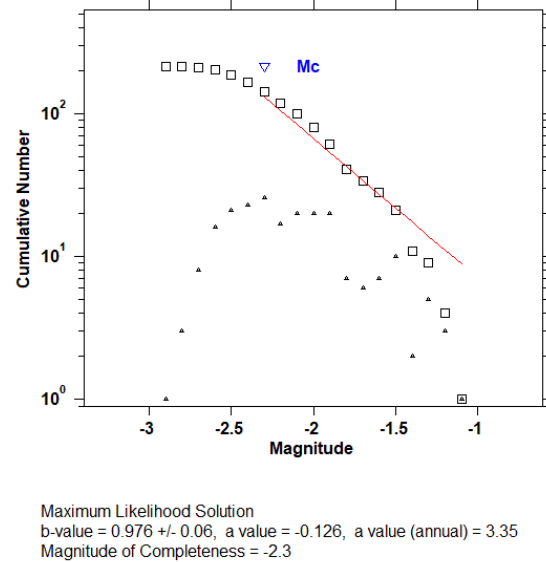
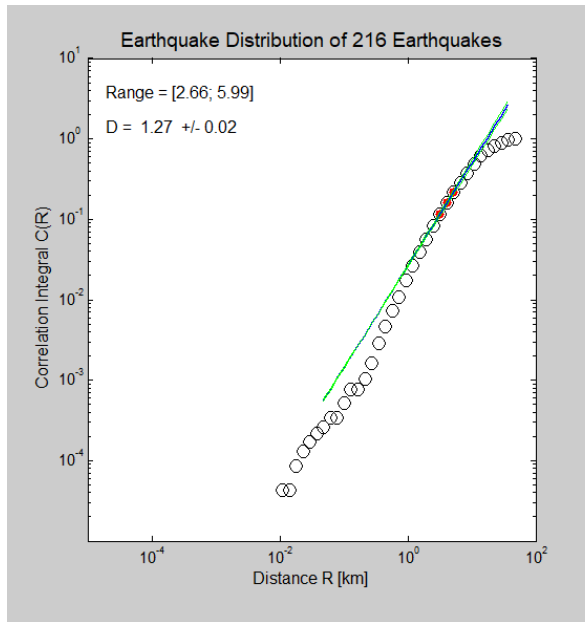


Figure 49 A08, stage 1 D -value = 1.27, b -value ~ 1 and $M_c = -2.3$.

A08 Stage 2: The stage started with an injection rate of 10 bpm and surface pressure of 6441 psi, microseismic events occurred from the beginning. Then rate was elevated to 15 bpm for the acid (HCl 15%) and pressure at 6931 psi. Surface pressure dropped to 6919 psi, which indicates the breakdown. As the rate was elevated to 82 bpm, the pressure kept rising to 9232 psi whereas slurry rate fell to 38 bpm. The crew tried again 30 minutes later but faced the same problem, with the pressure rising to 9062 psi whereas injection rate was 72 bpm. The next try was under the name Stage 2A. More acid was pumped into the stage to achieve breakdown. Surface pressure kept rose to 9000 psi with a slurry rate of 74 bpm. The rate was dropped and increased again. At rate of 61 bpm the pressure dropped to 7760 psi, which indicates the breakdown. Three types of proppant were delivered into the stage 100 mesh, 30/50 and 20/40 with highest concentration of 3.5 ppg.

Total clean water was 686,160 gal, total 100 mesh 106.3 sacks, total 30/50 195.8 sacks and total 20/40 151.6 sacks. Total microseismic events recorded for 2 and 2A was 369. The rose

diagram shows dominant azimuth 245°, whereas best fitting plane shows azimuth 212° and dip 75° (Figure 50).

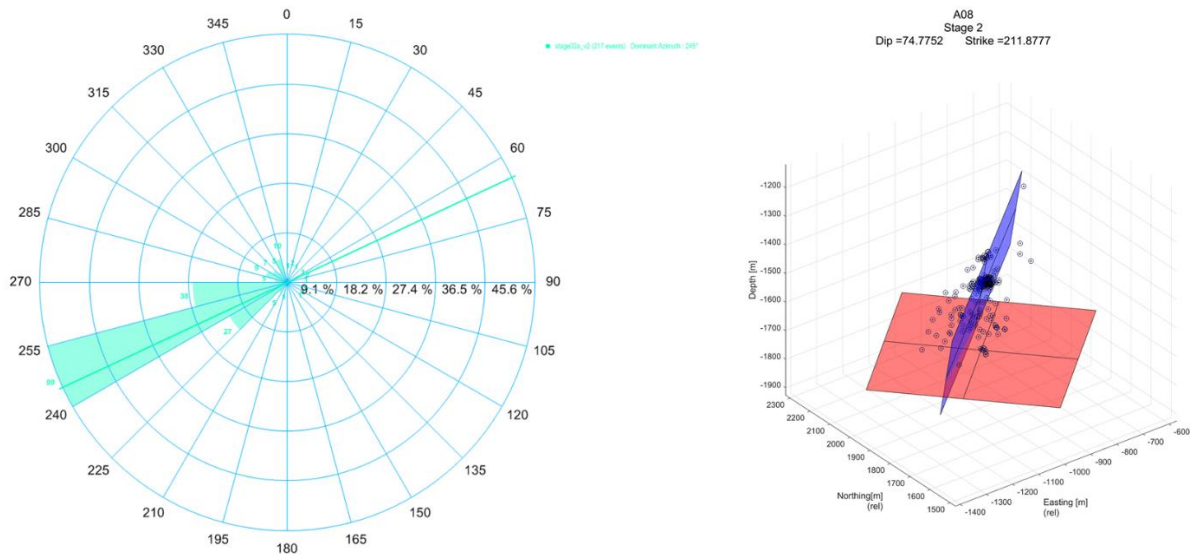


Figure 50 A08 stage 2 rose diagram (left), best fitting plane (right).

The map view of events shows growth in the direction of $S_{h_{max}}$, and growth is mostly vertical. The r-t plot for 2A shows 171 wet events and 47 dry events. The magnitude-time and cumulative moment plots show the steady growth of fractures over time (Figure 51) with no sudden changes.

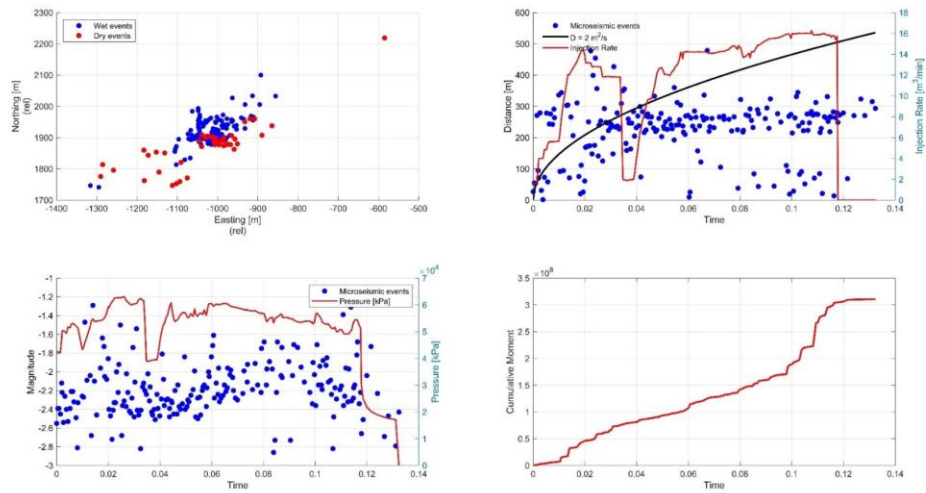


Figure 51 A08 stage 2A map view plot, r-t plot, magnitude plot and cumulative moment plot.

Further analysis on stage 2, shows some events were occurring on the same fractures of the previous stage and parallel to the bedrock plane where vertical stress is dominant, which explains the increase of surface pressure during the treatment.

The overall b-value for the stage is 1.46, D-value is 1.24, M_c is -2.3 and Σ is -4.04 (Figure 52). The total injected energy is 1.08×10^{11} joules and the radiated energy was 1.38×10^4 joules. The total stimulated volume was 3.33×10^6 m³ with overlap with the previous stage of 1.00×10^4 m³.

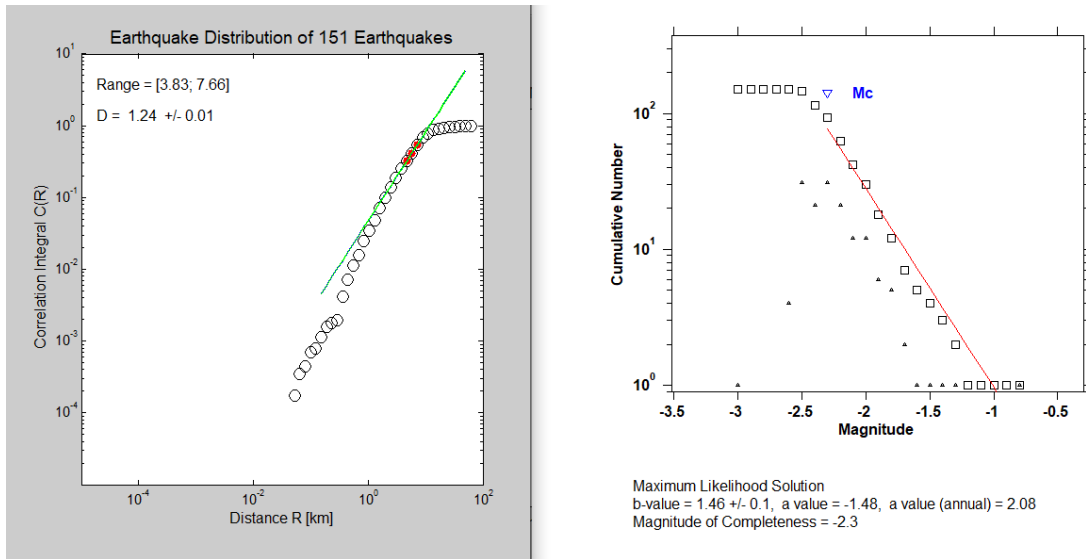


Figure 52 A08, stage2A D-value = 1.24, b-value = 1.46 and $M_c = -2.3$.

A08 Stage 4: The stage started with high pressure of 6396 psi and injection rate of 10 bpm. The rate was increased to 15.7 bpm and pressure of 7034 psi for the acid injection. Pressure dropped to 6645 psi indicating the breakdown. The injection rate was increased to reach 80 bpm and the pressure rose to 9250 psi. The injection rate was dropped to 37 bpm, whereas the surface pressure was 8169 psi. This part of the stage was ended at this point. The interval was reperforated and the stage restarted with pressure of 6800 psi. At the injection rate of 34 bpm the pressure dropped to 7394 psi. After an hour at rate of 43 bpm the pressure dropped by 752 psi, which indicates the breakdown. The rate was increasing gradually to reach 97 bpm and pressure 6769 psi and proppant concentration of 3.5 ppg. Total clean water pumped was 692,496 gal, total 100 mesh was 127.8 sacks, total 30/50 was 198.9 sacks and total 30/50 was 132.9 sacks.

The rose diagram (Figure 53) shows dominant azimuth is 245° , whereas best fitting plane shows azimuth of 230° and dip of 53° . The total number of events on stage 4 was 180 and stage 4A was 284 consist of 50 dry events and 234 wet events as revealed by the r-t plot (Figure 54).

In a closer look at the spatial location of the microseismic events and the dip of the best fitting plane, it is clear that events were occurring on a horizontal plane parallel to formation, which shows a similar case to stage 2 where the fractures were advancing on the bedrock plane.

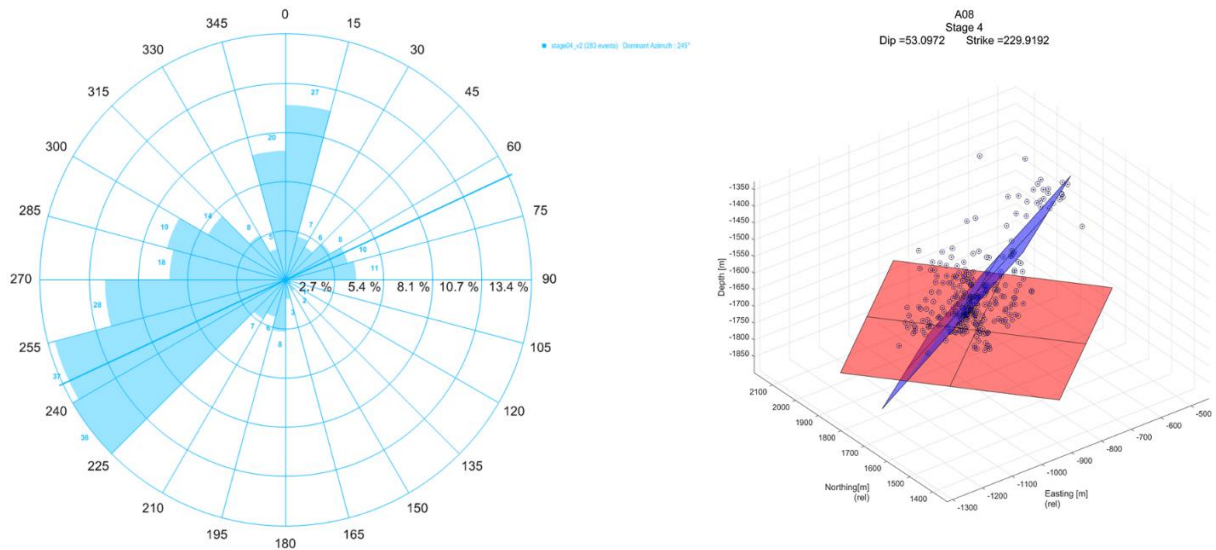


Figure 53 A08 stage 4A rose diagram (left), best fitting plane (right).

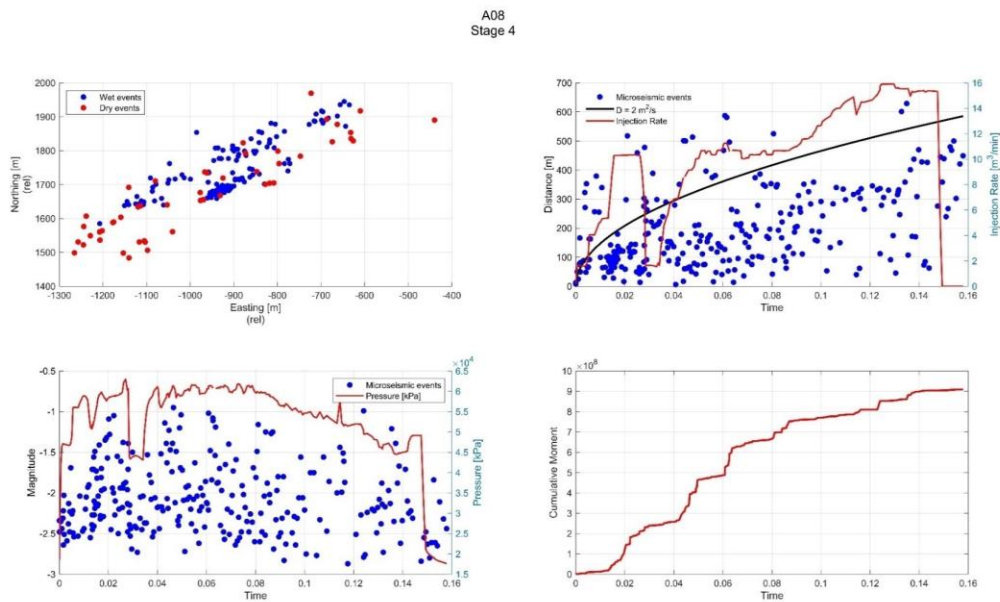


Figure 54 A08 stage 4A map view plot, r-t plot, magnitude plot and cumulative moment plot.

The overall b-value for the stage is 1.22, D-value is 0.66, M_c is -2.4 and Σ is -2.53 (Figure 55). The total injected energy is 1.08×10^{11} joules and radiated energy was 3.77×10^4 joules. The total stimulated volume was $7.95 \times 10^6 \text{ m}^3$ with overlap with the previous stage of $2.60 \times 10^4 \text{ m}^3$.

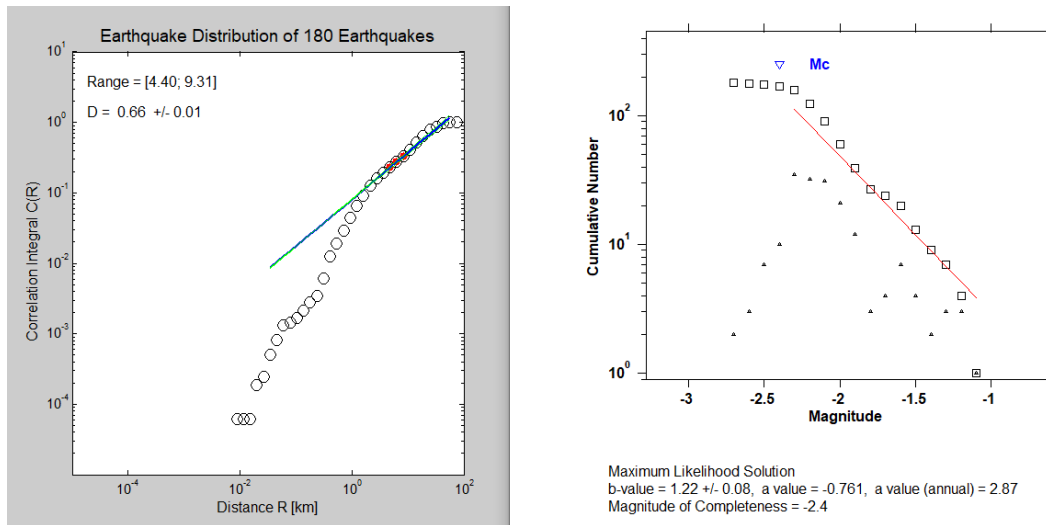


Figure 55 A08, stage 4A D-value =0.66, b-value =1.22 and M_c =-2.4.

B11 Stage 1: The stage started at pressure of 6050 psi and slurry rate of 10 bpm for the acid injection. Then slurry rate was elevated to 44.7 bpm and pressure rose to 9410 psi before dropping to 8692 psi indicating the breakdown, whereas slurry rate remained at 60 bpm pressure slowly decreased to reach 6140 psi when proppant was at 2 ppg. After an hour through the stage proppant was dropped and a shutdown followed shortly. It is unclear why the shutdown took a place, but technical difficulties with proppant is a possibility because proppant concentration went from 2.7 ppg to 1.6 ppg before it was completely dropped. 15 minutes later the stage resumed, and proppant started again at slurry rate of 56 bpm and pressure 8500 psi. The proppant reached 3.7 ppg then it was dropped signaling the end of the stage followed by the flush and shutdown. Closing

pressure 2100 psi. Total clean water pumped was 198,576 gal, total 100 mesh 354.6 sacks, total 30/50 710 sacks and total 20/40 472.2 sacks.

B11 Stage 18: The stage started at low pressure of 3850 psi at slurry rate of 8 bpm. The rate was elevated to 15 bpm and pressure rose to 5400 psi followed by a sudden increase to 8721 psi then slight decrease to 8356 psi, which appeared to be the indication of acid breakdown. The slurry rate was increased to 27.5 bpm and pressure reached 9000 psi, proppant started at 0.1 ppg then elevated to 0.2 ppg with slurry rate of 30 bpm and pressure of 9200 psi. Fifteen minutes later proppant was dropped due to high pressure and low slurry rate. Flush conducted at 17 bpm for slurry rate and 8600 psi for pressure. After 1.5 hours into the stage, the rate was dropped and closing pressure was at 4000 psi. Four hours later the well was open again at pressure 2440 psi. The slurry rate started at 4 bpm then increased to 30 bpm, whereas the pressure was slowly raising to 8500 psi. As the proppant started at 0.1 ppg the pressure reached 9070 psi. Proppant was dropped again, and pressure reached 9152 psi. Shortly after that, the slurry rate was dropped to 10 bpm and pressure decreased to 7650 psi. A third attempt to start proppant at 0.1 ppg, whereas the slurry rate was elevated to 35.5 bpm and pressure of 8800 psi. As the pressure reached 9200 psi, proppant was dropped followed by decrease of slurry rate to 28 bpm. After 20 minutes the slurry rate was dropped, and the well was closed after 17 minutes at pressure of 3770 psi. Total freshwater pumped 162,682.8 gal and total 100 mesh 57.78 sacks, no other type of proppant was delivered.

The overall b-value for the stage is 1.19, D-value is 1.31, Mc is -2.5 and Σ is -2.98 (Figure 56). The total injected energy is 2.50×10^{10} joules and radiated energy was 3.93×10^4 joules. The total stimulated volume was $7.39 \times 10^6 \text{ m}^3$ with overlap volume of $1.09 \times 10^6 \text{ m}^3$.

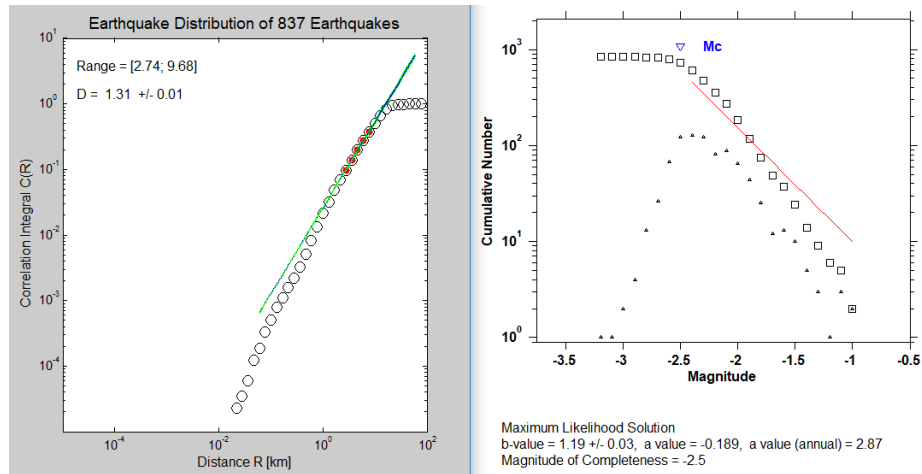


Figure 56 B11, stage 18 D -value = 1.31, b -value = 1.19 and M_c = -2.5.

B11 Stage 38: The stage started with an opening pressure of 2340 psi, as the slurry rate reached 10 bpm the pressure decreased from 6145 psi to 5900 psi. The acid breakdown occurred at slurry rate of 33 bpm and pressure of 7324 psi. The proppant started at 0.1 ppg, whereas the slurry rate was 47 bpm and the pressure at 8573 psi. As the slurry rate increased to 60 bpm, pressure fell to 6500 psi. The proppant reached concentration of 4.1 ppg then it was dropped at 60 bpm slurry rate and 6566 psi pressure, followed by the flush. The closing pressure was 2783 psi. Total clean water pumped was 173796 gal, total 100 mesh 404.4 sacks, total 30/50 990 sacks and total 20/40 690 sacks.

The rose diagram (Figure 57) shows dominant azimuth 265° , and best fitting plane shows azimuth 231° and dip 75° . The map view of events shows growth in the direction of Sh_{max} , and the growth is mostly vertical. The total microseismic events recorded was 298 ranged between moment magnitude of -3.19 and -1.19. The total dry events were 25 and wet events 273 illustrated in the r-t plot in Figure 58.

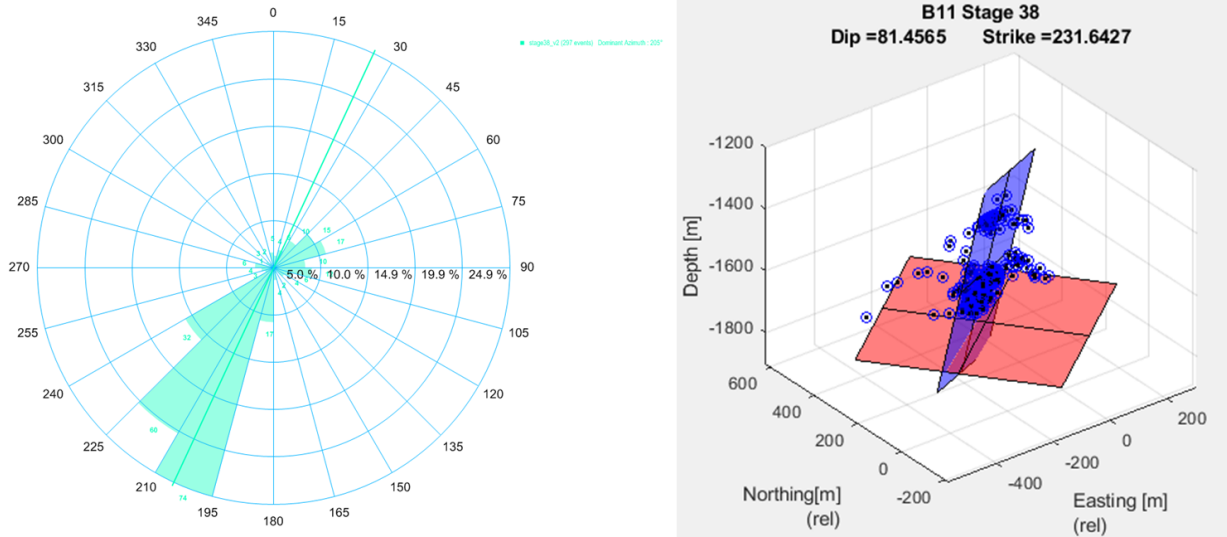


Figure 57 B11 stage 38 rose diagram (left), best fitting plane (right).

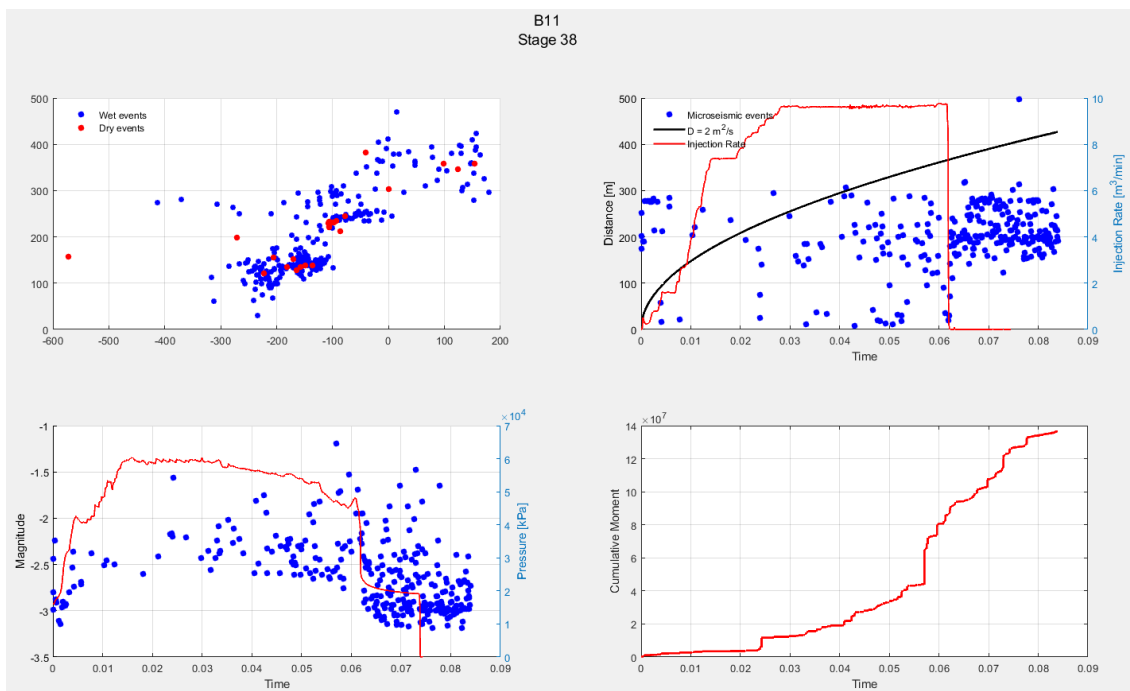


Figure 58 B11 stage 38 map view plot, r-t plot, magnitude plot and cumulative moment plot.

The overall b-value for the stage is 0.86, D-value is 1.06, $M_c = -3$ and Σ is -3.24 (Figure 59). The total injected energy is 2.65×10^{10} joules, and the radiated energy was 6.84×10^3 joules. The total stimulated volume was 1.49×10^7 m³ with overlap volume of 8.14×10^5 m³.

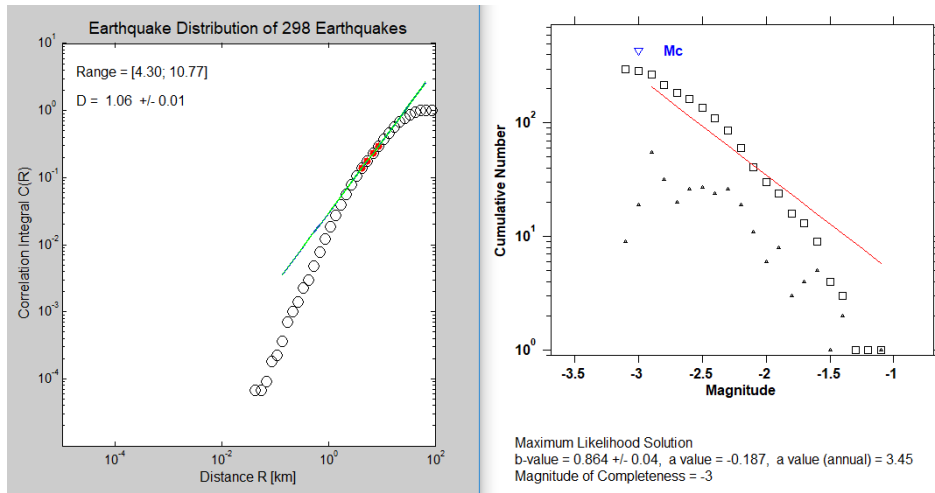


Figure 59 B11, stage 38 D -value = 1.06, b -value = 0.86 and $M_c = -3$.

5.0 Discussion

The focus of this thesis is to answer the main question attached to the dataset, which was presented to the Department of Geology and Environmental Science, University of Pittsburgh. The question was: why did the two wells behave differently throughout the process? Whereas the dataset consisted of microseismic data, treatment data and well logs, examining these components separately had proven to be difficult and confusing. Only by combining them I can produce a clearer picture and more accurate results. One of the most obvious observation on microseismic data in conjunction with treatment data was that events were occurring right after opening the well at a relatively long distance from the well. It is hard to overstate the importance of the work of (Shapiro 2015) with respect to triggering front and estimated diffusivity, it became clear that most events outside the triggering front are dry events. In many studies these events were ignored due to randomness and low concentration. However, in a case study conducted by (Starr and Dennis 2016) on Marcellus and Utica Shales, their conclusion was these events were an indication of preexisting fractures. The same pattern appeared in this case study, specifically on well A08. Ultimately, this method revealed the lack of communication between the two wells, no other evidence indicated a frac hit. It is a completely different story when it comes to a stage level because the lack of communication means undertreatment in the gaps between stages which can be seen on A08.

Well logs analyses in conjunction with microseismic analyses revealed that under similar circumstances the formation returns similar results. Thus, the answer to the question can be related to the stimulation design. A closer look at the wells shows the A08 is longer with fewer stages

than B11 which shorter by 25% and had more stages by 60%, which means different behavior was due to treatment design and not formations' properties.

Finally, during this study well logs yielded a lot of details regarding lithology and formations' properties. However, combining well logs with 3D seismic imaging could have helped produced broader image and reduced uncertainty with respect to formations' structural details. Seismic imaging could become a crucial tool when it comes to explaining difficulties during a stage.

6.0 Conclusions

Hydrofracturing -by definition- changes the 3 stresses within the formation and the reaction to those changes will lead to rock failure. Therefore, it is reasonable to assume that the possibility of natural fault activation is present within every stage. Based on the calculation of M_w , cumulative moment as time functions, Σ , b-value, and D-value, only one stage out of 65 total showed consistent signs of natural fault activation. Only B11 stage 1 showed signs of possible strike slip fault within the stimulated volume.

The extreme difficulties during treatment involving 2 stages on each well were not coincidental nor random. The analyses of the microseismic data and well logs revealed preexisting fractures or faults filled with cementing minerals. These have different mechanical properties from the overall formation that led to the fracture moving through the bedding plane and leaking to previous stages. Seismic imaging may provide clearer picture of these problematic region.

Although microseismic activity is the key to visualizing the stimulation process, it is crucial, for accurate results, to understand its correlation with other data such as well logs and the energy budget. The contrast in the event count between the horizontal and vertical geophone arrays was thought to be from the background noise from the treatment well. It became clear that background noise was not a factor in recording microseismic events nor was the array setup, and the low number of events recorded on some stages was due to well geometry and lithology changes. Thus, the first hypothesis is incorrect.

The triggering front method revealed that the assumption of frac hit between these wells is also incorrect due to the fact that while the observable events may appear to be a sign of communication between the two wells, only they were not. Instead, the triggering front method

revealed that these events were dry events occurring on preexisting fractures. Thus, there is no evidence of treatment fluid communication between wells. Interestingly, eliminating dry events from the analyses revealed gaps between stages, total of 9 stages on well A08, which means those regions were undertreated. On the other hand, the B11 data showed no such gaps, thus the treatment was more effective.

Finally, the collective analysis of formation properties and stimulation data provided an answer to the main question attached to this dataset. The different behaviors during stimulation are due to different treatment designs and execution, not the formations' properties and characteristics.

Appendix A Data Tables

Table 2 A08 b-value and manitude of completeness calculation from three different methods.

Stage	Petrel b-value-MC	MC	Petrel b-value-SVMC	SVMC	b-value Zmap	Mc Zmap	D value	Dominant azimuth
1	1.22	-2.21	0.81	-2.46	0.98	-2.3	1.27	225
2	1.65	-2	1.07	-2.49	1.29	-2.3	1.24	
3	1.23	-2.1	0.73	-2.69	1.17	-2	1.02	235
4	0.94	-2.35	0.72	-2.83	0.75	-2.5	0.66	
5	1.39	-2.27	0.99	-2.77	1.1	-2.4	0.6	235
6	1.31	-2.14	0.92	-2.39	1.1	-2.2	0.84	255
7	0.86	-2.52	0.75	-2.56	0.86	-2.3	1	235
8	1.2	-2.41	0.84	-2.63	1	-2.4	1.36	225
9	1.2	-2.15	0.85	-2.41	0.86	-2.4	0.88	245
10	2.93	-1.51	0.81	-2.56	0.88	-2.4	0.84	235
11	1.47	-1.5	0.71	-2.16	0.85	-2	0.78	235
12	1.76	-1.84	0.74	-2.61	1.05	-2.1	1.47	245
13	2.13	-1.5	0.74	-2.39	0.8	-2.2	1.15	245
14	1.47	-2.08	0.92	-2.49	1.03	-2.3	1.07	235
15	2	-2.03	1.06	-2.52	1.23	-2.3	1.26	275
16	1.81	-2.13	1.22	-2.52	1.57	-2	0.89	245
17	1.27	-2.02	0.8	-2.17	1.11	-2	0.75	235
18	1.39	-1.94	0.72	-2.43	0.88	-2.3	1.11	245
19	2.11	-1.71	0.85	-2.44	0.98	-2.4	1.04	255
20	1.57	-2.2	1.11	-2.33	1.26	-2.2	0.84	255
21	1.31	-2.17	0.78	-2.52	1.2	-2.1	0.93	265
22	1.74	-2.2	1.23	-2.33	1.35	-2.2	1.29	245
23	2.1	-1.93	1.12	-2.3	1.25	-2.2	1.15	215

24	1.85	-1.84	1.01	-2.3	1.02	-2.2	1.24	255
25	1.28	-2.28	1.05	-2.4	1.21	-2.1	1.19	245

Table 3 B11 b-value and manitude of completeness calculation from three different methods.

Stage	Petrel b-value-MC	MC	Petrel b-value-SVMC	SVMC	b-value Zmap	Mc Zmap	D value	Dominant azimuth
1	0.83	-2.4	0.7	-2.5	0.76	-2.4	1.59	245
2	2.73	-1.9	1.18	-2.51	1.24	-2.3	1.07	225
3	1.41	-2.46	0.99	-2.86	1.24	-2.4	1.28	235
4	1.01	-2.55	0.91	-2.65	0.92	-2.4	1.25	235
5	1.58	-2.09	1.01	-2.57	1.11	-2.2	1.51	245
6	1.73	-2.32	0.93	-2.92	1.47	-2.3	1.32	245
7	1.38	-2.36	0.99	-2.59	1.13	-2.4	1.54	235
8	1.69	-2.39	1.25	-2.83	1.47	-2.3	1.25	235
9	1.26	-2.31	0.9	-2.71	1.15	-2.2	1.49	245
10	0.85	-2.48	0.75	-2.55	0.81	-2.4	0.96	255
11	1.19	-2.38	0.92	-2.57	0.97	-2.5	1.42	245
12	1.63	-2.25	1.34	-2.42	1.3	-2.3	1.31	255
13	1.6	-2.37	1.36	-2.4	1.38	-2.3	1.46	265
14	1.41	-2.36	1.17	-2.44	1.21	-2.3	1.2	255
15	1.77	-2.3	1.44	-2.44	1.3	-2.4	1.34	245
16	1.19	-2.21	0.97	-2.61	1.02	-2.4	1.22	245
17	1.44	-2.37	0.95	-2.84	1.22	-2.4	1.34	245
18	1.76	-2.23	1.14	-2.74	1.19	-2.5	1.31	265
19	1.14	-2.4	0.97	-2.44	1.06	-2.3	1.49	235
20	1.47	-2.63	1.31	-2.71	1.16	-2.7	1.42	245
21	1.33	-2.43	1.07	-2.65	1.21	-2.5	1.11	235
22	1.94	-2.54	1.67	-2.65	1.5	-2.5	1.55	245
23	1.62	-2.03	0.93	-2.79	0.98	-2.6	0.88	255
24	1.78	-2.48	1.57	-2.54	1.43	-2.5	1	265

25	1.72	-2.58	1.5	-2.68	1.52	-2.5	1.07	275
26	2.04	-2.53	1.51	-2.79	1.41	-2.6	1.03	255
27	1.17	-2.41	0.8	-2.89	1.07	-2.3	1.35	235
28	1.8	-2.47	1.53	-2.61	1.38	-2.6	0.98	235
29	1.78	-2.43	1.43	-2.65	1.42	-2.4	1.38	245
30	1.22	-2.18	0.78	-2.8	0.83	-2.6	1.47	245
31	1.37	-2.38	1.18	-2.4	1.28	-2.3	1.6	255
32	1.64	-2.21	0.99	-2.84	1.07	-2.5	1.21	275
33	1.51	-1.87	0.76	-2.87	0.96	-2.3	1.52	265
34	1.93	-2.2	1.02	-2.78	1.46	-2.2	1.34	235
35	1.39	-2.47	0.97	-2.52	1.46	-2.3	1.05	265
36	0.83	-2.76	0.7	-2.77	0.78	-2.7	0.77	205
37	1.81	-2.12	0.95	-2.61	0.85	-2.6	0.43	195
38	1.22	-2.67	0.89	-3.07	0.86	-3	1.06	205
39	1.08	-2.61	0.71	-2.88	0.94	-2.6	1.48	205
40	1.31	-2.78	1.06	-2.88	1.17	-2.7	1.18	215

Table 4 Volume and energy calculation for each stage in A08 well, plus overlap volume and its energy.

Stage	stimulated volume m ³	Overlap volume m ³	volume ratio	Injected Energy joules	Radiated Energy joules	Overlap radiated energy joules	energy ratio	seismogenic index
1	1.20E+06	0.00E+00	0.00E+00	5.36E+10	2.19E+04	0.00E+00	0.00E+00	-3.34
2	3.33E+06	1.00E+04	3.01E-03	1.08E+11	1.38E+04	6.65E+02	4.81E-02	-4.04
3	5.14E+06	0.00E+00	0.00E+00	5.28E+10	4.03E+04	0.00E+00	0.00E+00	-3.67
4	7.95E+06	2.60E+04	3.27E-03	1.08E+11	3.77E+04	5.78E+03	1.53E-01	-2.53
5	1.28E+06	3.71E+03	2.89E-03	4.99E+10	6.41E+03	2.24E+02	3.50E-02	-3.72
6	7.52E+06	1.44E+04	1.92E-03	5.24E+10	3.40E+04	1.54E+02	4.54E-03	-3.24
7	9.99E+06	1.59E+04	1.59E-03	5.72E+10	3.70E+04	2.14E+02	5.78E-03	-3.20
8	6.33E+06	2.19E+05	3.45E-02	4.44E+10	1.28E+04	3.21E+03	2.51E-01	-3.54
9	7.80E+05	0.00E+00	0.00E+00	4.11E+10	2.95E+04	1.97E+02	6.68E-03	-2.81
10	1.53E+06	0.00E+00	0.00E+00	4.56E+10	2.27E+04	0.00E+00	0.00E+00	-2.82
11	8.07E+06	0.00E+00	0.00E+00	4.71E+10	6.92E+04	2.47E+03	3.58E-02	-2.88
12	9.29E+06	5.39E+05	5.81E-02	4.23E+10	1.96E+04	1.86E+03	9.52E-02	-3.42
13	3.71E+06	2.08E+05	5.61E-02	5.00E+10	1.35E+04	5.62E+02	4.15E-02	-2.97
14	1.05E+07	6.83E+03	6.53E-04	4.10E+10	9.37E+03	3.18E+02	3.39E-02	-3.36

15	7.21E+06	5.83E+05	8.09E-02	4.00E+10	1.06E+04	8.63E+02	8.10E-02	-3.81
16	1.32E+07	0.00E+00	0.00E+00	4.08E+10	1.30E+04	1.63E+02	1.25E-02	-4.16
17	6.81E+05	0.00E+00	0.00E+00	2.23E+10	1.08E+04	5.15E+02	4.75E-02	-3.50
18	8.43E+06	3.05E+03	3.62E-04	2.39E+10	1.63E+04	1.10E+02	6.77E-03	-2.85
19	1.91E+06	2.01E+05	1.05E-01	2.33E+10	1.00E+04	7.59E+02	7.58E-02	-2.94
20	1.21E+06	8.29E+03	6.82E-03	1.99E+10	7.88E+03	9.01E+02	1.14E-01	-3.46
21	3.82E+06	5.77E+03	1.51E-03	1.91E+10	8.23E+03	2.45E+02	2.98E-02	-3.40
22	1.63E+06	0.00E+00	0.00E+00	3.74E+10	4.41E+03	2.12E+02	4.80E-02	-4.10
23	4.51E+06	0.00E+00	0.00E+00	3.79E+10	1.10E+04	2.54E+02	2.32E-02	-3.90
24	7.69E+06	9.19E+04	1.20E-02	3.70E+10	2.71E+04	1.19E+03	4.38E-02	-3.18
25	3.04E+06	5.08E+05	1.09E+00	3.39E+10	2.82E+04	1.14E+04	4.03E-01	-3.46

Table 5 Volume and energy calculation for each stage in B11 well, plus overlap volume and its energy.

Stage	stimulated volume m ³	Overlap volume m ³	volume ratio	Injected Energy joules	Radiated Energy joules	Overlap radiated energy joules	energy ratio	seismogenic index
1	1.44E+06	0.00E+00	0.00E+00	2.74E+10	1.52E+05	0.00E+00	0.00	-2.36
2	3.36E+06	2.42E+05	0.072106013	3.29E+10	2.19E+04	4.35E+03	0.20	-3.34
3	5.81E+06	4.59E+05	0.079115054	2.35E+10	3.29E+04	5.56E+03	0.17	-3.52
4	2.88E+06	6.77E+05	0.23501339	3.35E+10	1.08E+05	3.26E+03	0.03	-2.79
5	2.54E+06	6.31E+05	0.248891611	3.29E+10	4.31E+04	2.64E+04	0.61	-2.92
6	2.35E+06	5.59E+04	0.023857827	2.25E+10	1.81E+04	7.84E+02	0.04	-3.64
7	1.05E+07	3.91E+05	0.037403586	2.80E+10	1.78E+04	5.71E+03	0.32	-3.13
8	5.11E+06	2.28E+06	0.445739057	2.66E+10	2.14E+04	8.17E+03	0.38	-3.12
9	1.56E+07	2.00E+06	0.128422537	3.36E+10	4.08E+04	1.40E+04	0.34	-3.29
10	7.39E+06	3.30E+06	0.447083136	2.66E+10	1.55E+05	4.24E+04	0.27	-2.37
11	8.33E+06	2.82E+05	0.033887125	2.18E+10	3.13E+04	1.02E+04	0.33	-2.63
12	1.11E+07	2.08E+06	0.186902078	3.16E+10	2.59E+04	1.48E+04	0.57	-3.56
13	4.43E+06	1.74E+06	0.392982447	2.32E+10	1.92E+04	1.41E+04	0.74	-3.81
14	9.96E+06	7.21E+05	0.072379102	2.93E+10	2.97E+04	8.97E+03	0.30	-3.37
15	1.35E+07	1.34E+06	0.099037625	3.57E+10	2.23E+04	1.01E+04	0.45	-3.93

16	1.79E+07	1.67E+06	0.092928488	2.58E+10	3.07E+04	1.30E+04	0.42	-3.57
17	6.38E+06	2.80E+06	0.439502635	2.08E+10	1.90E+04	1.65E+04	0.87	-3.57
18	7.39E+06	1.09E+06	0.147761031	2.50E+10	3.93E+04	2.74E+04	0.70	-2.98
19	6.70E+06	2.37E+06	0.352888322	5.16E+10	4.08E+04	2.20E+04	0.54	-3.15
20	7.95E+06	2.93E+06	0.36899877	2.82E+10	1.70E+04	8.76E+03	0.52	-3.61
21	8.85E+06	1.26E+06	0.142910032	3.16E+10	3.47E+04	1.74E+04	0.50	-3.19
22	1.14E+07	2.24E+06	0.197041478	2.73E+10	9.31E+03	4.12E+03	0.44	-4.1
23	4.73E+06	3.22E+06	0.680068726	1.35E+10	2.76E+04	2.44E+04	0.88	-3.61
24	1.06E+07	1.17E+06	0.110423073	5.23E+10	1.72E+04	1.17E+04	0.68	-4.1
25	1.02E+07	2.74E+06	0.269955256	2.74E+10	9.97E+03	6.85E+03	0.69	-4.12
26	5.96E+06	1.18E+06	0.198650801	2.91E+10	7.68E+03	1.68E+03	0.22	-4.77
27	9.96E+06	1.61E+06	0.161257774	3.08E+10	4.18E+04	1.65E+04	0.39	-3.21
28	7.25E+06	1.17E+06	0.161254277	2.56E+10	1.91E+04	4.21E+03	0.22	-3.83
29	9.24E+06	3.33E+06	0.360013658	2.18E+10	1.48E+04	4.84E+03	0.33	-3.94
30	7.22E+06	4.30E+05	0.059523413	2.53E+10	3.54E+04	6.86E+03	0.19	-2.55
31	1.45E+07	1.38E+06	0.0953829	2.63E+10	2.78E+04	1.80E+04	0.65	-3.45
32	3.19E+06	9.33E+05	0.292406655	2.97E+10	2.25E+04	1.68E+04	0.74	-3
33	1.38E+07	1.06E+06	0.076666124	6.05E+10	7.48E+04	1.85E+04	0.25	-2.88
34	1.49E+07	1.18E+05	0.007867777	3.85E+10	2.28E+04	1.66E+03	0.07	-4.1
35	5.39E+06	8.37E+05	0.155448788	5.25E+10	3.71E+03	1.52E+03	0.41	-4.5
36	6.76E+06	2.63E+05	0.038854133	6.12E+10	1.01E+04	4.19E+03	0.41	-3.35
37	4.17E+06	2.03E+05	0.0485279	2.17E+10	1.27E+04	9.88E+02	0.08	-2.95
38	1.49E+07	8.14E+05	0.054723142	2.65E+10	6.84E+03	2.06E+03	0.30	-3.24
39	1.17E+07	1.71E+06	0.146017995	2.59E+10	9.04E+03	5.60E+03	0.62	-3.38
40	1.40E+07	1.96E+06	0.140209017	2.63E+10	1.07E+04	2.79E+03	0.26	-3.69

Appendix B Complete Set of Stage Analyses

A08
Stage 3

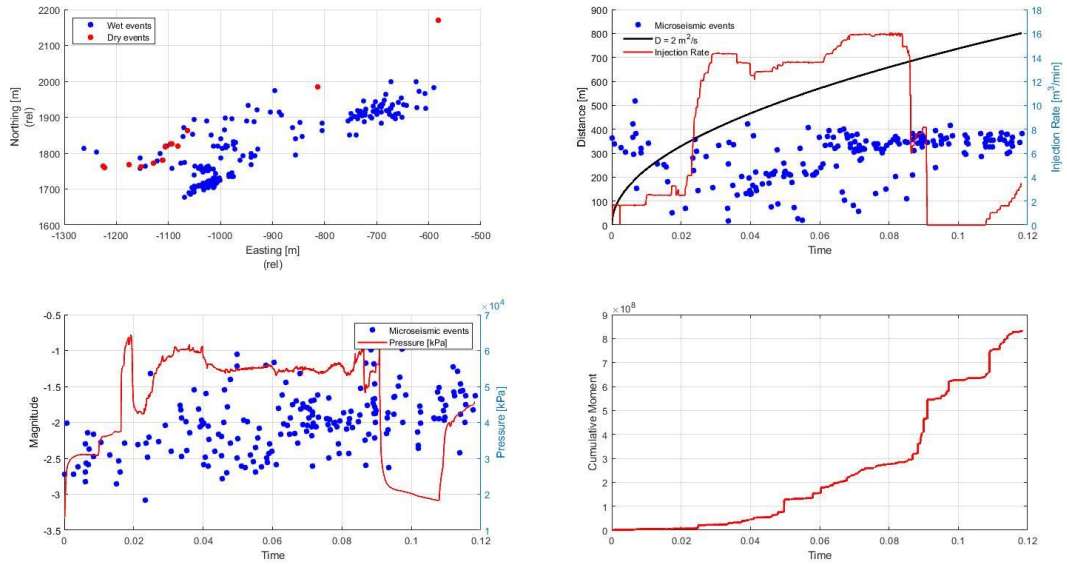


Figure 60 A08 stage 3 map view plot, r-t plot, magnitude plot and cumulative moment plot.

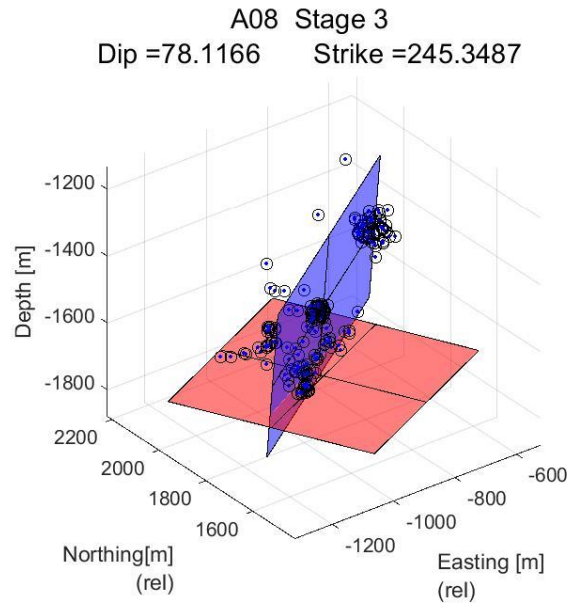


Figure 61 A08 Stage 3 best fitting plane.

A08
Stage 5

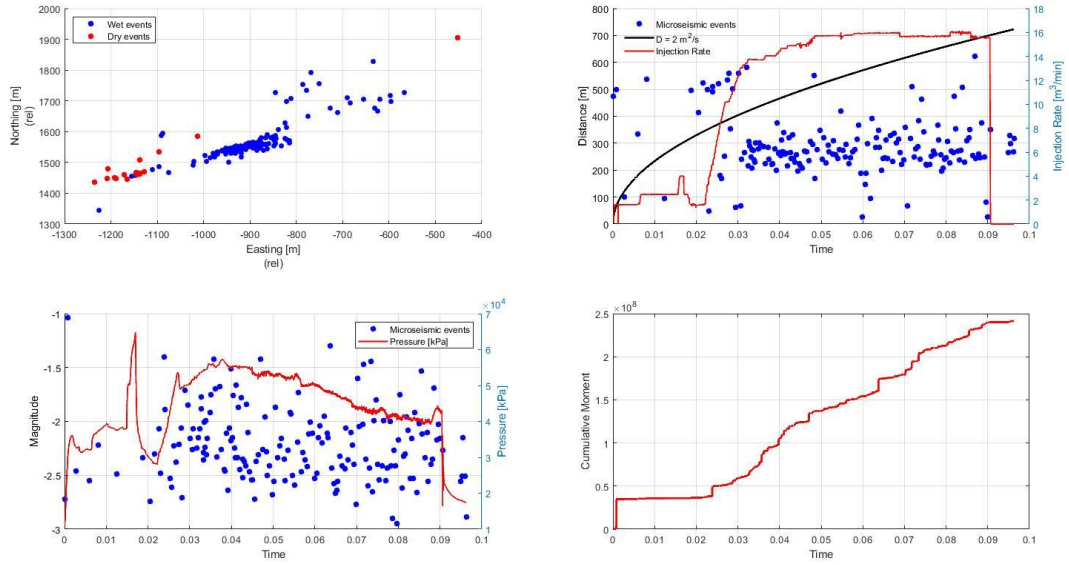


Figure 62 A08 stage 5 map view plot, r-t plot, magnitude plot and cumulative moment plot.

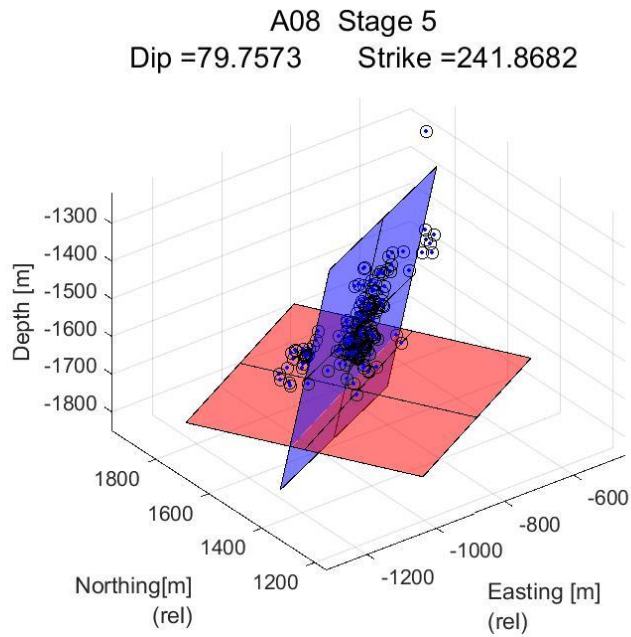


Figure 63 A08 stage 5 best fitting plane.

A08
Stage 6

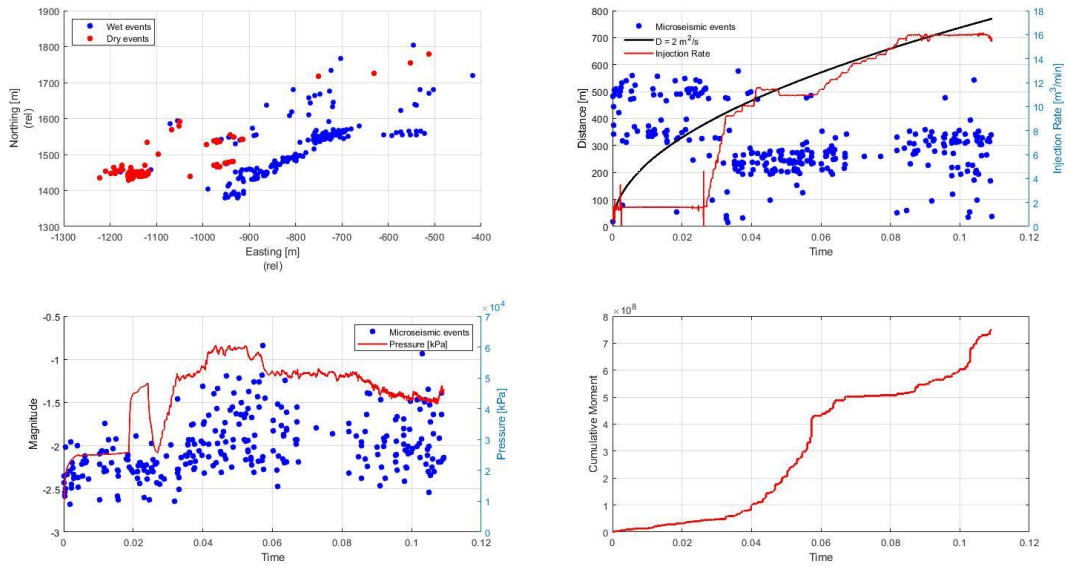


Figure 64 A08 stage 6 map view plot, r-t plot, magnitude plot and cumulative moment plot.

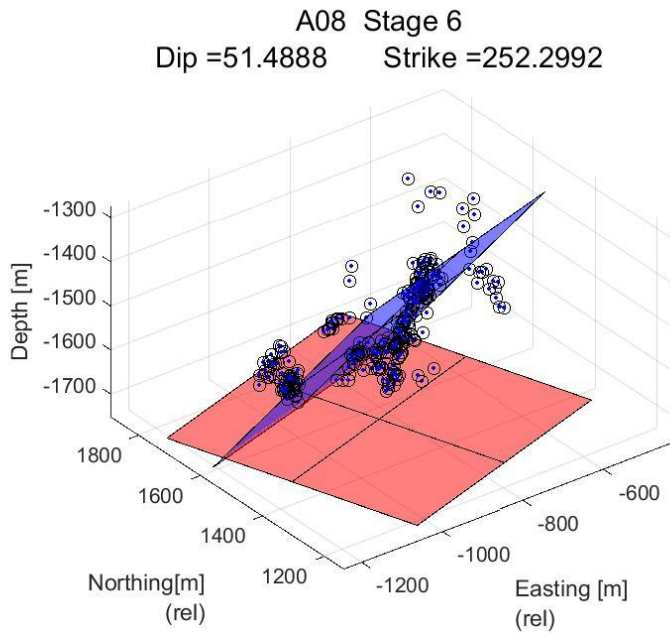


Figure 65 A08 stage 6 best fitting plane.

A08
Stage 7

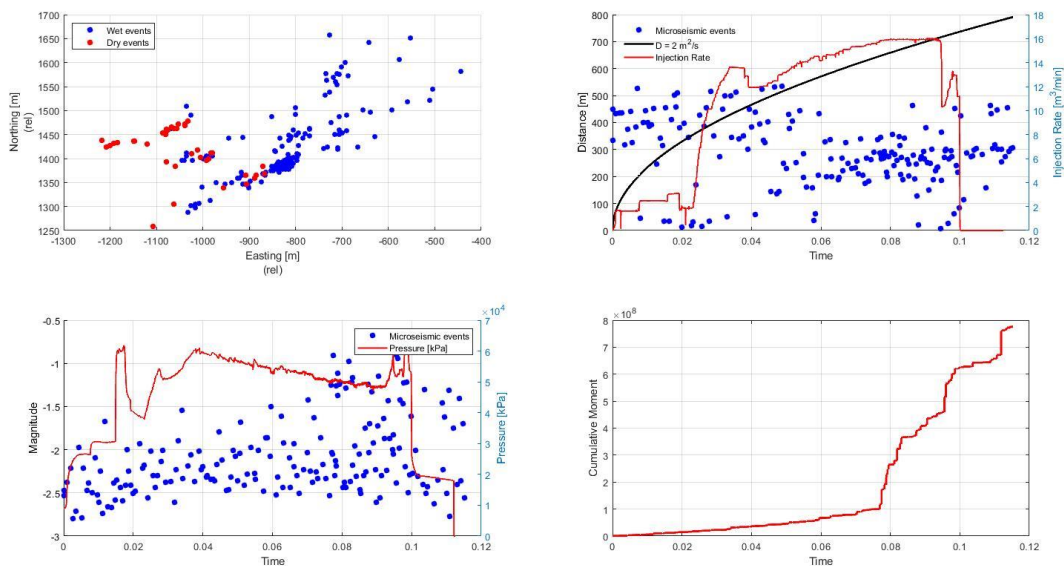


Figure 66 A08 stage 7 map view plot, r-t plot, magnitude plot and cumulative moment plot.

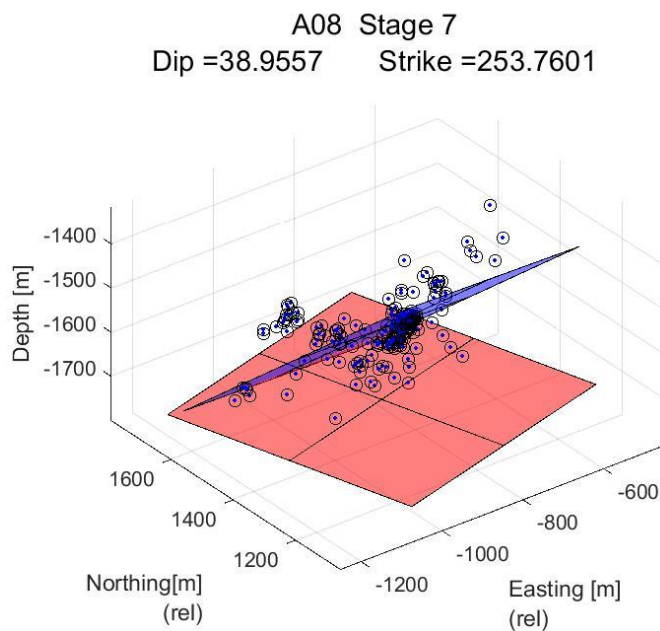


Figure 67 A08 stage 7 best fitting plane.

A08
Stage 8

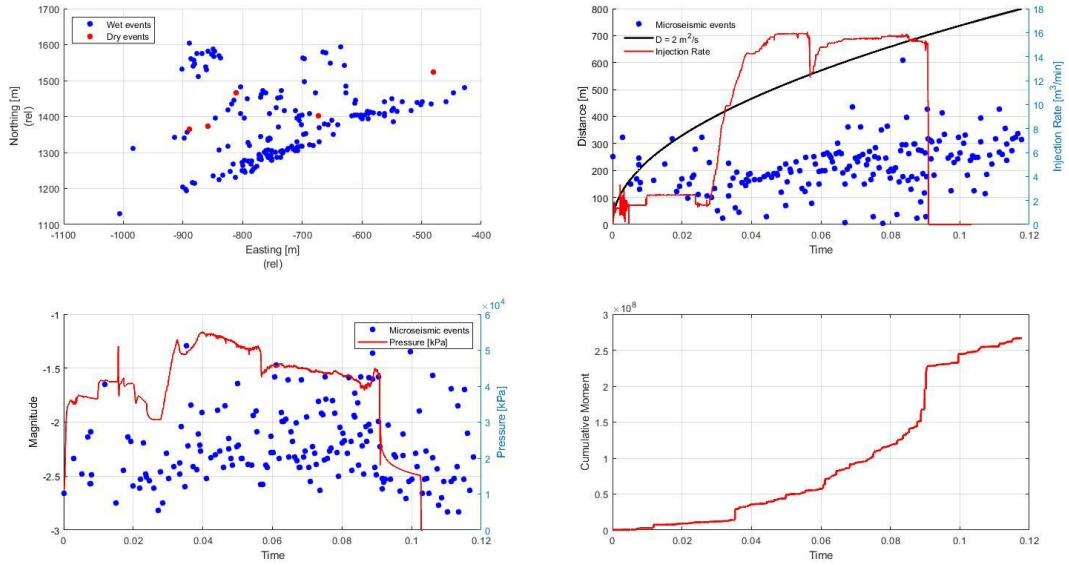


Figure 68 A08 stage 8 map view plot, r-t plot, magnitude plot and cumulative moment plot.

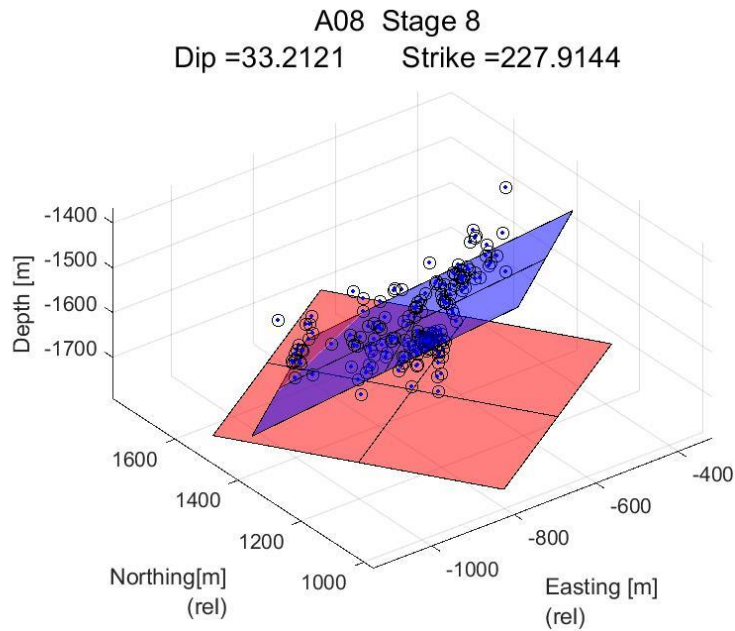


Figure 69 A08 stage 8 best fitting plane.

A08
Stage 9

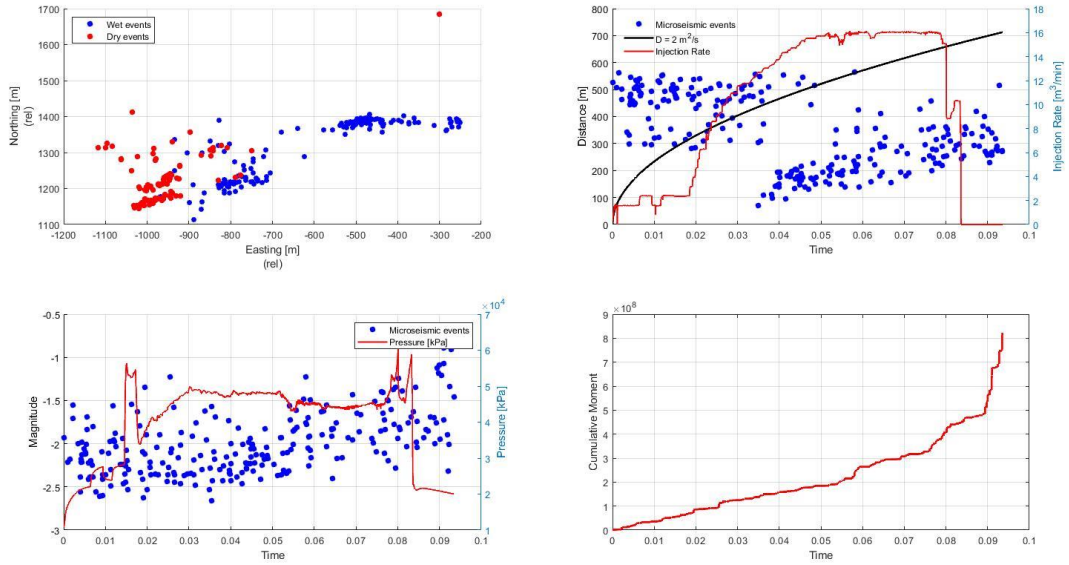


Figure 70 A08 stage 9 map view plot, r-t plot, magnitude plot and cumulative moment plot.

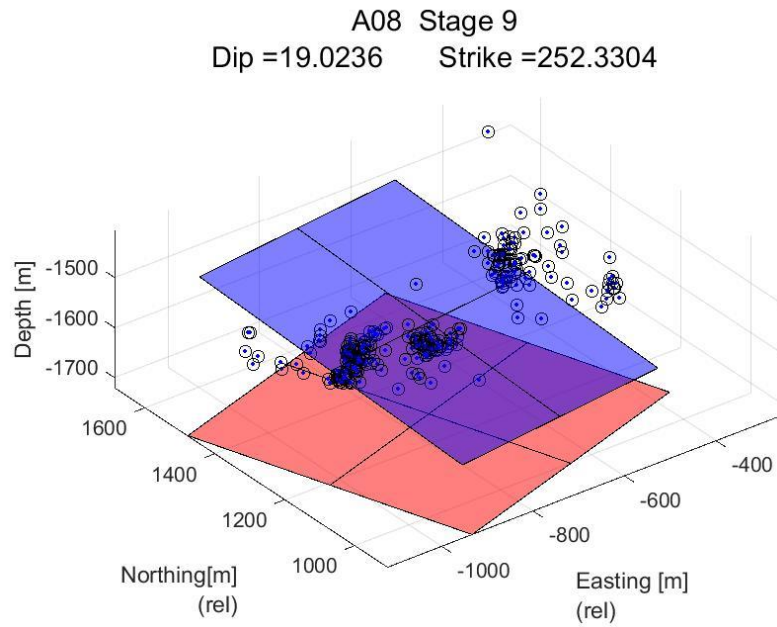


Figure 71 A08 stage 9 best fitting plane.

A08
Stage 10

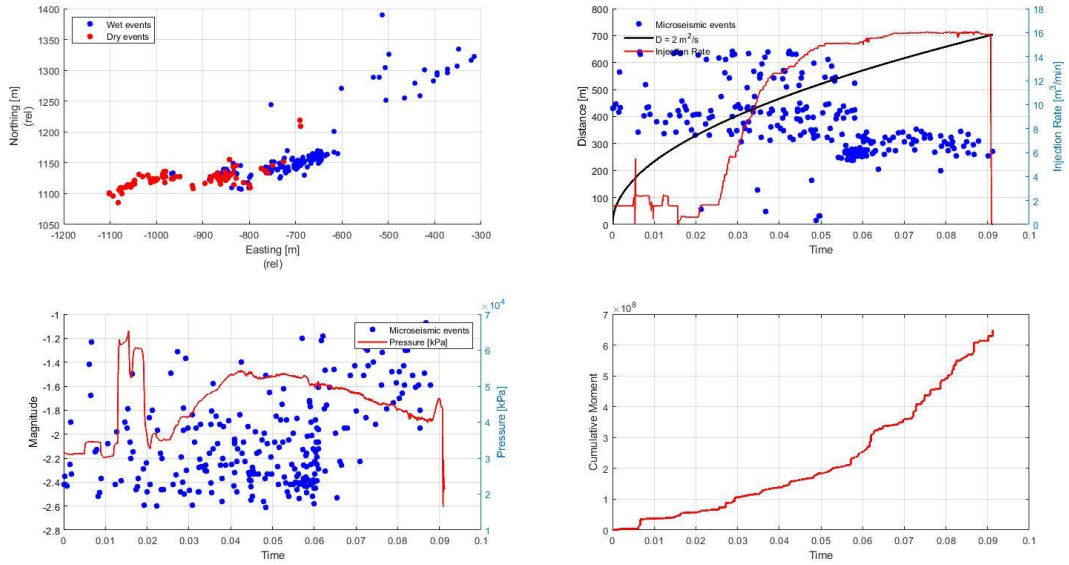


Figure 72 A08 stage 10 map view plot, r-t plot, magnitude plot and cumulative moment plot.

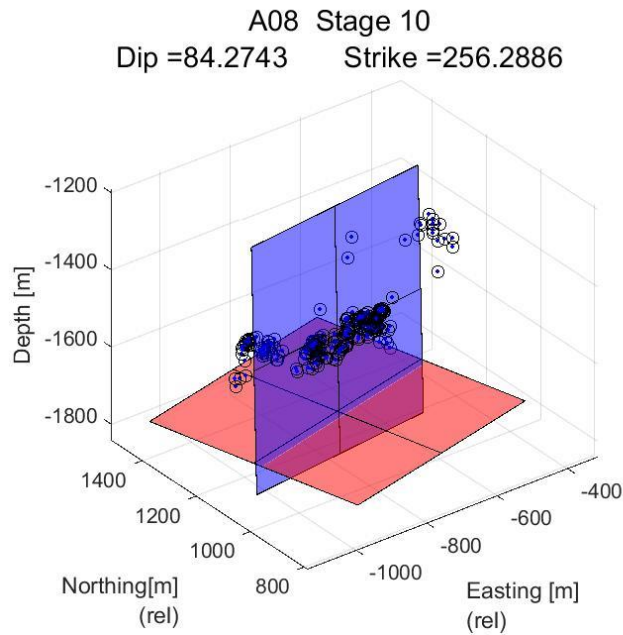


Figure 73 A08 stage 10 best fitting plane.

A08
Stage 11

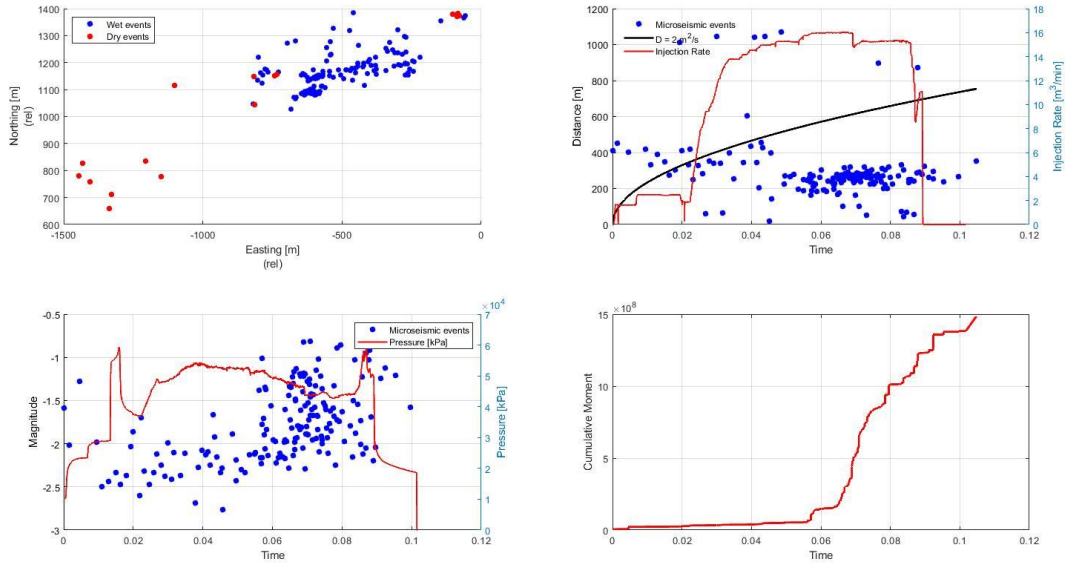


Figure 74 A08 stage 11 map view plot, r-t plot, magnitude plot and cumulative moment plot.

A08 Stage 11
Dip = 59.2713 Strike = 247.7186

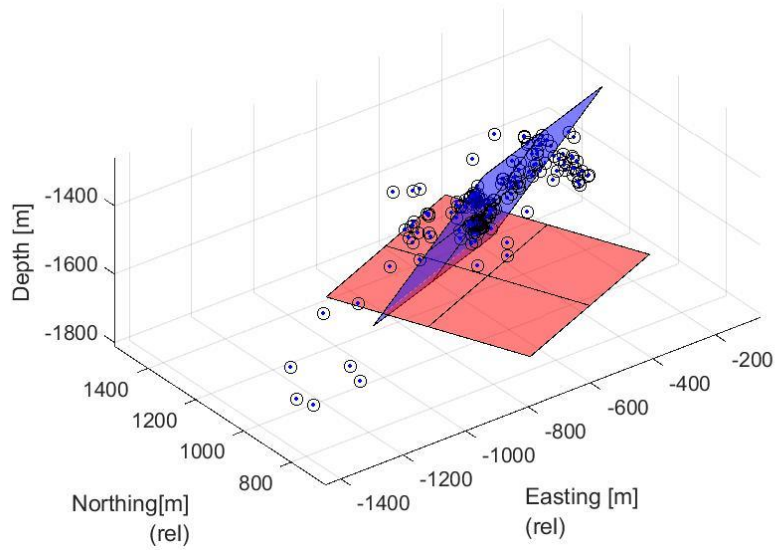


Figure 75 A08 stage 11 best fitting plane.

A08
Stage 12

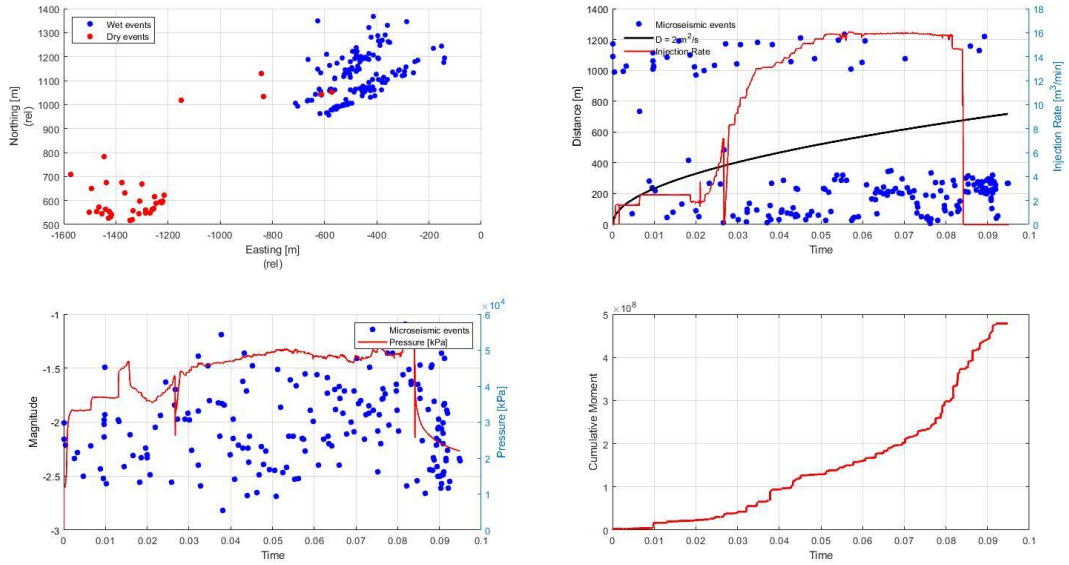


Figure 76 A08 stage 12 map view plot, r-t plot, magnitude plot and cumulative moment plot.

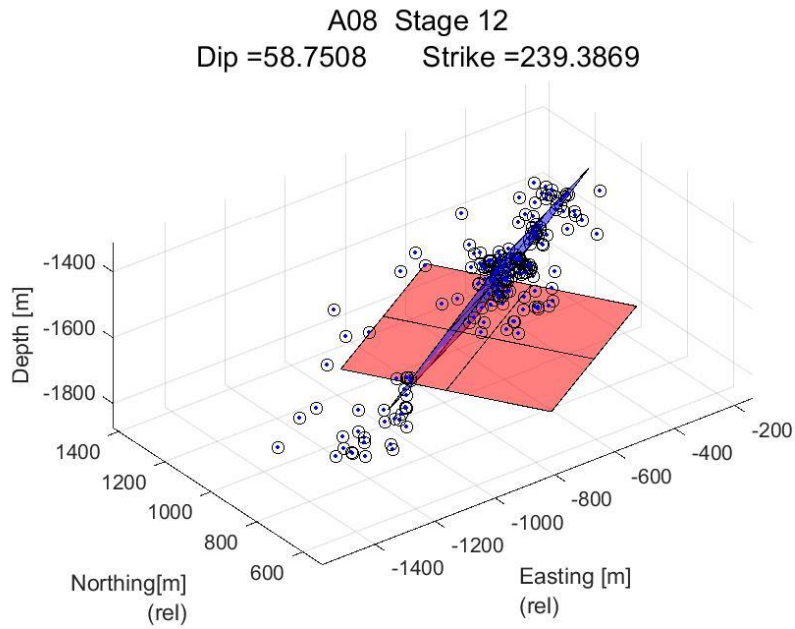


Figure 77 A08 stage 12 best fitting plane.

A08
Stage 13

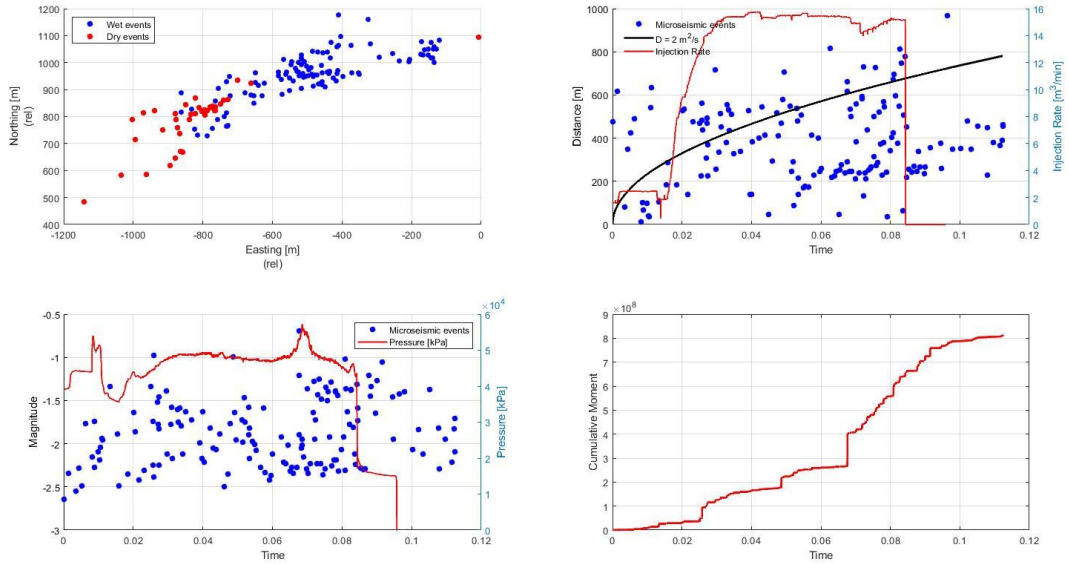


Figure 78 A08 stage 13 map view plot, r-t plot, magnitude plot and cumulative moment plot.

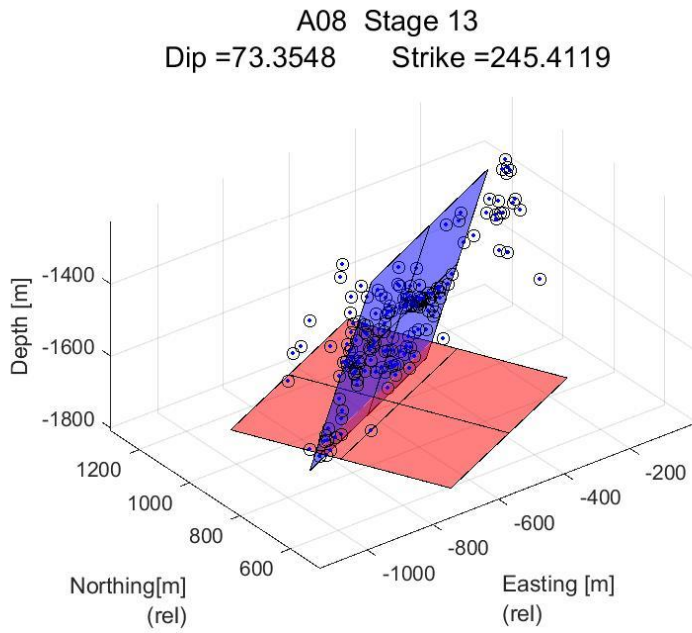


Figure 79 A08 stage 13 best fitting plane.

A08
Stage 14

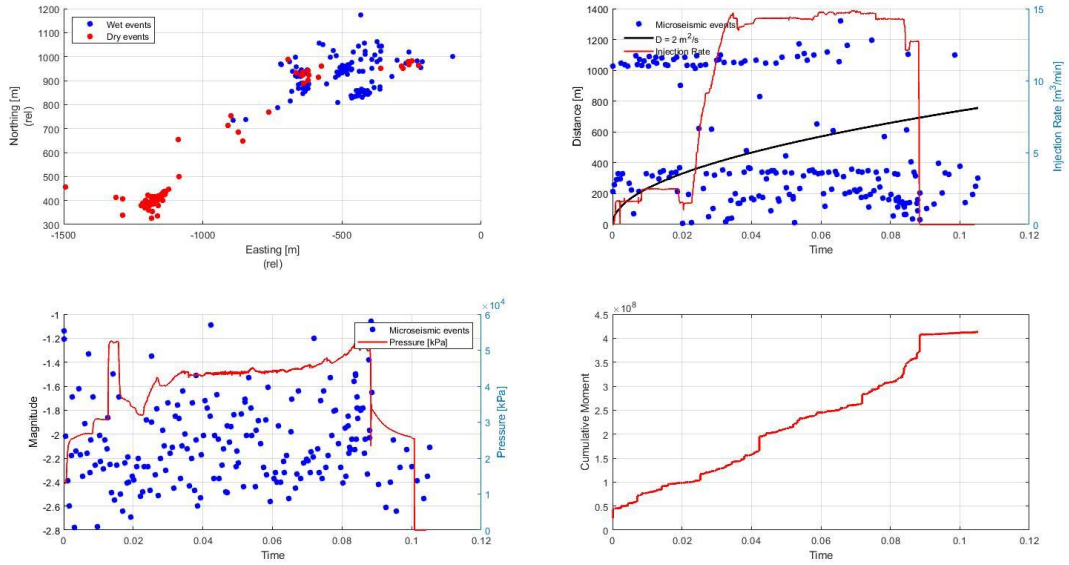


Figure 80 A08 stage 14 map view plot, r-t plot, magnitude plot and cumulative moment plot.

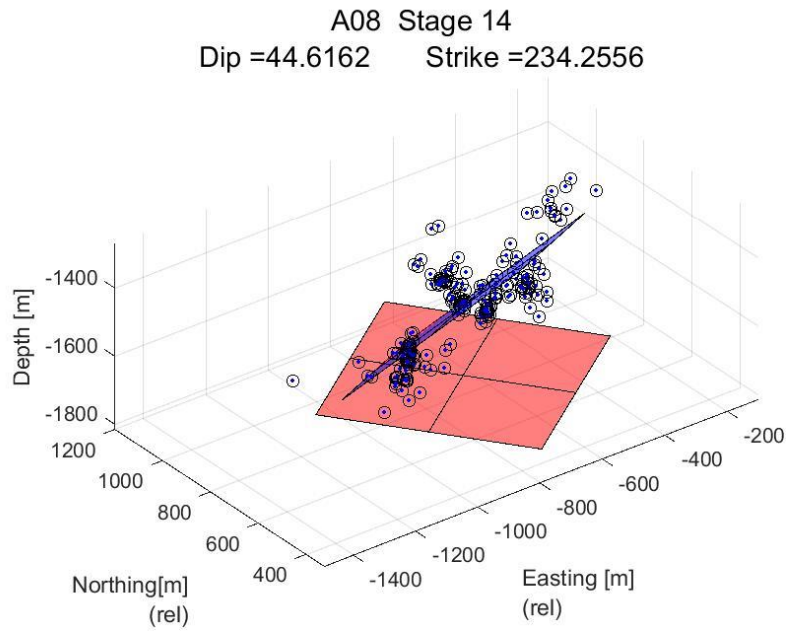


Figure 81 A08 stage 14 best fitting plane.

A08
Stage 15

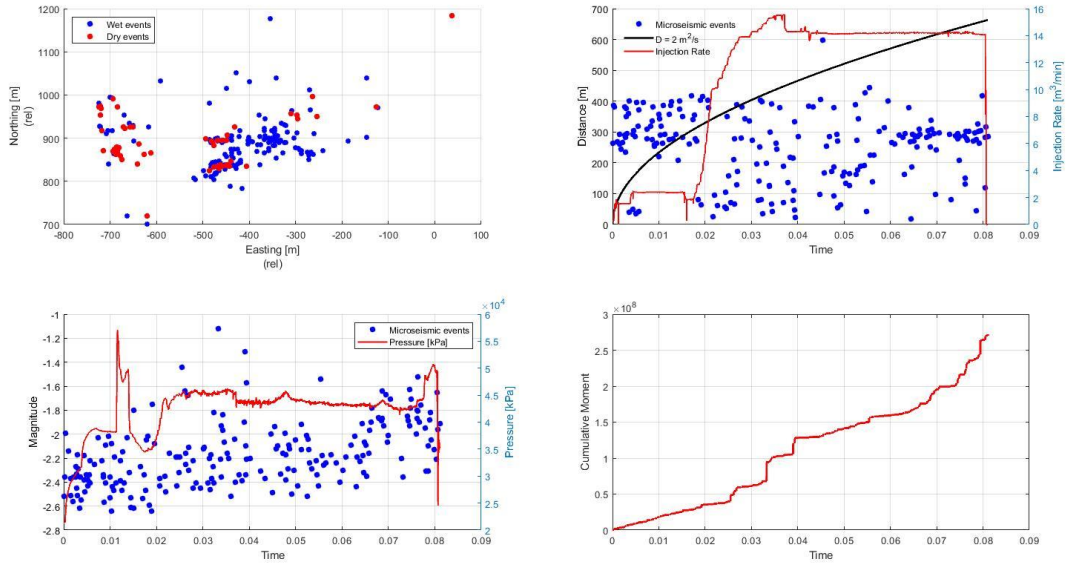


Figure 82 A08 stage 15 map view plot, r-t plot, magnitude plot and cumulative moment plot.

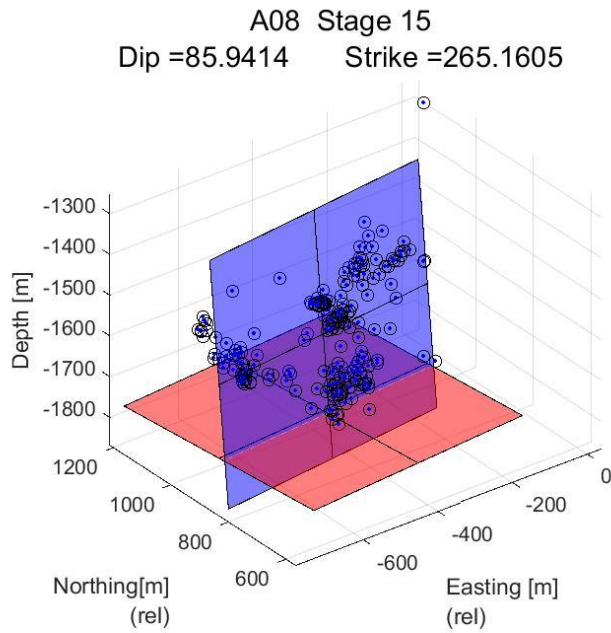


Figure 83 A08 stage 15 best fitting plane.

A08
Stage 16

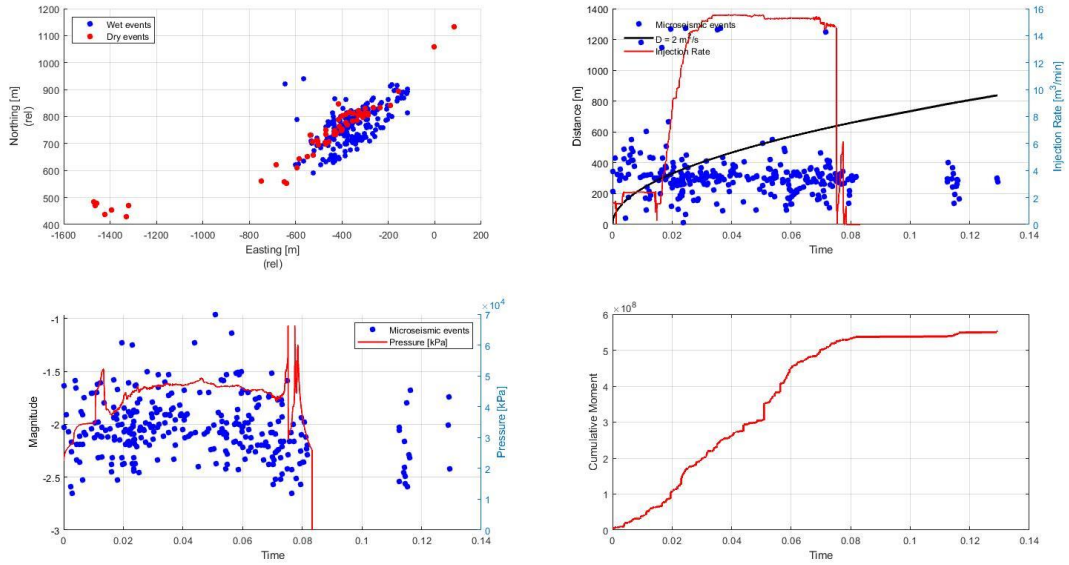


Figure 84 A08 stage 16 map view plot, r-t plot, magnitude plot and cumulative moment plot.

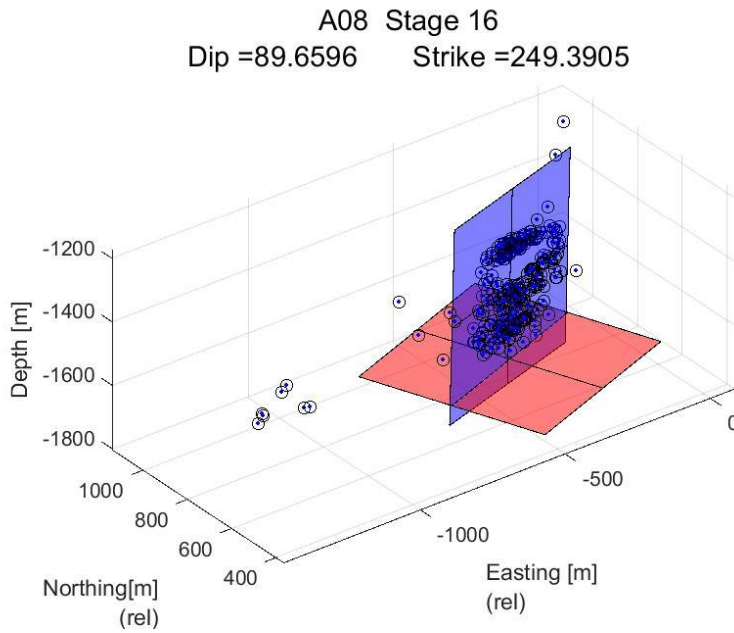


Figure 85 A08 stage 16 best fitting plane.

A08
Stage 17

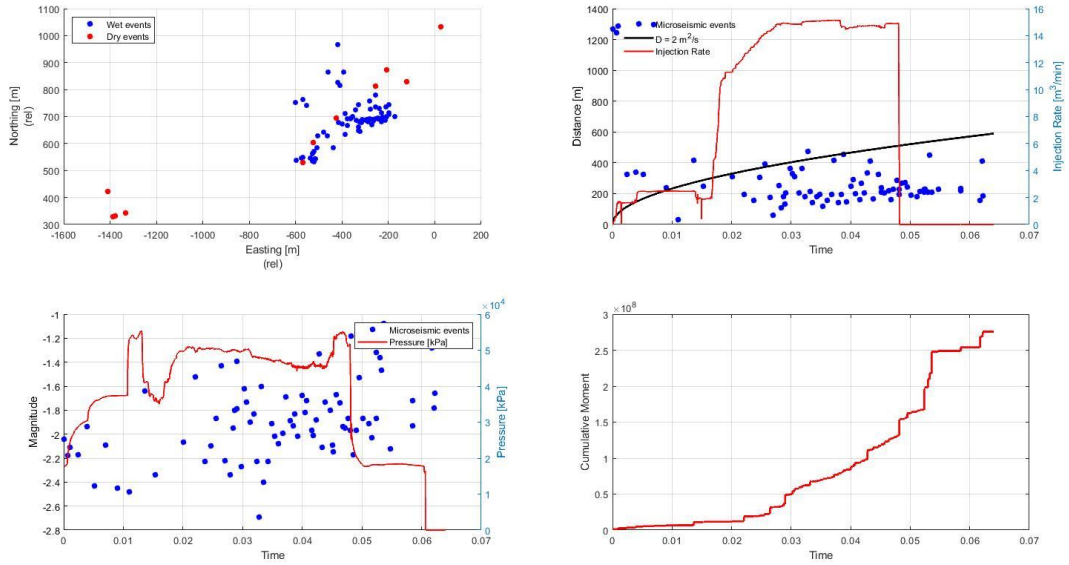


Figure 86 A08 stage 17 map view plot, r-t plot, magnitude plot and cumulative moment plot.

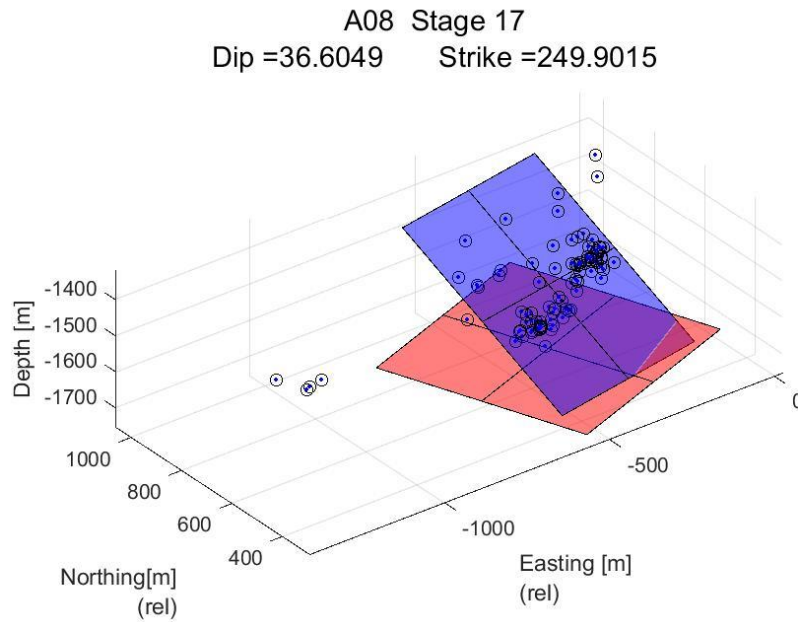


Figure 87 A08 stage 17 best fitting plane.

A08
Stage 18

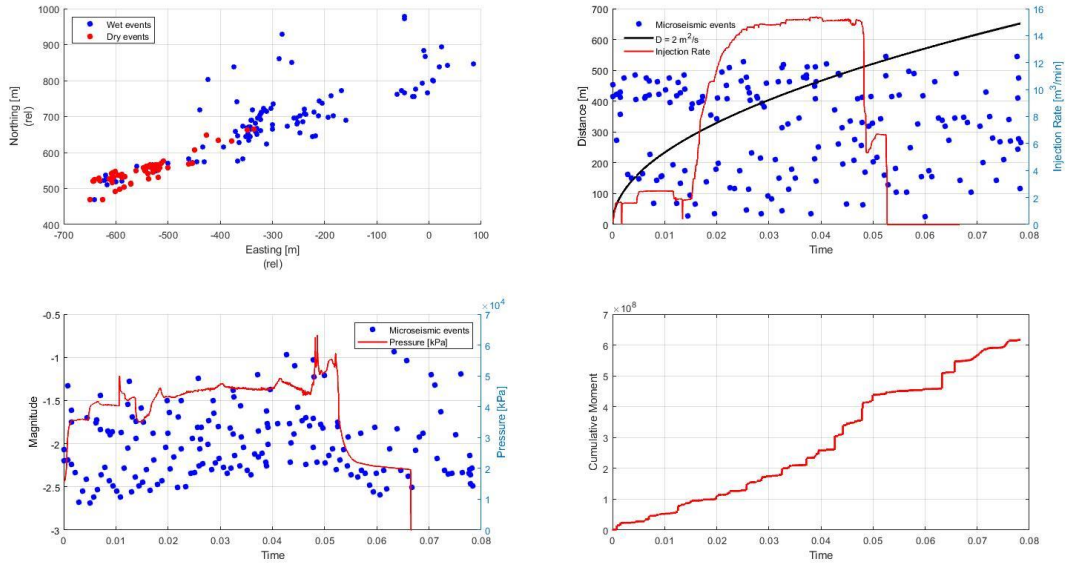


Figure 88 A08 stage 18 map view plot, r-t plot, magnitude plot and cumulative moment plot.

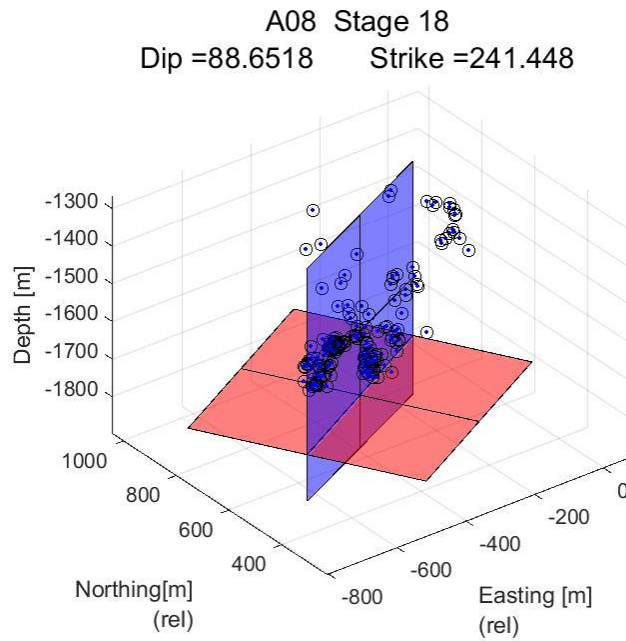


Figure 89 A08 stage 18 best fitting plane.

A08
Stage 19

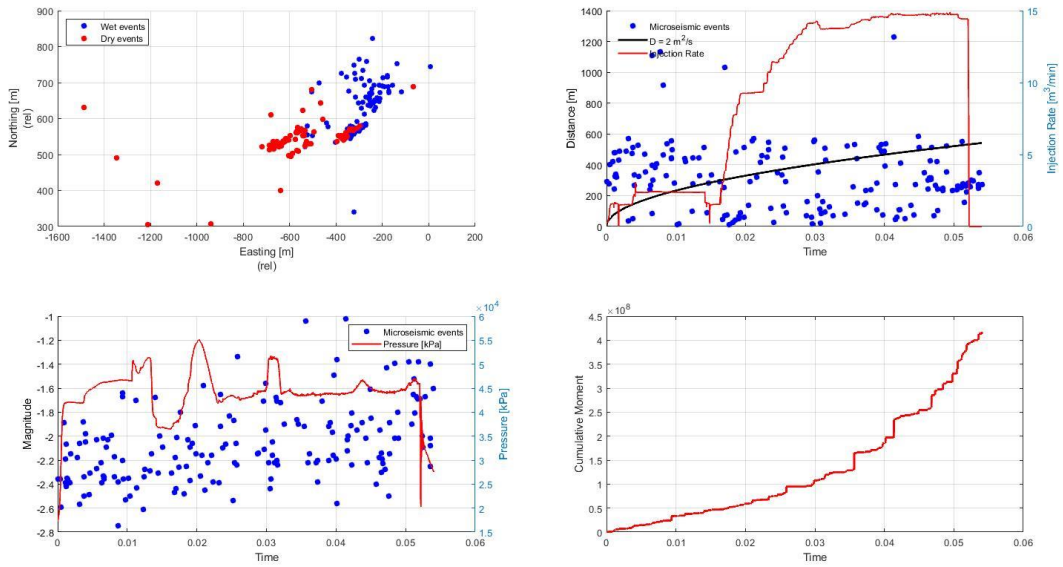


Figure 90 A08 stage 19 map view plot, r-t plot, magnitude plot and cumulative moment plot.

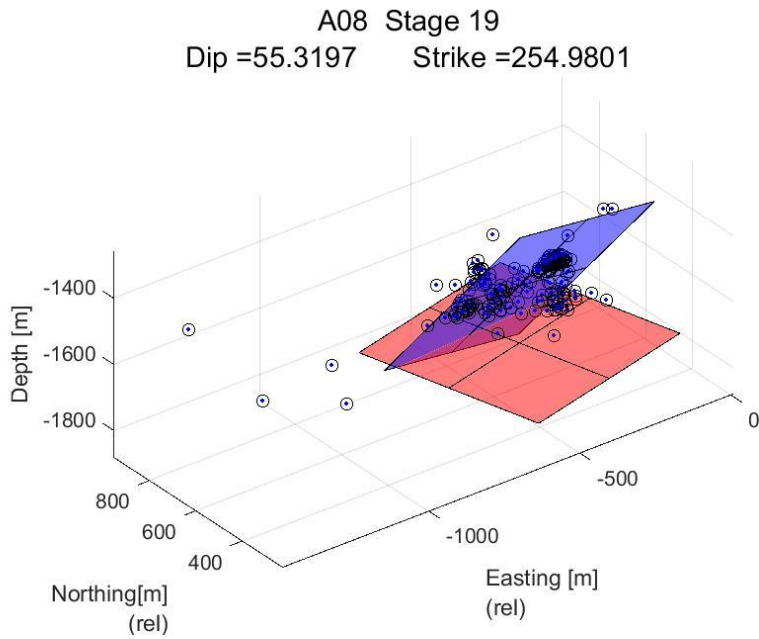


Figure 91 A08 stage 19 best fitting plane.

A08
Stage 20

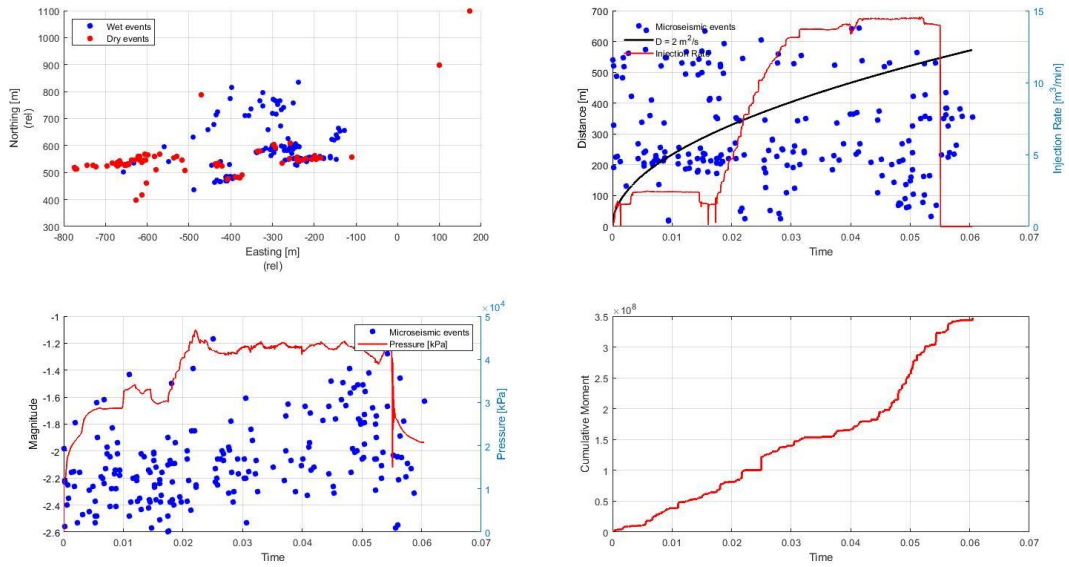


Figure 92 A08 stage 20 map view plot, r-t plot, magnitude plot and cumulative moment plot.

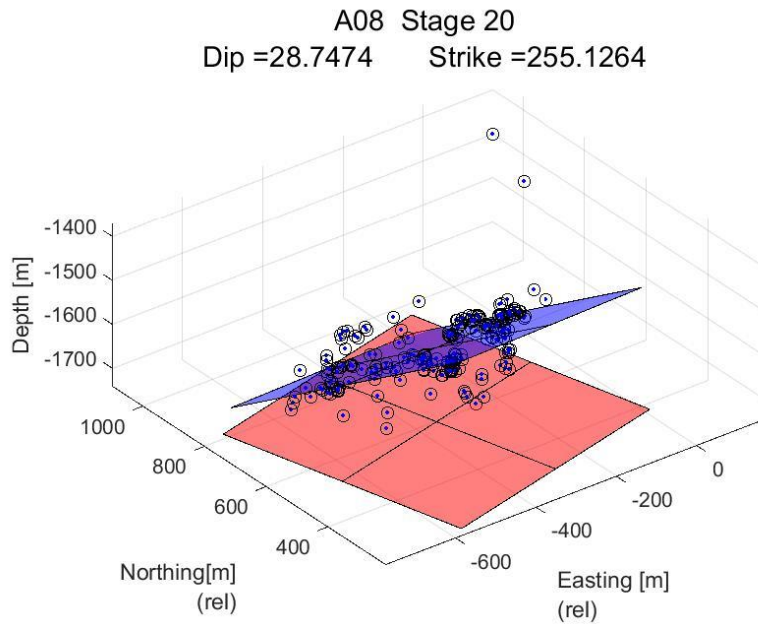


Figure 93 A08 stage 20 best fitting plane.

A08
Stage 21

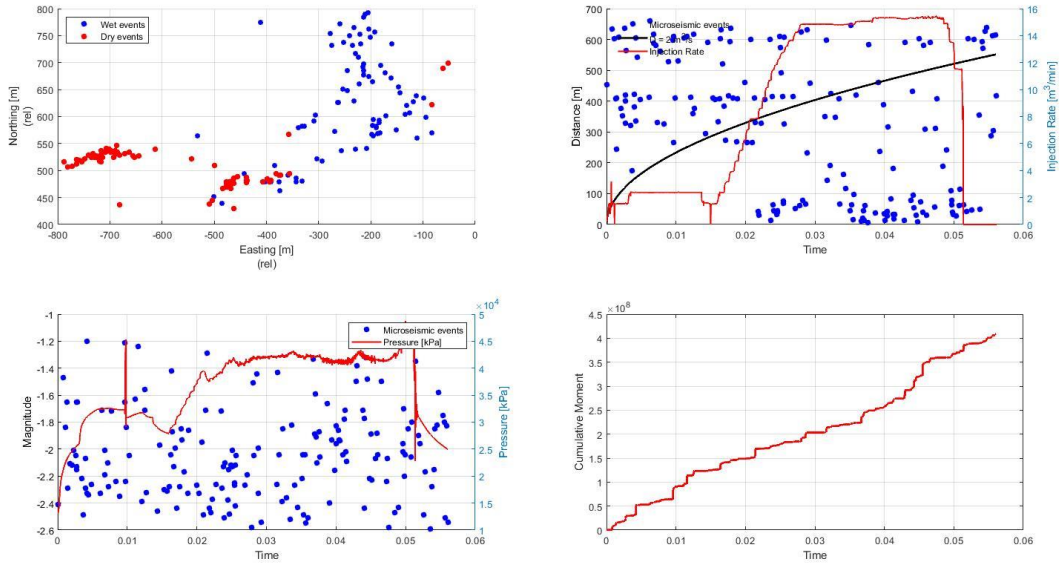


Figure 94 A08 stage 21 map view plot, r-t plot, magnitude plot and cumulative moment plot.

A08 Stage 21
Dip = 35.6909 Strike = 253.905

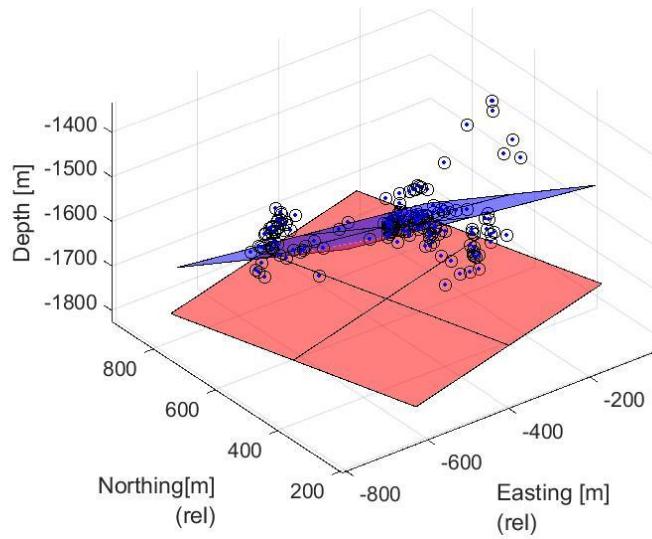


Figure 95 A08 stage 21 best fitting plane.

A08
Stage 22

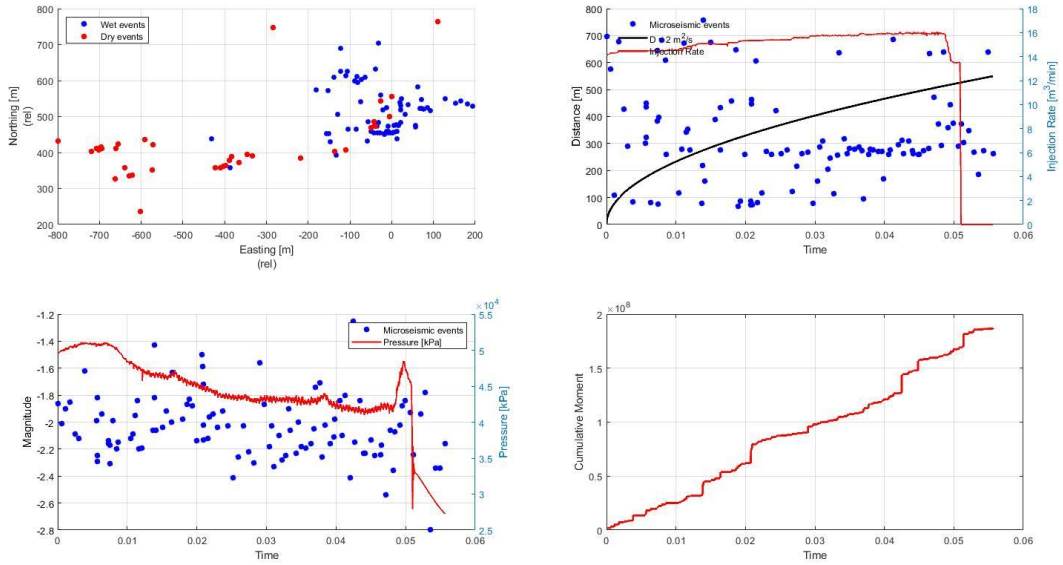


Figure 96 A08 stage 22 map view plot, r-t plot, magnitude plot and cumulative moment plot.

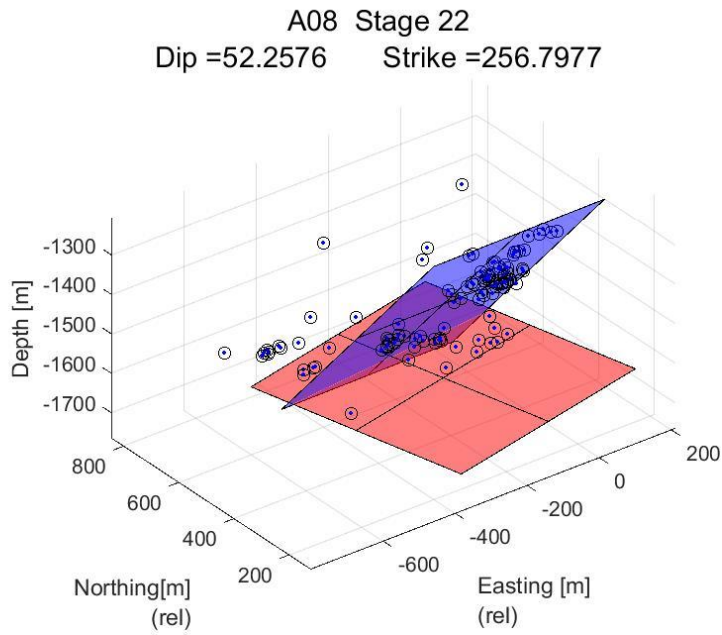


Figure 97 A08 stage 22 best fitting plane.

A08
Stage 23

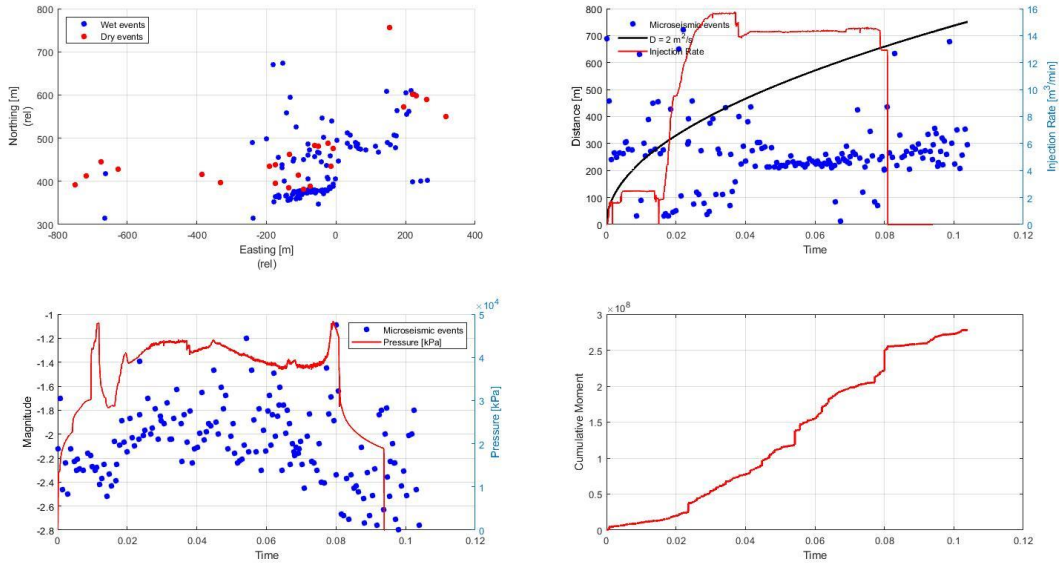


Figure 98 A08 stage 23 map view plot, r-t plot, magnitude plot and cumulative moment plot.

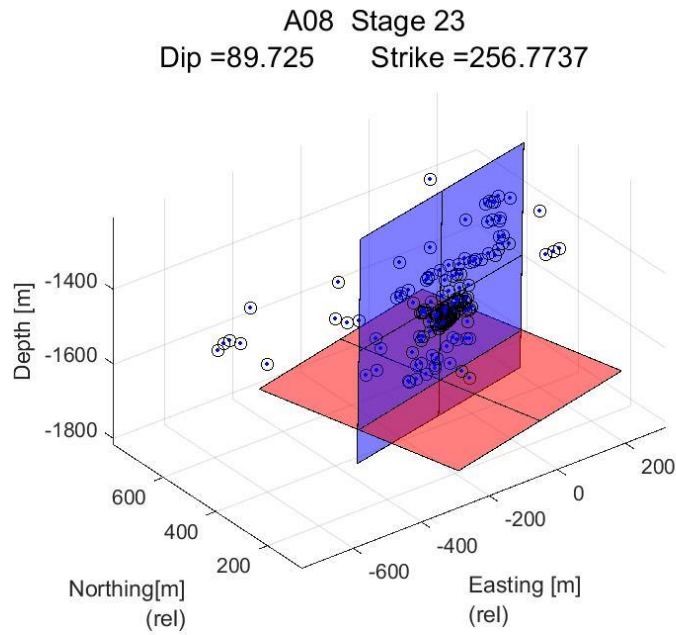


Figure 99 A08 stage 23 best fitting plane.

A08
Stage 24

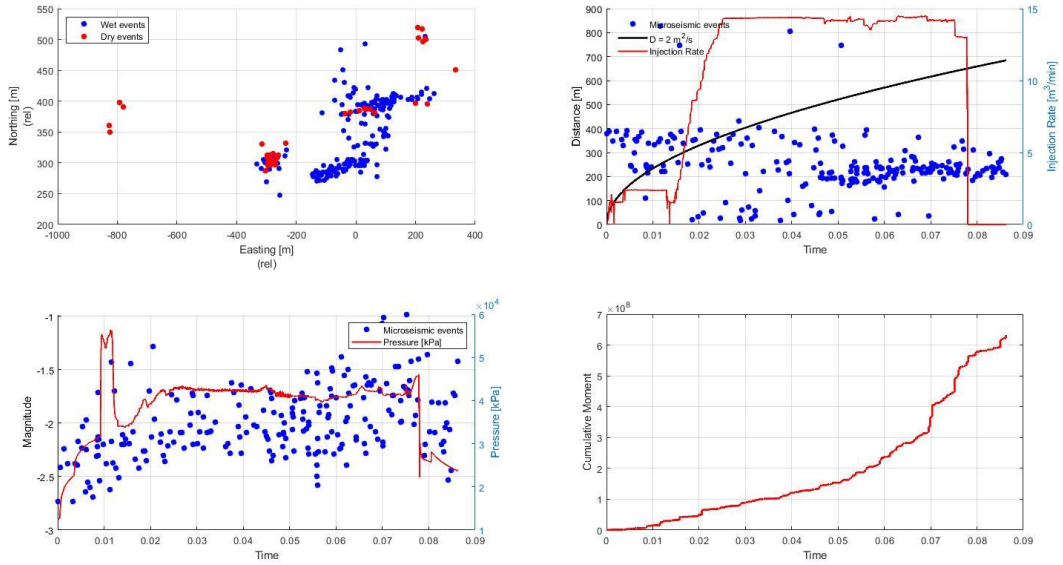


Figure 100 A08 stage 24 map view plot, r-t plot, magnitude plot and cumulative moment plot.

A08 Stage 24
Dip = 79.6768 Strike = 259.5807

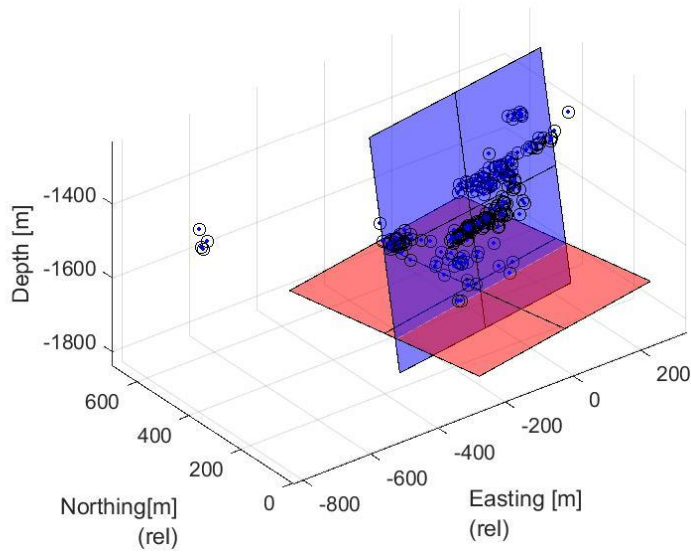


Figure 101 A08 stage 24 best fitting plane.

A08
Stage 25

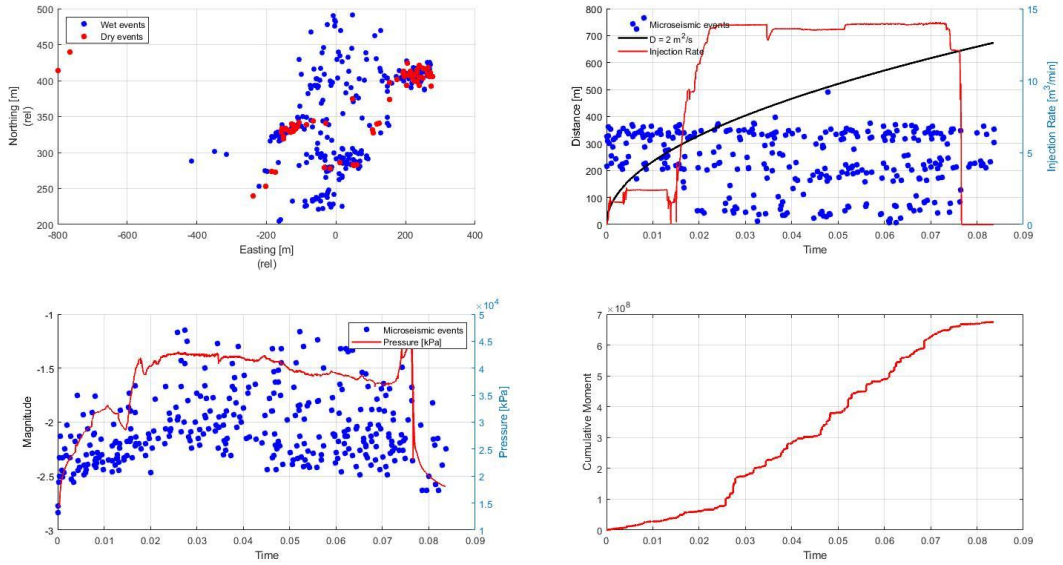


Figure 102 A08 stage 25 map view plot, r-t plot, magnitude plot and cumulative moment plot.

A08 Stage 25
Dip = 82.9593 Strike = 257.6423

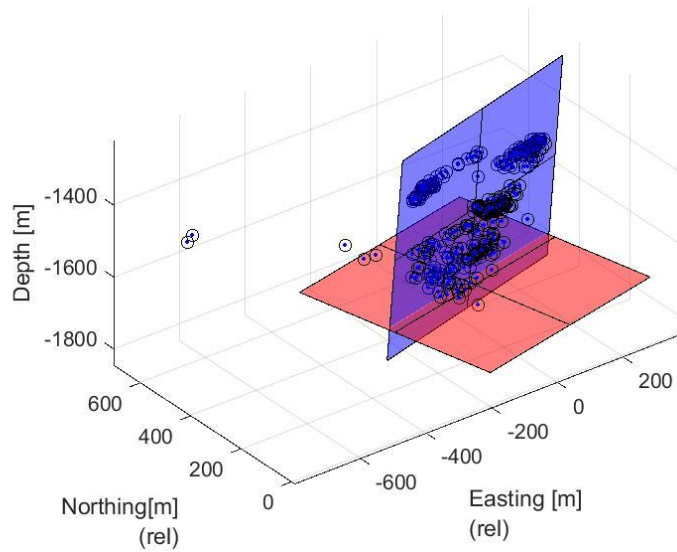


Figure 103 A08 stage 25 best fitting plane.

B11
Stage 2

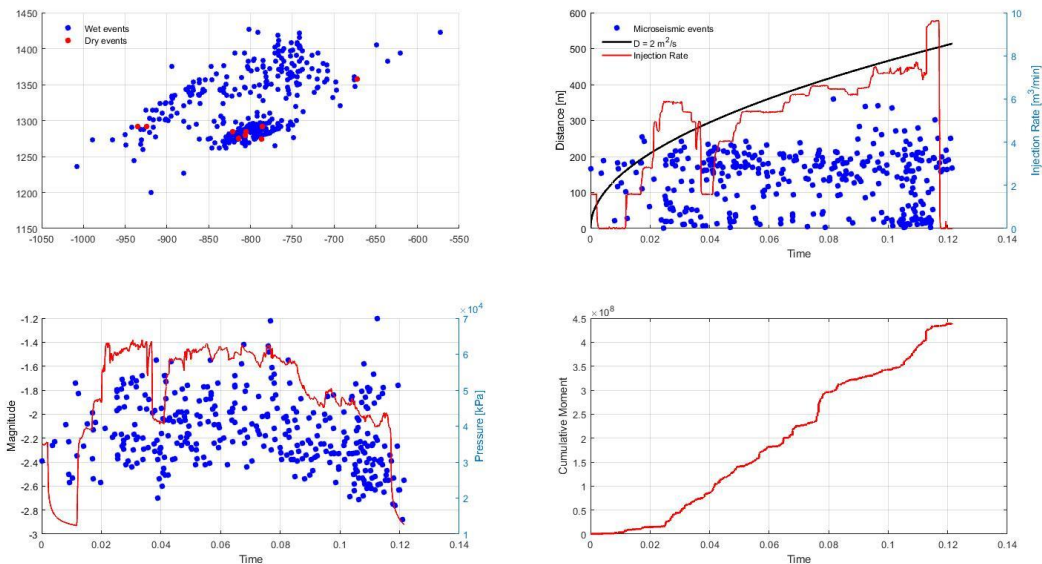


Figure 104 B11 stage 2 map view plot, r-t plot, magnitude plot and cumulative moment plot.

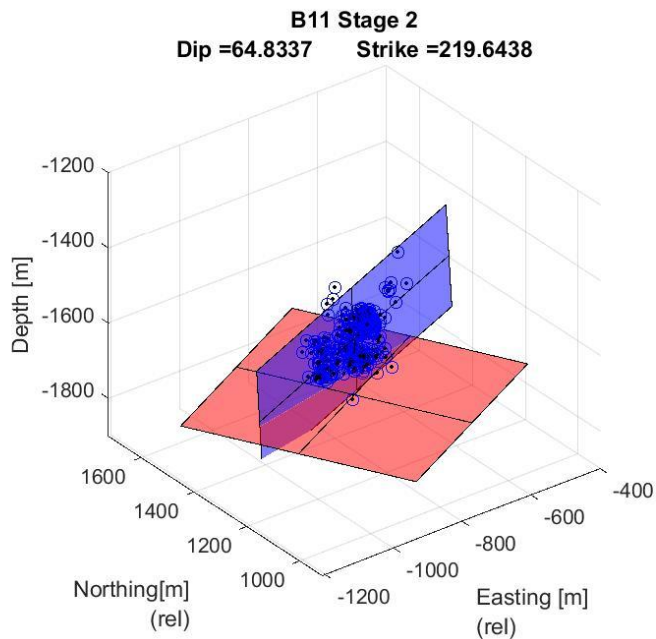


Figure 105 B11 stage 2 best fitting plane.

B11
Stage 3

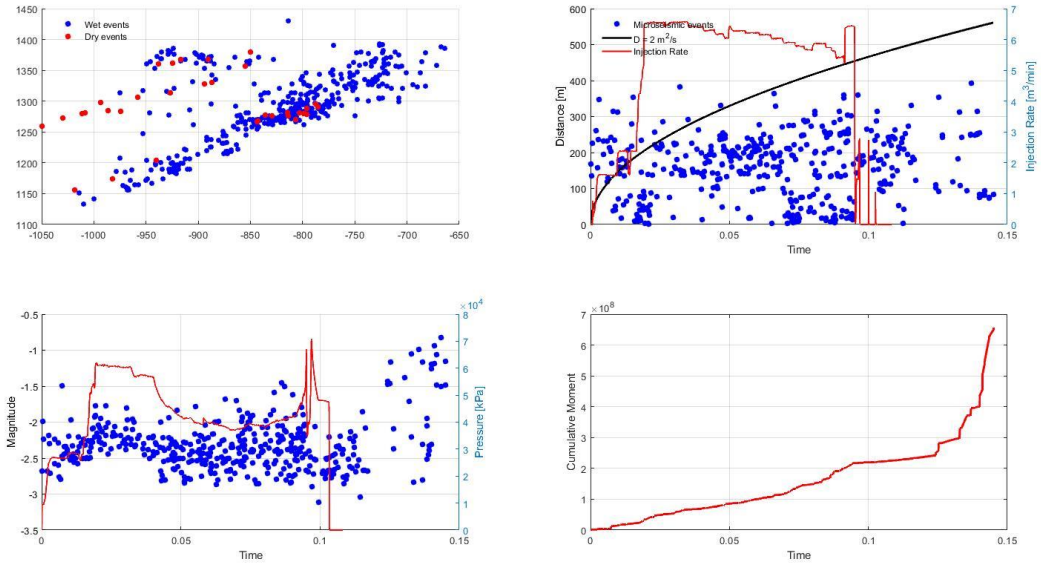


Figure 106 B11 stage 3 map view plot, r-t plot, magnitude plot and cumulative moment plot.

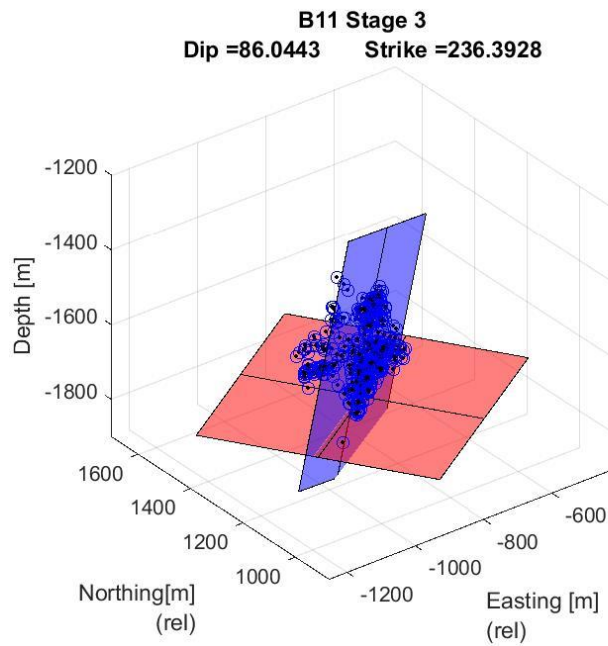


Figure 107 B11 stage 3 best fitting plane.

B11
Stage 4

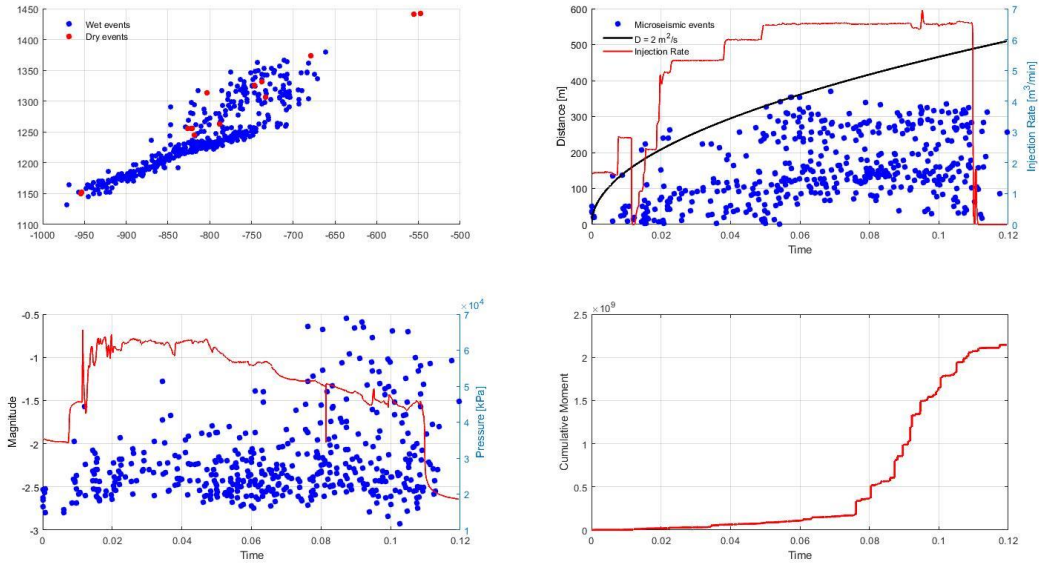


Figure 108 B11 stage 4 map view plot, r-t plot, magnitude plot and cumulative moment plot.

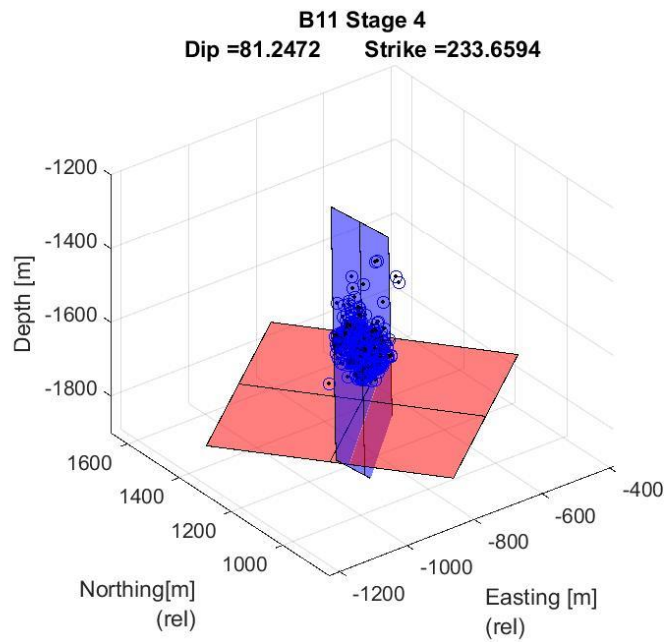


Figure 109 B11 stage 4 best fitting plane.

B11
Stage 5

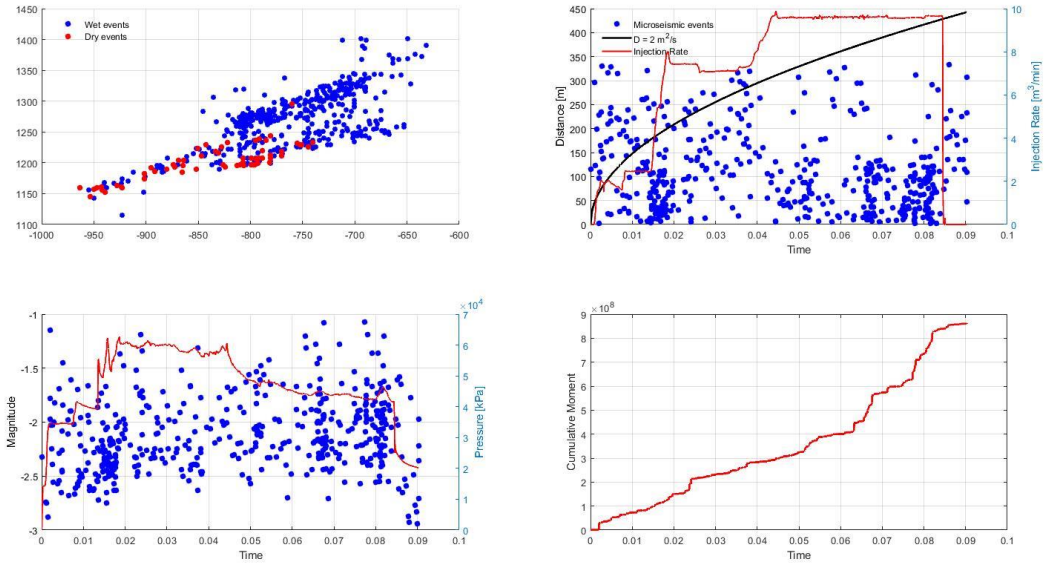


Figure 110 B11 stage 5 map view plot, r-t plot, magnitude plot and cumulative moment plot.

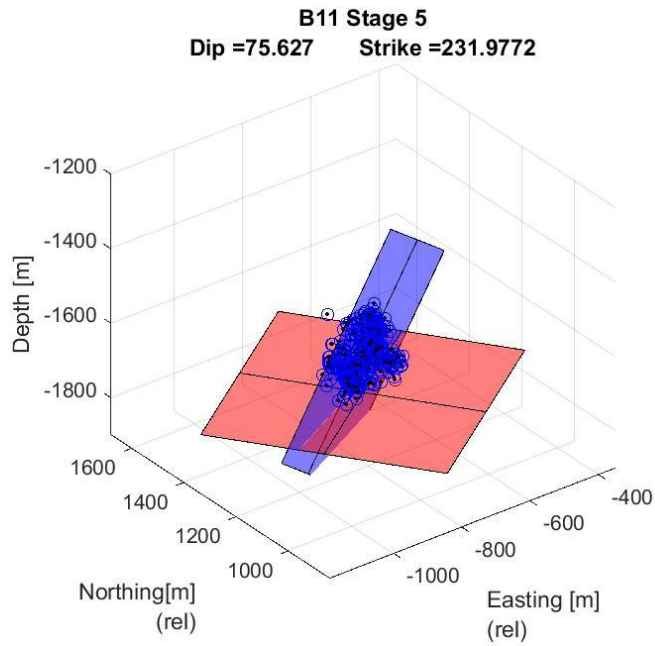


Figure 111 B11 stage 5 best fitting plane.

B11
Stage 6

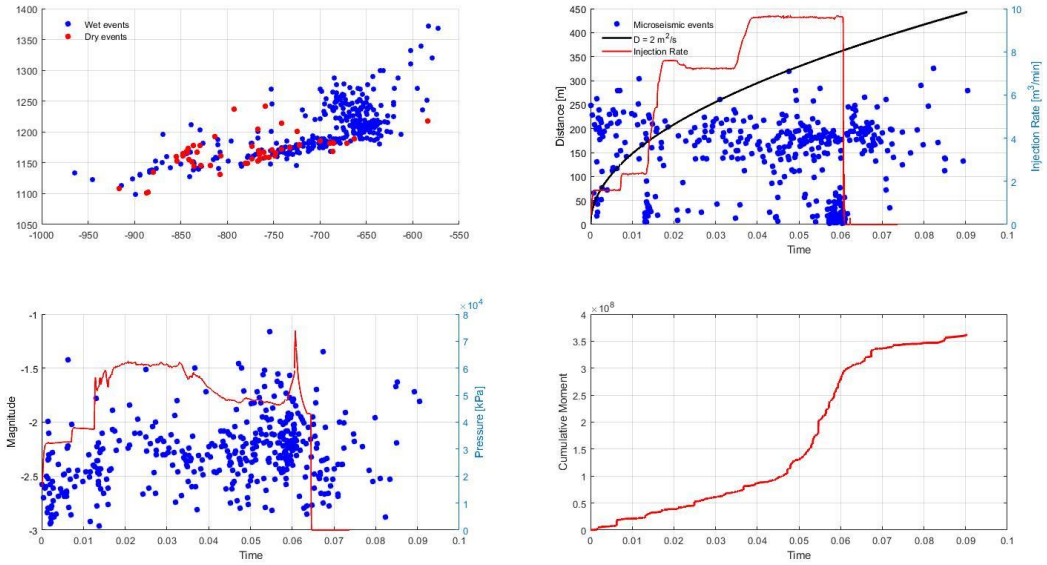


Figure 112 B11 stage 6 map view plot, r-t plot, magnitude plot and cumulative moment plot.

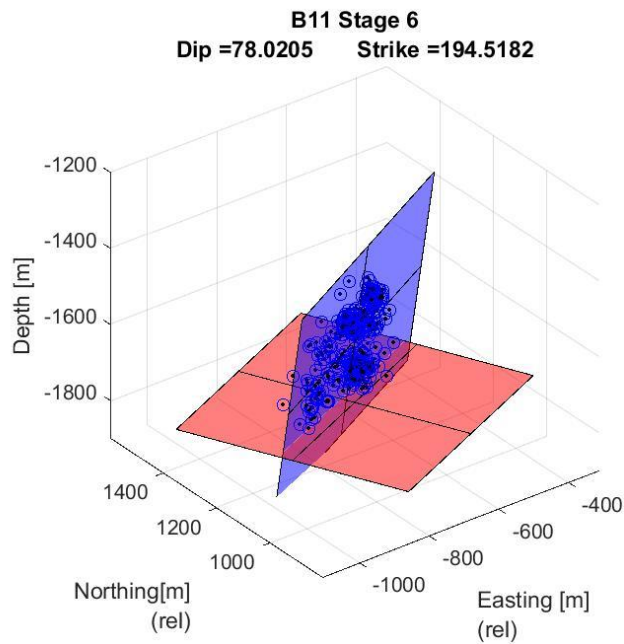


Figure 113 B11 stage 6 best fitting plane.

B11
Stage 7

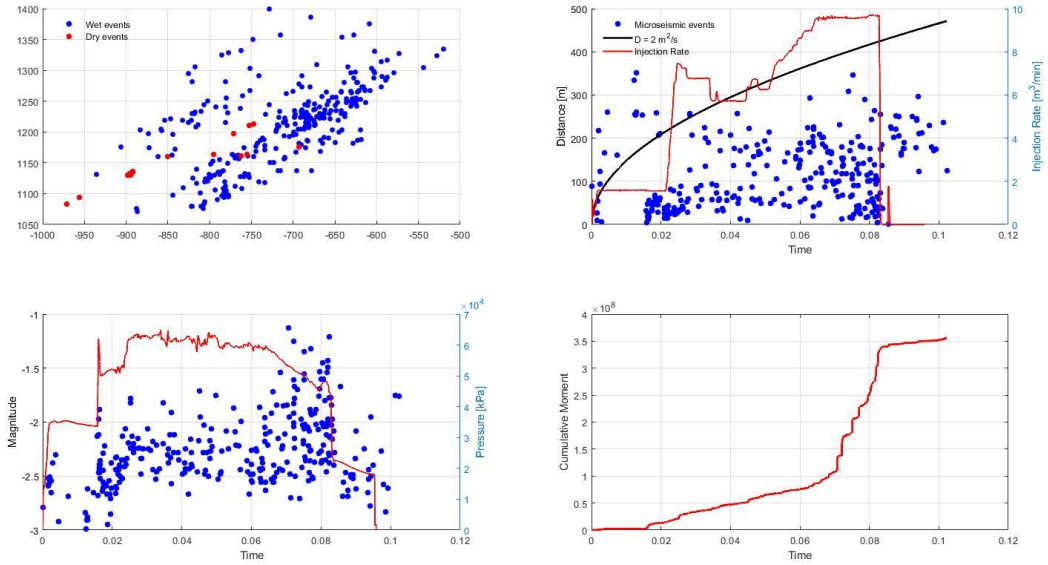


Figure 114 B11 stage 7 map view plot, r-t plot, magnitude plot and cumulative moment plot.

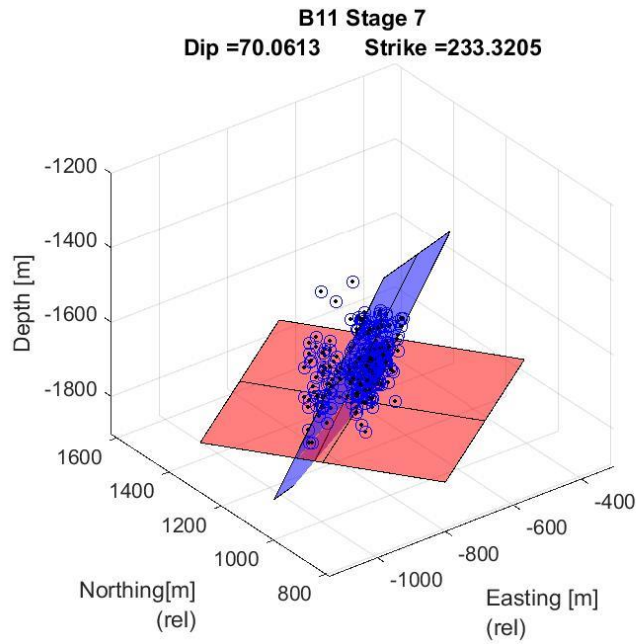


Figure 115 B11 stage 7 best fitting plane.

B11
Stage 8

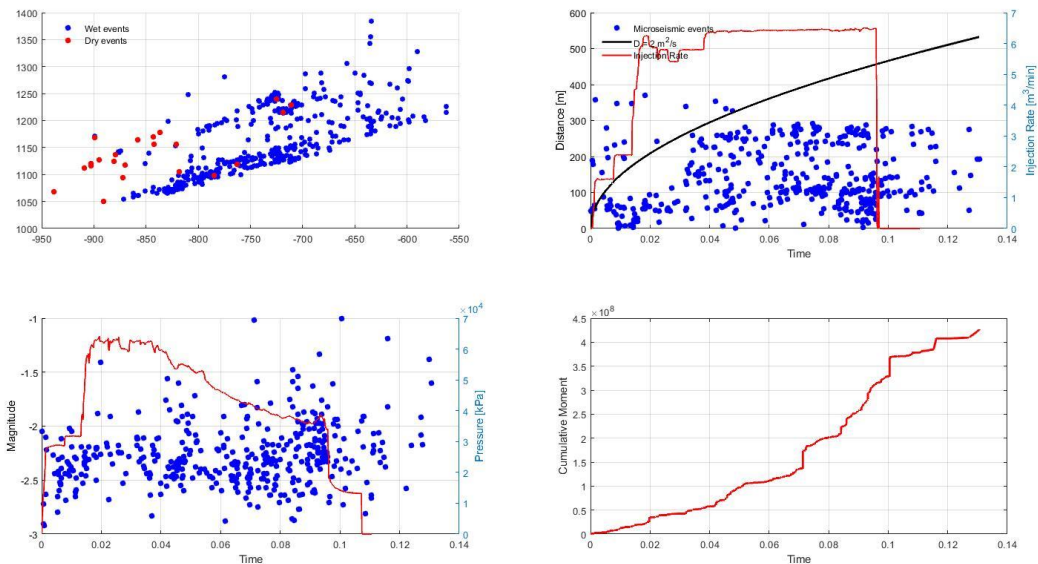


Figure 116 B11 stage 8 map view plot, r-t plot, magnitude plot and cumulative moment plot.

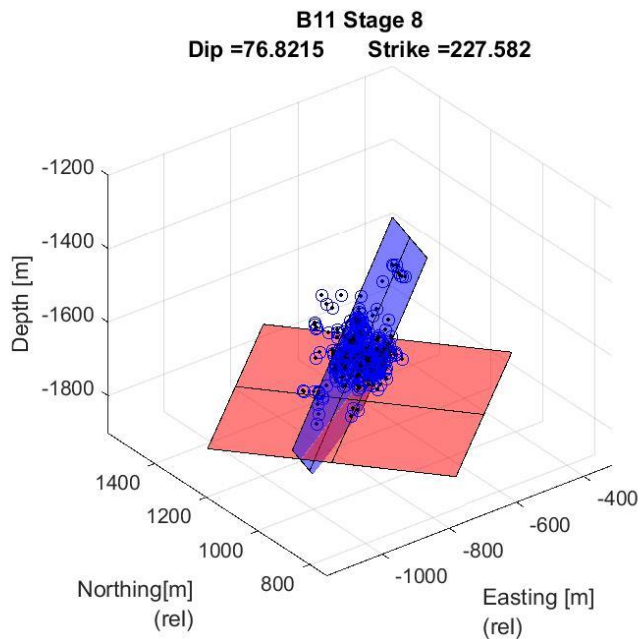


Figure 117 B11 stage 8 best fitting plane.

B11
Stage 9

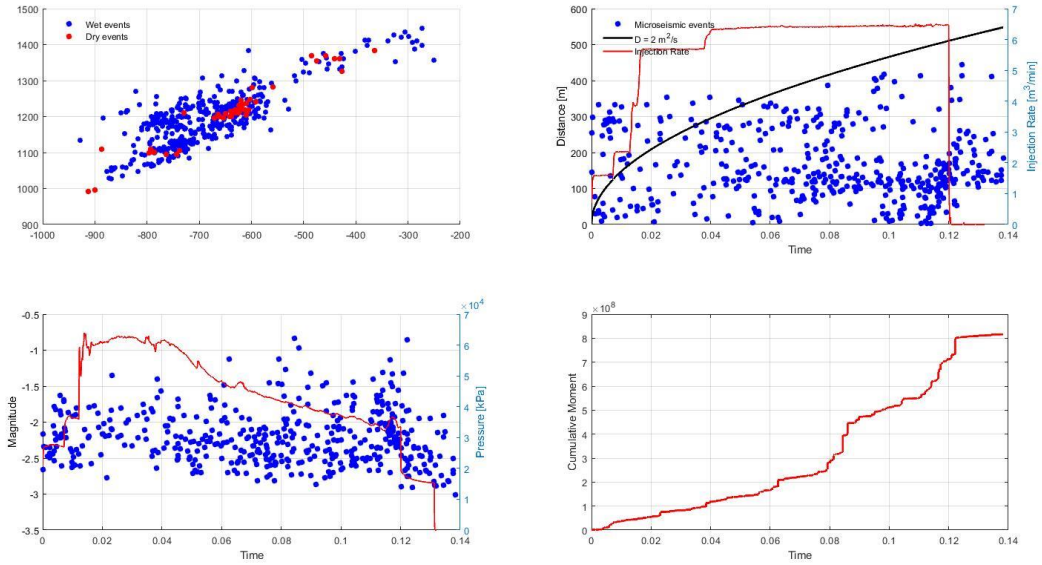


Figure 118 B11 stage 9 map view plot, r-t plot, magnitude plot and cumulative moment plot.

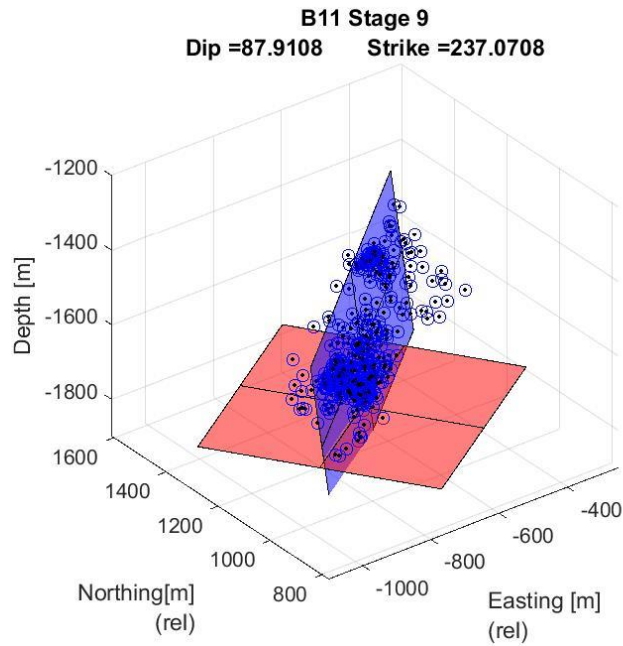


Figure 119 B11 stage 9 best fitting plane.

B11
Stage 10

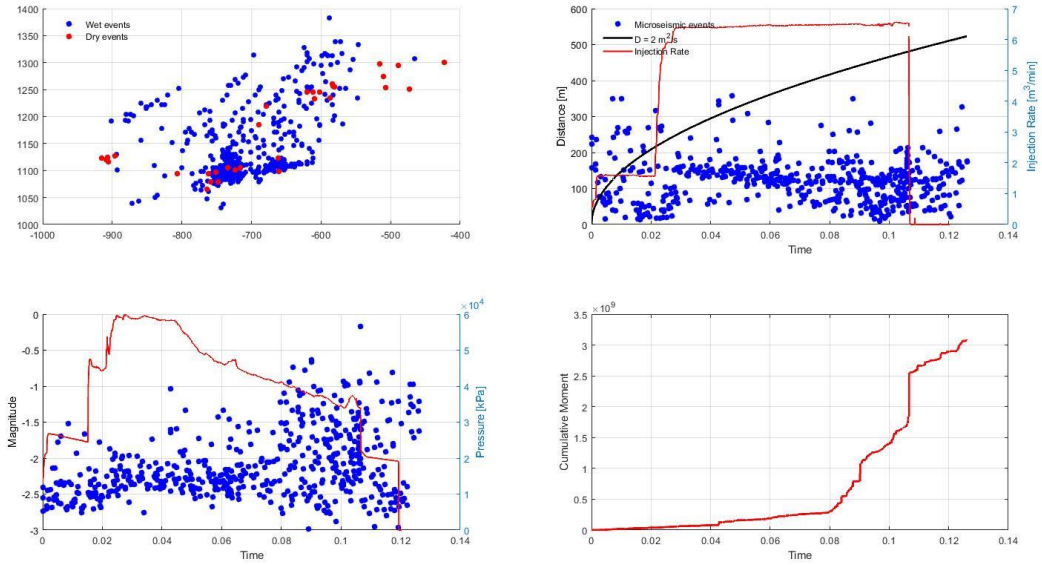


Figure 120 B11 stage 10 map view plot, r-t plot, magnitude plot and cumulative moment plot.

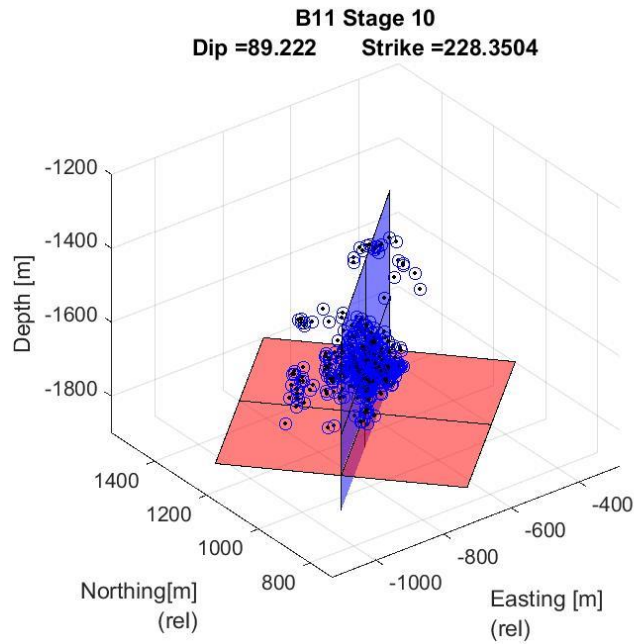


Figure 121 B11 stage 10 best fitting plane.

B11
Stage 11

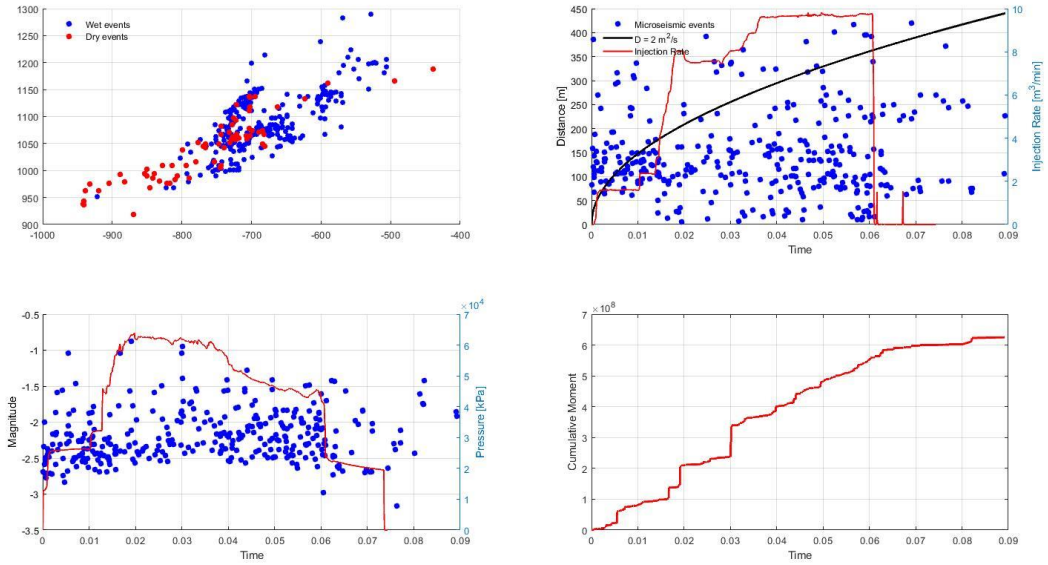


Figure 122 B11 stage 11 map view plot, r-t plot, magnitude plot and cumulative moment plot.

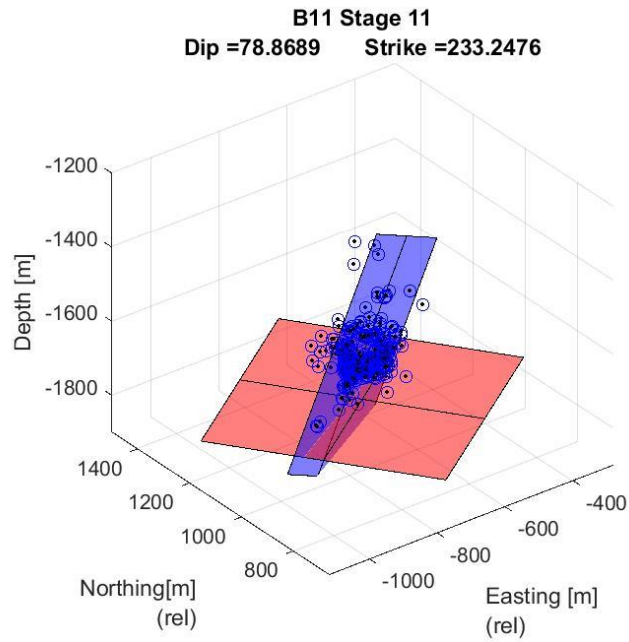


Figure 123 B11 stage 11 best fitting plane.

B11
Stage 12

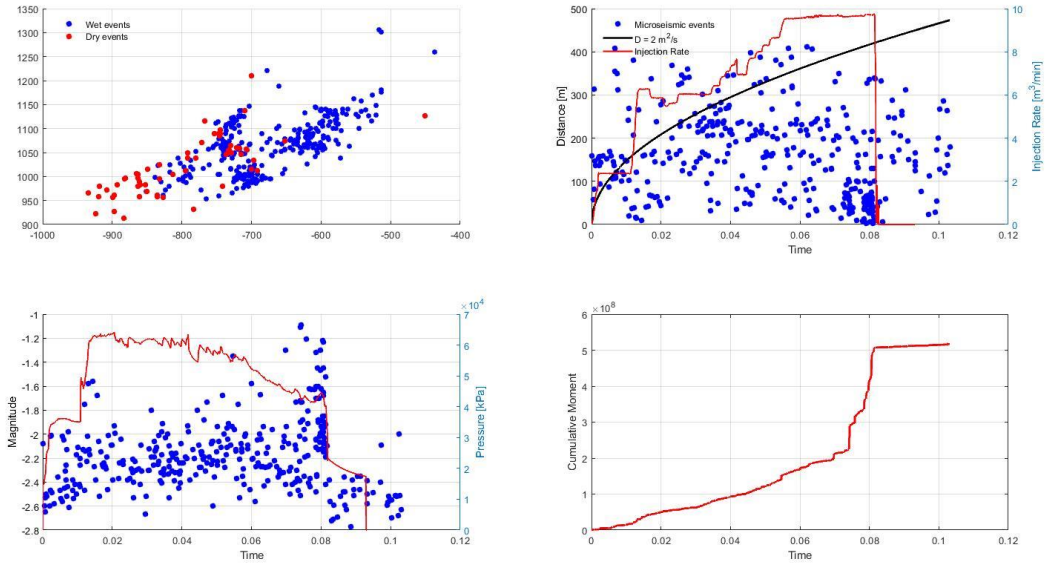


Figure 124 B11 stage 12 map view plot, r-t plot, magnitude plot and cumulative moment plot.

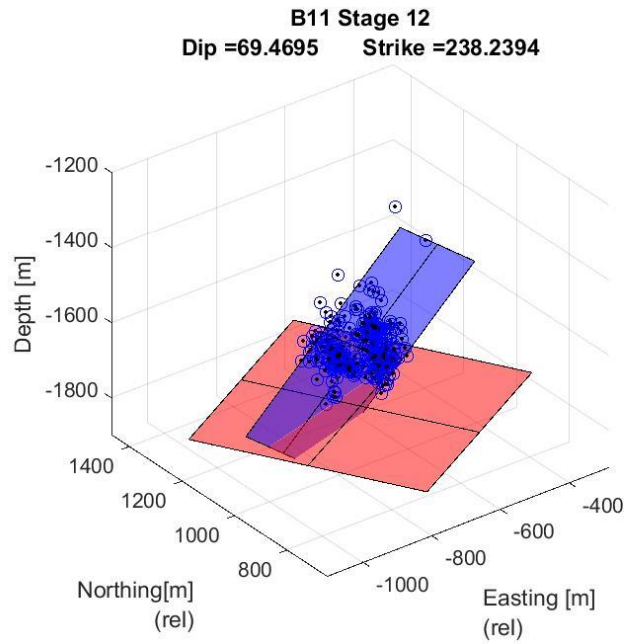


Figure 125 B11 stage 12 best fitting plane.

B11
Stage 13

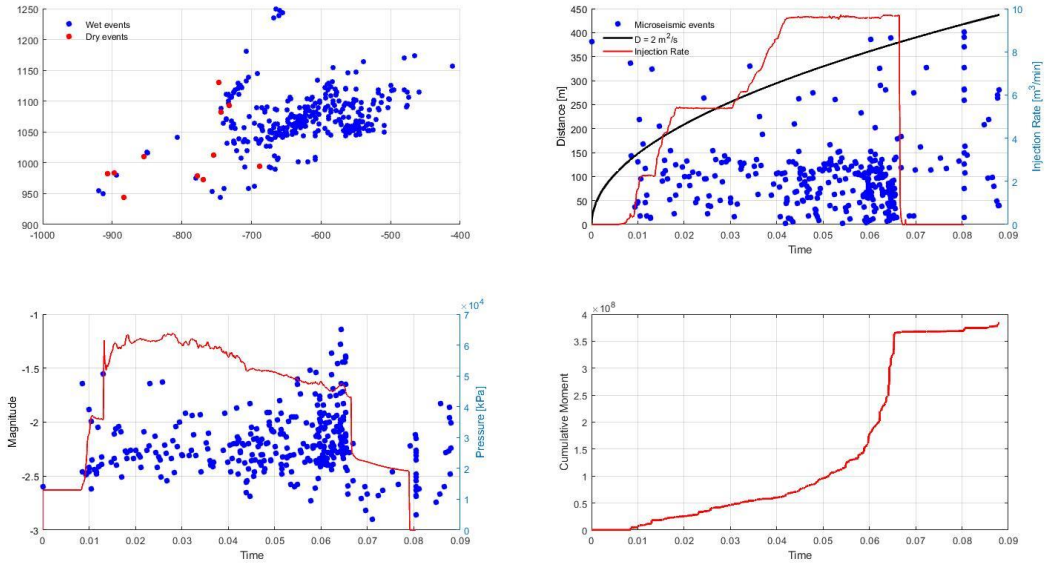


Figure 126 B11 stage 13 map view plot, r-t plot, magnitude plot and cumulative moment plot.

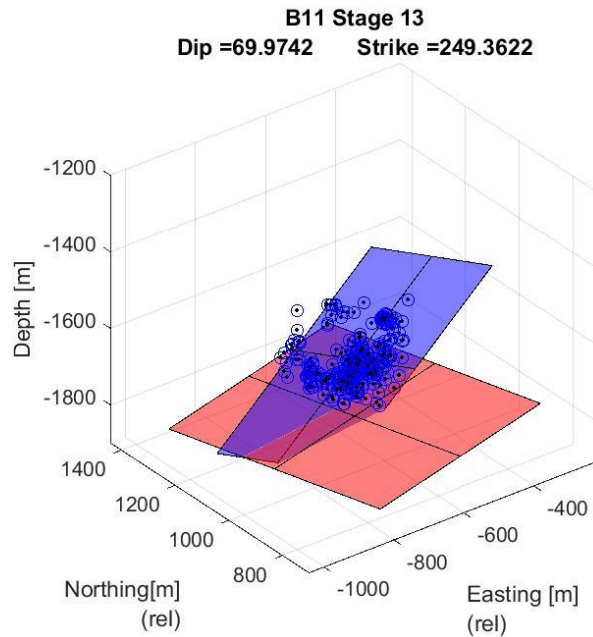


Figure 127 B11 stage 13 best fitting plane.

B11
Stage 14

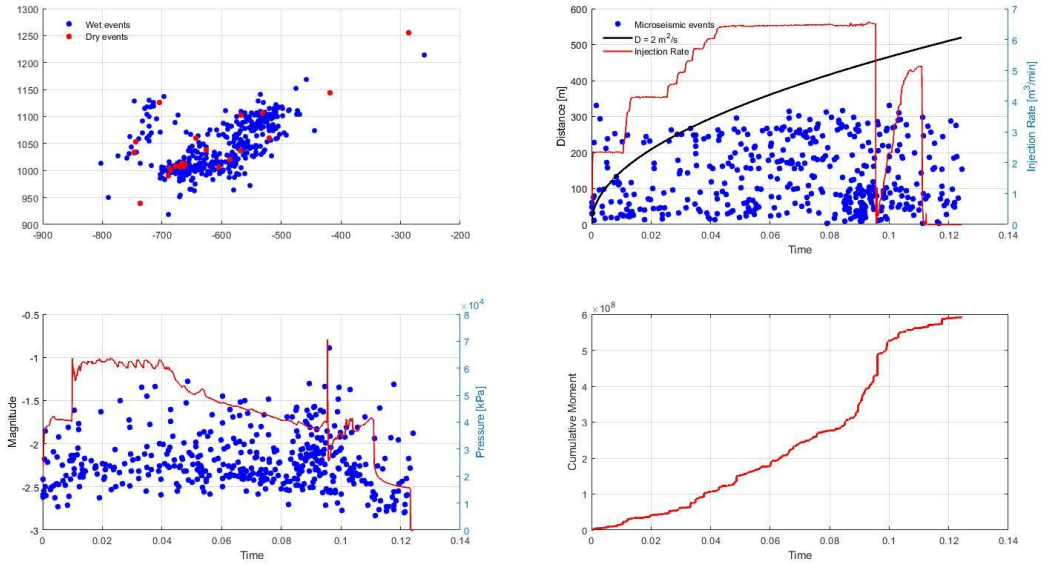


Figure 128 B11 stage 14 map view plot, r-t plot, magnitude plot and cumulative moment plot.

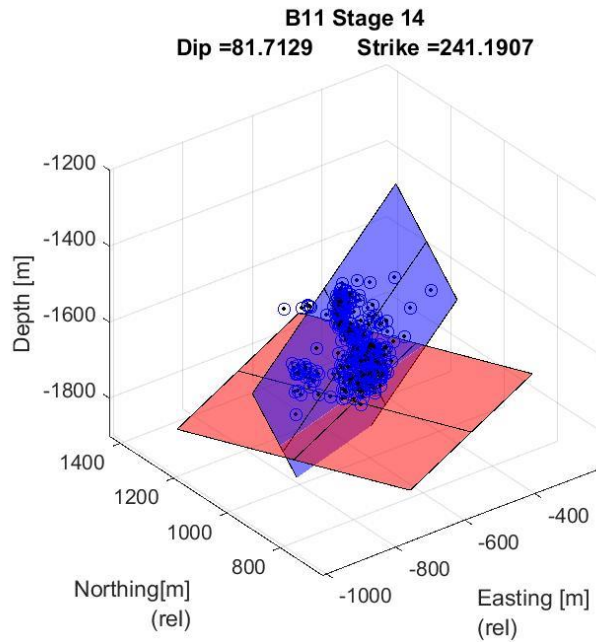


Figure 129 B11 stage 14 best fitting plane.

B11
Stage 15

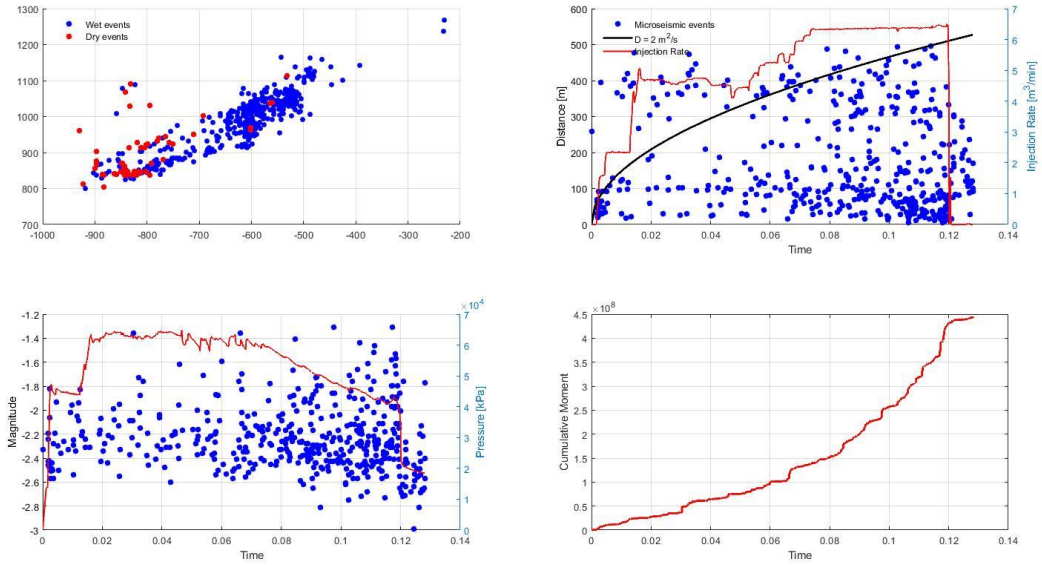


Figure 130 B11 stage 15 map view plot, r-t plot, magnitude plot and cumulative moment plot.

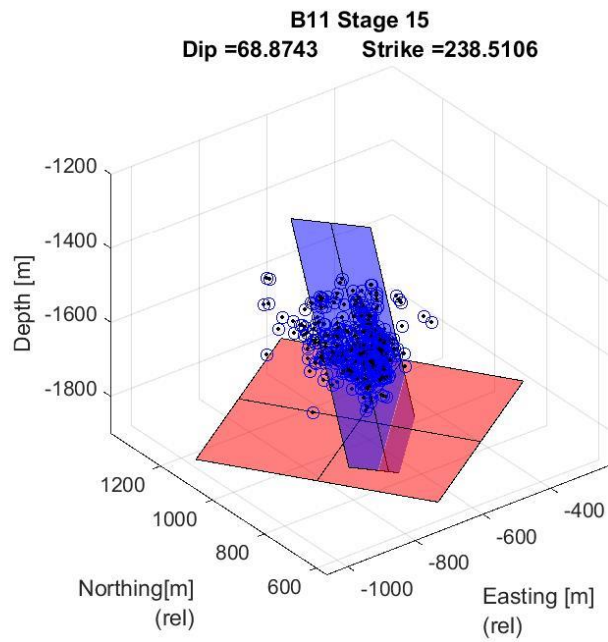


Figure 131 B11 stage 15 best fitting plane.

B11
Stage 16

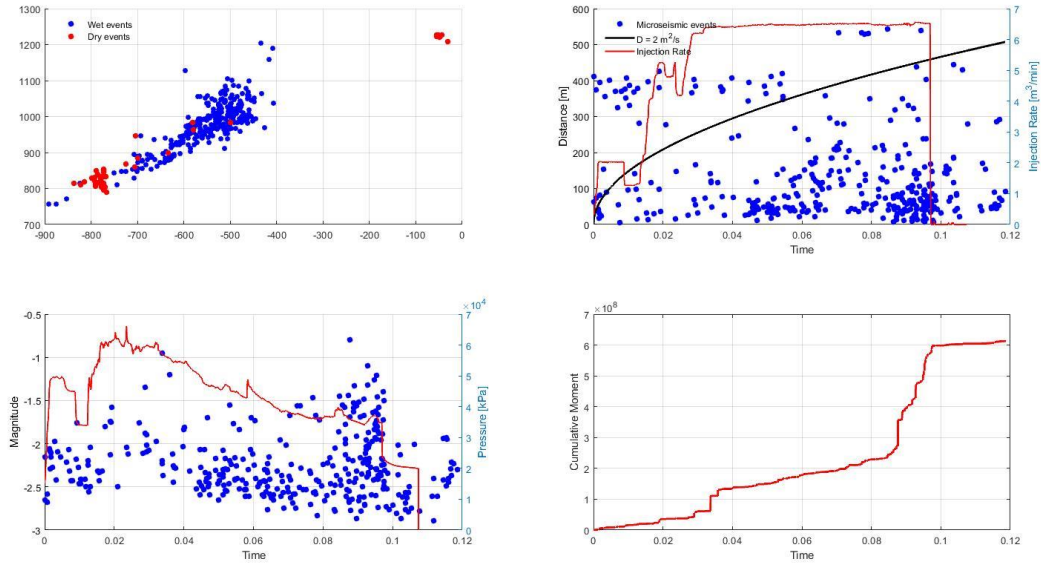


Figure 132 B11 stage 16 map view plot, r-t plot, magnitude plot and cumulative moment plot.

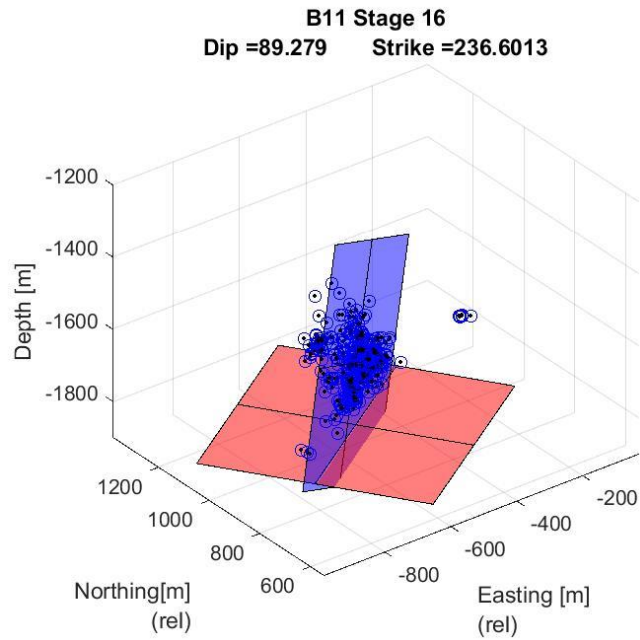


Figure 133 B11 stage 16 best fitting plane.

B11
Stage 17

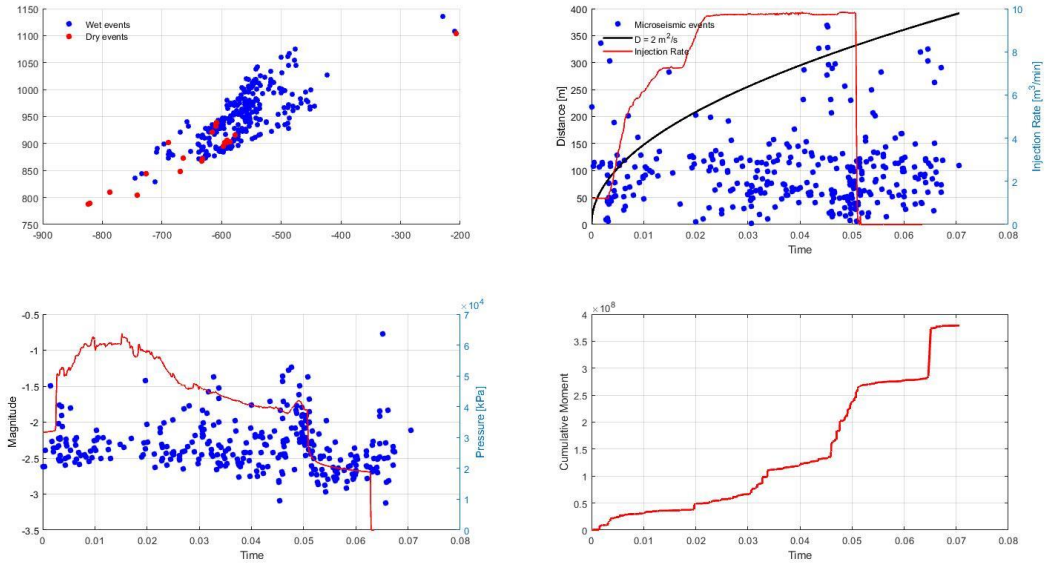


Figure 134 B11 stage 17 map view plot, r-t plot, magnitude plot and cumulative moment plot.

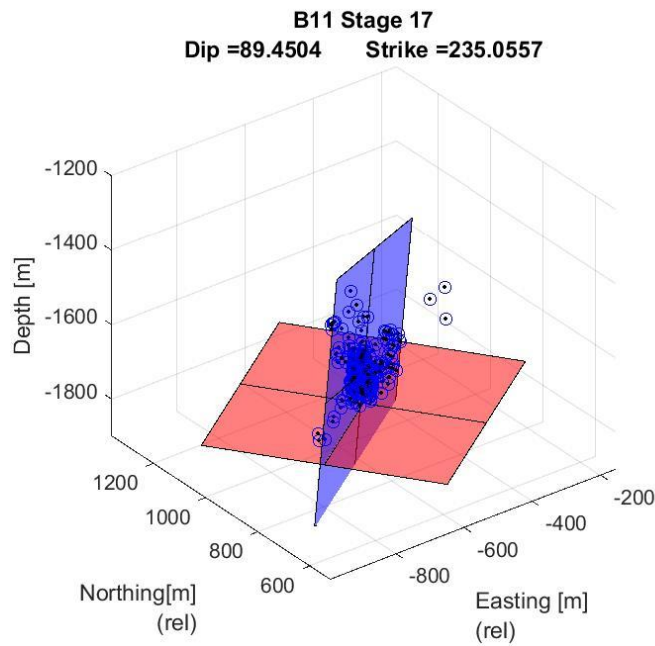


Figure 135 B11 stage 17 best fitting plane.

B11
Stage 19

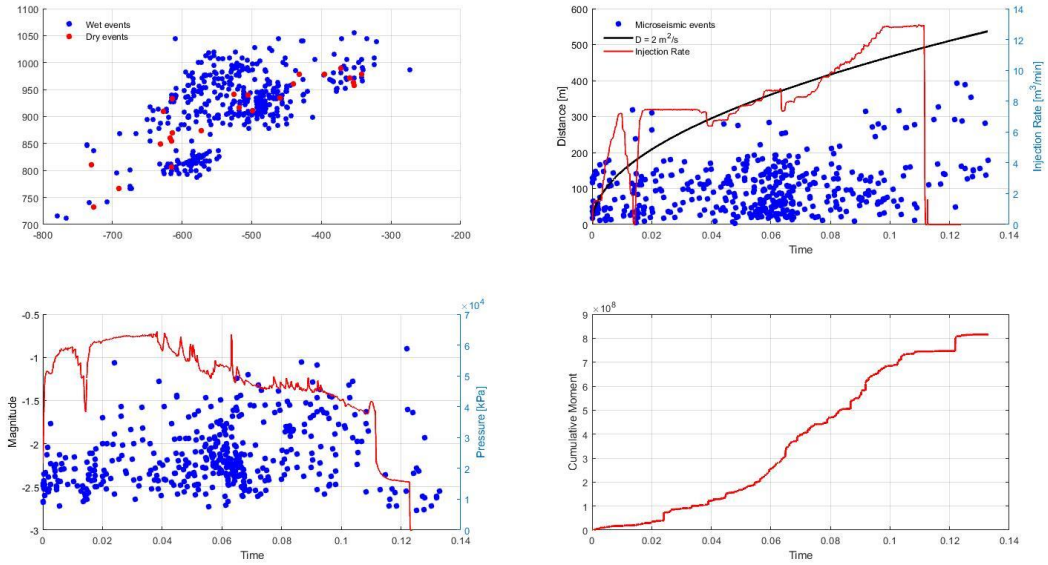


Figure 136 B11 stage 19 map view plot, r-t plot, magnitude plot and cumulative moment plot.

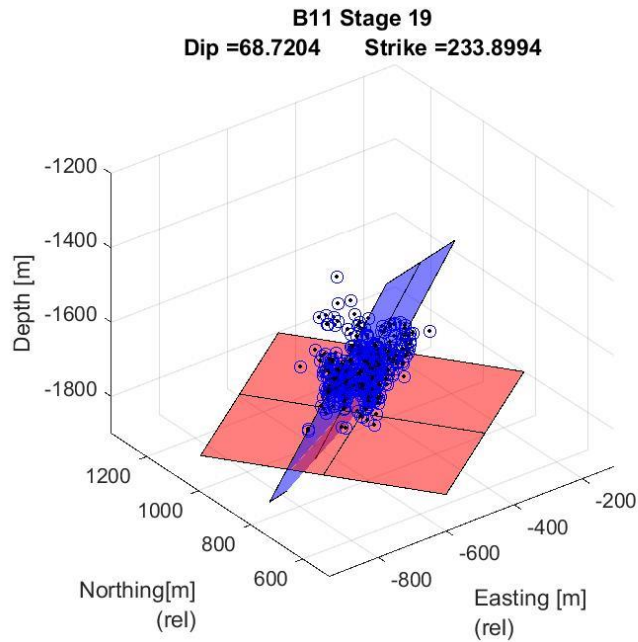


Figure 137 B11 stage 19 best fitting plane.

B11
Stage 20

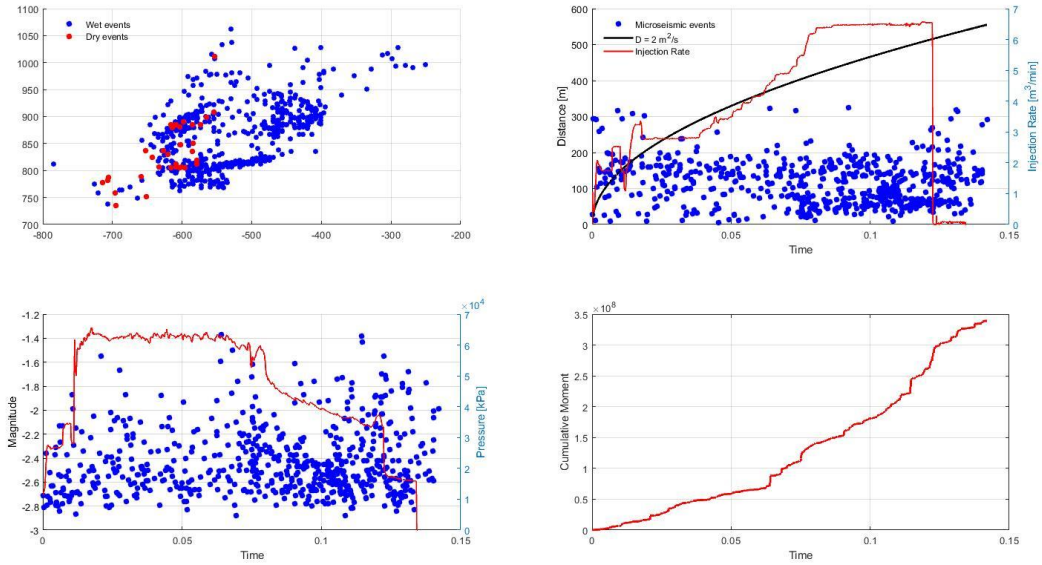


Figure 138 B11 stage 20 map view plot, r-t plot, magnitude plot and cumulative moment plot.

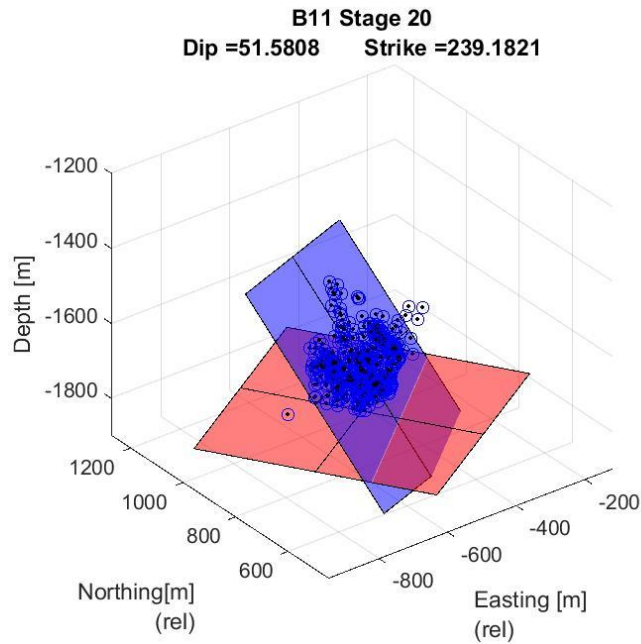


Figure 139 B11 stage 20 best fitting plane.

B11
Stage 21

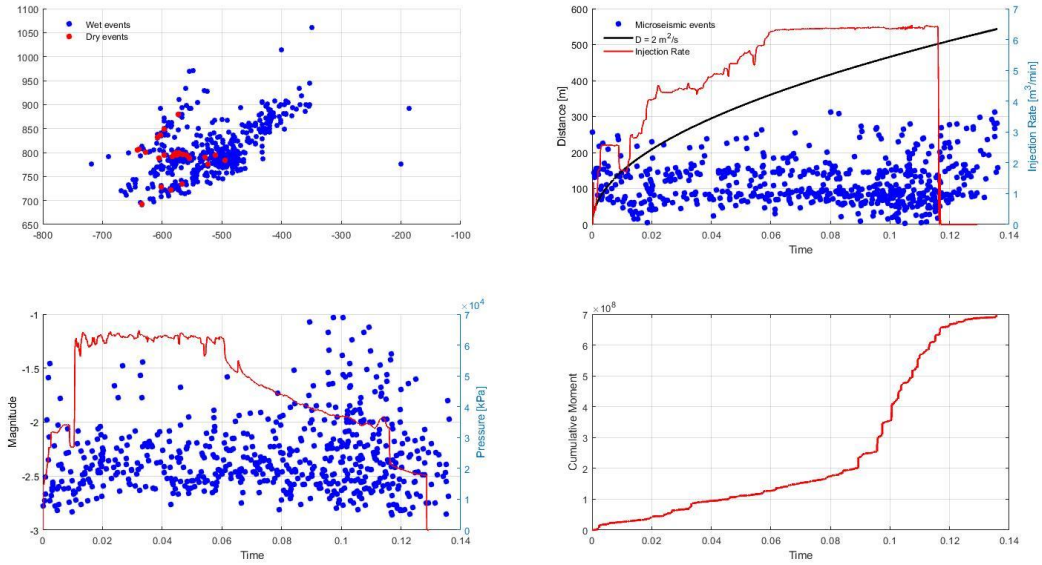


Figure 140 B11 stage 21 map view plot, r-t plot, magnitude plot and cumulative moment plot.

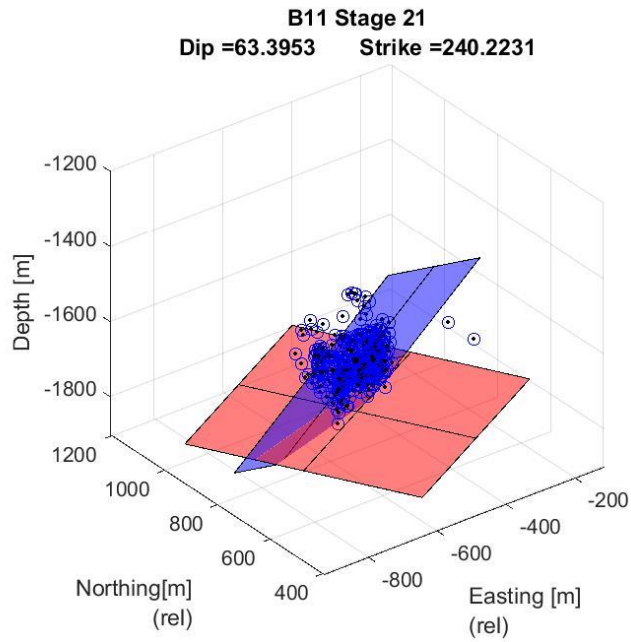


Figure 141 B11 stage 21 best fitting plane.

B11
Stage 22

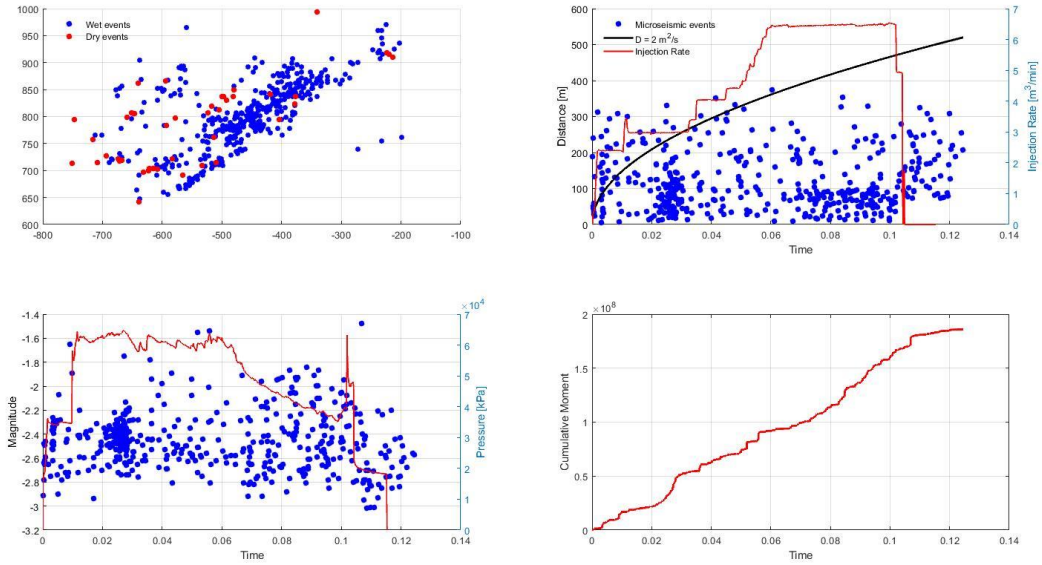


Figure 142 B11 stage 22 map view plot, r-t plot, magnitude plot and cumulative moment plot.

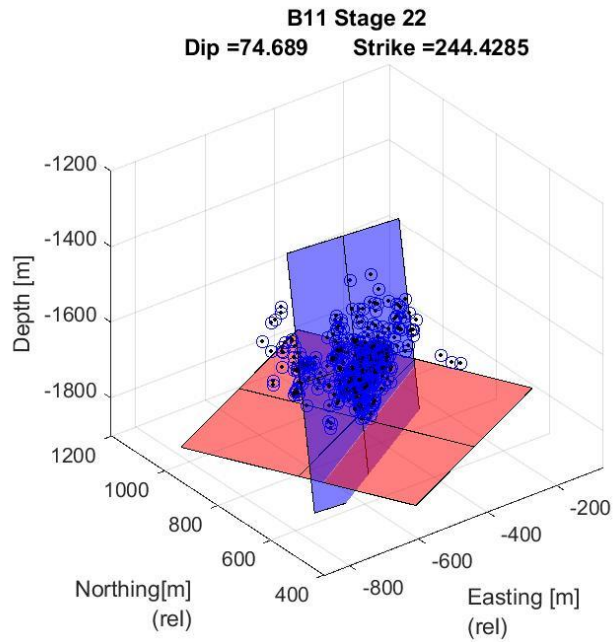


Figure 143 B11 stage 22 best fitting plane.

B11
Stage 23

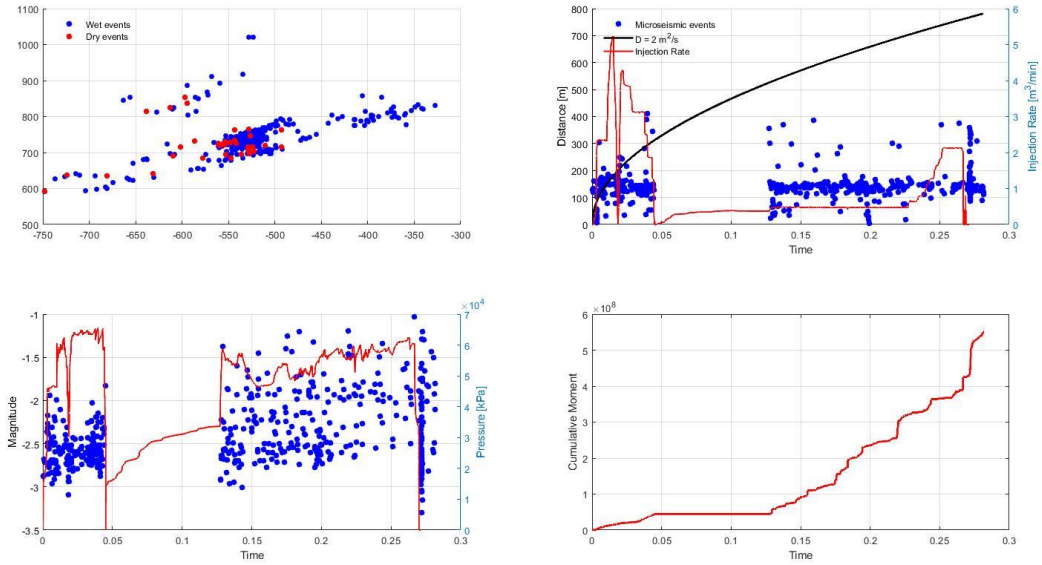


Figure 144 B11 stage 23 map view plot, r-t plot, magnitude plot and cumulative moment plot.

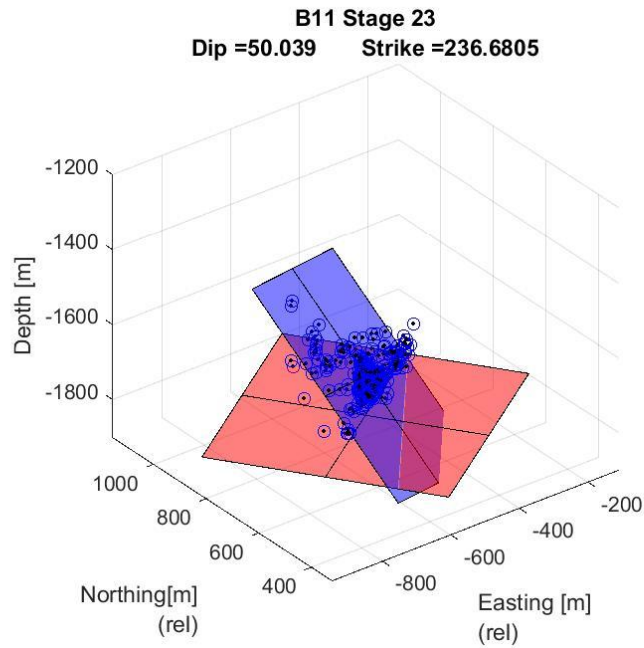


Figure 145 B11 stage 23 best fitting plane.

B11
Stage 24

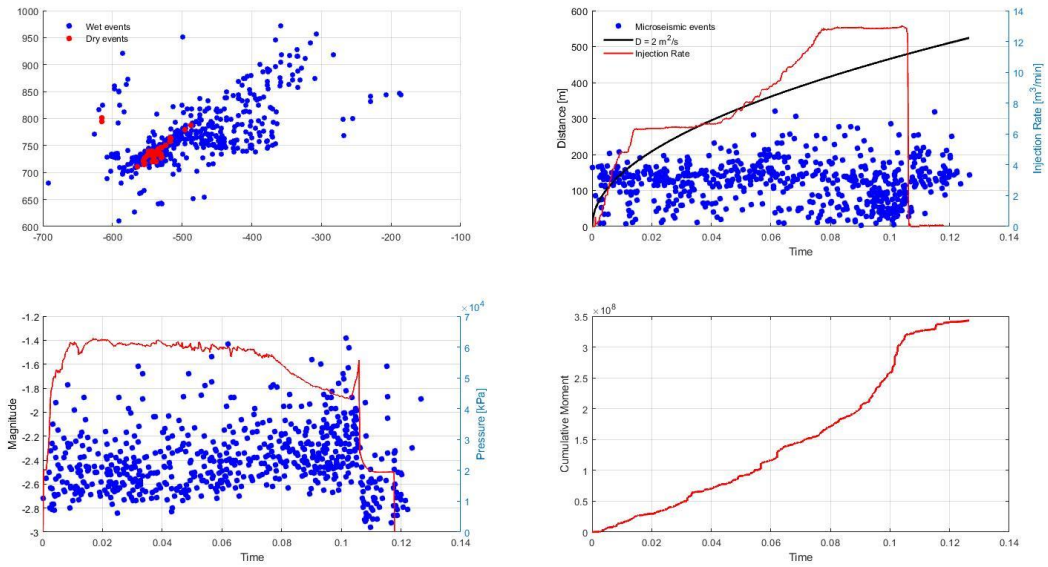


Figure 146 B11 stage 24 map view plot, r-t plot, magnitude plot and cumulative moment plot.

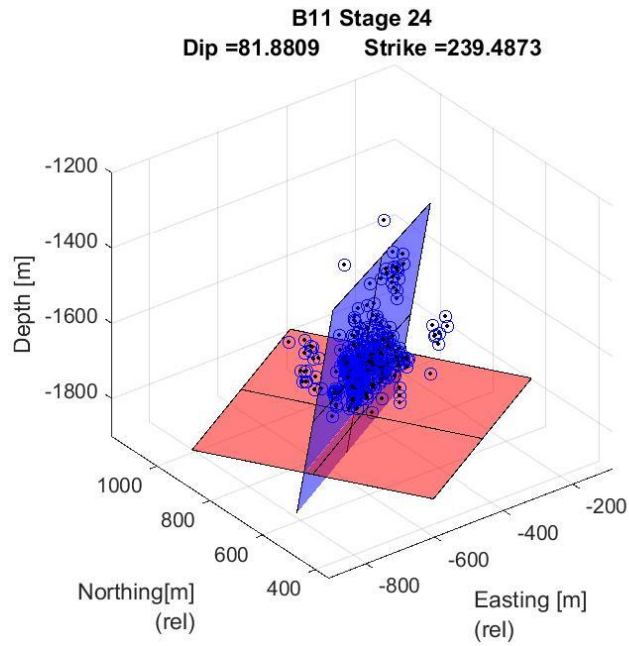


Figure 147 B11 stage 24 best fitting plane.

B11
Stage 25

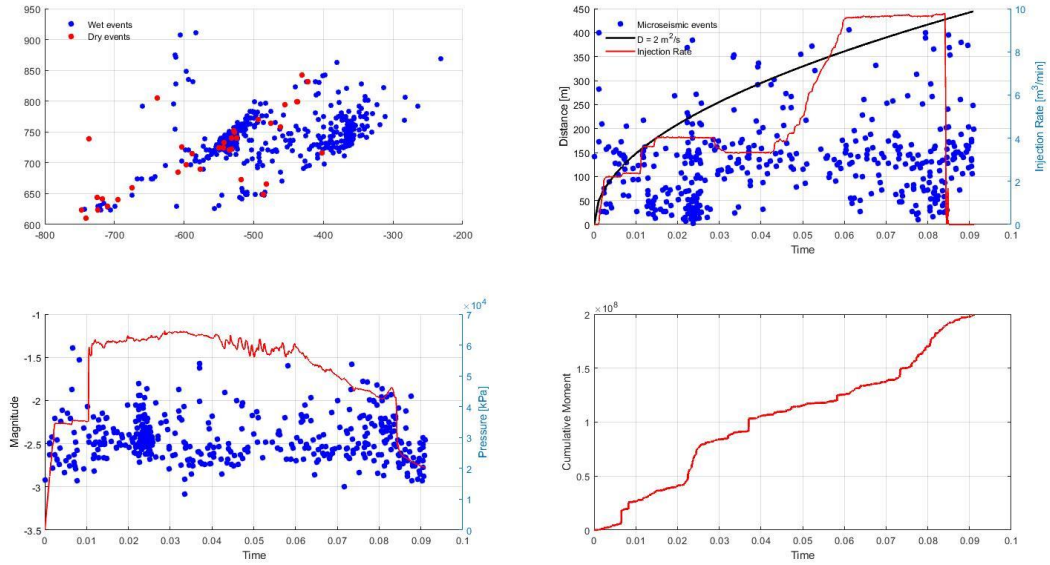


Figure 148 B11 stage 25 map view plot, r-t plot, magnitude plot and cumulative moment plot.

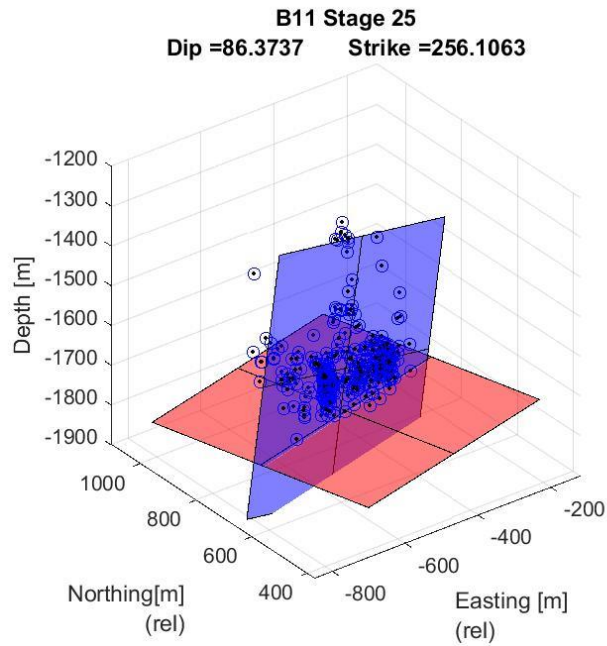


Figure 149 B11 stage 25 best fitting plane.

B11
Stage 26

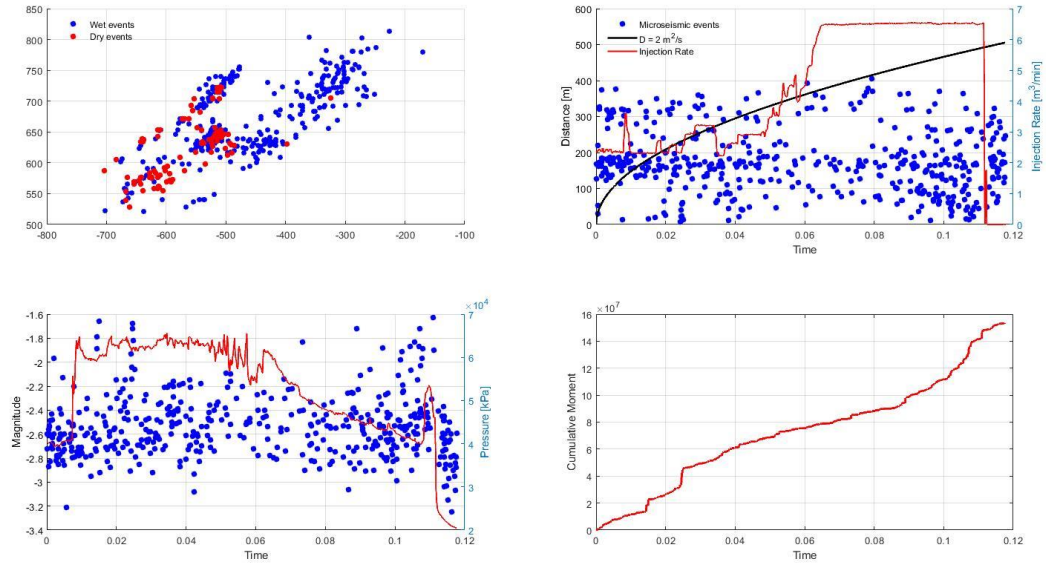


Figure 150 B11 stage 26 map view plot, r-t plot, magnitude plot and cumulative moment plot.

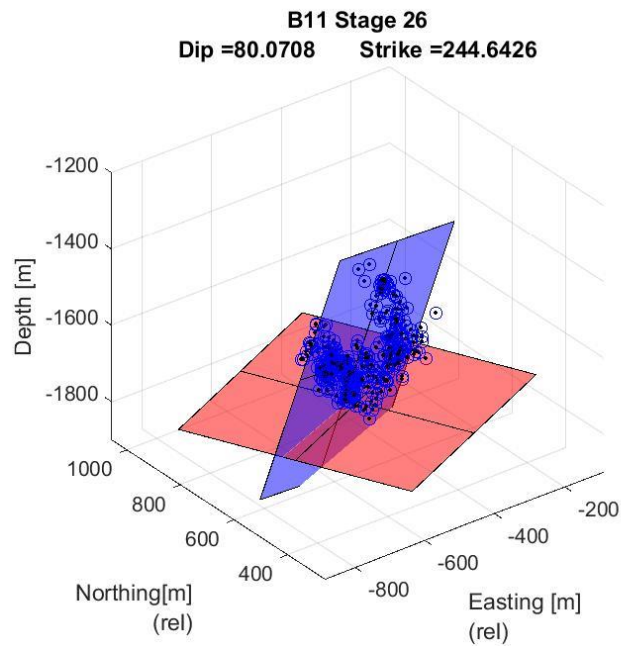


Figure 151 B11 stage 26 best fitting plane.

B11
Stage 27

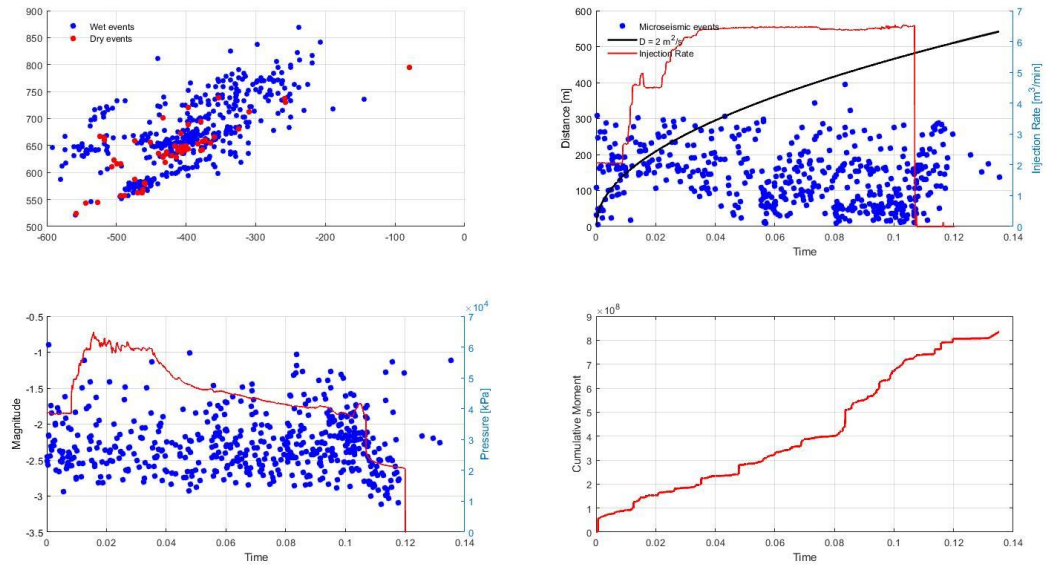


Figure 152 B11 stage 27 map view plot, r-t plot, magnitude plot and cumulative moment plot.

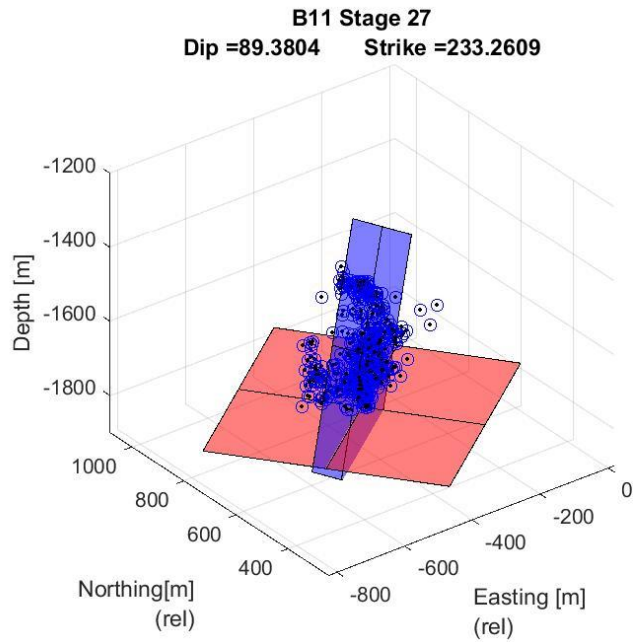


Figure 153 B11 stage 27 best fitting plane.

B11
Stage 28

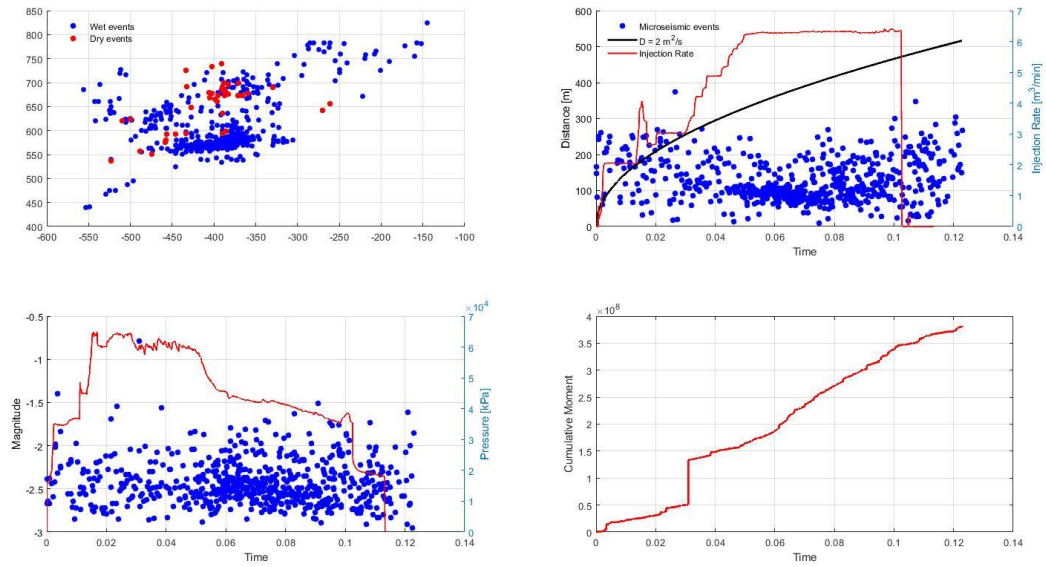


Figure 154 B11 stage 28 map view plot, r-t plot, magnitude plot and cumulative moment plot.

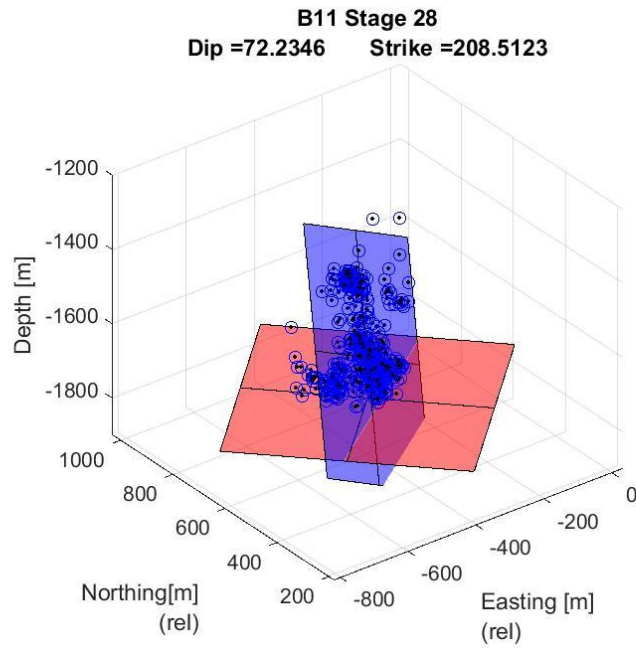


Figure 155 B11 stage 28 best fitting plane.

B11
Stage 29

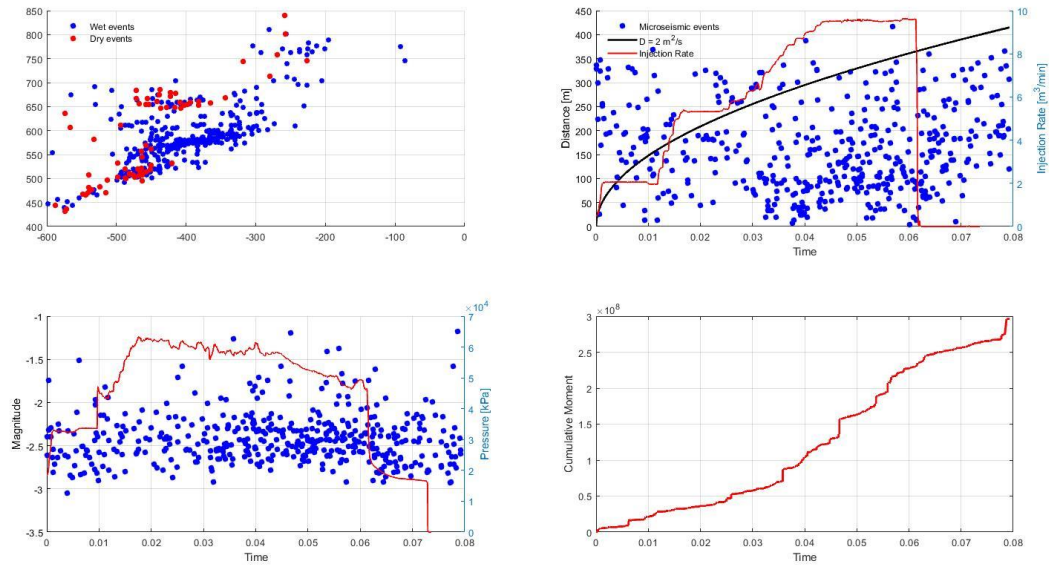


Figure 156 B11 stage 29 map view plot, r-t plot, magnitude plot and cumulative moment plot.

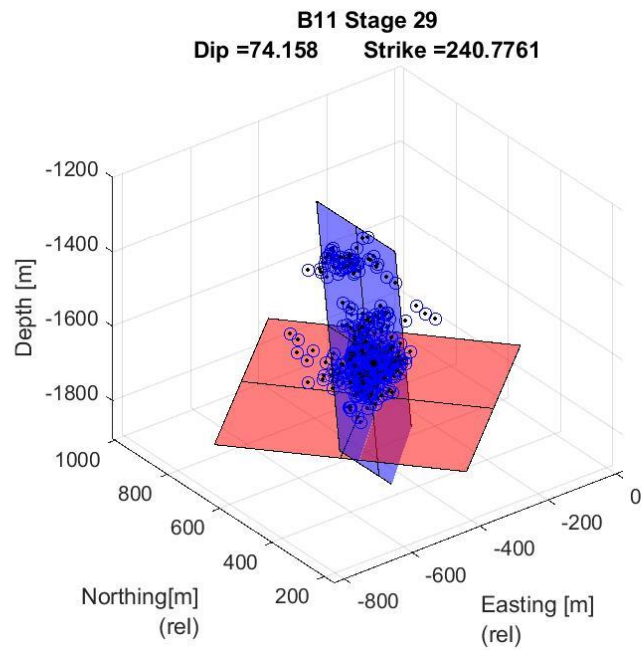


Figure 157 B11 stage 29 best fitting plane.

B11
Stage 30

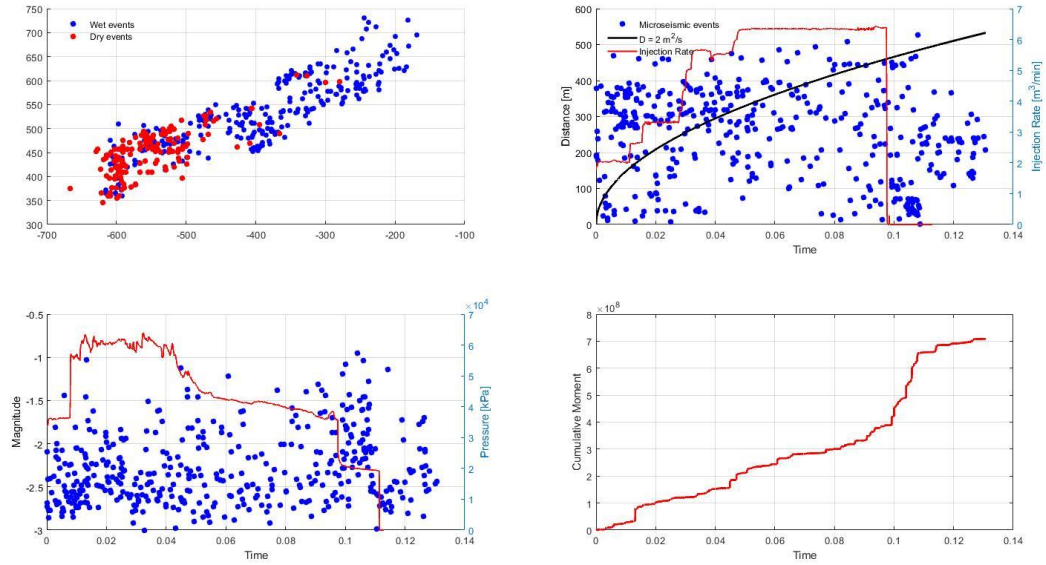


Figure 158 B11 stage 30 map view plot, r-t plot, magnitude plot and cumulative moment plot.

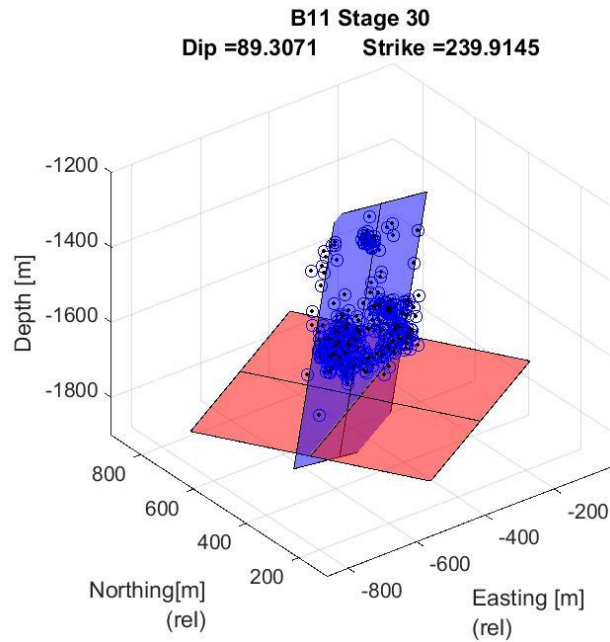


Figure 159 B11 stage 30 best fitting plane.

B11
Stage 31

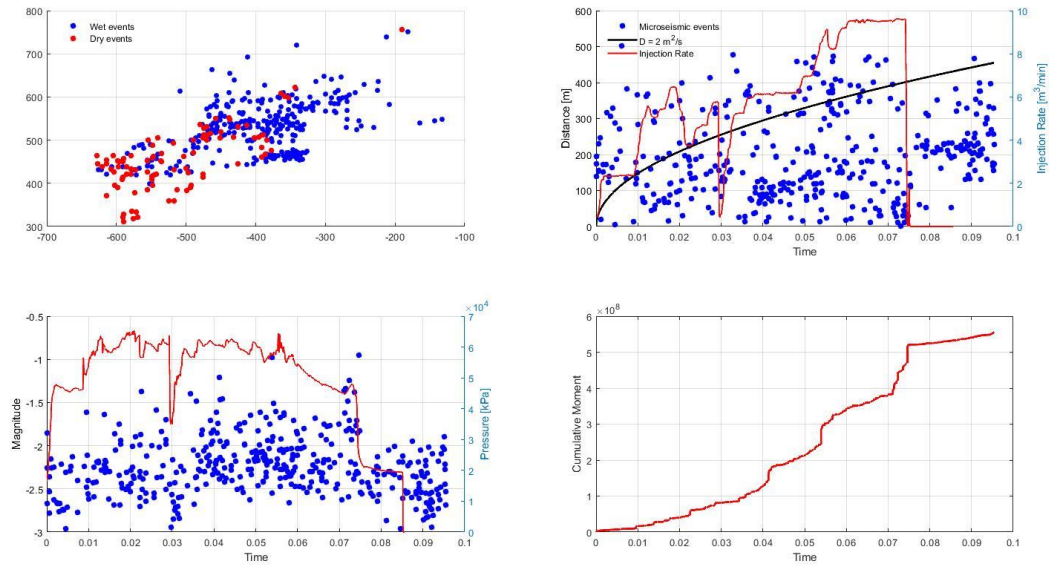


Figure 160 B11 stage 31 map view plot, r-t plot, magnitude plot and cumulative moment plot.

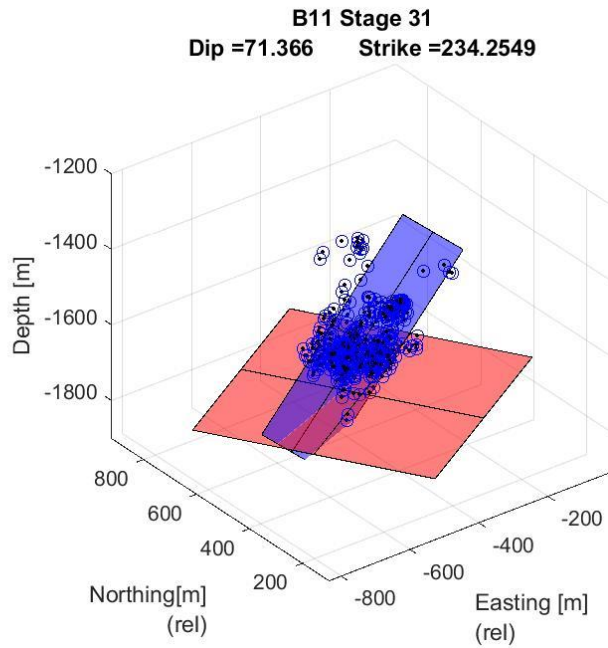


Figure 161 B11 stage 31 best fitting plane.

B11
Stage 32

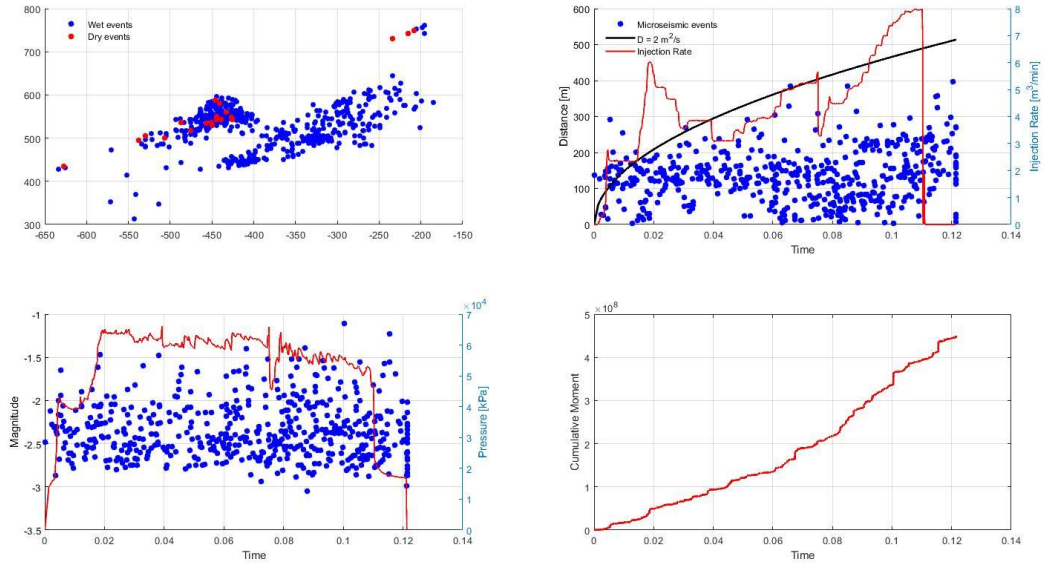


Figure 162 B11 stage 32 map view plot, r-t plot, magnitude plot and cumulative moment plot.

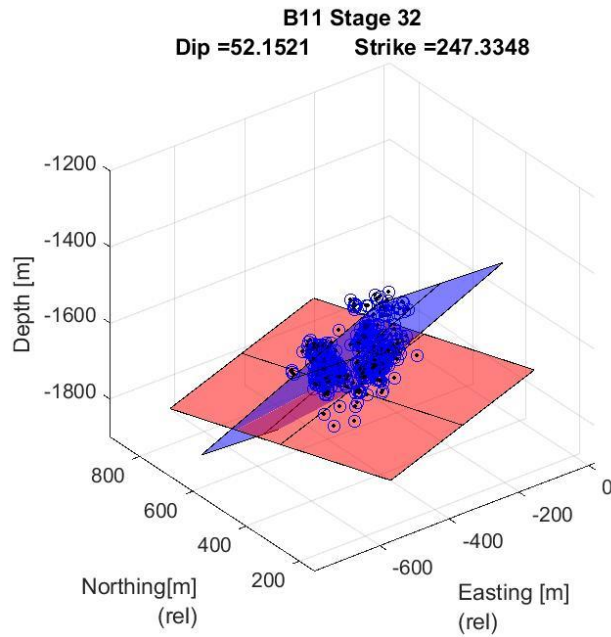


Figure 163 B11 stage 32 best fitting plane.

B11
Stage 33

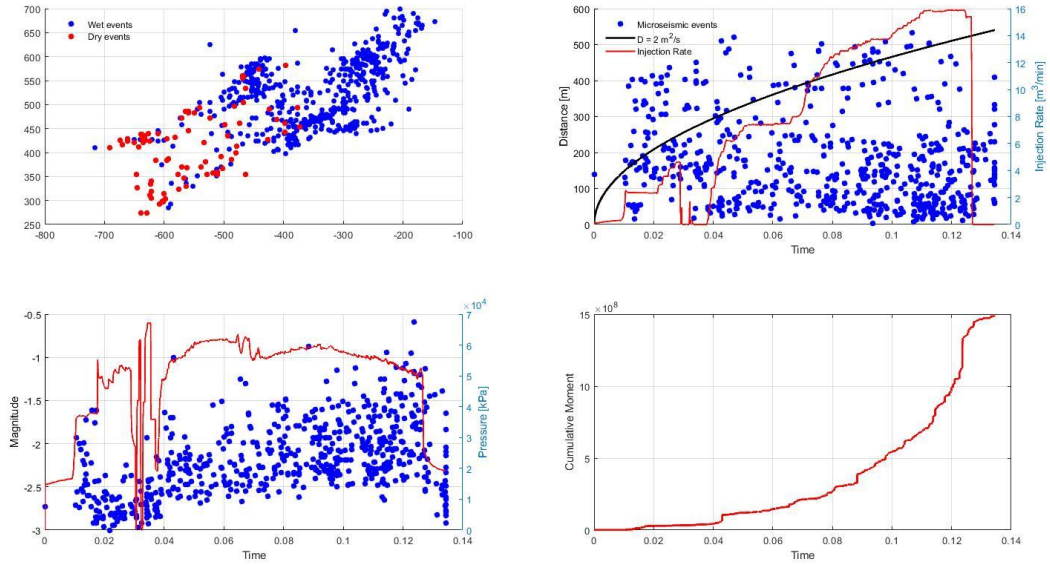


Figure 164 B11 stage 33 map view plot, r-t plot, magnitude plot and cumulative moment plot.

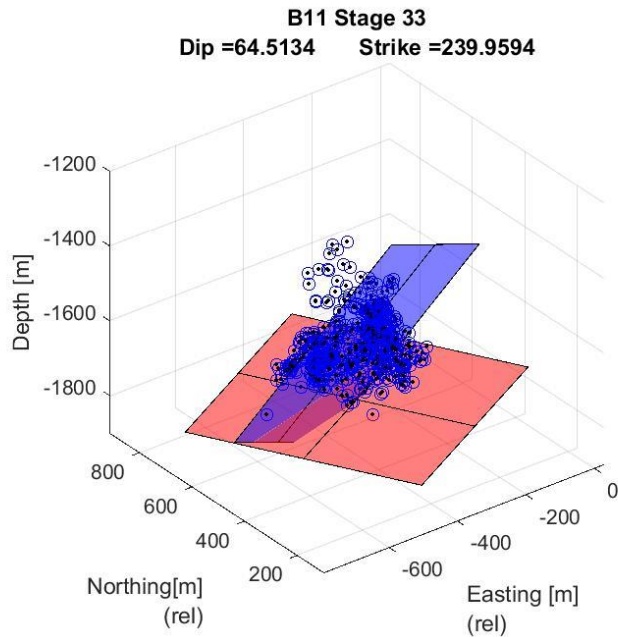


Figure 165 B11 stage 33 best fitting plane.

B11
Stage 34

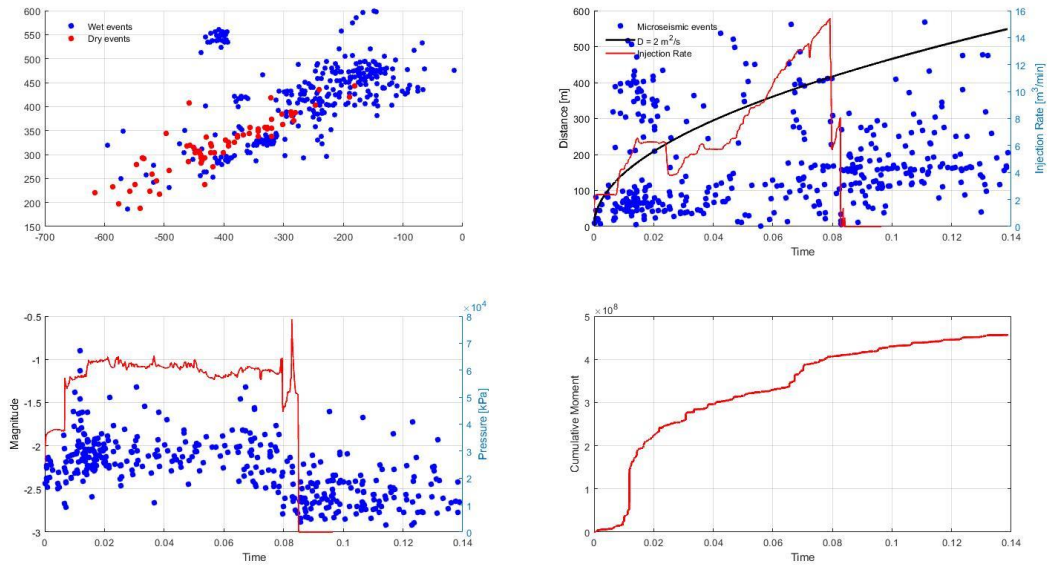


Figure 166 B11 stage 34 map view plot, r-t plot, magnitude plot and cumulative moment plot.

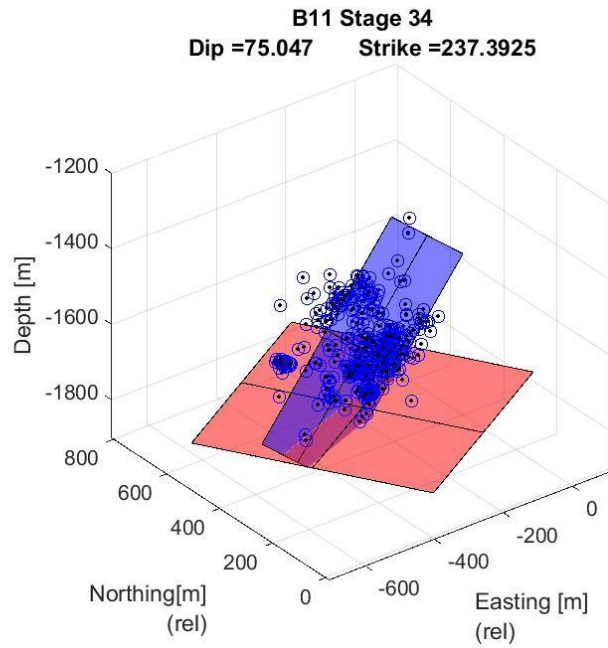


Figure 167 B11 stage 34 best fitting plane.

B11
Stage 35

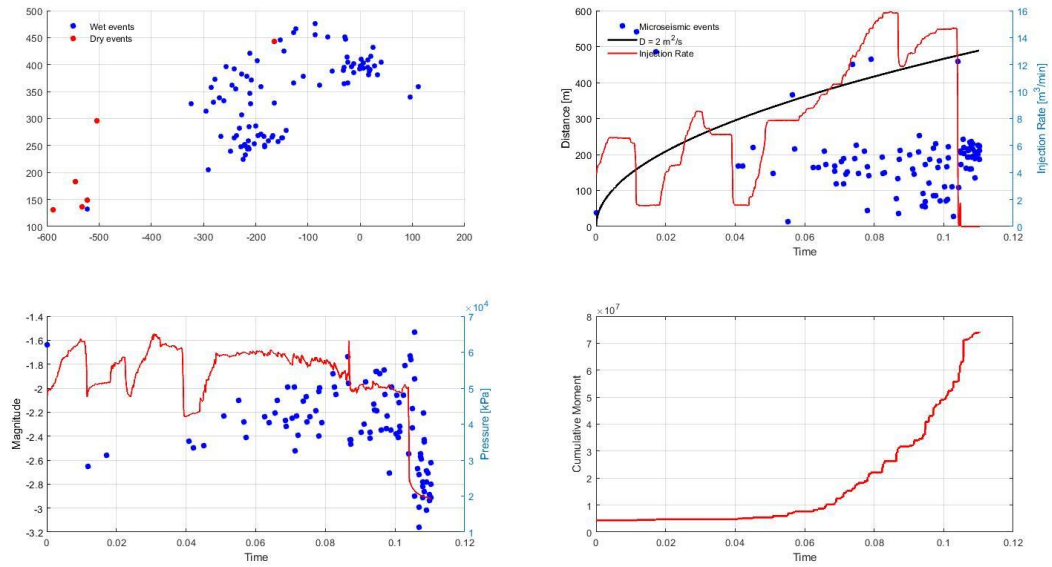


Figure 168 B11 stage 35 map view plot, r-t plot, magnitude plot and cumulative moment plot.

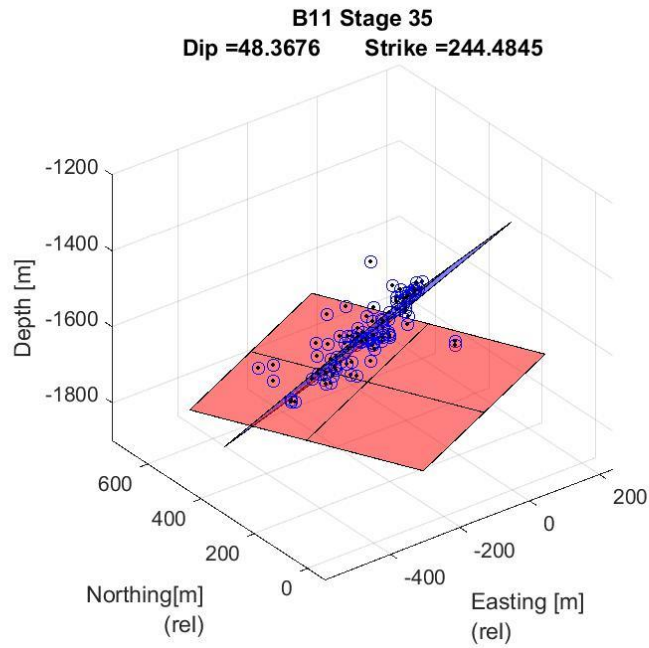


Figure 169 B11 stage 35 best fitting plane.

B11
Stage 36

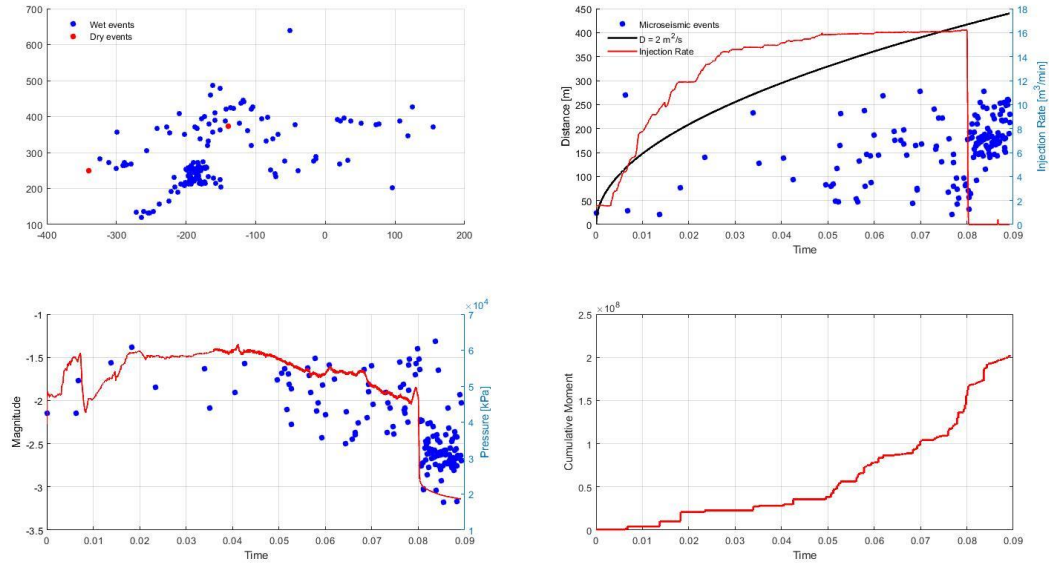


Figure 170 B11 stage 36 map view plot, r-t plot, magnitude plot and cumulative moment plot.

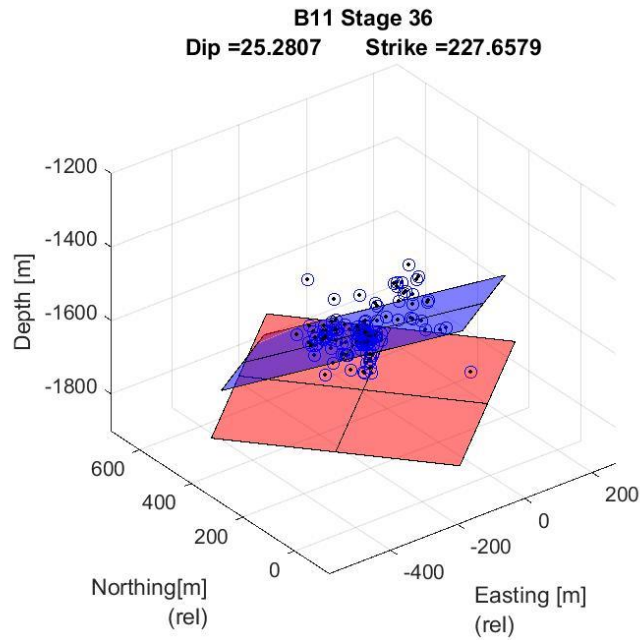


Figure 171 B11 stage 36 best fitting plane.

B11
Stage 37

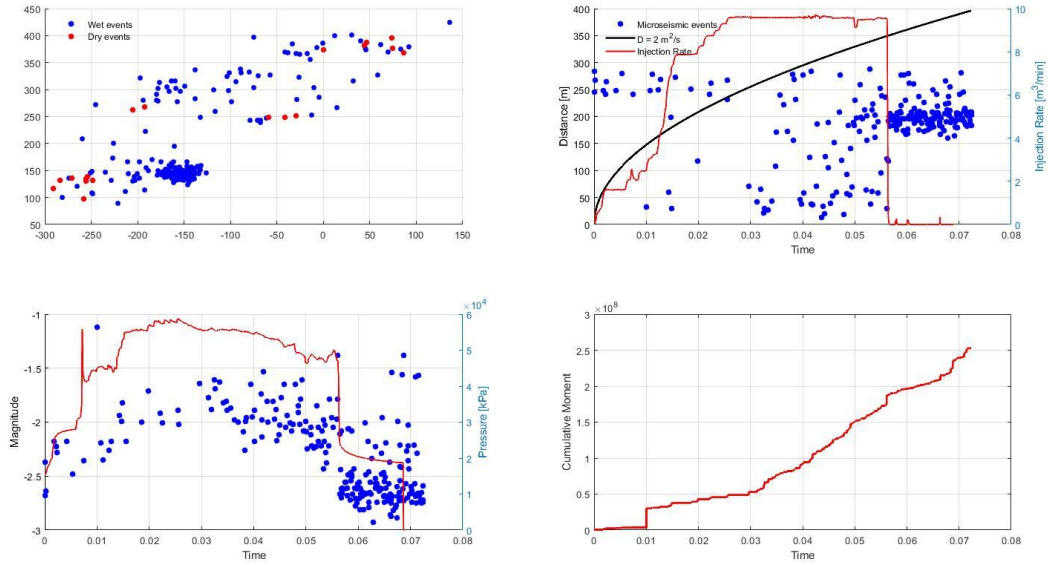


Figure 172 B11 stage 37 map view plot, r-t plot, magnitude plot and cumulative moment plot.

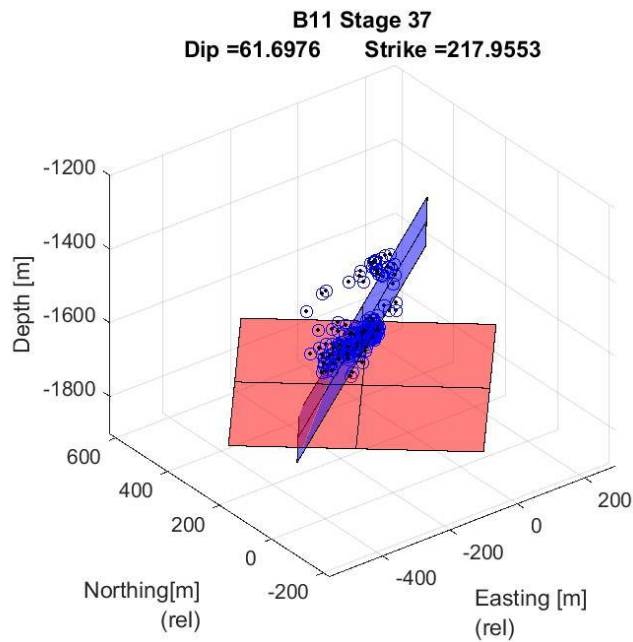


Figure 173 B11 stage 37 best fitting plane.

B11
Stage 39

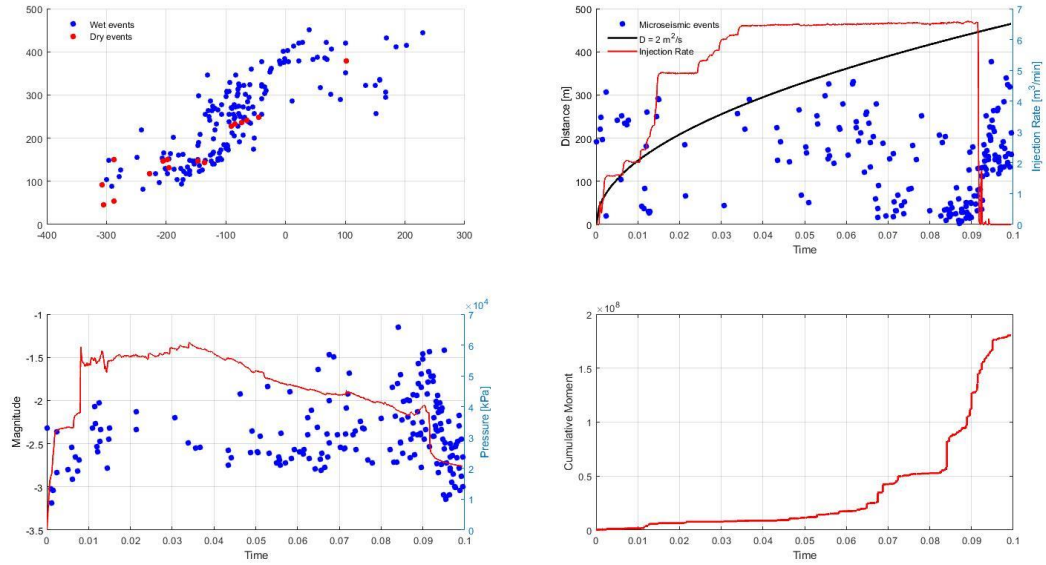


Figure 174 B11 stage 39 map view plot, r-t plot, magnitude plot and cumulative moment plot.

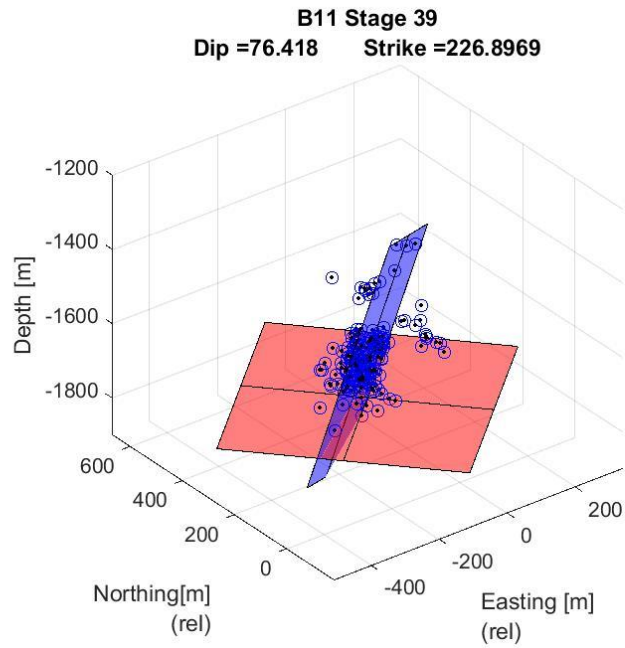


Figure 175 B11 stage 39 best fitting plane.

B11
Stage 40

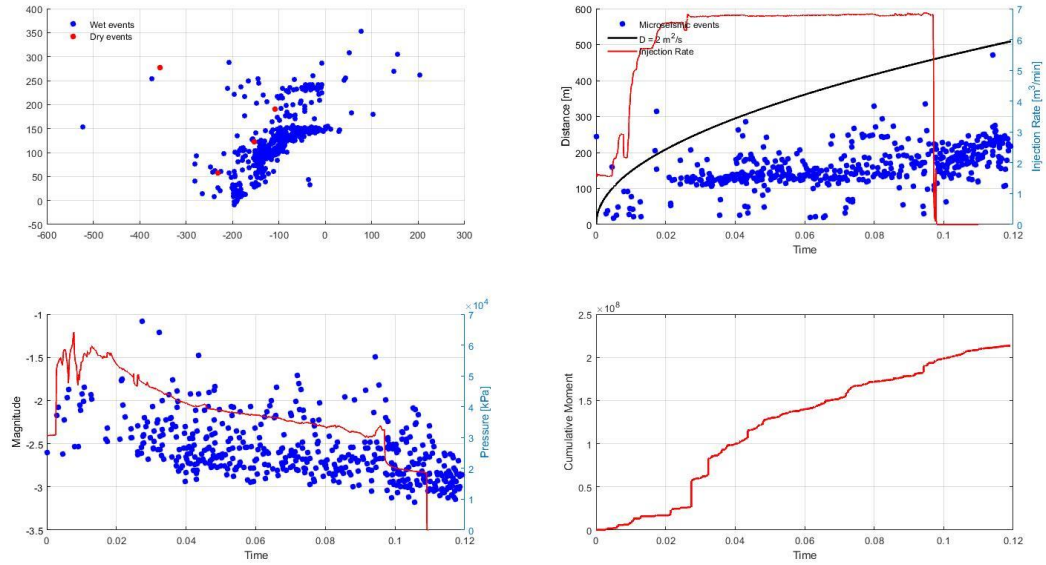


Figure 176 B11 stage 40 map view plot, r-t plot, magnitude plot and cumulative moment plot.

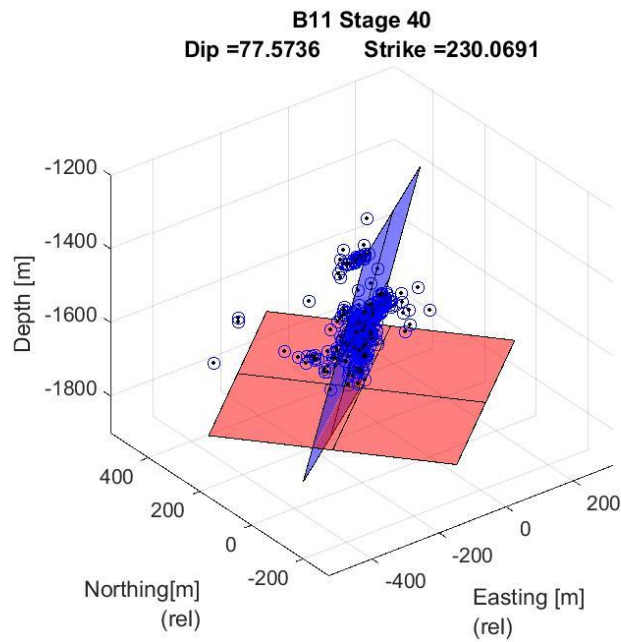


Figure 177 B11 stage 40 best fitting plane.

Bibliography

- Anderson, Paul F., F. David Gray, and DGC Inc Veritas. 2001. "Using LMR for Dual Attribute Lithology Identification." *SEG* 1-2.
- Bach, Torben, Thomas B. Espersen, Jacob M. Pedersen, Richard Hinkley, William R. Pillet, and Klaus B. Rasmussen. 2016. "Inversion of seismic AVO data." *Lecture Notes in Earth Sciences Springer Verlag 2000*, 12 22: 4.
- BGC Mistral Team. 2019. *Microseismic Evaluation User Manual*. Schlumberger.
- Boroumand, Neda. 2014. "Hydraulic fracture b-value from microseismic events in different regions." *GeoConvention 2014: FOCUS*.
- Boroumand, Neda, and Dr. Dave W. Eaton. 2012. "Comparing energy calculations: Hydraulic fracturing and microseismic monitoring." *GeoCovention 2012: Vission*.
- Cao, Richard, Ruijian Li, Chaohui Chen, and Alejandro Girardi. 2017. "Well Interference and Optimum Well Spacing for Wolfcamp Development at Permian Basin." *urtec*.
- Carafa, Michele M.C., and Gabriele Tarabusi. 2015. *the SHINE application*.
<http://shine.rm.ingv.it/index2.phtml>.
- Crain, E. R. 2017. *Crain's Petrophysical Handbook*. <https://www.spec2000.net/07-grlog.htm>.
- D.V. Satyanarayana Gupta, BJ Services and Peter Valkó, Texas A&M University. 2007. "Fracturing Fluids and Formation Damage." In *Modern Fracturing*, by Tony Martin Michael J. Economides.
2019. "Density Logging." *Wikipedia*. https://en.wikipedia.org/wiki/Density_logging.
- Earthworks. 2019. "Hydraulic Fracturing 101."
https://earthworks.org/issues/hydraulic_fracturing_101/.

- Grob, Melanie, and Mirko Van Der Baan. 2011. "Inferring in-situ stress changes by statistical analysis of microseismic event characteristics." *Canada, Arctic Technology* 1296-1301.
- Grob, Melanie, and Mirko van der Baan. 2012. "Statistics of microseismic events: implications of geomechanics." *GeoConvention 2012: Vision*.
- Gutenberg, B., and C. F. Richter. 1942. "Frequency and energy of earthquakes." 17–19.
- Gutenberg, Beno, and Charles Francis Richter. 1956. *Magnitude and energy of earthquakes*.
- Hanks, Thomas C., and Hiroo Kanamori. 1979. "A Moment Magnitude Scale." *JOURNAL OF GEOPHYSICAL RESEARCH*.
- Hobart M. King, Ph.D., RPG. 2016. "Utica Shale - The Natural Gas Giant Below the Marcellus."
- Horiba. 2010. "Frac Sand and Proppant Size and Shape." https://www.horiba.com/en_en/applications/materials/metal-and-mining/frac-sand-and-proppant-size-and-shape/#:~:text=The%20size%20range%20of%20the,106%20%C2%B5m%20%2D%2012%20%C2%B5m).
- Hummel, N., and S. A. Shapiro. 2012. "Microseismic estimates of hydraulic diffusivity in case of non-linear fluid-rock interaction." *Geophysical Journal International* 1441–1453.
- Jacobs, Trent. 2017. "Frac Hits Reveal Well Spacing May be Too Tight, Completion Volumes Too Large." *Journal of Petroleum Technology*.
- Jacobs, Trent. 2017. "Oil and Gas Producers Find Frac Hits in Shale Wells a Major Challenge." *Journal of Petroleum Technology* 69 (4). <https://pubs.spe.org/en/jpt/jpt-article-detail/?art=2819#:~:text=A%20frac%20hit%20is%20typically,well%2C%20called%20the%20child%20well>.

- Jafari, Mohammad Ashtari. 2008. "THE DISTRIBUTION OF B-VALUE IN DIFFERENT SEISMIC PROVINCES OF IRAN."
- Kijko, Andrzej, and Ansie Smit. 2017. "Estimation of the Frequency–Magnitude Gutenberg–Richter b-Value without Making Assumptions on Levels of Completeness."
- Malone, Mark, BJ Services, John W. Ely, and Ely & Associates. 2007. "Execution of Hydraulic Fracturing Treatments." In *Modern Fracturing*, by Michael J. Economides and Tony Martin.
- Manchanda, Ripudaman, Prateek Bhardwaj, Jongsoo Hwang, and Mukul Sharma. 2018. "Study Assesses Interference Between Parent, Child Wells In Horizontal Pad Developments."
- Martin, Tony, and Peter Valkó. 2007. "Hydraulic Fracture Design for Production Enhancement." In *Modern Fracturing Enhancing Natural Gas Production*, by Michael J. Economides and Tony Martin, 94-95.
- Maxwell, S., Molo Mack, Fengshou Zhang, D. Chorney, Sebastian Goodfellow, and Melanie Grob. 2015. "Differentiating Wet and Dry Microseismic Events Induced During Hydraulic Fracturing." 10.2118/178585-MS: 1-12.
- Maxwell, Shawn. 2014. "Interpretation of Microseismic Fracture Images." In *Microseismic Imaging of Hydraulic Fracturing: Improved Engineering of Unconventional Shale Reservoirs*, by Shawn Maxwell, 101-126. Society of Exploration Geophysicist .
- Popova, Olga. 2017. *Utica Shale Play*. U.S. Energy Information Administration.
2016. "Resistivity logging." *Wikipedia*. 04 09. https://en.wikipedia.org/wiki/Resistivity_logging.
- Schlumberger. 2020. *Schlumberger*. <https://www.slb.com/completions/well-completions/frac-plugs-and-sleeves/frac-plugs>.

- Shadlow, James. 2014. "A description of seismic amplitude techniques." *Journal of the Australian Society of Exploration Geophysicists* 154-163.
- Shapiro. 2015. "Seismicity and linear diffusion of pore pressure." In *In Fluid-Induced Seismicity*, by S. Shapiro, 118-163. Cambridge: Cambridge University Press. doi:10.1017/CBO9781139051132.004.
- Shapiro, Serge A., Carsten Dinske, and Cornelius Langenbruch, Freie Universität Berlin, Friedemann Wenzel, and Karlsruhe Institute of Technology. 2010. "Seismogenic index and magnitude probability of earthquakes induced during reservoir fluid stimulations." *MICROSEISMIC* 936-940.
- Smith, Langhorne B., Jr. 2015. *A geologic play book for Utica Shale Appalachian basin exploration, Final report of the Utica Shale Appalachian basin exploration consortium*. <http://www.wvgs.wvnet.edu/utica>.
- Spinningspark, Courtesy. 2011. *Gutenberg Richter law by low-end roll-off*. https://en.wikipedia.org/wiki/File:GR_law_roll-off.svg.
- Starr, Joel, and Kristen Dennis. 2016. "The Use of Diffusivity in Micro-seismic Analysis to Identify Pre-existing Fractures: A Case History in the Marcellus and Utica Shales."
- The MathWorks, Inc. 2015. *MATLAB Desktop Tools and Development Environment*. The MathWorks, Inc. <https://www.mathworks.com/help/matlab/ref/alphashape.html>.
- Wiemer, S. 2001. "A software package to analyze seismicity: ZMAP." *Seismological Research Letters*, 72(3) 373-382. <https://doi.org/10.1785/gssrl.72.3.373>.
- Wisselink, H.J. 2019. *point_to_line_distance*. <https://www.mathworks.com/matlabcentral/fileexchange/64396-point-to-line-distance>.

Zorn, Erich. 2016. *INTEGRATED ANALYSIS AND INTERPRETATION OF MICROSEISMIC MONITORING OF HYDRAULIC FRACTURING IN THE MARCELLUS SHALE.*

Zorn, Erich, Richard Hammack, and William Harbert. 2014. "SPE 168647 Time Dependent b and D-values, Scalar Hydraulic Diffusivity, and Seismic Energy From Microseismic Analysis in the Marcellus Shale: Connection to Pumping Behavior During Hydraulic Fracturing." *SPE International.*

Zorn, Erich, William Harbert, Richard Hammack, and Abhash Kumar. 2017. "Geomechanics of the Microseismic Response in Devonian Organic Shales at the Marcellus Shale Energy and Environment Laboratory (MSEEL) Site, West Virginia." *Unconventional Resources Technology Conference (URTeC) 6.*